NOVEL IMAGING APPLICATIONS FOR PHARMACEUTICAL MATERIALS AND FORMULATIONS

Adam Ward

Department of Pharmacy, School of Applied Sciences,
University of Huddersfield

A thesis submitted in partial fulfilment of the requirements for a Doctor of Philosophy in Pharmaceutical Sciences

Word Count: 53596

Page Count: 262

Copyright statement

Declaration

Some of the chapters of this thesis have been published in peer reviewed journals. Where this is the case, a note to the reader section is included in the relevant chapter to explain where aspects of the chapter have been published.

The experimentation using Isothermal Calorimetry (ITC) in Chapter 6 to determine potential interactions between Indomethacin and Soluplus was performed by Dr Ana-Maria Totea.

The extraction of the polysaccharide, Sesamum gum, from the leaves of the Sesamum tree was conducted in our lab by Dr Elijah Nep.

Acknowledgments

As I submit this thesis, I feel it is very important to thank a number of significant individuals that have helped me over the last few years.

First and foremost, I would like to thank my parents Alison and Michael who have supported me immensely over the last few years. I feel that it cannot be understated how important their advice was and how crucial they have been in keeping me level headed and focused on my research. Perhaps more importantly their love and confidence in me has helped forge me into the scientist and man I am today and for that I truly am grateful. Secondly, I want to thank my two brothers Matthew and Tim who helped create an environment for me to let off steam and laugh which not only helped keep me positive when times became tough, but also helped me make a significant and important breakthrough in my research.

Finally, I want to thank my supervisors who I have been privileged to know and work alongside during this PhD. The first is Dr Kofi Asare-Addo, I want to say it has been an absolute pleasure to work with and get to know you over the last four years, your determination to turn an undergraduate dissertation project into a PhD is the reason we are at this point today. The confidence you helped to develop in me and the freedom you allowed me to have in my research is testament to the number of research articles we have been able to publish during the last few years and the huge amount of fun we have had along the way. And to my co-supervisor Dr Karl Walton, you have been vital in helping to develop the use of focus variation microscopy within the field of pharmaceutics and I want to thank you for both your patience and time as I got to grips with the technique and began to test novel and complex surfaces. It truly was a pleasure to work with you.

To my team-mates, colleagues, and friends; Ana, Nihad, Maen, Benedict, Zayeem, Jack and Jess. Over the last 3 years it has been a pleasure to work with and get to know all of you and I am enormously grateful for all your help and advice with my own projects. You guys are truly the best and I wish you every success going forward not just in your own PhD's but also in the future too.

Contents

List of Figures

List of Tables

List of Equations

List of Abbreviations

Abbreviation	Description
ACF	Auto Correlation Function
AFM	Atomic Force Microscopy
API	Active Pharmaceutical Ingredient
APS	Active Pixel Sensor
BCS	Bio-pharmaceutical Classification System
CCD	Charge Coupled Device
CDS	Correlated Double Sampling
CE	Capillary Electrophoresis
CLSM	Confocal Laser Scanning Microscopy
CMC	Carboxy Methylcellulose
CMOS	Complementary Metal Oxide Semiconductor
DCP	Di-calcium Phosphate
DI	De-ionised
DSC	Differential Scanning Calorimetry
EMMA	Electrophoretically Mediated Microanalysis
FD	Freeze Dried
FVM	Focus Variation Microscopy
GDP	Gross Domestic Product
HG	Homogenised
HPMC	Hydroxy Propyl Methylcellulose
IDR	Intrinsic Dissolution Rate
ISO	International Organisation for Standardisation
ITC	Isothermal Calorimetry
LED	Light Emitting Diode
MCC	Micro Crystalline Cellulose
MEC	Molar Extinction Coefficient
MP	Mega Pixel
MRI	Magnetic Resonance Imaging
NIR	Near Infra-Red
NMR	Nuclear Magnetic Resonance
PAA	Polyacrylic acids
PEG	Polyethylene Glycol
PEO	Polyethylene Oxide
Sal	Autocorrelation length

SD	Spray Dried
SDI	Surface Dissolution Imaging
Sdr	Surface developed area ratio
SEM	Scanning Electron Microscopy
SLS	Sodium Lauryl Sulphate
Smr2	Areal Material Ratio
SPM	Scanning Probe Microscopy
Str	Texture Ratio
USP	United States Pharmacopeia
UV	Ultra Violet
XRPD	X-Ray Powder Diffraction

Abstract

This thesis presents a novel investigation into the use of two advanced imaging techniques in the field of pharmaceutics. The first is surface dissolution imaging (SDI). This technique utilises ultra-violet (UV) light and a Complementary Metal Oxide Semiconductor (CMOS) detector chip to image and film a wide range of dissolution phenomena. The second technique is focus variation microscopy (FVM). This powerful light microscope combines conventional microscopy with vertical scanning allowing for both high resolution images and surface topography data to be obtained. The introduction of this work thus provides a brief history and review into the design and development of dissolution imaging and the wide range of research that has currently been conducted. An introduction in to surface texture measurement and focus variation microscopy are also given to give the reader context as to how these are used in the detailed research.

This thesis focuses on the second generation of the surface dissolution instrument (SDi2) which has an additional dosage cell, compared to its predecessor the SDI300, and the ability to record images in both the UV and visible ranges simultaneously. Chapter 3 therefore details and describes the development of a methodology that allows the utilisation of dissolution imaging for the purposes of monitoring accurate swelling of hydrophilic matrices. The successful results showed a set of specific parameters needed to be followed in relation to both absorbance threshold and the width of the measurement zone. This developed method was also successfully used in the swelling determination of other hydrophilic polymeric matrices in chapter 4. The results also showed this methodology to be a material sparing technique as compared to the traditional methods of investigating swelling processes.

Chapters 5-7 uses gemfibrozil (GEM), indomethacin (INDO) and propranolol hydrochloride as model drugs in salt formation, solid dispersions and liquisolid compact formulations. Focus variation is used in understanding the surfaces that are prepared prior to intrinsic dissolution rate determination (IDR). Techniques such as X-ray powder diffraction (XRPD), differential scanning calorimetry (DSC) and scanning electron microscopy (SEM) were used for salt and solid dispersion confirmation as well as morphological characterisation. The results from the focus variation for both the salts and solid dispersions indicated that compacts prepared for IDR determination picked up the tooling “imprint” on the surfaces which can impact on IDR values obtained. A web-like phenomenon was also observed for the solid dispersions during IDR imaging which seemed to increase with increasing polymer content. This process explained the lower IDR values obtained for the solid dispersion relative to that of the “pure drug (INDO)”. The use of the whole dose cell showed the dissolution of the solid dispersion to increase with increasing polymer content. Chapter 7 also recorded the first simultaneous drug release and swelling of liquisolid compacts.

The information from this thesis therefore demonstrates the versatility and use of both imaging techniques in providing vital information for the formulator in the early stages.

Chapter 1 – General Introduction to thesis and a brief history of UV imaging

1.1 Imaging Sensors CCD and CMOS Technology

1.1.1 Introduction

In the field of imaging, two primary detector technologies have been developed. These are charged coupled devices (CCD's) and complementary metal oxide semiconductors (CMOS). Since the 1980's, development of CCD's has been influenced strongly by the military and by the scientific community, more specifically biologists, chemists and astronomers (1). This influence led to technological developments such as:

- Back thinning – To increase sensitivity to ultraviolet (UV) and near infra-red (NIR) light sources.
- Direct detection of X-rays.
- Micro lens arrays – to increase effective detection area.
- Deep depletion to increase near infra-red (NIR) sensitivity.

In contrast, the development of CMOS detector chips was driven largely by a necessity to reduce costs and extend battery life in consumer devices such as mobile phones and digital cameras (1). Therefore, many of these improvements were engineering advancements such as:

- Increased sensitivity due to a reduction in pixel size.
- Utilisation of standard manufacturing processes.
- Reduction in the number of support circuits needed.

1.1.2 Charged Coupled Devices

A CCD image sensor contains a two dimensional array of photodiodes used to convert optical light into electrical charge. Storage buckets or wells capture and store the charge, whilst a readout register and readout amplifier convert the charge into an analogue signal. To obtain an image, the accumulated charge must be transferred from one horizontal row to another until the charge reaches the readout register. Once here, the accumulated charge is transferred horizontally to the read out amplifier and converted into a signal (1). Figure 1-1 displays a schematic representation of CCD image sensor and the movement of charge throughout the circuitry. A CCD image sensor offers a number of advantages over CMOS image sensors however there are also some limitations that need to be considered. Table 1-1 displays a summary of the advantages and limitations of CCD image sensors.

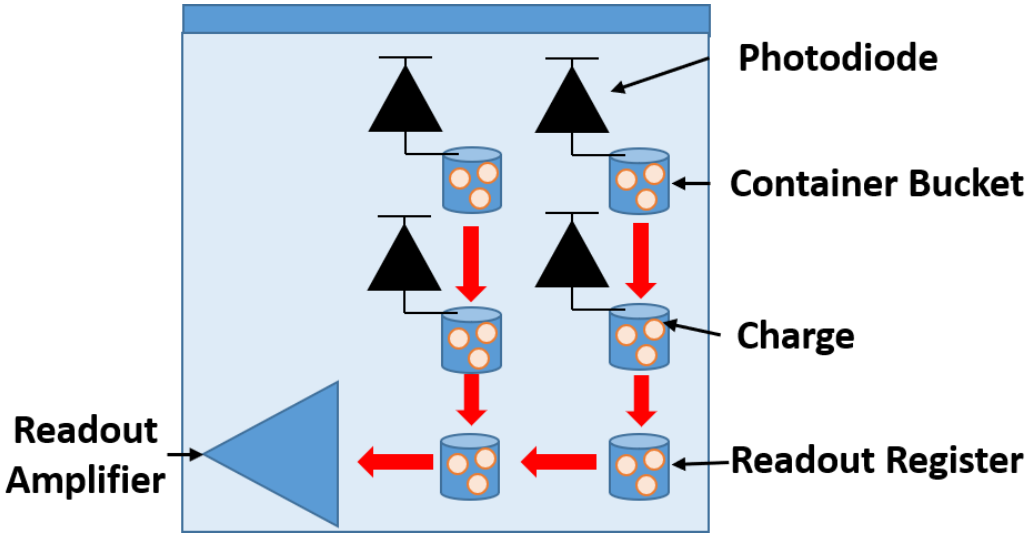

Figure 1-1 - A schematic representation of a Charge Coupled Device (CCD) image sensor including photodiodes, read out register, read out amplifier and movement of charge.

Table 1-1 - A summary of the advantages and limitations of CCD image sensors.

Advantages	Limitations
Lower Noise	Higher power consumption (1-5 W)
Smaller pixel size	Very restrictive temperature and illumination ranges
Lower Dark Current	Potential for blooming and smearing (2)
100 % fill factor	High power dissipation
Greater sensitivity	Limited Readout rate
Electronic shutter without artefacts	Sensitive to radiation

1.1.3 Complementary Metal Oxide Semiconductors (CMOS)

Current UV imaging systems utilise a CMOS based image detector to record images.

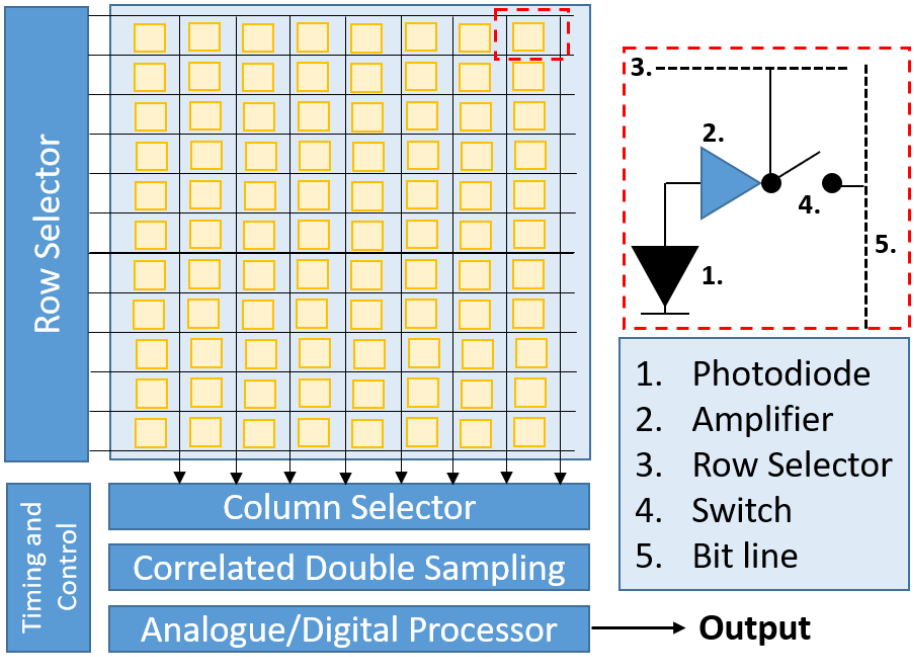

Figure 1-2 - A schematic representation of CMOS active pixel sensor with row and column selection, correlated double sampling (CDS), analogue to digital processor and timing control.

The architecture of a CMOS imaging chip is different from that of a CCD in that each photodiode is connected to an amplifier (1). This combination is referred to as an active pixel sensor (APS) (3), a schematic representation of CMOS architecture is displayed in Figure 1-2.

Typically, multiple pixels are arranged into a pixel array in a CMOS detector. The term ‘pixel’ was made popular by the digital photography industry to advertise advancements in digital cameras. Effectively, a pixel is a funnel that produces a current of electricity when a photon of light of a given wavelength contacts the inside of the funnel (4). Typically, a single pixel can range between 5 and 10 μm^2 in size. APS have some advantages over CCD’s in that incorporating an amplifier into each pixel greatly improves pixel performance. Power use is also lower in APS as the amplifier is only activated upon readout. In early designs, APS suffered from fixed pattern noise due to wafer process variations. However, current versions have removed this issue due to the addition of correlated double sampling (CDS) circuits which effectively eliminate variations in background readout (5). It is important to state that a number of alternative pixel circuit designs can be found in the market depending on application. These are summarised in Table 1-2.

Table 1-2 – Alternative pixel circuit architecture found in CMOS detectors and their use.

Pixel Circuit	Description
Passive Pixel	The first CMOS imager, the circuit is based on photodiodes without internal amplification. Despite having a small pixel size and large fill factor these circuits suffer from low sensitivity and high noise (6).
Photogate (PG) APS	Introduced in 1993, it utilises principles obtained from CCDs. These circuits transfer charge and utilise CDS circuits to offer a low noise operation. These circuits are suitable for low light operations (6).
Logarithmic APS	Logarithmic APS are suitable for high dynamic range applications but do suffer from fixed pattern noise. These circuits are typically found in silicon retinas (2).
Capacitive transimpedance amplifier APS	CTIA APS were designed to reduce fixed pattern noise. These pixels are capable of achieving low FPN whilst also achieving high gain and low read noise (7).
Pinned photodiode pixel	Pinned photodiodes were previously used in CCDs. These pixels offer lower pixel noise and reduced dark current, and therefore are an alternative to PG-APS due to higher sensitivity (6).
Complementary APS	Refers to a highly integrated high performance CMOS image sensor designed in the sub quarter micron range. These sensors have low power consumption and high voltage capability (8).

CMOS detectors offer many advantages over CCD sensors including; lower power consumption, a higher integration capability, lower cost of manufacture and the use of a singular power supply. However, some limitations of CMOS detectors include; higher noise, lower image quality, lower sensitivity, and a limited dynamic range.

1.2 Early Literature on UV Imaging as a Scientific Technique

One of the earliest published references to UV imaging was first reported in Analytica Chimica 570 in 2006 (9). Groups from Tallinn University of Technology and the University of York looked to develop a method for real time visualisation of reactions performed via electrophoretically mediated microanalysis (EMMA). This was largely achieved through the use of a complementary metal oxide semiconductor (CMOS) active pixel sensor and an Ultra-Violet (UV) light source.

The design of the CMOS detector was fundamentally based on a detector developed by the University of York and the University of Manchester Institute of Science and Technology. They utilised a charge coupled detector (CCD) along with a multi wavelength UV light source provided by a fibre optic bundle (10). The authors reported that whilst the manufacturing process of CCD's allowed for very high quality low noise sensors, CMOS active pixel sensors allowed for high speed imaging at a much lower cost. Further positives for the switch to a CMOS detector included:

- Reduced contribution from dark current and shot noise – due to the high levels of UV light used and a short exposure time.
- No mechanical shutter – this allowed for a 100 % duty cycle compensating for the lower sensitivity when compared to a front illuminated CCD sensor.

A schematic representation of the first UV imaging set-up is displayed in Figure 1-3. A review of the CCD literature also revealed more information about the detector including a glass slide, phosphor coat and a fused silica cover slip.

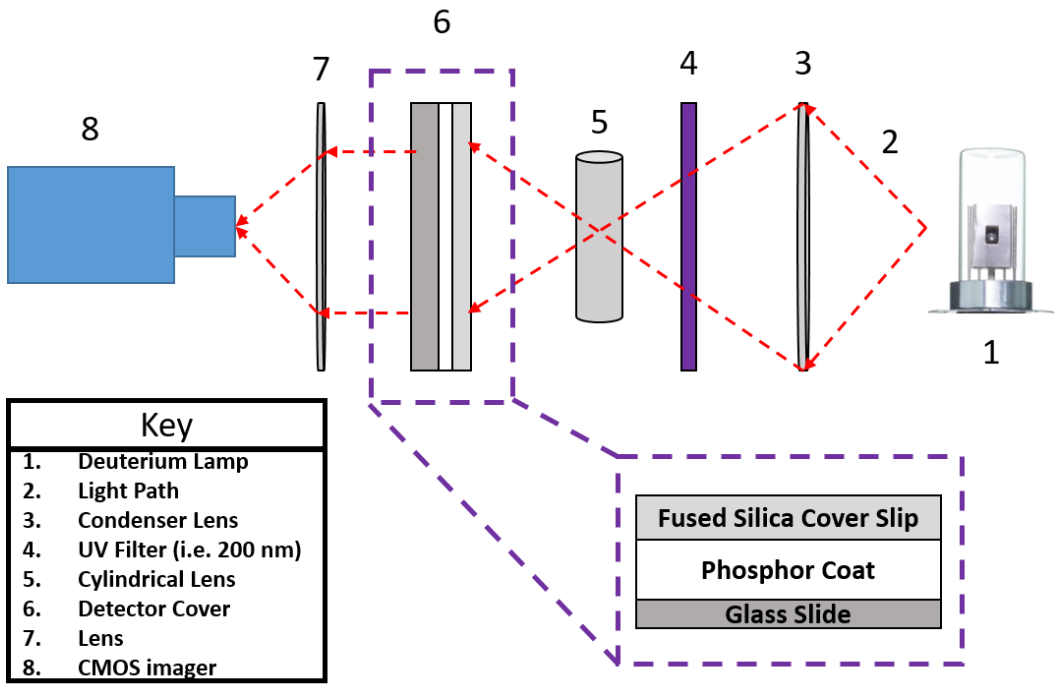

Figure 1-3 - A schematic representation of the layout of the initial CMOS based absorbance detector, consisting of a CMOS imager, phosphor coat and UV light source.

To produce the detector, a glass microscope slide was coated with a UV sensitive phosphor coat. This phosphor coat allowed UV light in the region of 200 to 400 nm to be converted to visible light in the region of 540 to 580 nm. To protect the phosphor coat, a fused silica cover slip was glued into place. Any image formed on the phosphor coat was relayed onto the imager using standard camera lenses.

The resulting conclusions from this study were that for the first time a CMOS detector could be used for the visualisation of chemical reactions and highlighted the wider benefits of UV imaging. Fundamentally, this reported work laid the foundations for a new novel area of chemical analysis.

1.3 Commercial Development of UV Imaging

Paraytec Ltd. was founded in 2005 as a spin out company of the University of York, after filing a patent for an ‘optical assembly and method for detection of light transmission’(11), Paraytec launched the D100 Actipix UV Imaging detector. The D100 was the first commercially available UV imaging detector chip and opened the door to researchers to test new areas of research as well as various applications.

1.3.1 – Actipix D100 Chip 2007 to Early 2010

Many of the earliest works using a commercial UV imaging detector came as a collaboration of Paraytec with a number of academic partners often from the University of York. Many of these early studies focused on the use of the technique within bio-chemistry often focusing on capillary electrophoresis (CE) and the measurement of bio-chemical entities.

In early 2007, a research article was published that documented the use of UV imaging in combination with CE to measure reactions of the enzyme penicillinase with a variety of substrates. The prototype D100 UV imaging chip was used to image two capillary tubes, one containing penicillinase whilst the other was used as a blank reference. The

paper concluded the use of UV imaging to be a success as not only could the reaction be ‘filmed’ but also rapid screening of enzymatic processes could be achieved often with excellent precision (12).

This research paper was subsequently followed by two further research articles using the same methodology. The first article also used penicillinase however, this article went on to incorporate more substrates including antibiotics such as amoxicillin and carbenicillin (13). The second research article employed the prototype D100 chip with a different enzyme in the form of yeast alcohol dehydrogenase. This article also reported an increase in the number of parallel capillaries used in the methodology from 2 to 6 allowing for 5 simultaneous reactions to be measured (14). This research article was fundamental in the development of UV imaging as an analytical technique as it started to show the versatility of the technique. From 2008 to early 2010 five more research articles were published further cementing the use of UV imaging within the field of biochemistry (combining UV imaging with CE)(15-19).

1.3.2 The SDI300 system – 2010 to 2014

In early 2010, Paraytec Ltd. licensed the Actipix D100 technology to Sirius Analytical Ltd. based in East Sussex. This was subsequently followed by the release of the SDI300 system. The SDI300 system was a purpose-built UV imaging system combining the UV imaging detector with a syringe pump, water bath and UV light source (Figure 1-4).

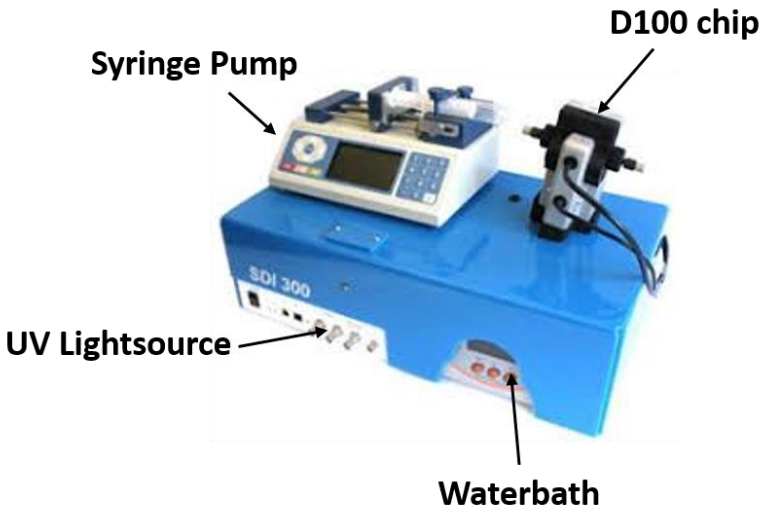

Figure 1-4 – A schematic of the SDI300 UV imaging system detailing the key components of the unit.

Paraytec Ltd. also began to collaborate with the University of Copenhagen and began to establish the use of UV imaging within the field of pharmaceutics.

In late 2010, a paper was published by the Østergaard research group in the University of Copenhagen detailing the use of UV imaging for the measurement of nicotine release from a transdermal patch (20). The primary purpose of this work was to determine and characterise UV imaging as a tool for performing *in vitro* drug release studies. To achieve this the group fixed a small section on nicotine transdermal patch to the centre of the D100 chip before flowing a phosphate buffer over its surface. These results were then compared to data taken from a paddle over disk test. The results from this study showed that qualitatively, release profiles from the SDI system agreed with release profiles taken from the paddle over disk method. Also, real-time visualisation of nicotine release was achieved by the system. In conclusion to this study the authors highlighted that UV imaging had the potential to become an important platform for conducting *in vitro* drug release studies. This work was important to the field of UV imaging as it opened the possibility for the new SDI300 system to be used not just in bio-chemistry but also in the field of pharmaceutics.

5 further research papers came out of research from groups within the University of Copenhagen and covered a wide range of pharmaceutical materials and behaviours including; Active single crystal dissolution (21), hydrophillic matrices (22), drug release from hydrogels (23,24) and drug release from oils (25).

Alongside, these articles other groups began to use the technology in other areas of pharmaceutics. Groups from the University of Otago in New Zealand collaborated with the University of Copenhagen to investigate early dissolution events of the model drug amlodipine by combining UV imaging with Raman Spectroscopy. The primary aim of this research was to establish a methodology for characterising dissolution events close to the surface of a solid compact. This was to be achieved by comparing the dissolution profiles of the amlodipine besylate salt with the amlodipine free base to determine if any solvent mediated transitions occurred, once this was complete, Raman spectroscopy would be used to confirm any hypothesis. Through UV imaging, the authors suggested that a transition was occurring between amorphous amlodipine besylate and amorphous free base forms. Raman spectroscopy subsequently confirmed this behaviour by finding that the amorphous samples recrystallised to the monohydrate form during dissolution. This work further highlighted the versatility of UV imaging by combining the technique with another powerful analytical technique. This particular research paper was ground breaking for UV imaging as it paved the way for the system to become an important analytical tool in the field of pharmaceutics (26).

Groups from The University of Copenhagen continued to develop the technique with six more publications investigating a variety of topics from Bio-relevant dissolution (27,28) and sub-cutaneous drug delivery (29) to novel materials such as nanocrystal powders (30) and coated extrudates (31). Additionally, the group also coupled UV imaging with Finite elemental solutions as a novel analytical combination (32).

In 2013, a research group from De Montfort University based in Leicester, UK found a new novel use for UV imaging in the assessment of co-crystal formulations. Their first paper established the methodology for using UV imaging in combination with Raman spectroscopy for *in situ* monitoring of the dissolution of a co-crystal. The primary aim of this work was to investigate if solvent mediated transitions occurred during the dissolution of a carbamazepine-nicotinamide co-crystal as these can greatly reduce apparent solubility and dissolution of a co-crystal. The authors discovered that the intrinsic dissolution rate (IDR) of the co-crystal decreased slowly during dissolution. This was confirmed to be due to a slow recrystallisation of carbamazepine to carbamazepine dihydrate during dissolution (33).

The group then built upon this work by publishing a paper later in the year which investigated the influence of additives on the dissolution performance of carbamazepine-nicotinamide cocrystals using UV imaging as the dissolution tool. The authors investigated the influence of the surfactants SLS and Tween 80 on both solubility and dissolution of manufactured co-crystals. The authors initially found that the addition of the additives during co-crystal manufacture had little effect on the solubility of the co-crystal. The authors also observed as a result of footage from the SDI imaging system that each additive had an opposite effect on the IDR of the co-crystal. SLS was found to significantly increase the IDR, whilst the Tween 80 was found to significantly decrease the IDR of the co-crystal (34).

The University of Copenhagen continued to contribute to the field of UV imaging going into 2014 with papers detailing the use of UV imaging for the measurement of Insulin diffusion (35), Microenvironmental pH changes (36), and further details for using UV imaging in combination with Raman spectroscopy (37). These papers also culminated in a small review article summarising UV imaging as a tool for *in vitro* dissolution (38).

A group based in Switzerland also published an article in 2014, using UV imaging alongside other analytical techniques detailing the biorelevant dissolution of a number of poorly soluble weakly acidic drugs. The authors aimed to mathematically model the fractal-like kinetics of the compounds using IDR generated by the SDI system. The authors found that fractal-like dissolution behaviour was found with all model compounds and that Intrinsic dissolution rate exhibited a power law at early time points before reaching equilibrium and a constant dissolution rate towards the end of the experiment. The authors also detailed their future aspirations for this investigation with potential works investigating if similar behaviour could be observed with drugs other than weak acids (39).

Overall, this initial four year period since the release of the SDI300 system was very productive with many research groups across the globe contributing to the development of UV imaging as a novel dissolution technique within the field of pharmaceutics.

1.3.3 The SDI300 system – 2015 to 2017

By early 2015, surface dissolution imaging was fast becoming a novel and robust technique with multiple publications and novel pharmaceutical uses. In early 2015, the University of Copenhagen continued using UV imaging for the assessment of insulin dissolution from sub-cutaneous hydrogel mimics. The article identified the role of pH in insulin dissolution behaviour in hydrogel-based subcutaneous tissue surrogates and focused on the influence microenvironmental pH changes had on the release of Insulin and how these could be imaged and tracked via UV imaging (40).

In 2015, Kuentz from the University of Northern Switzerland published a review article which detailed and described a wide range of analytical techniques used for real time small scale dissolution and precipitation testing. This article described many of the

novel features of UV imaging and helped to highlight how far the system had come from its conception in early 2006 (41). His second paper was a collaborative piece with a group in Germany to investigate the feasibility of using UV imaging for the measurement of drug-phospholipid complexes. The research paper concluded that UV imaging revealed pronounced surface swelling of the solid dispersions tested in the study and that only the monoacyl PC was found to substantially enhance *in vitro* dissolution compared to pure drug. They also claimed that understanding gained from UV imaging would further support future development of solid drug dispersions (42). An interesting development in 2015 was a paper published by a group from the Novartis Institute for Biomedical Research based in Basel, Switzerland. Whilst this group did not explicitly use the SDI300 system, they did utilise the D100 chip to conduct Taylor dispersion analysis in a similar manner to previous publications published between 2007 and 2010. Primarily their aim was to rapidly screen antibody candidates using the looped capillary method and the Actipix detector. Their experiments were largely successful and highlight that there was still a need and use for the original looped capillary design (43).

Between, 2016 and 2017, 6 more research articles using UV imaging were published. In a similar trend to previous years 5 of these articles came out of groups from across the University of Copenhagen and investigated a variety of topics including an investigation into the performance of UV imaging (44), drug release from lipid implants (45), dissolution enhancement of a poorly soluble drug (46), and phase separation of implants (47). Their published works also included a summary/review article into the use of UV imaging within formulation development (48).

The remaining article published over this period came out of the group based at De Montfort University. In the paper, the authors proposed a new methodology using UV imaging to calculate both solubility and diffusion coefficients simultaneously. Principally, a 2 step optimal method was proposed based on Fick's 2nd law of diffusion and measurements obtained from the UV imaging apparatus. The author concluded that results demonstrated that the new proposed method could be used to determine both coefficients with a reasonable level of accuracy. The authors also stated that this indicated that UV imaging may provide a new opportunity to accurately measure the solubility and diffusion coefficients of a poorly water-soluble drugs simultaneously and rapidly (49).

1.3.4 – 2018 publications and the release of the SDi2 system.

4 more articles were published in 2018 using the SDI300 system. These included a further article on subcutaneous delivery using implants (50) and a review article on UV imaging (51) from the University of Copenhagen. Also, a group based in Singapore published an article using UV imaging to investigate the effects of excipient shielding on initial drug release (52). The final article was a collaboration project between the University of Greenwich and Pfizer UK. In this article UV imaging was used to assess high quality co-crystals of carbamazepine formed via twin screw hot melt extrusion (53).

2018 also introduced a newly developed instrument in the form of the SDI2 system, an upgraded version of the SDI300. Sirius Analytical now trading as Pion Inc, developed the system from the ground up with the new system showing many improved features including:

- Automated PC controlled pumps, valves and fluid lines replacing the need for a syringe pump.
- An improved detector with an increased resolution and imaging area.
- A robust purpose built flow through cell removing the need for fragile quartz cells.
- A novel whole dosage cell mimicking a USP 4 flow through cell.
- LED based UV light sources removing the need for a UV light box and filters.
- Dual Imaging capabilities and dual buffer support enabling *in situ* transfer of dissolution media.
- Digital temperature control and an improved software package.

To conclude this chapter, UV imaging has grown from strength to strength on the back of the SDI300 system showing robustness, versatility, and novelty in the assessment of a wide range of pharmaceutical ingredients and materials. The following chapters of this thesis will continue to develop UV imaging by testing a number of pharmaceutical materials on the new SDI2 system. This new system is the main feature of this thesis and will be discussed in more detail throughout the following chapters.

1.4 Primary goal of this thesis – UV Imaging

The primary aim of this thesis with regards to UV imaging is to establish the use of the SDI2 system as a routine dissolution instrument capable of providing robust and accurate data in the measurement of pharmaceutical actives, excipients, and formulations. To achieve this, a number of milestone objectives will be explored throughout this thesis:

1. Develop an operational methodology for the SDI2 system exploring all of the systems features and capabilities.
2. Test any developed methodologies with different classifications of pharmaceutical materials to build up a knowledge base and aid method development.
3. Improve system versatility and reliability by identifying areas of improvement in the system and its operation.
4. Conduct comparative testing between already established techniques and the SDI2.
5. Highlight and showcase how the novel features of the SDI2 system can be a benefit to a formulator.

Chapter 2 – General Introduction to Surface Texture Measurement

2.1 – Surface Texture Measurement and Optical Instruments

2.1.1 Background

In the field of mechanical engineering, surface texture measurement plays a crucial role in the development of a component. It is estimated that surface defects cause approximately 10 % of all manufactured parts to fail, which can have a significant impact on a nation's gross domestic product (GDP). In the early development of surface texture measurements, a contact stylus method was used. This involved tracing a single line across the surface of the part and recording the vertical motion of the stylus. This produced a surface profile measurement and was particularly useful in providing enough information to control production of a part. Alongside, the development of contact stylus instruments, optical instruments were developed which allowed for non-contact measurements to be achieved and in some cases at a faster rate than with the conventional stylus instruments.

2.1.2 Profile and Areal Measurement

To understand surface texture measurement, it is important to understand profile and areal surface measurement. Surface profile measurement is the measurement of a single line across the surface which can be represented mathematically as a height function with lateral displacement (z(x)). Areal surface texture measurement is described as the measurement of an area on the surface that can be defined mathematically as a height function with displacement across a plan (z(x,y)). Areal surface measurement offers many benefits over profile measurement including; a more realistic representation of the whole surface with greater statistical significance, Lower chance of significant surface features being missed and provides a better visual record of the overall structure of the surface.

All surface texture measurements fall under the scope of the International Organization for Standardisation (ISO) and as a result a number of specification standards have been released governing both profile and areal measurement. These are summarised in Table 2-1.

Table 2-1 – A summary of the ISO guidelines governing profile and areal measurement of surfaces.

Profile Standards	**Areal Standards (ISO 25178) (54)**
Nominal characteristics of contact (stylus) instruments. (ISO 3274)	Part 1: Areal surface texture drawing indications.
Rules and procedures for the assessment of surface texture (ISO 4288)	Part 2: Terms, definitions and surface texture parameters.
Metrological characteristics of phase correct filters (ISO 11562)	Part 3: Specification operators.
Motif Parameters (ISO 12085)	Part 4: Comparison rules
Surfaces having stratified functional properties – Part 1 (ISO 13565 part 1)	Part 5: Verification Operators
Surfaces having stratified functional properties – Part 2 (ISO 13565 part 2)	Part 6: Classification of methods for measuring surface texture.
Terms definitions and surface texture parameters (ISO 4287)	Part 601: Nominal characteristics of contact stylus instruments
Measurement Standards – material measures (ISO 5436 part 1)	Part 602: Nominal characteristics of non-contact (confocal chromatic probe) instruments.
Software measurement standards (ISO 5436 part 2)	Part 603: Nominal characteristics of non-contact (phase shifting interferometric microscopy) instruments.
Calibration of contact stylus instruments (ISO 12179)	Part 604: Nominal characteristics of non-contact (coherence scanning interferometry) instruments.
Surfaces having stratified functional properties – Part 3 (ISO 13565 part 3)	Part 605: Nominal characteristics of non-contact (point autofocus) instruments
Indication of surface texture in technical product documentation (ISO 1302)	Part 606: Nominal characteristics of non-contact (variable focus) instruments

This thesis will describe in subsequent sections the analysis and measurement of pharmaceutical surfaces following the above guidelines and how this work has pushed the boundaries of these regulations to test a variety of complex surfaces.

2.1.3 Common instrumentation for conducting areal surface measurements.

This thesis focuses on the areal surface measurement of pharmaceutical surfaces. The following section will highlight and provide a brief explanation of the major techniques that can be utilised to conduct these measurements and how they operate.

2.1.3.1 Stylus Instrumentation

In a typical standard stylus instrument a ‘conispherical’ diamond tip is pulled across a surface and the vertical response as a result of surface topography is measured. The vertical motion of the stylus tip and the displacement of the instrument parallel to the measured surface allow for a profile of the surface to be constructed. One of the biggest advantages of using a stylus instrument over an optical based instrument is that due to its relatively simple operation and well understood mechanics it is easier to calculate trajectory and thus predict the output of the instrument. Where stylus instruments suffer when compared to optical instruments is that when conducting an areal measurement in the region of several thousand data points it can take significantly longer to complete. Also, as stylus instruments require contact with a surface to produce a response this can often lead to surface damage which makes the technique unsuitable in some applications (55).

2.1.3.2 Atomic force microscopy

Atomic force microscopy (AFM) belongs to a family of instruments referred to as scanning probe microscopes (SPMs). These instruments are often used to measure surface topography on a much smaller scale than capable of reaching with either a stylus or optical instrument. In a conventional AFM a sample surface is scanned continuously across two axes underneath a force sensing probe. This force sensing probe consists of a tip that is part of a cantilever mechanism. A typical AFM will also have a scanner in the z-axis which compensates for changes in sample height between the tip and the sample surface. During operation, the force sensing probe moves across the surface and the presence of attractive and repulsive forces cause the cantilever to bend. This deflection is commonly recorded by the instrument using a laser (positioned behind the cantilever) and a photodiode array. This method of detection is particularly sensitive to sub-nanometre deflection of the cantilever (56).

2.1.3.3 Scanning Electron Microscopy (Angle resolved and stereoscopy)

Scanning electron microscopy (SEM) uses a very fine beam of electrons to scan a sample in a series of continuous lines. Upon hitting the specimen, the electrons are backscattered to a detector which constructs an image that resembles one taken from an optical microscope but at a much higher resolution. The main advantage of using SEM to measure surface topography is that it can measure on a much smaller scale than both stylus and optical instrumentation but can be used over a much larger area than AFM. However, the primary disadvantage of using SEM is that it is fundamentally a 2 dimensional technique and requires the tilting of the sample in combination with very specialised analytical techniques such as stereo imaging and angle resolved scanning. This generally results in other measurement techniques being preferred. Alongside this, some samples require coating with a metallic coat to allow for effective measurement which results in destruction of the samples post measurement (55).

2.1.3.4 Interferometry

Interferometry takes advantage of the wave properties of light to analyse surface characteristics with a particular focus on surface height variations. Interferometers operate by separating a source of light into two distinct paths, one which includes a reference surface and the other which includes the object surface. The light beams are then recombined (interference signal) and directed towards a digital camera which measures the resulting light intensity over multiple image points simultaneously. Following the recombination of the light paths, the fringe frequency is also measured and this corresponds mathematically with the rate at which the interference signal oscillates as a function of changes in the sample surface height. Phase shifting interferometry relies on the movement of the reference plate to change the wavelength of the reference signal and is particularly suited to the measurement of fine surface features and roughness. Coherence scanning interferometry extends interferometry to more complex surfaces which can include greater roughness and steps in the topography. Coherence scanning interferometry also adds additional further benefits including autofocus at every point in the field of view and a suppression of interference from any scattered lights (55).

2.2 – Focus Variation Microscopy

2.2.1 Introduction

This thesis also introduces Focus Variation Microscopy (FVM) to the field of pharmaceutics, with a primary purpose to characterise and profile the surface roughness of IDR compacts and tablets.

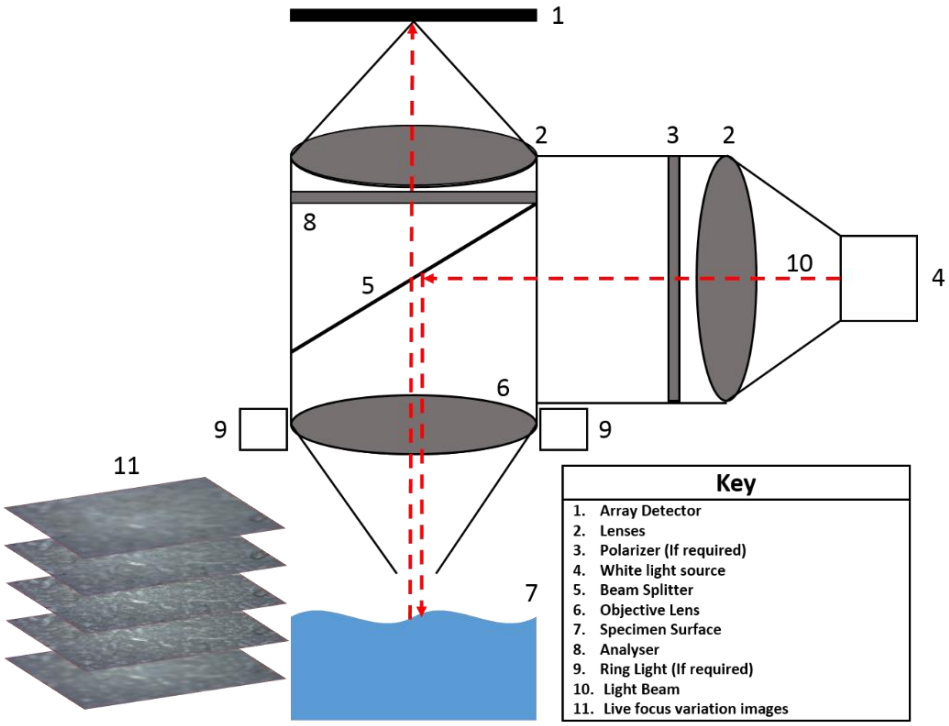

Figure 2-1 - A schematic representation of a focus variation microscope and how this system varies focus to obtain topography information.

Focus variation microscopy is an optical 3D micro coordinate measurement system for complete form measurement of cutting edges. Form, contour, and roughness are measured in high resolution in areal (2.5D) and three-dimensional (Real3D) perspectives. Focus variation combines the small depth of focus of an optical system with vertical scanning (Figure 2-1). This allows for the provision of topographical and colour information from the variation in focus (57). The FVI has many applications but has found significant use in both the forensic and aerospace sectors.

2.2.2 Method of operation

All analysis conducted using the focus variation microscope in this thesis followed a similar set of steps to produce good quality data suitable for further data analysis. This section will provide a description of each step.

2.2.2.1 Method parameters

Magnification

The focus variation microscope used in this thesis has four magnification options available for use. These are at; 5, 10, 20 and 50x magnifications. This thesis specifically used only the 5 and 10 x magnifications. Once a magnification was selected the next step was to focus the image and define the depth of field.

Depth of Field

Focus variation microscopy benefits from movement in the z-axis during data collection. This allows for a greater detail to be achieved from the variation in focus and allows for topography data to be collected. Once a magnification has been selected, the next step is to define the upper and lower limits of the depth of field. This process improves analysis efficiency by reducing the amount of time needed per acquisition by reducing the size of the data set obtained.

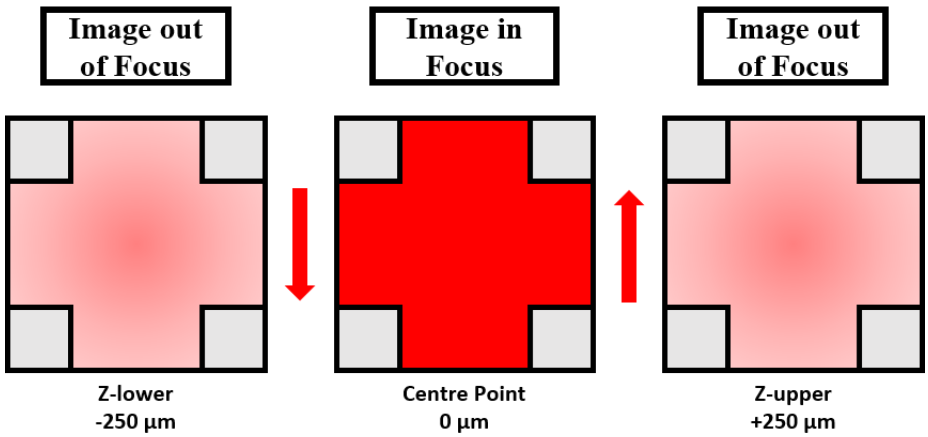

Figure 2-2 – A schematic representation of the determination of the upper and lower limits of the depth of field.

The process for defining the upper and lower limits is displayed in Figure 2-2. The first step is to manually focus the image by moving the lens up and down and defining '0'. Once this is complete the next step is to move the lens down past the point of focus until the image is completely blurred. The distance the lens travels to achieve this is recorded and defined as the z-lower limit. This process is repeated in the opposite

direction past the point of focus until the image blurs again. The distance travelled is recorded and set as the z-upper limit. This process is specific to each surface measured and is often different between samples of the same material. However, in this thesis, typical values for the upper and lower limits of depth of field were found to be between 250 and 300 µm.

Image quality – Brightness and Contrast

With the upper and lower limits defined, the next step is to tailor the image field so that there is sufficient brightness and contrast available to define the detail of the surface. Pharmaceutical materials produce low contrast surfaces, often this is due to the pure white nature of the bulk powder used. To help account for this, the contrast parameter was set to the maximum available on the microscope at a value of 2.

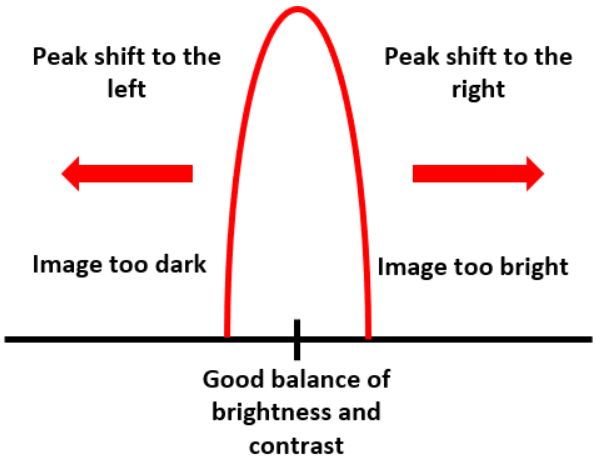

Figure 2-3 – A schematic displaying how to utilise a histogram to improve image quality by varying brightness and contrast.

With the contrast set, the next step is to adjust the brightness of the image. This is achieved by increasing the intensity of the light source from the microscope. A histogram produced live on the microscope is used to determine a good quality brightness level for each image. Similarly, to the depth of field values, the level of brightness varied image to image and sample to sample. But it is important to note that all image fields were tailored in the same way as detailed here using the histogram.

Resolution

The final step before data acquisition is to define the resolution of the image. In focus variation microscopy this is governed by both lateral and vertical resolution. Lateral resolution is defined as the ability of the system to distinguish two points in the direction perpendicular to the light source. In this technique it describes the spacing of the grid pattern across the image area from which peak height and depth information is recorded. If this value is set incorrectly it can lead to an error known as aliasing whereby the true detail of the image is replaced by an artificial texture. Due to the investigative nature of this thesis, the value for lateral resolution was kept at the default value for each objective, this was 7.82 µm at 5x magnification and 3.91 µm at the 10 x magnification.

Vertical resolution is defined as the resolution of the system in the same direction as the lightsource and describes the minimum peak height which can be resolved at each grid point. As this thesis focused on the measurement of surface roughness, this value was often set to the lowest level capable of each objective. However, in some specific cases this was not required. The specific vertical resolution used is described in each subsequent chapter.

2.2.2.2 Data processing and analysis

Levelling

One of the most common and often necessary data processing options in focus variation microscopy is levelling. This is defined under ISO guidelines as the process to remove a known or assumed form from the dataset to ensure a level data set for the determination of ISO parameters.

There are six types of levelling that can be removed from the measured dataset all of which are based on a specific mathematical shape. These are:

- Plane removal – the tilt and pan of the dataset.
- Parabola
- Polynomial
- Cylinder
- Cone
- Sphere – ball bearings and ball joints.

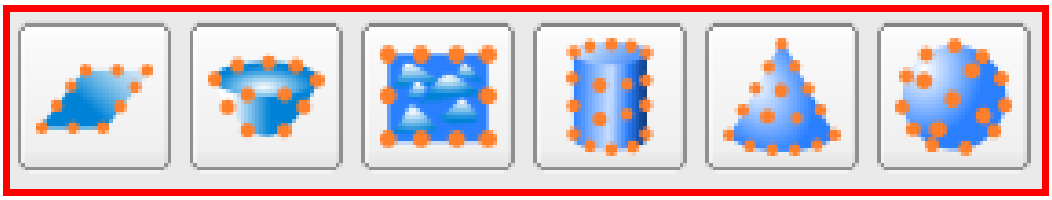

Figure 2-4 – Visual representation of each levelling option that can be removed from the data set.

Whilst all removal options have their purpose and place in surface metrology Plane removal is the most commonly used, and throughout this thesis, it is the only levelling option used to produce level datasets suitable for data analysis and the calculation of surface parameters. Plane removal is designed to level a surface by calculating the tilt and pan of a plane in the surface and subtracting this from the raw data set. An example of this is shown in Figure 2-5. Once the plane was removed from each data set, the image was saved ready for data analysis.

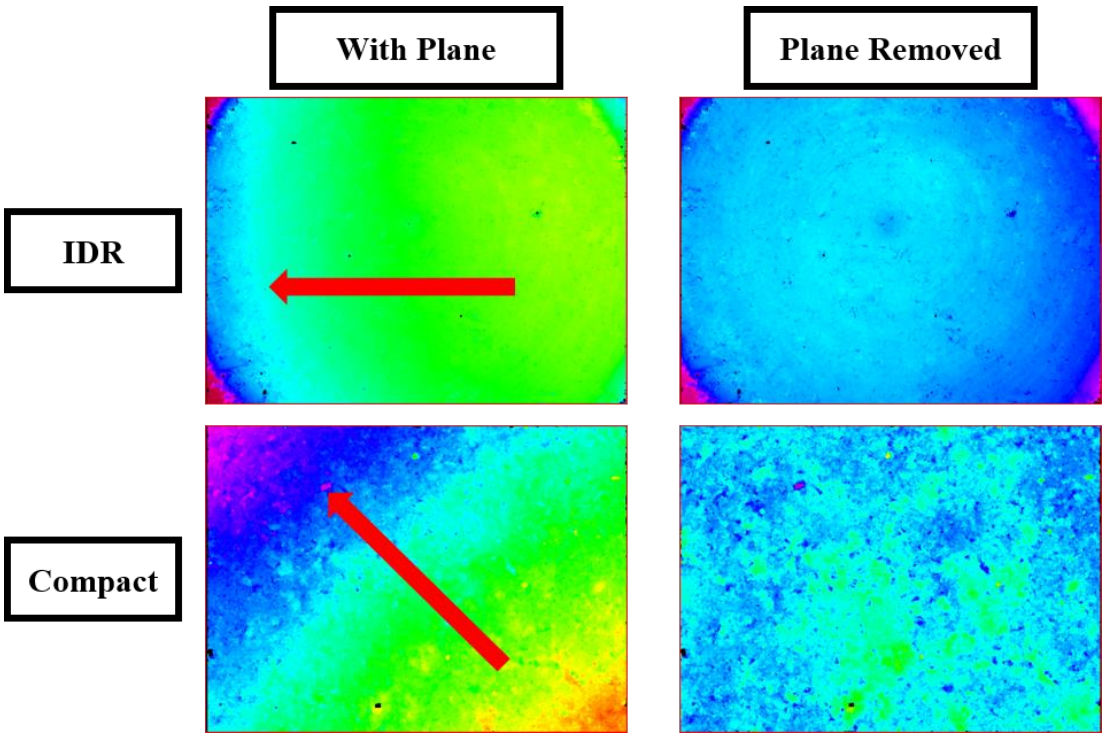

Figure 2-5 – A figure depicting surfaces with a consistent plane and with the plane removed. Note: the red arrows indicate the direction of the plane.

Surfstand and Data Analysis

Once each data set is levelled, they are transferred to a bespoke surface analysis software known as Surfstand™. Here all ISO surface parameters can be calculated. The first step is to define the type of analysis. For the purposes of this thesis, roughness was always selected followed by filtration. Filtration is essential as this separates the measured data into different scales of interest and thus allows for “s” parameters to be calculated. In this thesis, a spline filter was used. Spline filtering is based on the mathematics of splines that were used in shipbuilding whereby the bending of the beam between two fixed points was calculated. It is therefore important to visualise that between given data points in the data set, an arch representing surface texture is drawn. An example of this is shown in Figure 2-6.

With these parameters selected, the upper and lower cut offs for the filter were then established. Due to the investigative nature of this the ISO standards were followed as closely as possible however due to the nature of the surfaces studied, a wider tolerance was used.

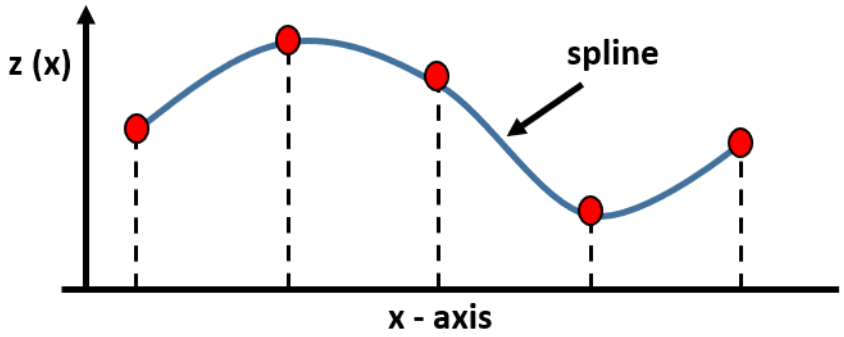

Figure 2-6 - A schematic representation of spline filtering. The schematic shows a spline drawn between 5 data points.

The lowest cut-off was set at 0.008 mm for all surfaces in this thesis. This ensured that any wavelengths smaller than this were excluded from the s-parameter calculation. It is important to state that wavelengths lower than this are often considered noise and that they can mask crucial roughness data. The upper limit was then set at 0.8 mm. This ensured that wavelengths bigger than this value were excluded from the s-parameter calculation. Again, it is important to state that wavelengths bigger than this value often contribute to the waviness and form of the surface and would mask surface roughness.

With the software now set up each surface used in this thesis is filtered and s-parameters calculated accordingly. Currently, there are 25 surface parameters that can be calculated following ISO 25178 which are divided up into six families based on their function, these are; amplitude, spacing, hybrid, Sk family, volume and other. This thesis focuses on four surface parameters identified as showing significant potential for formulation studies. These are; S*tr*, S*al*, S*dr* and S*mr2*. A detailed description of these parameters is given over the next few pages and for all other parameters the reader is directed towards the ISO 25178 series (54) for further information.

The autocorrelation function used in surface metrology is based on the process of cross correlation. Cross correlation is a measure of the similarity between two signals at different lag times. The correlation value is calculated by multiplying the vertically aligned points together and summing the values. An example of this is shown in Figure 2-7.

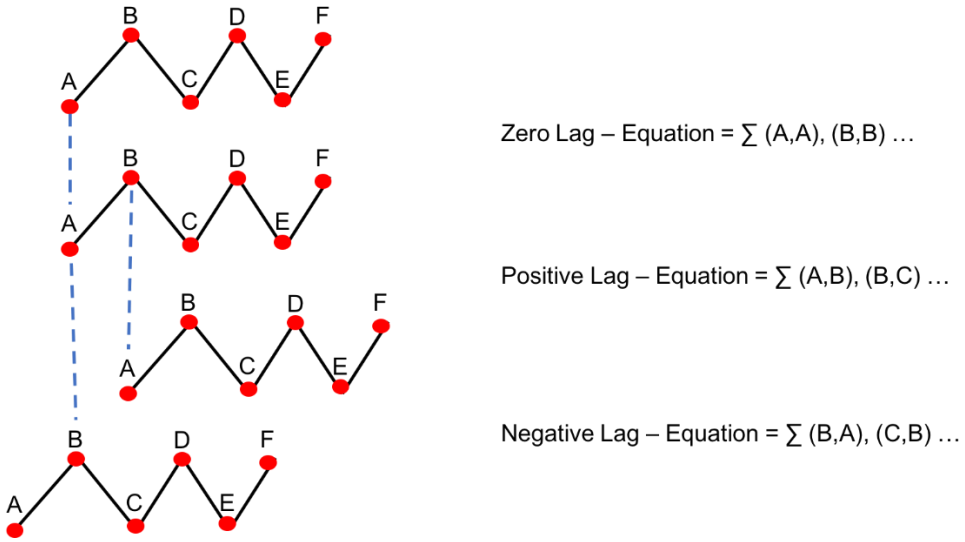

Figure 2-7 – A schematic of cross correlation in signal theory.

Positive and negative lag continues in sequence until each possible vertical aligned point has been calculated. This leads to the production of a correlation sequence at the different lag intervals. Often the correlation values are normalised to help with identification of trends in correlation between the two signals. Normalised correlation values are effectively a scaled version of the original correlation values based on the actual value or energy. Normalised data sets tend to stretch from -1 to 1 where 1 represents a completely correlated signal at a given lag point, 0 indicates an uncorrelated signal at a given lag point and -1 indicates the peaks in the signals match identically to the valleys of the signal at a given lag point.

The autocorrelation function (ACF) within areal surface measurement builds upon the principles of cross correlation using the gathered data set. It is important to state that the time based signal seen in cross correlation has been replaced with a space based topography. This switch facilitates the use of cross correlation from a profile time domain to an areal spatial domain.

The ACF's for a surface are found by taking a duplicate version of the measured surface and overlaying the data set against the original. The duplicate data set is then moved with a relative lateral displacement (*d*x,*d*y) and correlation values calculated. This is similar to the aligning of two signals at different lag points to create a correlation sequence as described above. The resulting function from the autocorrelation calculation is normalised so that if the shifted (duplicate) version of the data set is identical to the original the ACF value will approach 1. The less similar the shifted surface is to the original, the ACF value will begin to approach 0. In some cases, the peaks on the duplicate surface line up identically with the valleys on the original surface. When this occurs the ACF value approaches -1. The calculation of the ACF's on the surface of a sample leads to the generation of an areal autocorrelation plot. This plot is a visual representation of each correlation value for each of the lateral displacement (lag) positions in both the x and y directions. This plot then forms the basis of calculating the parameters *Sal* and *Str* as shown in Figure 2-8a.

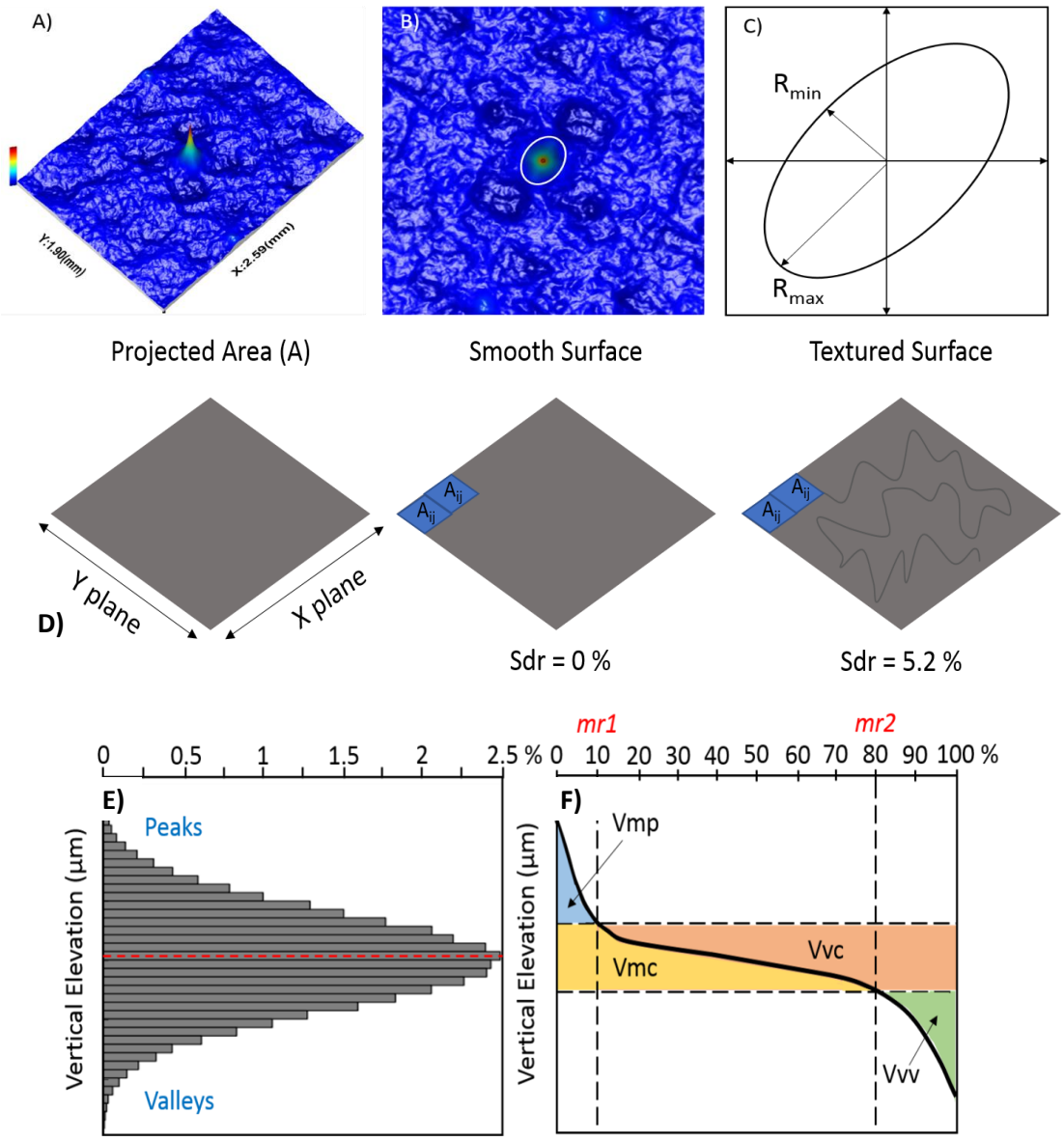

Figure 2-8 - An autocorrelation plot and calculation of Sal and Str (a) autocorrelation plot of the surface, (b) threshold boundary of the central position, (c) autocorrelation lengths in different directions, (d) visual representation of Sdr calculation (values for illustrative purposes only), (e) surface distribution chart, (f) a bearing ratio curve displaying key volume parameters

Sal (Equation 2-1) is a parameter that is used to characterise the autocorrelation character of surface Areal Autocorrelation Functions (AACF's). It is defined as the horizontal distance of the ACF (dx,dy) which has the fastest decay to a specified value s, where s is between 0 and 1. In this work, a value of 0.2 was set for s in line with guidance described in ISO 25178 (54). This parameter can also be viewed as a measure of the lateral scale of the surface.

$$Sal = min\sqrt{tx^2 + ty^2}$$

Equation 2-1 – Equation for the calculation of the Sal parameter.

Figure 2-8b highlights the autocorrelation functions (ACF's) above the threshold of 0.2. A boundary is then placed around the central threshold position as shown in Figure 2-8c. Two radii are then calculated from the centre of the boundary to the outer perimeter. The shortest radius (Rmin) is retained for S*al*. A large value for S*al* indicates that a surface is dominated by low frequency components i.e. waviness whereas a low value for S*al* denotes the opposite i.e. roughness.

S*tr* (Equation 2-2) is the texture aspect ratio parameter and is used to characterise the isotropy of the surface. S*tr* is calculated in a similar manner to S*al* described earlier, however, S*tr* considers the minimum and the maximum radii lengths under the same conditions after applying the same threshold. S*tr* is a unit less parameter and provides a value between 0 and 1. The closer to 1 the value lies the more uniform the surface is, whereas the closer to 0 the value lies the more likely a dominant texture direction is influencing the surface.

$$Str = \frac{r_{min}}{r_{max}}$$

Equation 2-2 – Equation for the calculation of the Str parameter.

Surface Developed Area Ratio - Sdr

S*dr* is a parameter that belongs to the hybrid family of surface character parameters. This parameter describes the developed interfacial area ratio of a surface and is a measure of the surface area gained by a sample area as a result of the texture of the surface (Figure 2-8d). This parameter is described by Equation 2-3 below where A_{ij} is the mean area calculated at a point and A is the projected area of the surface calculated from the lengths of x and y.

$$Sdr = \frac{\sum\sum A_{ij} - A}{A}$$

Equation 2-3 – Equation for the calculation of the Sdr parameter.

This parameter can be quoted as a unit less positive number or as a percentage. Typically, the parameter produces a value of between 0 and 10 % for most surfaces with 0 % representing a completely smooth surface.

Areal Material Ratio, Smr2

S*mr2* is one of a number of parameters determined from the cumulative material ratio curve (Figure 2-8e-f). By definition S*mr2* represents the ratio of the area of the material at the intersection line which separates the dales from the core surface to the evaluation area. Put into context, this means that S*mr2* represents the percentage of the measurement area that comprises of the deeper valley structures associated with the S*vk* and V*vv* parameters. Figure 2-8f highlights the calculation of S*mr2* and its relation to other areal parameters. S*mr2* can also be converted to calculate the percentage of valleys that will retain lubrication*. This is described by Equation 2-4.

$$Lubrication = 100 - Smr2$$

Equation 2-4 – Equation for the conversion of Smr2 into percentage lubrication.*

*Note: lubrication here means the volume of a liquid medium that may be on the surface of a compact.

These four carefully selected parameters are of interest in this study due to their potential interest to formulation scientists. S*al* was primarily used in this work as confirmatory parameter to determine whether the filtration of the data had been successful and that all conclusions were based on the small scale roughness of the tablet surface. S*al* can also be used to measure the lateral scale of the tablets' surface which can be useful when assessing materials of different particle morphologies as in this work. S*tr* is of interest to a formulator as it gives an indication to the uniformity of the texture on the tablet surface. If S*tr* displays a value closer to zero for example this would indicate that a dominant texture direction was influencing the surface, possibly as a result of the upper or lower punches. S*dr* is of interest to formulators as it provides

information on the percentage surface area gained by a tablet as a result of its texture. This is particularly important with regards to dissolution testing as any significant difference could give rise to higher or lower dissolution rates. Intrinsic dissolution rate for example may be influenced by changes in surface area (58). As S*mr2* can be converted to measure lubrication, this could help to provide an early insight into the wettability of a surface before conventional methods are used e.g., contact angle testing.

This chapter has explored the assessment of surface metrology and described how focus variation microscopy was utilised for the assessment of pharmaceutical materials. The following chapters will provide any deviations away from the methodology described here.

2.3 Primary goal of this thesis – Focus Variation Microscopy

The primary aim of this thesis with regards to Focus variation microscopy is to introduce the technique as a novel tool for the for the assessment of pharmaceutical surfaces and correlate data gathered with behaviour. To achieve this, a number of milestone objectives will be explored throughout this thesis:

1. Build upon preliminary published data to establish a robust methodology for assessing pharmaceutical surfaces.
2. Identify useful meteorological parameters that can help predict pharmaceutical behaviour.
3. Assess the versatility of the system by using different materials and different forms of surface i.e., conventional tablets, IDR compacts.
4. Combine Focus Variation Microscopy with UV imaging to correlate observed behaviour with surface properties.

Note to reader: Due to the method developmental nature of this thesis, a material and methods chapter was not suitable as such each chapter of the experimental work from chapters 3-7 have their specific material and methods section. Also, as stated, with regards to the focus variation section, sections written in relevant experimental chapters are a deviation from chapter 2.

Chapter 3 - Developing a method for the measurement of swelling in hydrophilic matrices.

3.1 Note to Reader

Some aspects of the following chapter are published in the International Journal of Pharmaceutics X Volume 1 under the title 'Development of a novel method utilising dissolution imaging for the measurement of swelling behaviour in hydrophilic matrices.'(59)

3.2 Rationale

The following chapter explores the use of the novel whole dosage cell supplied with the SDI2 instrumentation and the use of the additional 520 nm LED to image the initial stages of gel formation and swelling within a hydrophilic matrix system (using hypromellose as a model polymer). This chapter also aims to showcase the design, development and validation of a methodology devised to perform these assessments.

3.3 Introduction

To determine swelling and erosion rates of hydrophilic polymers in controlled release dosage forms a traditional method developed by Tahara et al. in 1995 is often used (60). This method involves the preparation of multiple compacts of polymer or formulation and placing them in a conventional USP 2 dissolution apparatus, typically at 37 °C and allowing the polymer to hydrate for set intervals of time in the dissolution medium at a set stir rate. Once each time point is reached the compacts are removed into a pre-weighed weighing boat, blotted dry and weighed. In some cases, the compacts can be placed in an oven at 37 °C to dry to a constant weight then weighed again (61). Figure 3-1 provides a schematic of how this methodology is performed.

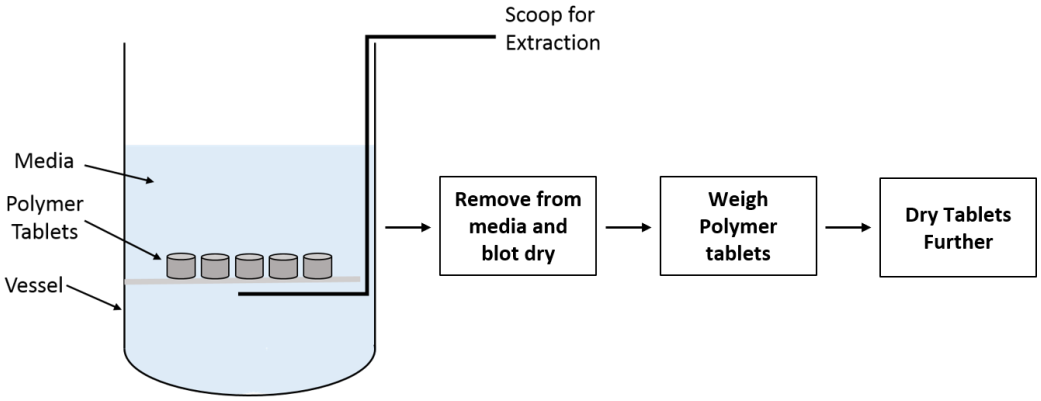

Figure 3-1 - A schematic to display the steps taken when measuring the hydration, swelling and erosion of hydrophilic matrices using a conventional USP 2 dissolution bath.

From these measurements, indicators such as relative swelling and dissolution medium uptake can be determined. The removal of the tablets from the dissolution media has to be completed with a great deal of care to ensure the gel layer is not disturbed or damaged. Particularly when blotting and removing excess water from the compacts before weighing. Another issue is the amount of material and resources required to complete the test. Each dissolution vessel is often filled with 900 to 1000 mL of dissolution medium and multiple compacts are often needed for each time point, which can be difficult to obtain in the early stages of formulation development. These issues have led to researchers looking for novel approaches for the measurement of polymer hydration.

A variety of imaging techniques are being employed to help researchers understand polymer behaviour *in situ* in lower volumes with fewer compacts. These imaging techniques include Magnetic Resonance (MRI), Confocal Laser Scanning Microscopy (CLSM), Infra-Red (NIR), Nuclear Magnetic Resonance (NMR) and Terahertz Imaging. MRI has been utilised by Kaunisto et al. to model polymer dissolution (62) with Kulinowski et al. developing the technique to monitor the structural evolution of hypromellose tablets (63). CLSM has been utilised in a number of different pharmaceutical applications described by Pygall et al.(64). Melia et al. have utilized the technique for the monitoring of gel layer growth and water penetration in hydrophilic

matrices (65). NIR has been developed by Avalle et al. to monitor the gel layer formed in compacts containing hypromellose (66) as well as monitoring drug release from the gel layer as a result of erosion (67). A novel imaging application using NMR has been developed to measure water front penetration (68) with Rajabi-Siahboomi et al. utilising the technique to monitor water mobility and drug diffusion in hydrophilic matrices (69). Finally, the novel use of terahertz radiation has recently been employed by Yassin et al. to monitor the swelling and drug diffusion of tablets containing hypromellose (70).

Surface Dissolution Imaging (SDI) has begun to prove its versatility in the field of pharmaceutics. Traditionally used to determine the intrinsic dissolution rates (IDR) of pharmaceutical ingredients (58,71) the technique has started to diversify into an analytical tool for monitoring dissolution events. These events can be with active pharmaceutical ingredients (API) (72), release from devices such as transdermal patches (20) or the dissolution behaviour of polymers (22). The new model of surface dissolution imaging apparatus employed in this chapter allows imaging of whole dosage forms using a flow cell based on the USP 4 flow through apparatus. Figure 3-2 shows the whole dosage cell and a schematic representation of how this flow cell operates in the SDI system.

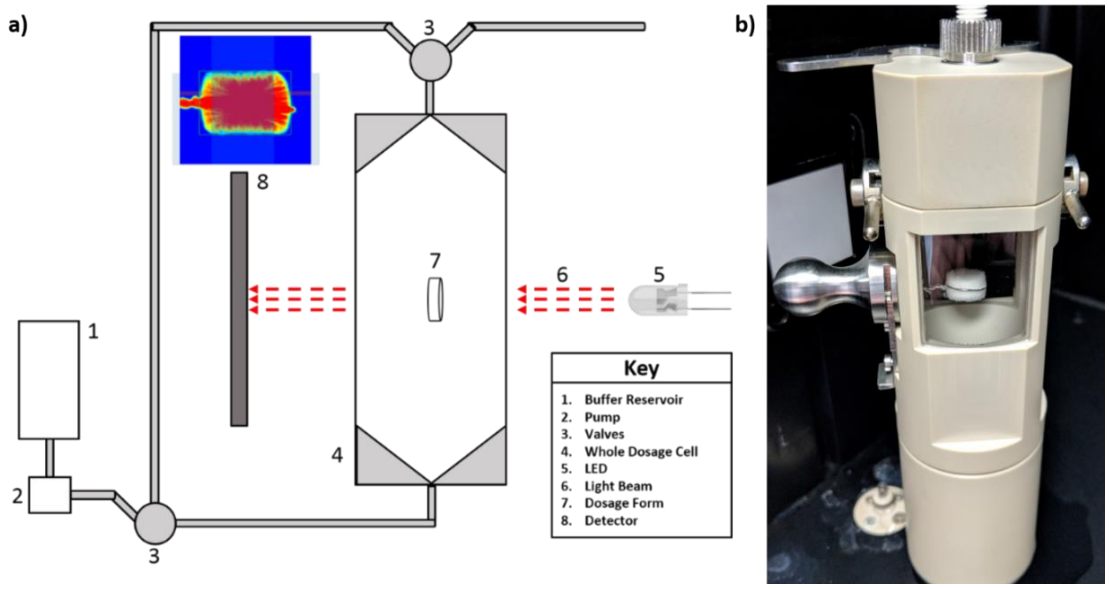

Figure 3-2 - a) A schematic representation of how the whole dosage cell operates in the SDI2 System. b) A photograph of the whole dosage cell containing a tablet suspended in dissolution media using a stainless steel wire holder.

The new model of the SDI, the SDI2 is an upgrade on its predecessor in a number of ways. Firstly, the new model, introduces a 520 nm optical LED alongside four UV LED's at 255, 280, 300 and 320 nm. Secondly, the system can record two different wavelengths of light simultaneously allowing for example, drug release and tablet disintegration to be monitored at the same time. Finally, the CMOS detector chip in the new model has been upgraded to 13 MP allowing greater resolution and detail to be monitored in real time. As stated in 3.2, the primary aim of this chapter is to design and develop a method for monitoring swelling behaviour of hydrophilic matrices in the SDI2 system and take advantage of the 520 nm and real time recording of the system.

3.4 The current methodology for testing whole dosage forms

3.4.1 Manufacturer Method

The manual supplied with the SDI2 system details a generic method for monitoring dissolution of whole dosage forms.

The first step in the method is to design a suitable holder for the dosage form out of stainless steel wire. Several options are recommended these are; the loop, the hook and the ‘v’ shape. The next step is to ensure that the dosage form and holder sit centrally in the observation window (Figure 3-3).

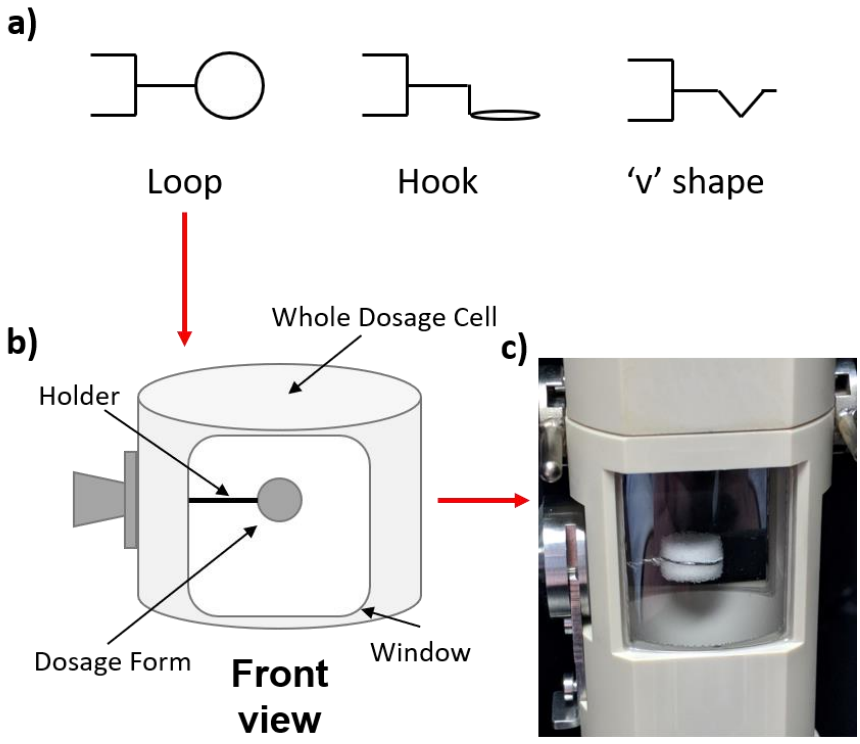

Figure 3-3 - a) A schematic representation of three recommended wire holder designs for the whole dosage cell. b) A schematic representation of whole dosage positioning within the whole dose cell. c) A photograph of a whole dosage form in the whole dose cell.

Once the holder for the dosage form has been produced, the next step is to prepare the whole dosage cell for analysis. This includes placing a quantity of 2 mm borosilicate beads into the bottom of the whole dosage cell to approximately fill the bottom third of the cell. This is designed to help remove turbulence and reduce the presence of air bubbles during an experiment.

Once this is complete the whole dosage cell is placed inside the system and connected to the fluid lines. A rinse step is performed with de-ionised water, to remove any dust, fibres, and other contaminants. The rinse step also cleans both fluid pumps and all fluid lines in the system. After rinsing, the system can then be prepared to run an experiment. The SDI2 offers open and closed loop functionality and the ability to transfuse between two different media *in situ*. For the measurement of hydrophilic polymers, the system was set to record for 2 hours using the primary solution (DI water) at 37 °C at the manufacturer recommended a flow rate of 8.2 mL/min. The optical wavelength of 520 nm was also used.

Once data collection has completed, analysis is performed on the data file to establish growth measurements. For this, the horizontal and vertical measurement zones are set to 1 mm and placed over the tablet. Next, a tablet edge threshold absorbance is set with the manufacturer recommending an absorbance of 350 mAu. Data points at 1-min intervals were recorded (Figure 3-4).

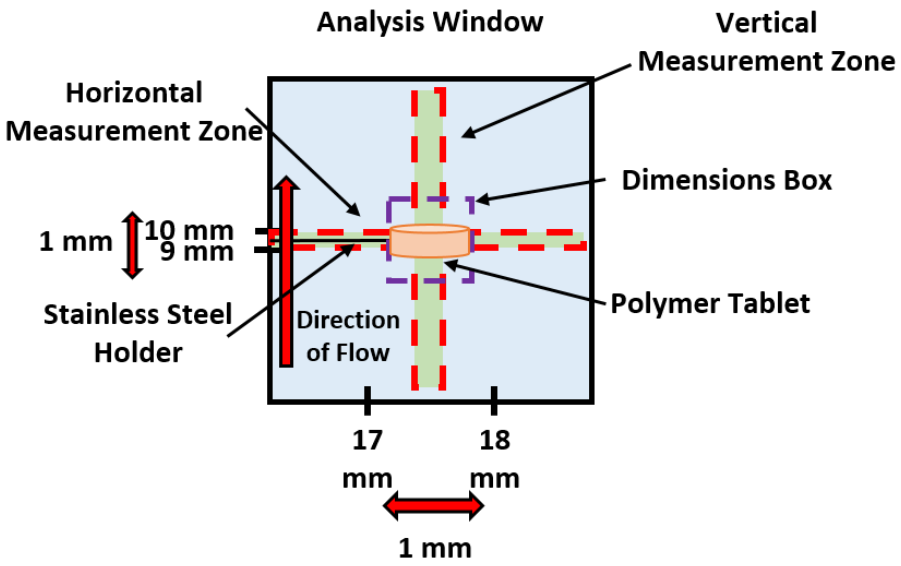

Figure 3-4 - An example schematic of how the analysis window is set-up following the manufacturer method for monitoring tablet growth/disintegration.

3.4.2 Initial challenges

After preliminary studies with HPMC polymer only tablets a number of key issues were observed.

3.4.2.1 Stainless steel interference

One of the first immediate issues identified was absorbance from the stainless steel holder designed to secure the dosage form in place. This absorbance meant that the tracking box designed to measure tablet width tracked the holder instead of the edge of the tablet leading to an inflated width measurement by the SDI2 analysis software. The reason for this issue is that due to the nature of the system measuring relative absorbance of light by objects in front of the detector, placing a solid object in front of the detector is going to produce a reading. An example of this issue is indicated in Figure 3-5.

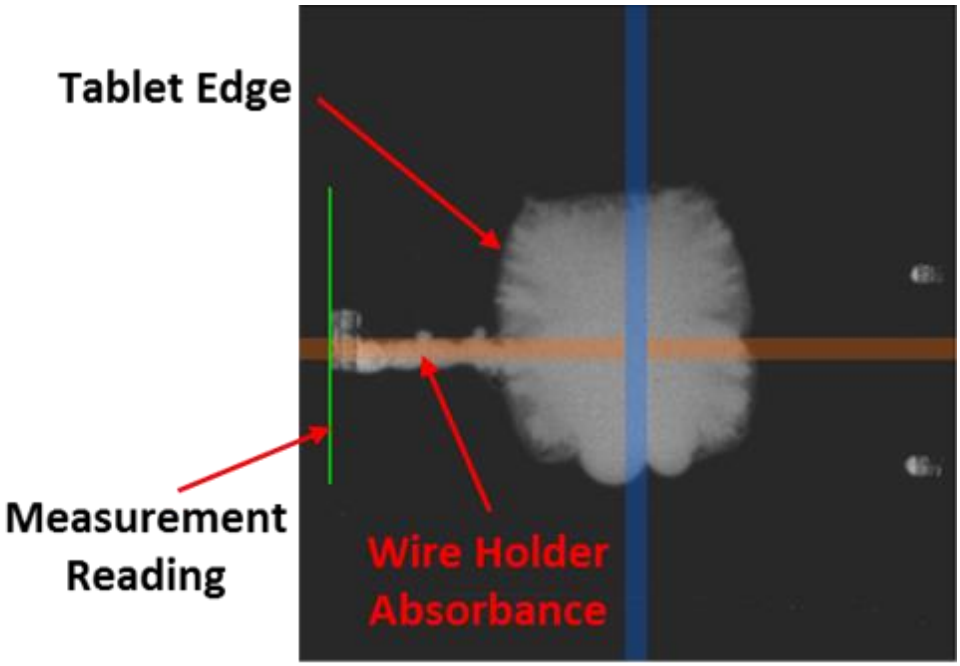

Figure 3-5 - An example of measurement interference caused by absorbance from the stainless steel holder.

3.4.2.2 Absorbance Threshold

Another issue identified with the manufacturer's methodology was the choice of absorbance threshold for dosage form tracking. The purpose of this threshold was to provide an absorbance marker for the edge of the tablet thus allowing the tracking box to follow the edge of a dosage form as it swells or disintegrates. However, at the recommended threshold of 350 mAu, the tracking box lost track of the edge of the gel layer as it swelled during measurement. A possible reason for this issue was that, as the gel layer forms and grows it becomes more hydrated and often more translucent leading to an edge absorbance lower that the threshold. An example of this issue is displayed in Figure 3-6.

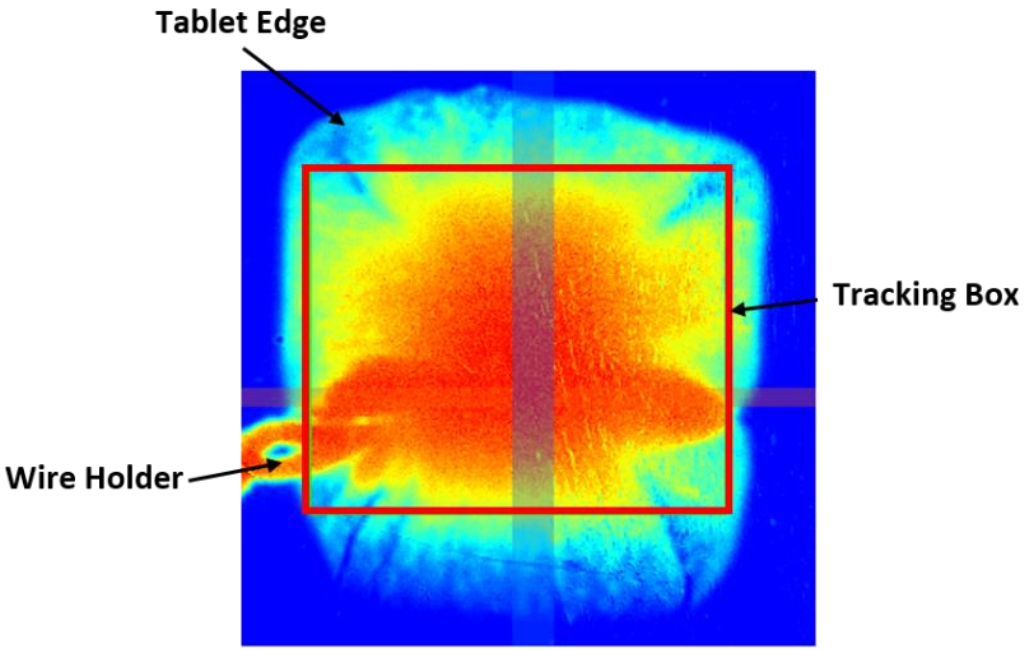

Figure 3-6 - An example of tracking box issues caused by a high absorbance threshold resulting in incorrect growth measurements.

3.4.2.3 Measurement zone size and position

A further flaw identified relates to the set-up of the system for monitoring the growth of dosage forms in the system. The default method recommends that both the horizontal and vertical measurement zones used for producing the tracking box that monitors growth or disintegration, are given widths of 1 mm and must be placed in a cross over the centre of the dosage form. The issue with following this recommendation was that hydrophilic polymers often grow and hydrate at different rates in different locations. Therefore, different results could be observed depending on where these zones were positioned. An example of this issue is indicated in Figure 3-7.

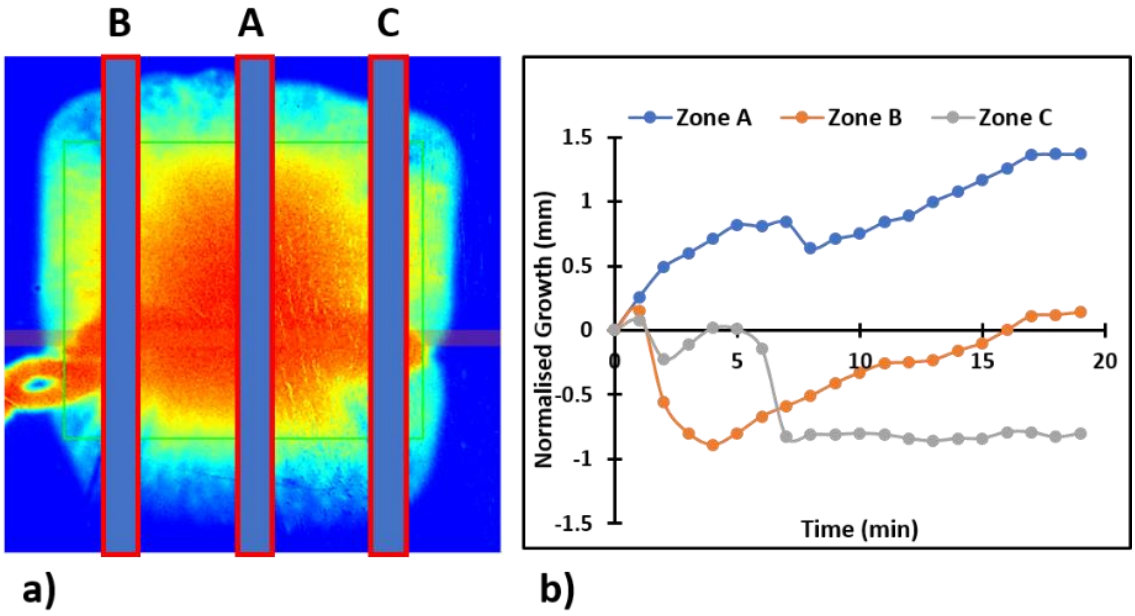

Figure 3-7 - a) A schematic representation of different measurement locations when monitoring polymer swelling. b) Example results at default mAu at the different locations.

3.4.2.4 What influence does flow rate have on measurement of growth?

Whilst flow rate was not identified as an issue, it was nevertheless still important to check what influence flow rate had on growth and hydration of a polymer in this system. As a default, the manufacturer recommends a flow rate of 8.2 mL/min however the system is capable of going as low as 4 mL/min and as high as 32 mL/min. An added advantage of looking at the influence of flow rate is that it will also provide an insight into the hydrodynamics of the whole dose cell of the SDI2.

3.4.2.5 Image colouring and tailoring

The SDI2 analysis software defaults to display all experiments in black and white with a white balance value of 100. However, the software does offer further colour options that could provide more definition when monitoring hydrophilic polymer growth. Also, the analysis software can be adjusted to zoom in on a particular area of a sample which could be of use in growth and swelling experiments (Figure 3-8).

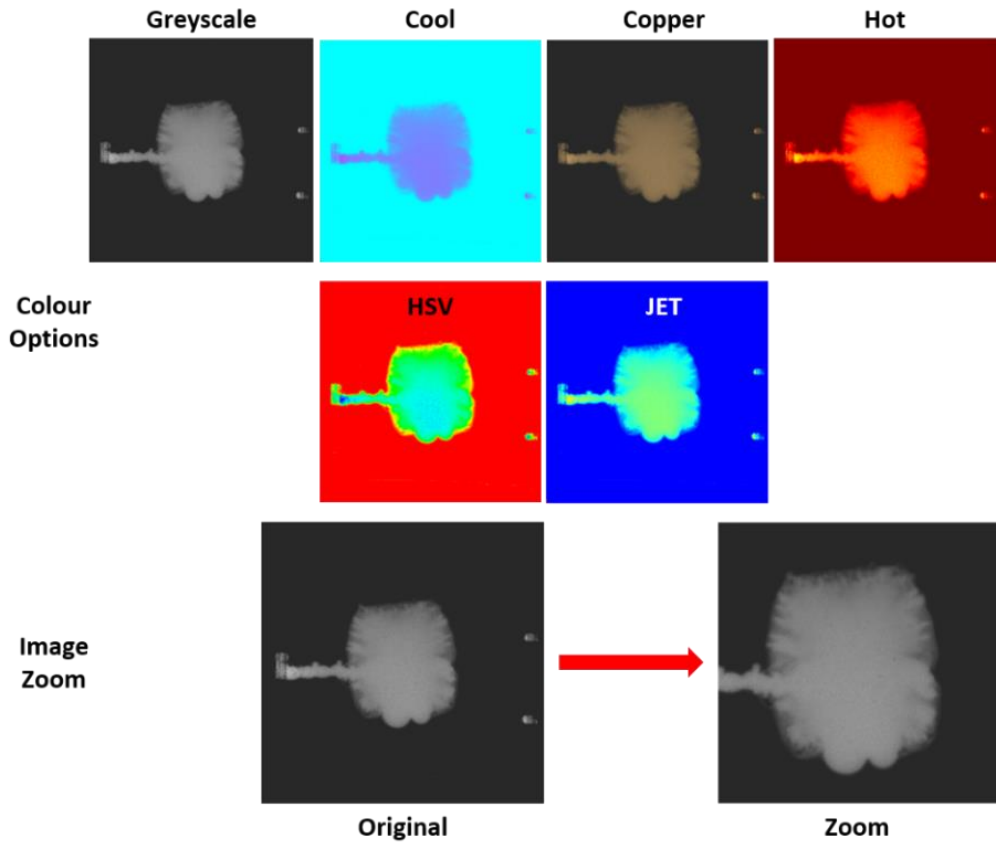

Figure 3-8 - A representation of the colour options available when analysing experiments conducted on the SDi2 system and also the zoom capabilities of the system.

3.4.3 Objectives for new methodology

After identifying the potential drawbacks in the manufacturer's methodology, a number of objectives were set for the development of a new more robust methodology:

- Investigate the influence of both measurement zone size and location alongside tablet edge threshold to produce a more robust method for tracking gel hydration and growth.
- Establish how flow rate can influence tablet growth and hydration in the SDI2 system and how this influences method development.
- Review the analysis software capabilities to find the best image colouration to display and identify gel layer growth in hydrophilic matrix tablets.

3.5 Method Development

3.5.1 Absorbance Threshold

Absorbance threshold is one of the key parameters used by the SDI2 system to monitor tablet growth and degradation. As shown in Figure 3-6 in section 3.4.2.2, it was discovered that in some instances the default recommended edge threshold could lose track of the edge of the gel layer as a hydrophilic polymer hydrated and grew. To rectify this issue a test was devised to find a suitable threshold to monitor gel growth accurately and robustly. This test involved analysing 2 different polymer grades of HPMC. The grades selected were the K100M CR and the K100M DC2 grades manufactured by Colorcon Ltd. Both grades offer the same K100M chemistry of HPMC but differ fundamentally in particle morphology. The CR grade contains longer, thinner ribbon like particles whereas the DC2 grade contains particles of a more spherical nature (The DC2 grade will be referred to as DC from henceforth).

Compacts of both polymers were placed in the whole dose cell under flow at 8.2 mL/min with de-ionised water at 37 °C for 2 hours. Once each test was completed, the resulting video files were analysed at 7 different absorbance thresholds (25, 50, 75, 100, 150, 350 and 500 mAu) to determine the appropriate threshold to use for these hydrophilic matrices. Also, during analysis the measurement zones were kept consistent as described in section 3.4.2.3.

The results from the absorbance threshold test were clear and conclusive, in both cases the images as displayed in Figure 3-9 a-b confirmed that once the threshold reached 350 and 500 mAu the tracking box failed to monitor the edge of the gel accurately. However, the images also show that when the threshold was set between 25 mAu and 75 mAu the tracking box remained close to the edge of the gel layer throughout the experiment. This trend was also confirmed by the growth profiles from the SDI2 analysis software as shown in Figure 3-9 c-d.

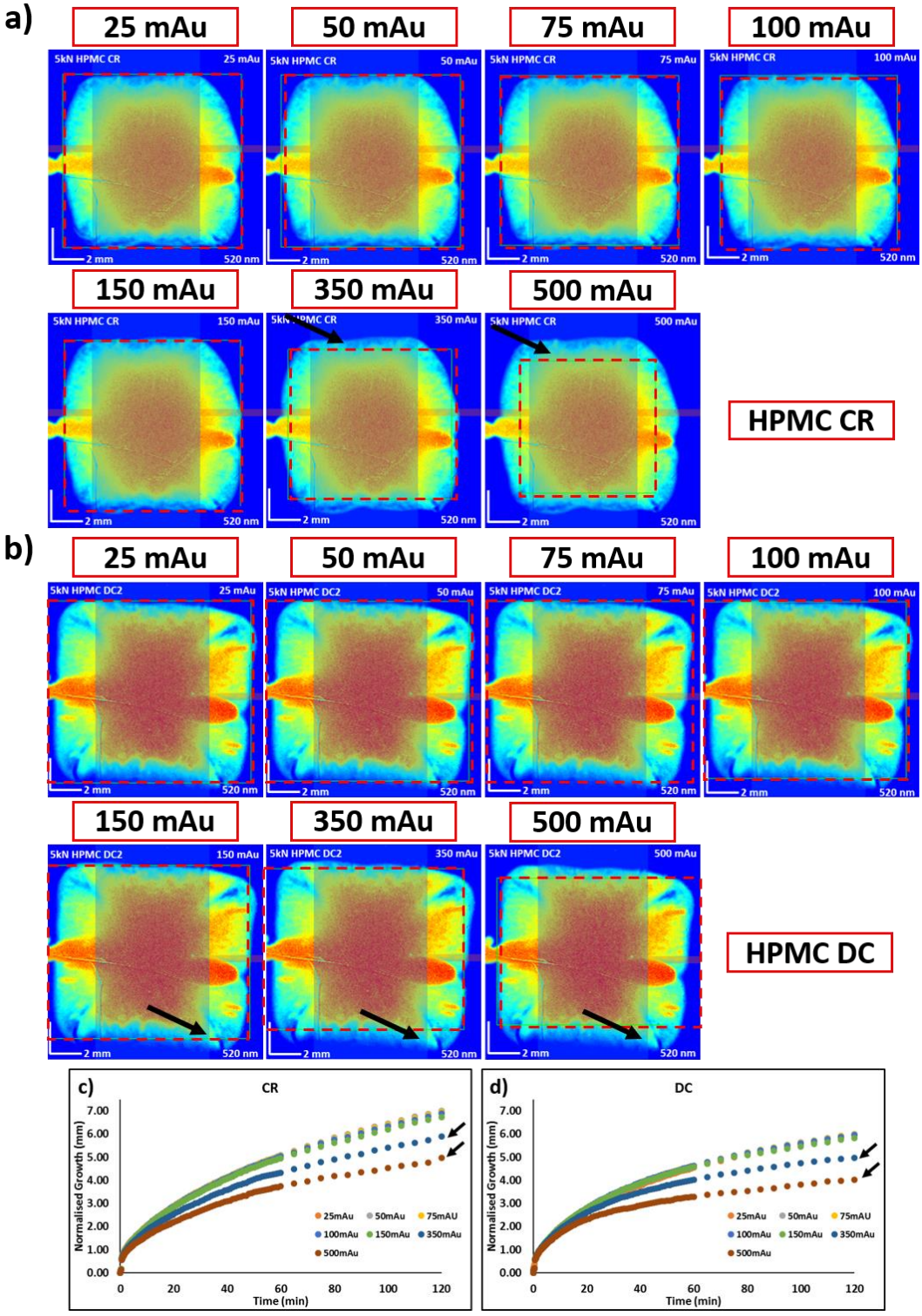

Figure 3-9 - Results of the absorbance threshold test for HPMC CR grade. b) Results of the absorbance threshold test for HPMC DC. c) Growth profiles at different absorbance thresholds for HPMC CR. d) Growth profiles at different absorbance thresholds for HPMC DC. Black arrows indicate where the tracking box failed to monitor the true edge of the gel.

The conclusion from this test was, to accurately measure the edge of the gel layer during dissolution experiments, the manufacturer recommended threshold should be discarded and replaced with an absorbance between 25 and 75 mAu from the new developed methodology.

3.5.2 Measurement zone size and position

The locations of the horizontal and vertical measurement zones are another key parameter used by the SDI2 system to monitor tablet growth and erosion. The analysis software uses these zones as reference points alongside the absorbance threshold to draw the tracking box used to produce the growth profiles seen in Figure 3-9. Similarly, to absorbance threshold, the position of these zones drastically affected the growth measurement recorded by the software as shown in Figure 3-7. The vertical measurement zone was used due to the potential interference of the stainless steel holder on the horizontal zone. As a result, a test was devised to determine the best location for the vertical zone only. Using the same experimental procedure described in section 3.5.1 3, zone positions were monitored at both the new methodology 50 and manufacturer recommended 500 mAu absorbance thresholds. These zone positions were labelled A, B and C (Figure 3-7). Figure 3-10 displays the results of this test. On review of the 500 mAu data, it appeared that location had very little effect on growth as the absorbance threshold was dominating the error in the data gathered as described in section 3.5.1. However, once the threshold was lowered to 50 mAu, the influence of zone location became more apparent. As indicated by the black arrows in Figure 3-10, zone B produced a profile that displayed a greater amount of growth than zones A and C. This was due in part, to the uneven nature of the gel growth. However, this did indicate that the vertical zone calculated an average reference point from all the pixels within its area at the absorbance threshold. Therefore, it was determined that if the zone was made wider to cover the majority of the tablet area, it should provide a more representative reference point of the edge of the gel by considering the uneven nature of the edge of the gel.

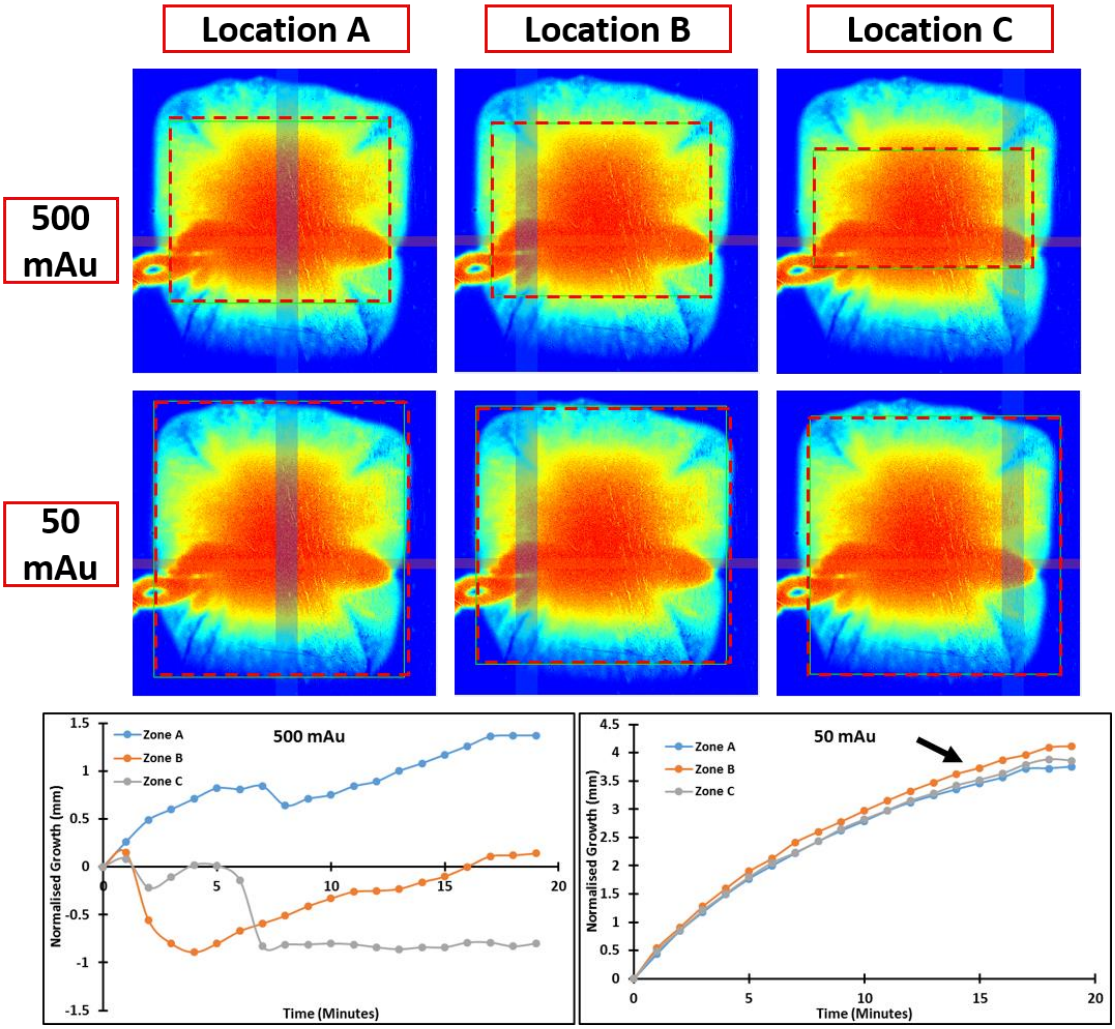

Figure 3-10 - SDi2 images and associated growth profiles for the vertical zone location test at absorbance thresholds of 50 and 500 mAu.

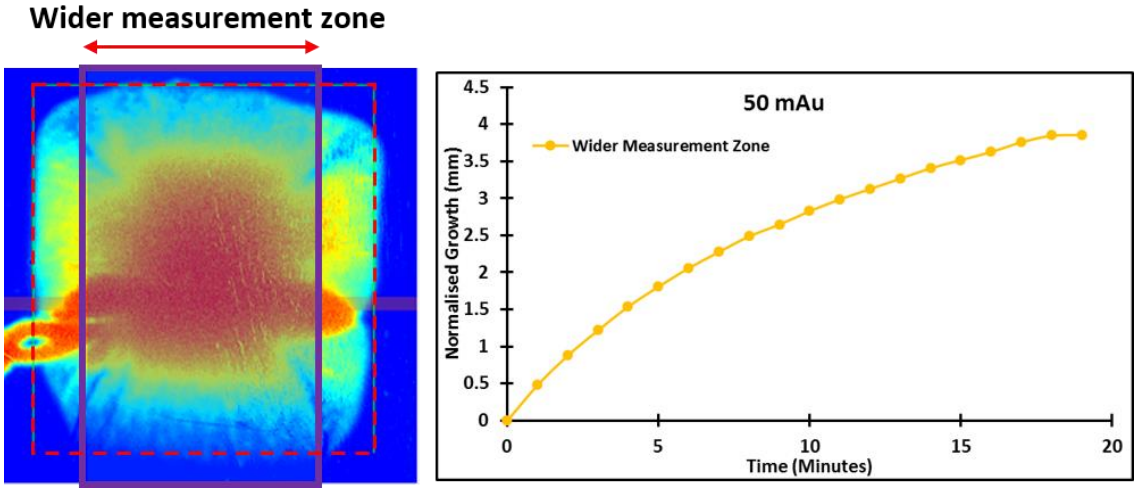

Figure 3-11 - A schematic representation of the wider measurement zone trialled, along with the resulting growth profile data.

Figure 3-11 displays the wider measurement zone tested. The width of the zone was designed to cover the centre most portion of the tablet running from the outer edge of zone B to the outer edge of zone C. The initial hypothesis was found to be correct and the wider measurement zone did provide a more representative reference point for growth measurements. The growth profile also displayed in Figure 3-11 was found to bisect zones A, B and C and appeared to consider the uneven nature of the surface.

The conclusion from this test was that to improve robustness of growth measurement, a wider measurement zone combined with the lower absorbance threshold should be used in all future measurements of hydrophilic matrix systems.

3.5.3 Influence of flow rate

As stated in section 3.4.2.4, the manufacturer recommends a flow rate of 8.2 mL/min however the system is capable of going as low as 4 mL/min and as high as 36 mL/min. To test the influence of flow rate on polymer growth, 3 flow rates were selected 4, 8.2 and 16 mL/min, to mimic low, medium and high settings respectively for the SDI2 system.

The flow rate results are depicted in Figure 3-12 and Figure 3-13. Figure 3-13 displays the effect of flow rate on the normalized gel growth of the CR and DC compacts at 5 and 15 kN. The flow rate at 16 mL/min seemed quite turbulent and as a result often lodged bubbles next to the compacts (indicated by the black arrows in Figure 3-12). This produced erroneous results. This can be observed as the jumps in the normalized gel growth in Figure 3-13 (highlighted by the black arrows).

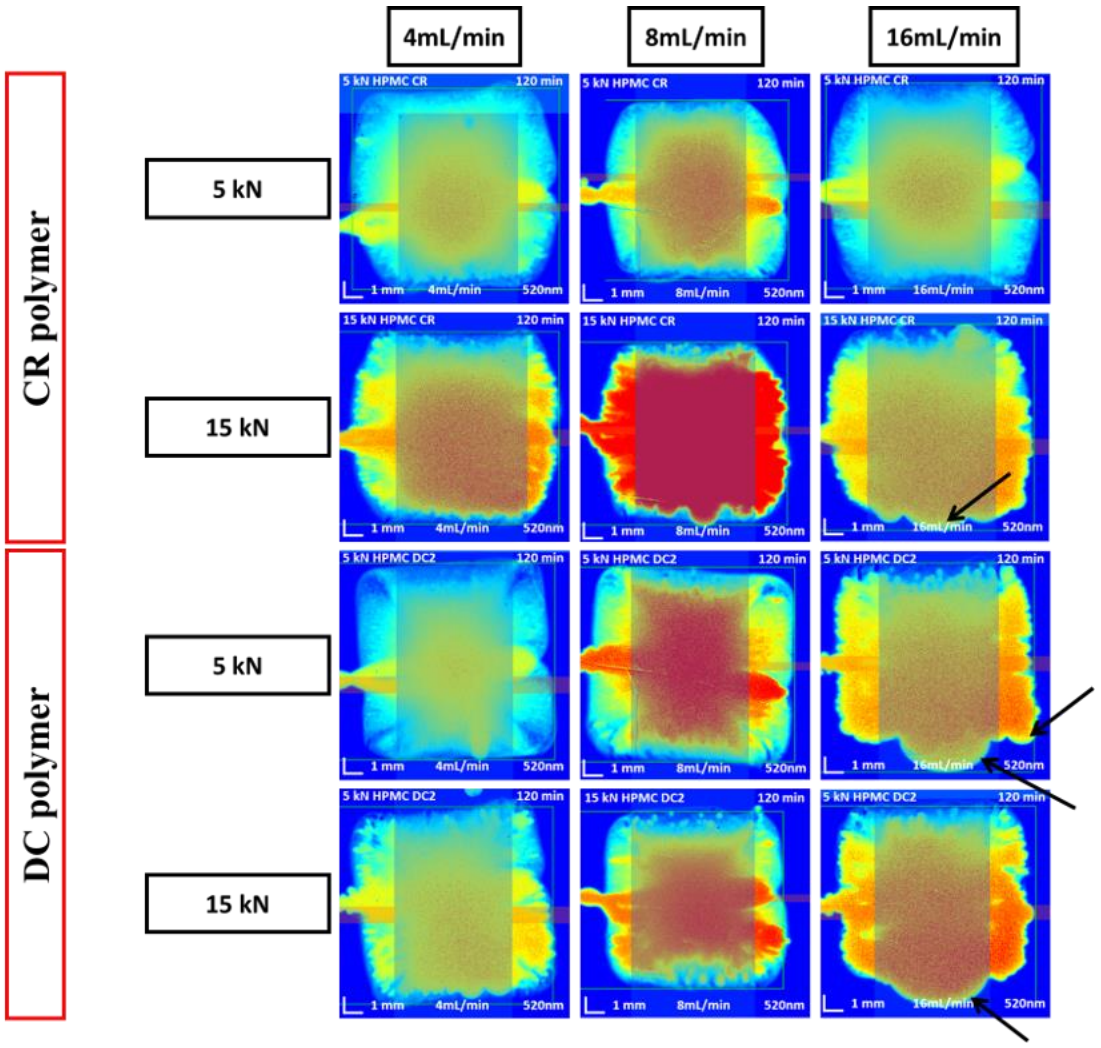

Figure 3-12 - SDi2 images for polymer compacts obtained from the SDi2 system for both the CR and DC polymer compacts at 5 and 15 kN at flow rates 4, 8.2 and 16 mL/min. Note: The black arrows indicate air bubbles lodged next to the compacts potentially giving erroneous results.

Figure 3-13 suggested that the gel layer growing extensively at the higher flow rate was false as visual inspection (Figure 3-12) showed the higher flow rate to disrupt the gel layer. Also, as the instrument is designed for small scale dissolution studies to aid preformulation studies, the large volumes of dissolution media required to conduct experiments at 16 mL/min is unwarranted. The flow rates of 4 mL/min and 8.2 mL/min worked well in determining the gel growth of the CR and DC compacts with the latter proving extremely consistent with both polymers and at both 5 and 15 kN.

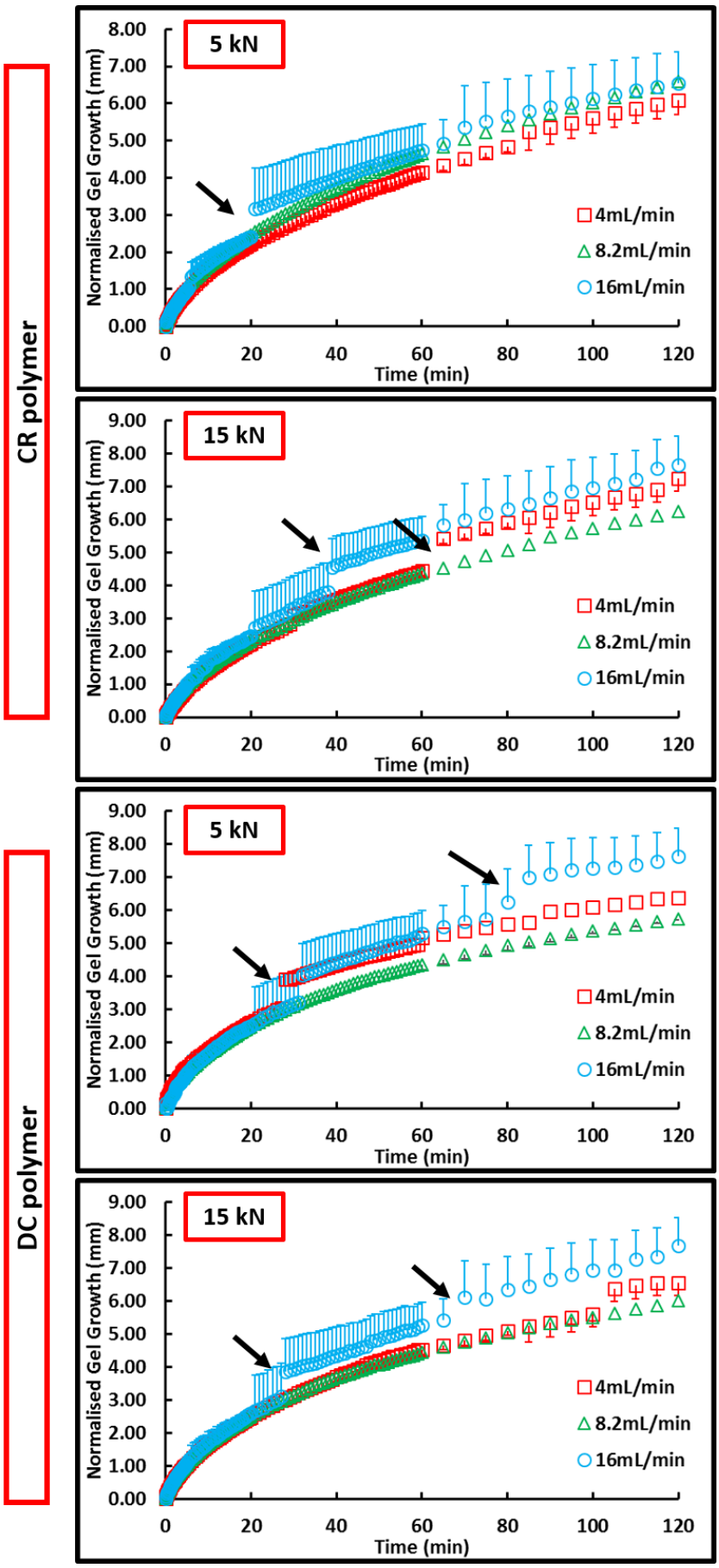

Figure 3-13 - Gel growth measurement for CR and DC polymer compacts at 5 and 15 kN at flow rates of 4, 8.2 and 16 mL/min. Note: The black arrows here indicate the influence of the air bubbles lodged next to the edge of the compact potentially giving erroneous results. These can be observed as 'jumps' in the normalised gel growth profile.

This test showed that a flow rate of 4 to 8 mL/min was suitable for conducting repeatable and reliable dissolution experiments. However, one flaw that should be stated with the 4 mL/min flow rate is with regards to its practicality. For conducting swelling experiments, the slow flow rate adds an additional 20 minutes to the experiment time and also prevents the recording of potentially crucial initial hydration phenomena as recording cannot start until the whole dosage cell is filled with the dissolution media. As a conclusion to this study, the 8.2 mL/min was retained as the flow rate most suitable for the new methodology.

3.5.4 Image Tailoring

As displayed in Figure 3-8 in section 3.4.2.5, the analysis software has a number of features to aid the analysis of the dissolution including a variety of colour schemes and the ability to zoom in on the recorded footage. The instruments analysis software defaults to the manufacturer recommendations of the grey colour scheme with zero zoom.

3.5.4.1 Colour Scheme Selection

To find a suitable set-up for the purpose of monitoring polymer hydration and growth, all the colour schemes were tested using a HPMC compact dissolution film from section 3.5.1.

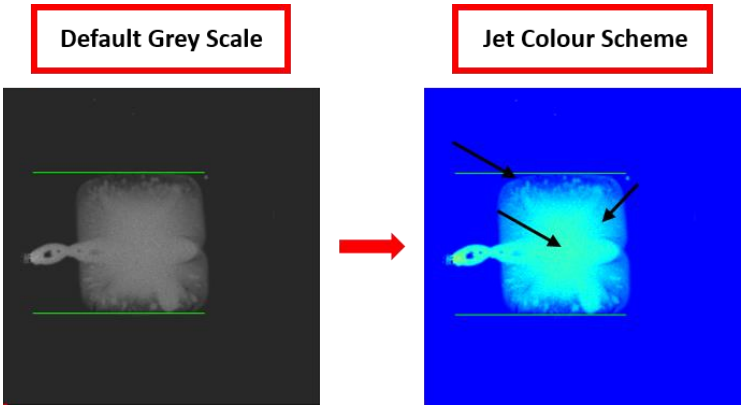

Figure 3-14 - A schematic display of the difference between the default grey colour scheme and the jet colour scheme from the SDi2 analysis software. Note: The black arrows indicate increased visible detail using the jet colour scheme.

The jet colour scheme was selected for use in analysing the dissolution footage for hydrophilic matrices. Figure 3-14 displays the difference in image quality between the default grey scale colour scheme and the jet colour scheme. One of the main reasons for selecting ‘jet’ was that a greater level of resolution could be achieved allowing for smaller more subtle details of the gel to become visible, this is indicated by the black arrows in Figure 3-14. Alongside the greater resolution, the ‘jet’ colour scheme also produces a brighter image which allows for the subtle density differences between the dry core and the hydrated layer to be fully realised.

As a conclusion to this test, the jet colour scheme was selected for use in the new methodology.

3.5.4.2 Zoom Location

The ability of the analysis software to zoom in on the dosage form was found to be very useful. By zooming in on the dosage form, a greater resolution could be achieved thereby producing more detailed images that could aid the formulator in making more informed decisions about how the hydrophilic polymers were behaving in the system.

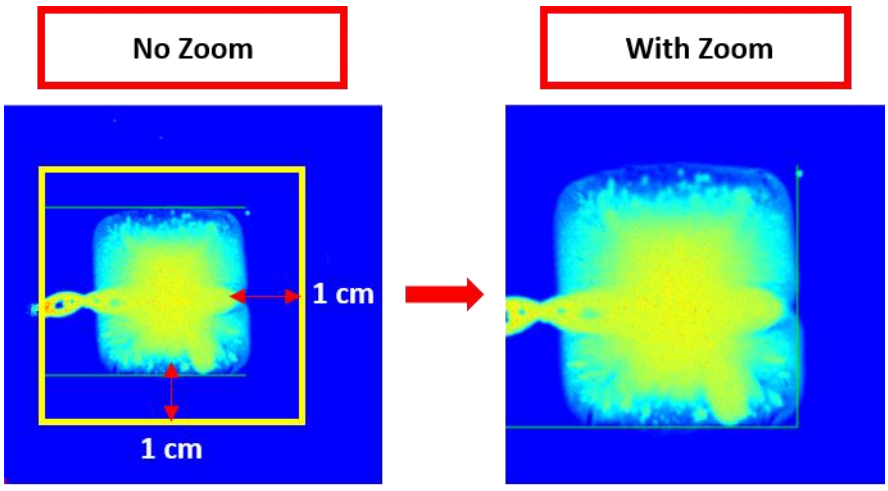

Figure 3-15 - A schematic displaying the effect of system zoom on the images obtained from the SDi2 analysis.

Figure 3-15 shows that for the zoom to be achieved in the software, a box has to be drawn around the dosage form. To aid comparison between different experiments it was important that this was standardised. This was achieved by first navigating to the

final image of the dissolution film where the growth of the polymer compact was at its largest. Next, a box was drawn around the dosage form ensuring a 1 cm gap was created between the edge of the gel and the edge of the box. As a result of this methodology, consistent zoom could be achieved between different tests producing images similar to those in Figure 3-15. This zoom technique was added to the new methodology and applied to all hydrophilic matrix experiments.

3.5.4.3 Absorbance colour scale adjustment

The final image adjustment tested in the analysis software for this methodology was the effect of the white balance figure. By default, this figure is set to 100 by the analysis software. However, upon investigation it was found that by adjusting this value, the colour scale could be condensed or extended. This was found to be very useful as adjustment of the colour scale could allow for visual differentiation between the dry core, semi-hydrated and fully hydrated layers present as a hydrophilic matrix system swells and develops. To accurately calculate the best white balance for each experiment, two equations were developed. Figure 3-16 displays the equations used. This equation was designed to determine the mAu value associated with 1 white balance unit from the white balance scale. This would be used to determine the white balance value required to make the dry core of the tablet red based on this colour scheme. A value of 20 mAu was calculated per unit of white balance.

In equation 2 in Figure 3-16, a reference absorbance value is taken from the centre of the tablet from the earliest possible image in the dissolution video. This is referred to as the dry core absorbance value. This value is then divided by 20 mAu to determine the required white balance to make this dry core red.

For example, a dry core absorbance reading of 1200 mAu, will provide a white balance value of 60 to ensure the dry core is coloured red. The effect of this adjusted white balance can be seen in the images in Figure 3-16. As the tablet hydrates this

condensed colour scale allows for the differences between the dry core, saturated polymer layer and hydrated layer to be visualised and distinguished more accurately.

In conclusion to this section, this image tailoring of adjusting white balance was applied in the new methodology to all hydrophilic matrix tablet assessments.

1) $$\frac{2000\ mAu}{100\ WB} = 20\ mAu = 1\ WB$$

2) $$WB = \frac{Dry\ Core\ Absorbance}{20\ mAu}$$

Where:
WB – Refers to the white balance ratio of the images
mAu – Refers to the milli absorbance units of the SDi2 Detector

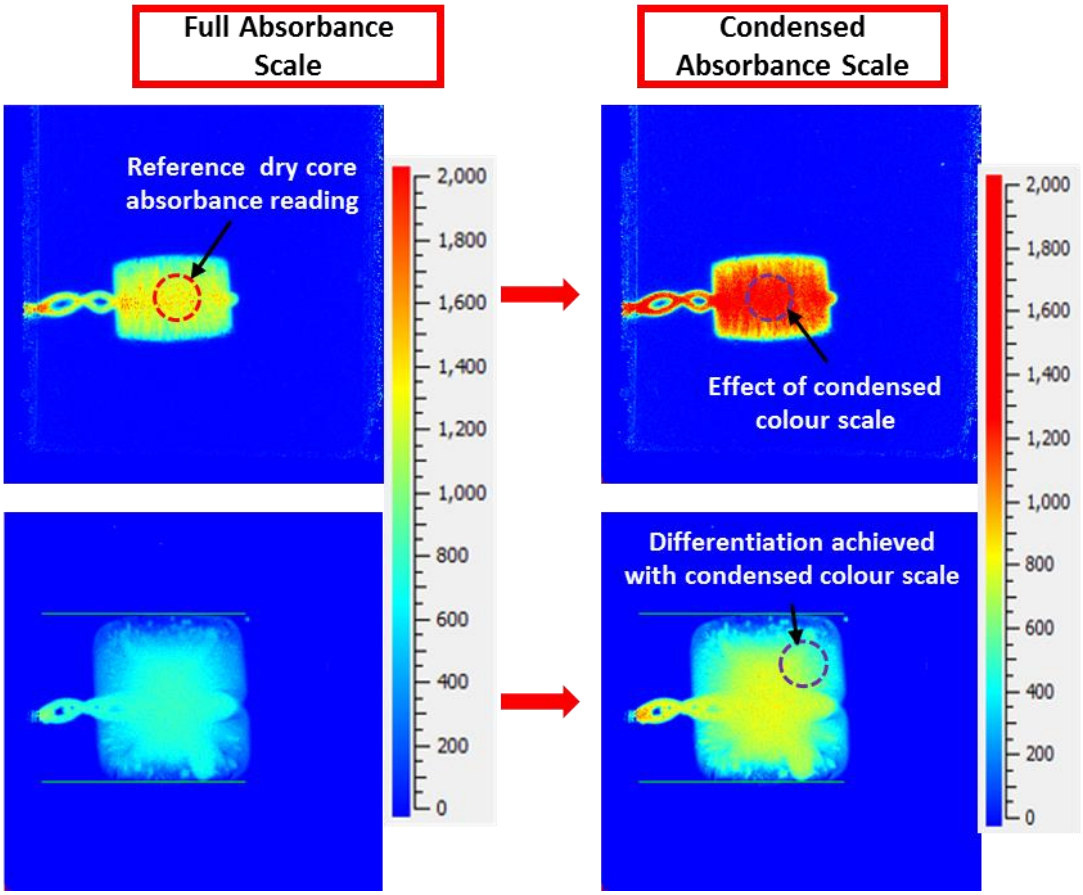

Figure 3-16 - 1) Calculation to determine the mAu value for each white balance unit based on a scale of 2000 mAu. 2) Equation to determine the white balance value to ensure that the dry core is set as the reference colour of red. This figure also displays images of the effect of the condensed colour scale on differentiation of the gel layers in a hydrated matrix tablet.

3.5.5 Summary of new methodology protocol

The following section details the protocol put forward to testing based on the preliminary studies:

- Hydrophilic matrix tablets to be assessed in axial orientation using a loop stainless steel wire holder.
- Experiments to be conducted using a temperature of 37 °C at a flow rate of 8.2 mL/min.
- Tablet edge threshold of 50 mAu to be used.
- Wider vertical measurement zone to be used.
- Jet colour scheme to be used with zoom and white balance adjustment.

3.6 Method Testing: HPMC K100M CR and DC2

3.6.1 Materials and Methods

3.6.1.1 Materials

For this investigation HPMC was selected as the model hydrophilic polymer. Two grades were selected, K100M CR and K100M DC manufactured by Colorcon Ltd. De-ionised water (~pH = 5) was used as the dissolution media.

3.6.1.2 Methods

Tablet manufacture and characterisation

Flat faced round polymer compacts with a diameter of 8 mm were manufactured to a target weight of 250 mg using a 10-station automated tabletting machine (Riva, Argentina) at a compression force of 5 and 15 kN. The porosity of the polymer compacts at the different compression forces was determined using Equation 3-1 below. Tablet porosity was reported as a mean of five determinations.

$$Tablet\ porosity = \left[1 - \left[\frac{tablet\ weight / tablet\ volume}{true\ density\ of\ powder}\right]\right] X\ 100$$

Equation 3-1 - Equation for determination of tablet porosity

The true density of the bulk polymer powder for HPMC CR and DC was determined using a Micromeritics Accupyc II 100 gas pycnometer (Micromeritics, USA). Approximately, 2.5 g of powder was required to conduct each test (recovered post analysis) with helium used as the inlet gas. All true densities are reported as a mean of three determinations. To determine compact hardness of each polymer at the 2 compression forces tested, five compacts were fractured diametrically using the Pharmatest hardness tester (Germany). Tests were conducted 48 h post compaction and are reported as a mean of five determinations.

Surface Dissolution Imaging

The dissolution imaging system was set-up to perform dissolution experiments using the method specifically designed and summarised in the new methodology (section 3.5.5).

Once the compact was placed in the wire stainless steel holder, the whole dosage cell was prepared for dissolution analysis. Firstly, borosilicate glass beads of 3 mm diameter (Supplied by Sigma-Aldrich ltd.) were added to the whole dosage flow cell such that they covered the one-way valve and evenly covered the bottom third of the flow cell. Approximately 12.3 g of glass beads were required. Next, the whole dosage cell was placed over the inlet valve and connected to the fluid lines before being locked in place. Prior to analysis, a flush program was run to clean the pumps, fluid lines and the whole dosage cell. De-ionised water was used as the rinse solution. Once completed, the data collection software was set to the following dissolution specifics: open loop flow, whole dosage cell, single solution, temperature: 37 °C and wavelength of 520 nm. For this test, 3 polymer compacts per grade and compression force giving a total of 12 compacts (6 CR compacts at 5 kN and at 15 kN; 6 DC compacts at 5 kN, and at 15 kN) were analysed.

Prior to data collection, the flow cell was filled with approximately 70 mL of deionised water to allow for system blank before reducing to 30 mL to allow for sample insertion. The wire holder containing the tablet was inserted into a removable stainless steel seal situated on the left side of the flow cell and placed into the flow cell. Extra care was taken to ensure that no water came into contact with the tablet surface during sample insertion. The experiment was restarted, and data collection resumed as the whole dosage cell filled with dissolution media.

Once each experiment completed, the cell was drained, and the flow cell disconnected and removed from the system. The hydrated polymer compact was removed from the flow cell and the wire holder and discarded. The glass beads were emptied and rinsed with de-ionised water and isopropanol before being allowed to dry in an oven. The cell and the wire holder were also rinsed with de-ionised water and isopropanol and dried using paper towels. Once all components were dry the whole dosage cell was re-assembled and placed back into the system ready for the next experiment.

SDI Data analysis

Each experiment was analysed using the bespoke dissolution imaging analysis software tailored for the instrumentation using the method specifics discussed in section 3.5, including the jet colour scheme and lower measurement threshold.

3.6.2 Results and discussion

3.6.2.1 Physical properties of the tablets

Table 3-1 - Summary of the physical properties of the HPMC CR and DC polymer compacts used in this study (n=5).

Sample	Porosity (%)	Solid Fraction (%)	Tablet Hardness (N)
5 kN CR	15.3 ± 1.8	84.7 ± 1.8	123.1 ± 18.9
15 kN CR	11.3 ± 0.6	88.7 ± 0.6	193.3 ± 12.4
5 kN DC	25.1 ± 0.8	74.9 ± 0.8	122.6 ± 3.9
15 kN DC	18.6 ± 1.8	81.4 ± 1.8	188.4 ± 10.5

The true density values for the CR and DC grades were 1.3174 ± 0.004 g/cm^3 and 1.3239 ± 0.001 g/cm^3 respectively. It was interesting to note that the differences in particle morphology described earlier in 3.5.1 impacted on the tablet porosity and solid fraction for all the samples at the different compactions studied (5 and 15 kN) (Table 3-1). The DC compacts had the highest porosity when compared to that of the CR

grade at all the different compactions studied (Table 3-1). For both the CR and DC samples, there was a general decrease in porosity and therefore an increase in their solid fraction with an increase in the compressional forces they were subjected to. This relatively higher porosity in the DC samples as well as their relatively lower solid fraction to their CR counterpart may impact on their rate of water ingress. Table 3-1 also shows that despite the differences discussed above, the mechanical strength of both the CR and DC grade compacts had similar values at the same compaction forces used with the DC grade having a smaller standard deviation value each time. It was also observed that there was an increase in mechanical strength with increase compaction for all the samples.

3.6.2.2 Swelling analysis of CR and DC Compacts

3 compacts were tested on both the CR and DC polymers at each compaction level. The time points selected for the images were 1, 5, 30, 60, 90 and 120 min. Following on from the method development discussed in section 3.5, an absorbance threshold of 50 mAu and a wider measurement was used during analysis of the data. Also, the image alterations were adopted including the ‘jet’ colouration and the adjustment of the white balance.

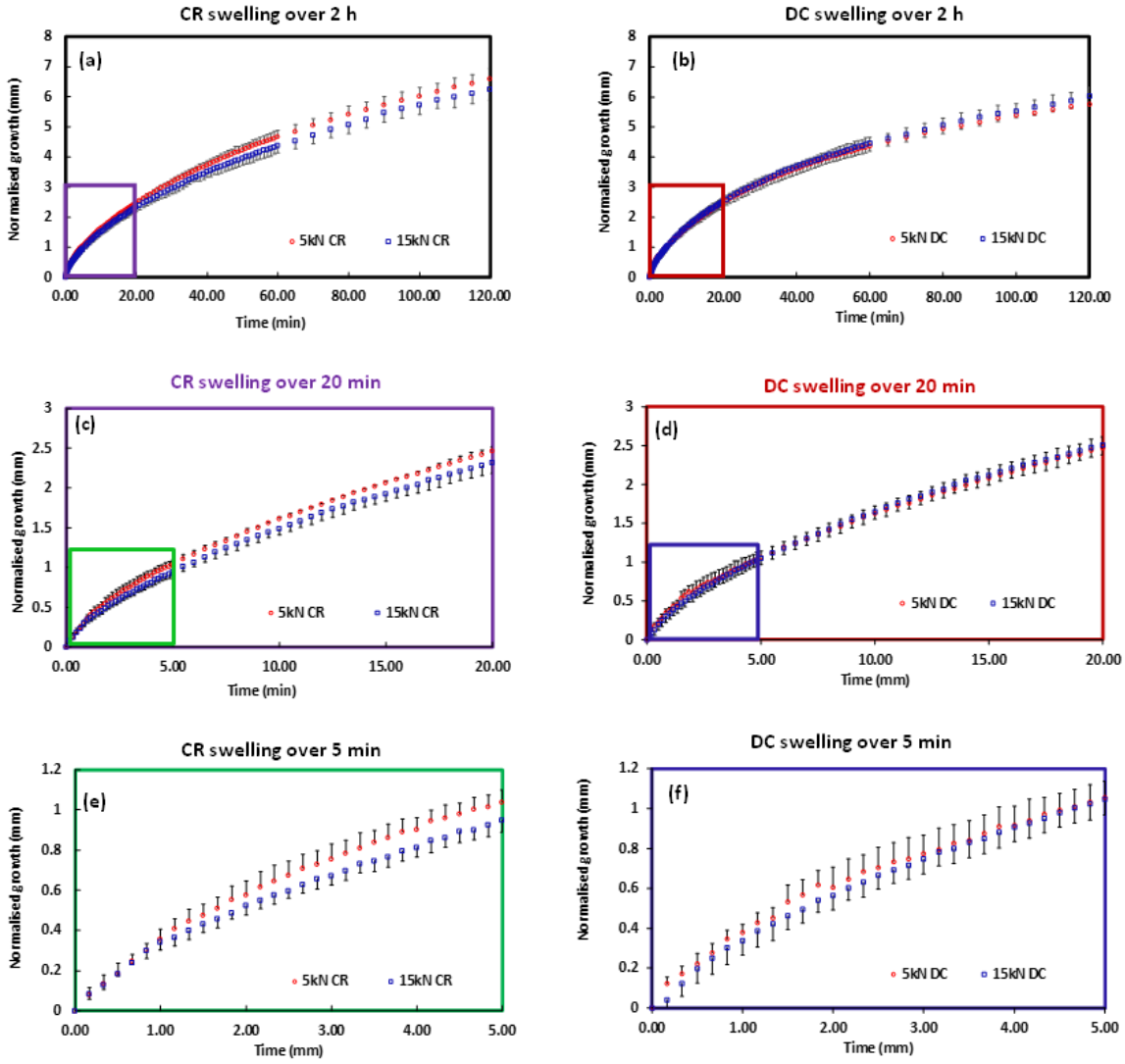

Figure 3-17 - Swelling data for polymer compacts obtained from the SDI2 instrument at a) 120 min for CR compacts at 5 and 15 kN compaction levels (purple box insert relates to Fig. 20c), b) 120 min for DC compacts at 5 and 15 kN compaction levels (red box insert relates to Fig. 20d), (c) 20 min for CR compacts at 5 and 15 kN compaction levels (green box insert relates to Fig. 20e), (d) 20 min for DC compacts at 5 and 15 kN compaction levels (blue box insert relates to Fig. 20f), (e) 5 min for CR compacts at 5 and 15 kN compaction levels and (f) 5 min for DC2 compacts at 5 and 15 kN compaction levels

The swelling plots shown in Figure 3-17, highlight the differences between the two polymers at the different compaction levels over the course of the experiment. The images depicted in Figure 3-18 highlight the subtle but important differences in the initial hydration of the gel layer between the two polymers at the different compaction levels.

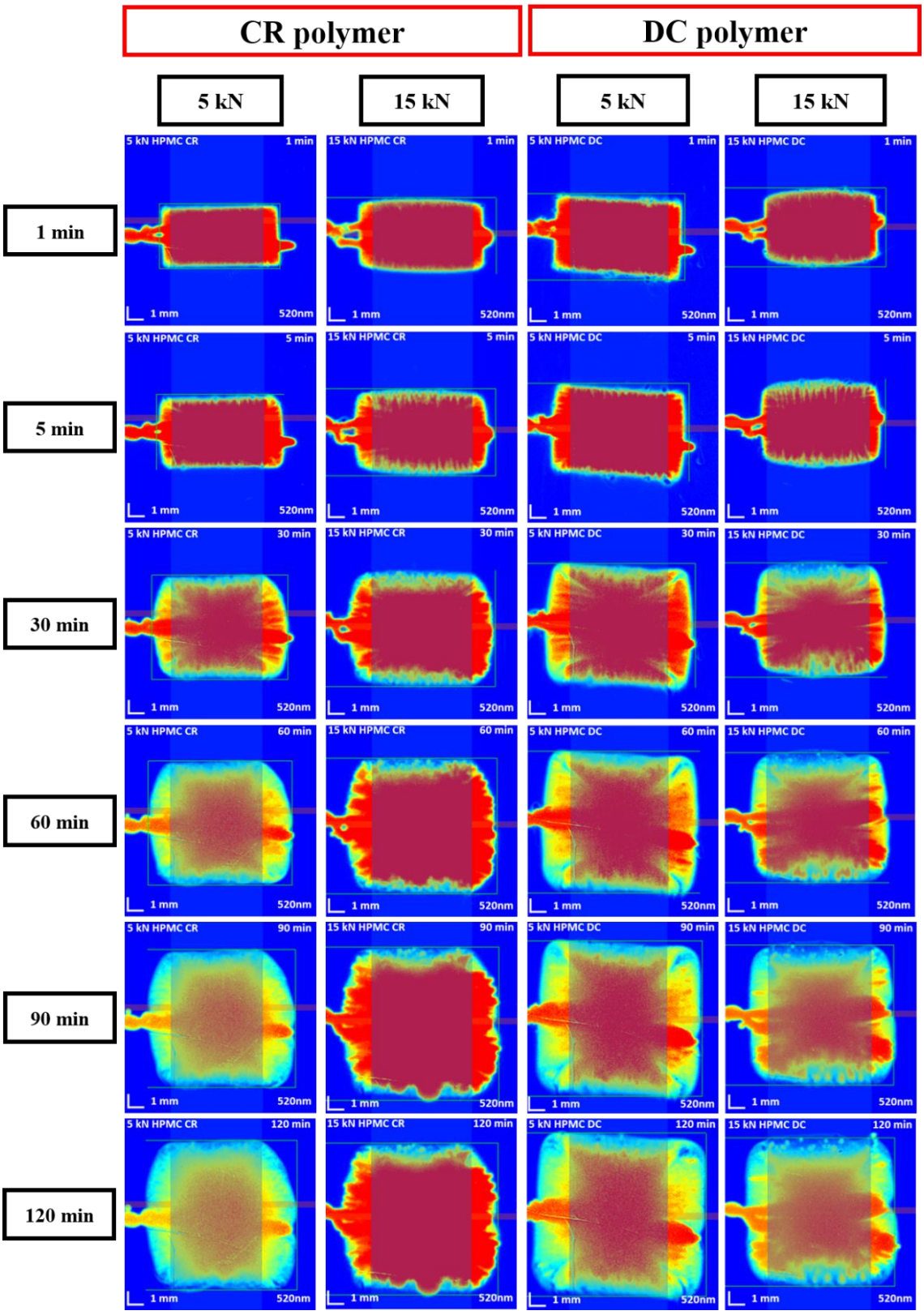

Figure 3-18 - Jet coloured SDI2 images of CR and DC polymers from time points 1 min to 120 min at two compressional levels (5 and 15 kN). Note: HPMC K100M CR is referred to as just CR in the manuscript whereas HPMC K100M DC is referred to as just DC in the manuscript.

Pajander et al. investigated the behaviour of two different grades of hypromellose using the Actipix SDI300 dissolution imaging system, the authors found the different polymers to behave similarly with regards to swelling, gelling and erosion at the compacts surface (73). Kavanagh and Corrigan studied a range of different molecular weighted HPMC polymers and observed that the change in weight which reflected swelling for the higher molecular weight polymers (HPMC K100M) had the highest maximum swelling over a 12 h period with very little erosion occurring. These polymers also showed the highest dissolution medium uptake. Table 3-1 shows the initial compact heights used for the imaging analysis. From Figure 3-17, where the initial heights were normalised, it can be observed that the compacts had imbibed the media and swollen to ~6-7 mm in just 2 h reflecting Kavanagh and Corrigan's observations (61).

An independent sample *t*-test with equal variances (performed using IBM® SPSS® Statistics) was used to test the statistical significance of the difference between the two polymers at the different compaction levels. The null hypothesis was that the profiles were the same using a 95 % confidence interval. The results were that the null hypothesis could be retained for all the profiles over the 0 to 120 min range. There was however a statistical difference between the 5 kN CR vs. DC which was detected between 60 and 120 min ($p = 0.007$).

Overall, the instrumentation detected very similar growth patterns between the CR and DC polymers across the forces tested. A key observation was that at 5 kN, the CR polymer swelled to a slightly greater size than the DC polymer (Figure 3-17 a-b) This correlated with the statistical findings from the independent t-test that overall, the CR and DC polymers behaved similarly with the exception of 5 kN post 60 min which showed statistical difference.

From 20 min onwards for the compacts, the gel layer in the DC compact appeared to be less dense (especially for the 5 kN compacts). In contrast the CR polymer was denser for the same images (Figure 3-18). This observation was in-keeping with similar differences observed by previous studies (74,75). These studies suggested that polymers with fibrous morphology i.e. CR form denser gels due to the inter-locking and entanglement of the fibres and as a result may be able to control drug release more effectively. This observed difference was less pronounced as the compacts were subjected to higher compaction force. This phenomenon can also be explained by the differences in porosity and solid fractions for the CR and DC polymers. DC had a solid fraction (converted into percentage) of 85 % for the compact compacted at 5 kN whereas the CR had a solid fraction of 75 % for the compact compacted at 5 kN suggesting that the more porous DC was bound to have a much higher ingress of water. The swelling data plot shown in Figure 3-17 also displays the trends observed in the swelling images.

3.7 Chapter Conclusions

This chapter displayed and tested a number of the key parameters used in the testing of hydrophilic matrices in the dissolution imaging system. A number of solutions were proposed in section 3.5 to the challenges identified in section 3.4. These solutions were tested with HPMC CR and DC compacts at 5 and 15 kN. With the new developed methodology, swelling of whole polymer compacts could be measured accurately in real time with a high level of detail by the dissolution imaging instrument. The new methodology also allowed for small subtle differences between the two polymers to be observed. The results showed that overall, both polymers swelled similarly at the compaction forces tested. The growth rates of the DC compacts were inhibited despite its larger porosities as compared to the CR compacts resulting in the similarities seen between the two polymers. The methodology also detected other differences in the gel layers formed by both the DC and CR polymers indicating that the CR grade forms denser gels which could also be attributed to the differences in the solid fraction. One consideration to be taken is that care should be given to an appropriate selection of threshold absorbance used as this may potentially differ based on the nature of polymer tested.

Crucially, with the update in methodology this test highlighted an area of research that can provide a formulator insight into the behaviour of a range of formulations thereby informing decisions of choice of appropriate formulation for further investigation.

Chapter 4 – Use of advanced imaging techniques for measuring hydrophilic polymers.

4.1 Note to Reader

Some aspects of the following chapter are published in Pharmaceutics Volume 12 under the title ‘Application of Focus Variation Microscopy and Dissolution Imaging in Understanding the Behaviour of Hydrophilic Matrices.(76)’

4.2 Rationale

The following chapter demonstrates an explorative study into the use of dissolution imaging and focus variation microscopy with hydrophilic polymers. The purpose of this chapter is to build upon the methodology developed in chapter 3 and use dissolution imaging to provide an insight in to the hydration of different hydrophilic polymers. Also, focus variation microscopy will be employed to assess the topography of the polymer compacts prior to dissolution.

4.3 Introduction

Hydrophilic matrix systems can be found in a wide range of controlled release formulations within pharmaceutics. The main principle of these systems is that on contact with water, the hydrophilic component swells to form a hydrated gel layer. This gel layer then controls the rate of further water penetration into the tablet core and the diffusion of the drug from the core out (77). Over time the outer edge of the hydrated matrix begins to erode as the system becomes more dilute (Figure 4-1). The dissolution rate of soluble drugs is principally controlled by diffusion out of the hydrated gel layer. For poorly soluble drugs, the dissolution rate is controlled by the rate of erosion of the hydrated gel layer which consequently, is dependent on the type of polymer used in the formulation.

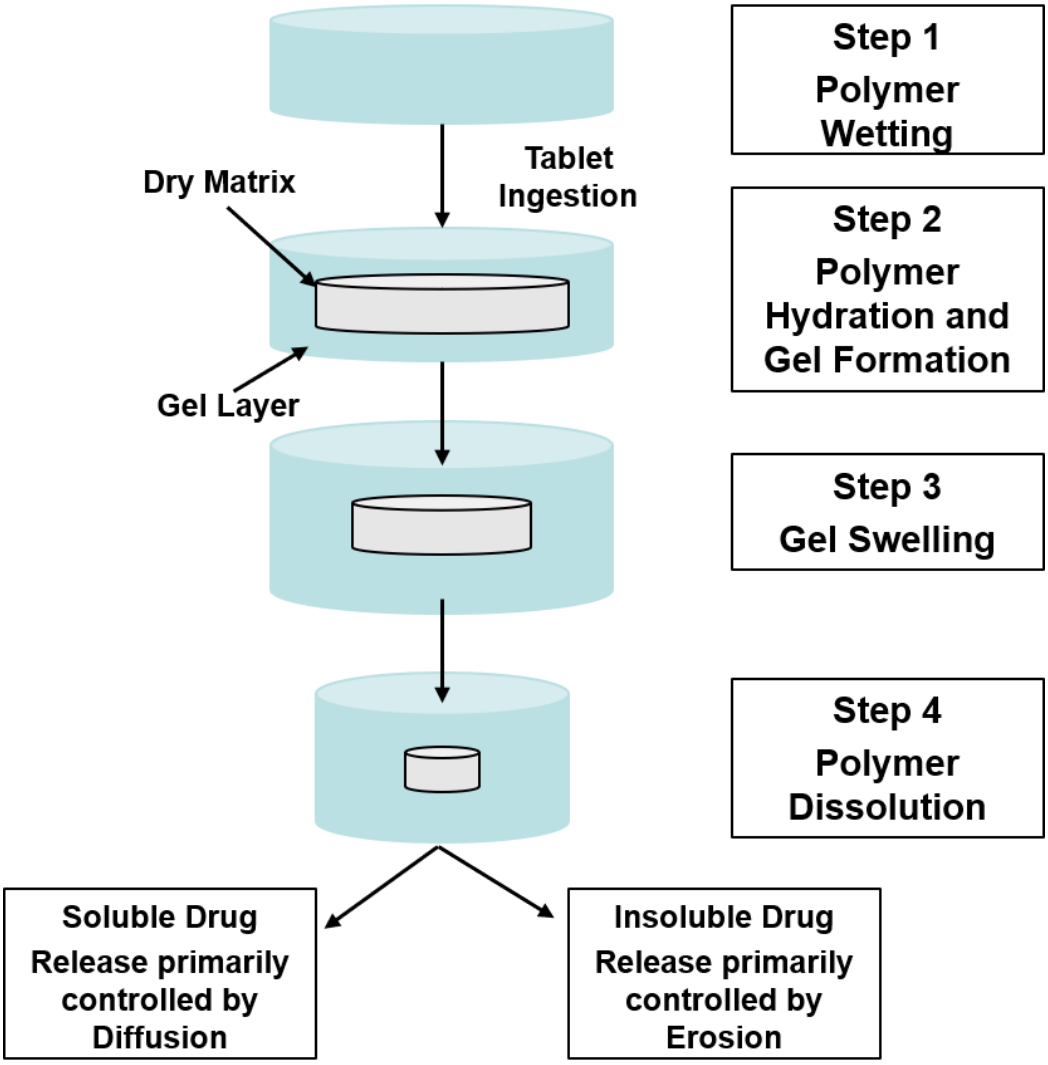

Figure 4-1 - Mechanism of action for hydrophilic polymers in controlled release formulations.

There are many advantages and limitations to the use and manufacture of formulations containing hydrophilic polymers. These are summarised in Table 4-1 below.

Table 4-1 – Advantages and limitations of controlled release formulations containing polymers.

Advantages	Limitations
Low Dose Frequency	High development costs
Minimised Side Effects	Release rate can be compromised by food and gastric transit
Improved Patient compliance	Cannot be crushed or chewed.
Cost effective manufacture	

A wide range of hydrophilic polymers are available for use in controlled release formulations. These can be classified in a number of ways based on their structure, degradability, or chemistry. However, one of the most common ways of classifying the polymers is based on their source e.g. natural or synthetic. Examples of common synthetic polymers include; polyacrylic acids (PAA) such as Carbopol™ and polyethylene glycol (PEG). Examples of polymers from natural sources include; xanthan gum and chitosan derivatives. Polymers can also be classified as semi-natural or semi-synthetic, these polymers are usually derived from natural sources before being chemically modified to improve efficacy or physical characteristics. Examples of these polymers include cellulose ethers such as sodium carboxymethylcellulose (Na – CMC) and Hydroxypropyl methylcellulose (HPMC). This chapter introduces two additional polymers to UV imaging alongside HPMC CR and DC. These are Xanthan Gum and Polyethylene Oxide (PEO).

Xanthan Gum

Xanthan gum is a natural high molecular weight anionic polysaccharide that is obtained through the fermentation of carbohydrates with *Xanthamonas campestris* (78). The primary structure of xanthan gum (Figure 4-2) consists of repeating pentasaccharide units consisting of two D-mannopyranosyl units, two D-glucopyranosyl units, and one D-glucopyranosyluronic unit (79). Xanthan gum is a free flowing powder soluble in both hot and cold water to give viscous solutions at low concentrations. It is a very effective thickener and stabilizer because it can produce highly viscous solutions even at low concentrations when compared to other polysaccharide solutions. Xanthan gum solutions are also very stable across a broad range pH values (80). Xanthan gum has been widely used in oral and topical formulations as well as in the food and cosmetic industry as a stabilising or suspending agent. Due to the hydrophilic nature of Xanthan gum it has also become a polymer of choice in the manufacture of hydrophilic matrix

systems. Previous studies have focused on the polymers' compactability, in vitro release and rheology (81,82). More recently, the polymer has found uses in alcohol resistant formulations (83), nanoparticle loaded gels (84) and sustained release pellets (85).

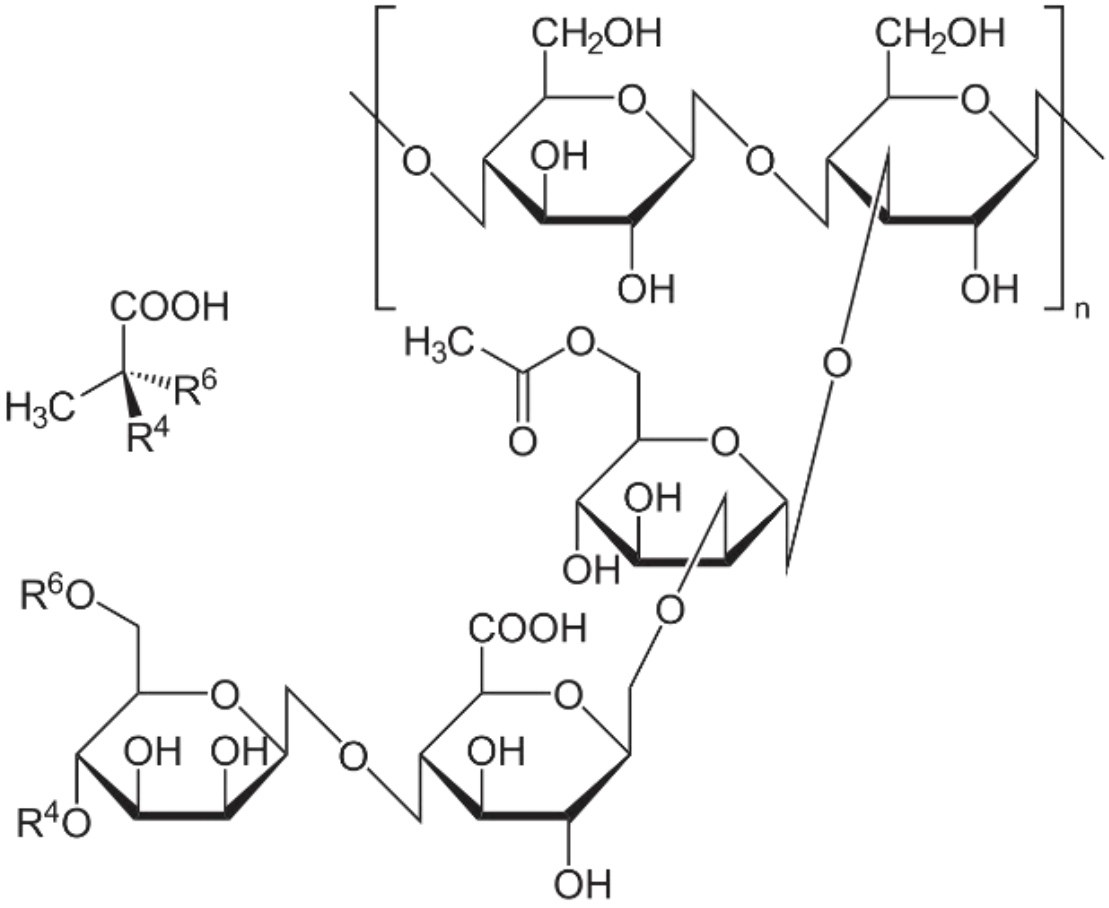

Figure 4-2 – Chemical structure of Xanthan gum

Polyethylene oxide (PEO)

PEO is a synthetic thermoplastic homopolymer synthesized by the heterogeneous catalytic polymerization of the ethylene oxide monomer (Figure 4-3) (86). PEO is available in a wide range of molecular weights and due to the oxide present in the polymer chain is highly soluble in water.

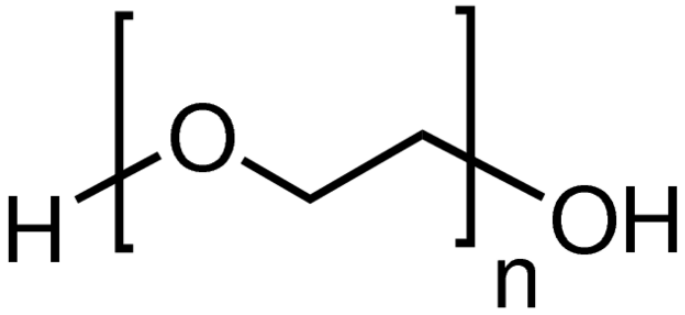

Figure 4-3 – Chemical structure of Polyethylene Oxide

PEO has been utilised in a number of controlled release applications and has been shown to control the release of both high and low solubility drugs from matrix formulations manufactured via direct compression (87-89). PEO has also been used in other formulations and techniques including buccal adhesives (90), hydrogels (91), controlled release capsules (92) and hot-melt extruded tablets (93).

Hydroxypropyl methylcellulose (HPMC)

Amongst the wide range of hypromellose grades available, the high molecular weight METHOCEL™ Premium K (hypromellose 2208, USP) chemistry is the most widely used in ER matrix formulations (94). The METHOCEL® K100M CR and the METHOCEL® K100M DC2 grades were selected for this work. METHOCEL® K100M CR is designed and can be used for wet and dry granulation in controlled release applications, (95) in combinations with other hydrophilic polymers (96) and in 3D printed dosage forms (97). Following on from the availability of the CR grade, METHOCEL® DC2 is a new addition to the polymers supplied by the Dow Chemical Company. This polymer is particle engineered by the manufacturer to form more spherical particle morphologies (in comparison to the CR grade) to help facilitate a switch from granulation to a more efficient direct compression tableting process. The DC2 grade is also designed to offer the same performance and reliability of the CR grade. The DC2 grade was compared recently to its CR equivalent and the results concluded that the DC2 grade did in fact flow better than its CR counterpart. Tablets

produced to a standard porosity also provided similar strength tablets (98). A similar comparison study also concluded that the CR grade was able to control release of ibuprofen better than the DC2 grade (74).

4.4 Materials and Methods

4.4.1 Materials

The materials for this experiment were as follows:

The four polymers; Xanthan Gum (CP Kelco Ltd.), PEO (Arcos Organics Ltd.), HPMC CR and HPMC DC (Colorcon Ltd.) and de-ionised water (~pH = 5) as the dissolution media. Note: HPMC DC2 is referred to as DC from henceforth.

4.4.2 Methods

4.4.2.1 Compact Manufacture

Approximately 312.5 ± 1 mg of polymer was weighed out using a micro balance. This was then added to 10 mm flat faced die. Next, the powder was compacted at 10 kN using a Testometric™ hydraulic press. The compacts were ejected from the die and stored prior to use. 312.5 mg was selected as the target weight as this represented an equivalent polymer ratio to the 8 mm 250 mg compacts used in Chapter 3 for the method development manufactured on the 10-station automated tabletting machine (Riva, Argentina).

4.4.2.2 True Density and tablet properties

True Density

True density measurements were performed on the four polymers, for each measurement, approximately 2 g of powder was added to a stainless steel sample cup. The sample cup was then placed in a Micromeritics Accupyc II gas pycnometer and sealed. Helium gas was chosen as the inlet gas at a pressure of approximately 20

mbar. Each measurement took approximately 10 minutes to complete and post analysis all powder used was recovered.

Tablet Dimensions and Hardness

5 compacts for each polymer were used to measure tablet hardness and tablet dimensions. The weight of each compact was measured prior to placement in a Pharmatest Hardness tester. Each compact was placed on its edge to allow the hardness tester to measure height, before then being placed flat to allow for the measurement of diameter. The compact was then exposed to an increasing force until the tablet fractured. The force at which the tablet fractured was recorded in Newtons (N) to two decimal places. All broken tablets were then discarded.

Tablet Porosity

Using the mass and the dimensions recorded from the hardness study, porosity of the compacts was calculated. The first step of the calculation was to determine the volume of each compact. (Equation 4-1)

$$V = \pi r^2 \times h$$

Equation 4-1 – Equation to determine compact volume. Where v is volume, r is the radius and h is the tablet height.

Next, using the mass and volume of each compact, the density of each compact was determined using Equation 4-2.

$$\rho = \frac{mass}{V}$$

Equation 4-2 – Equation to determine compact density. Where ρ is compact density and v is compact volume.

Finally, porosity was determined as the difference between the apparent density (ρ_{app}) of the compact and the true density of the powder (ρ_{true}). (Equation 4-3)

$$Porosity = \left(\left(\frac{\rho_{app}}{\rho_{true}} \right) - 1 \right) \times 100$$

Equation 4-3 – Equation to determine compact porosity.

4.4.2.3 Scanning Electron Microscopy (SEM)

SEM was utilised in this chapter to assess the particle morphology of each of the polymers tested. Prior to analysis on the SEM, each sample was mounted on double-sided carbon adhesive tape on a metal stub and sputter-coated with a thin coating of gold/palladium (80:20) for 60 s using a Quorum SC7620 Sputter Coater under vacuum. A Jeol JSM-6060CV SEM operating at 20 kV was used to obtain the electron micrographs. Different magnifications were taken to aid the study of particle morphology.

4.3.2.4 Focus Variation Microscopy

The methodology for conducting focus variation microscopy is discussed in more detail in chapter 2. The method specifics are outlined as follows; for this work the 10 x magnification used a 4X4 image area to produce a comparative image size to 5x magnification. Also, the vertical resolution for the 5x magnification was 0.42 µm and 0.21 µm at 10x magnification.

4.4.2.5 Dissolution Imaging

In this study the whole dosage cell was exclusively used.

Dissolution Media Preparation

This study used de-ionised water as the dissolution medium. This was to prevent the influence of ions on the hydration of the gel layer for each polymer tested.

Whole Dosage Cell measurement

Following the new methodology outlined in chapter 3, all hydrophilic polymer compacts were analysed in axial orientation using a stainless steel wire holder (Figure 4-4). All experiments were then conducted at 37 °C at a flow rate of 8.2 mL/min over a 2 h period with de-ionised water as the dissolution media. All images were recorded using the 520 nm LED. Once each experiment was completed, the experiment files were analysed using the bespoke analysis software, with the wider measurement zone and absorbance threshold of 50 mAu described in Chapter 3. The data was extracted to Microsoft Excel™ for data processing. The images obtained from the analysis were also adjusted to highlight the dry core and subsequent hydrated layers.

Tablet growth measurements were displayed as a percentage gain based on the initial reading of tablet size (Equation 4-4). Microsoft Excel was used to calculate and plot all growth data points.

$$Growth\ (\%) = \left(\left(\frac{h_{t=0} + h_{t=x}}{h_{t=0}}\right) - 1\right) \times 100$$

Equation 4-4 – Equation for determining percentage growth based on initial compact size. Where; h = tablet height, t = time and x = a given time point.

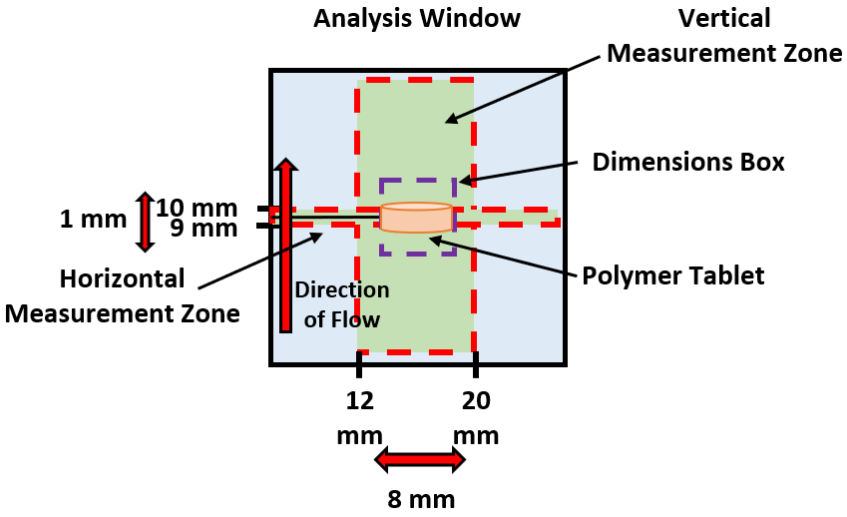

Figure 4-4 - A schematic representation of the analysis conducted on the polymer compacts, displaying the measurement zones and the tablet orientation.

4.5 Results and discussion

4.5.1 Scanning Electron Microscopy

From the analysis of the micrographs displayed in Figure 4-5, Xanthan Gum (Figure 4-5a) displayed a blend of particle morphologies within the bulk powder including rod-like and irregular particles. This blend of particle morphologies could be due to the extraction and manufacturer processing of the natural polymer. In contrast to the Xanthan Gum, the PEO (Figure 4-5b) displayed larger particles which were more rounded in nature. On closer inspection using a higher magnification these particles appeared to be agglomerates of smaller particles present in the bulk powder giving the larger agglomerates a microporous structure. The uniformity of the bulk powder could be attributed to the synthetic nature of the polymer and the systematic manufacturing processes used to produce the polymer.

The HPMC CR micrographs displayed in (Figure 4-5c) displayed particles with a thin ribbon like morphology. This morphology is suitable for controlled release formulations as the particle morphology allows for entanglement of the hydrating polymer chains producing stronger and denser gels. These micrographs also highlight that this grade has undergone some manufacturing process indicated by the uniformity of morphology in the sample. The DC powder (Figure 4-5d) displayed some subtle differences to the CR powder. The first was the presence of some rounded angular particles whilst the second was the coiling of longer structures producing more rounded particles. This can be attributed to the engineering of this grade of HPMC to achieve a powder with increased flowability suitable for direct compression. All the polymers have characteristics that could influence the surface topography of the tablets and therefore the hydration of its polymer compacts.

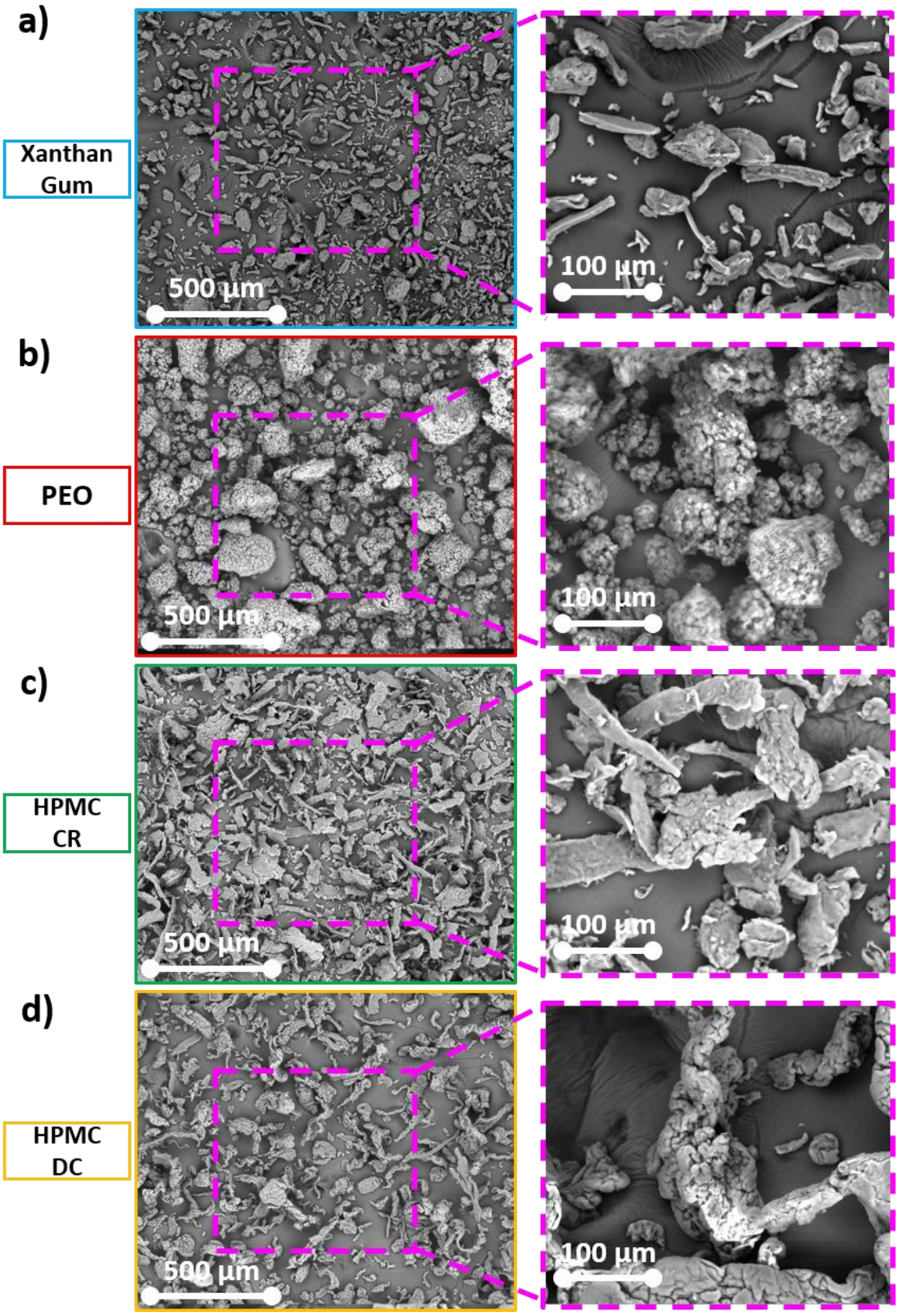

Figure 4-5 - Scanning Electron Micrographs of the polymers tested. a) Xanthan Gum, b) PEO, c) HPMC CR and d) HPMC DC.

4.5.2 Compact Hardness and Compact Porosity

Figure 4-6 displays the results from the porosity and hardness measurements for the polymer only compacts. Xanthan Gum displayed the highest porosity of all the polymers compacted at 10 kN with a porosity of approximately 17%.

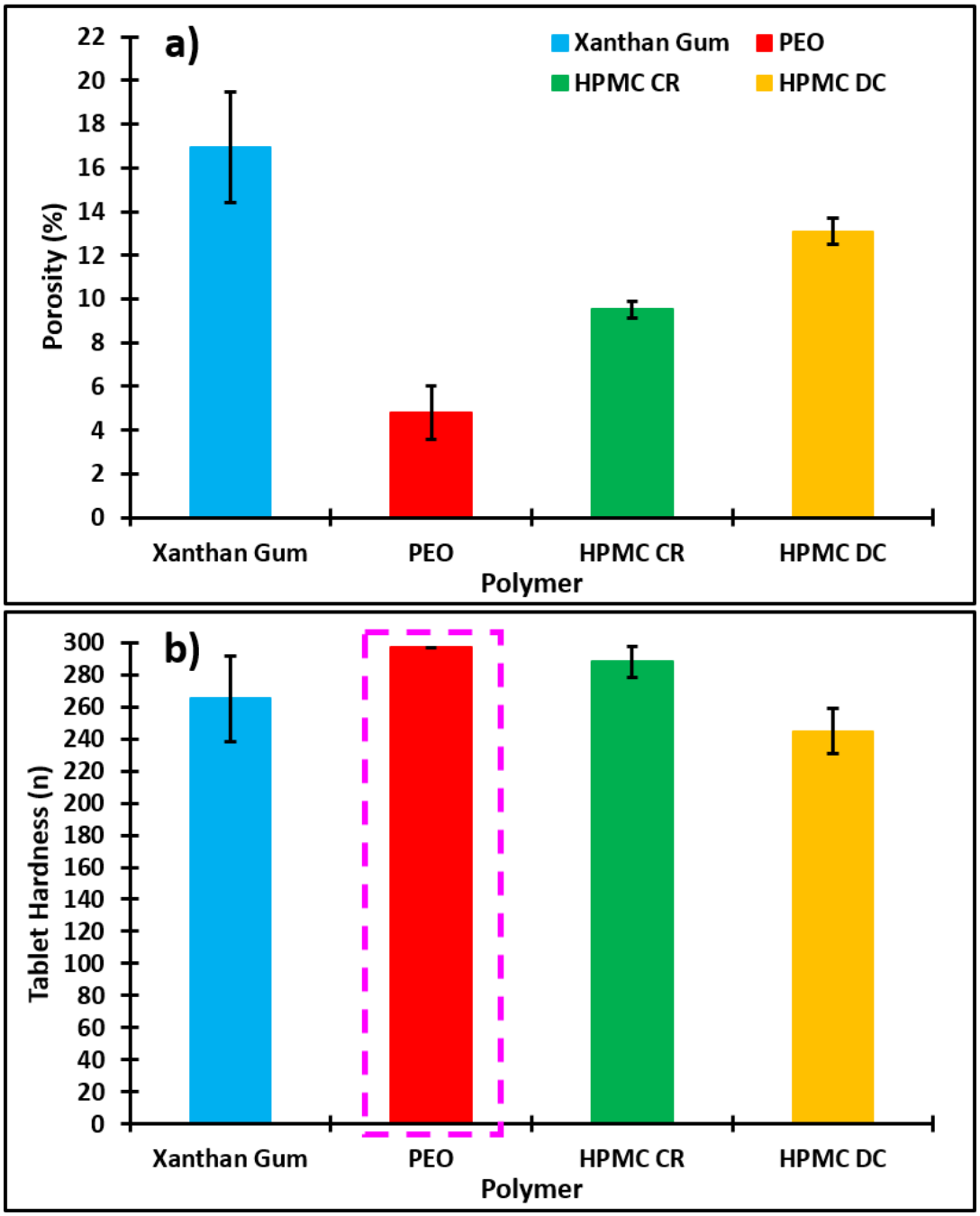

Figure 4-6 - Bar charts displaying the results (mean +/- SD) from the hardness and porosity assessment of the four polymers. a) Tablet Porosity and b) Tablet Hardness. Note: The pink dashed box indicates that this polymer reached the maximum force of the hardness tester without fracturing.

It is therefore expected that the dissolution media will penetrate deeper into the compact at a faster rate than with the other polymer compacts, potentially leading to a greater hydration and rate of swelling. Xanthan gum also produced comparably softer compacts with a hardness of 265 N and with a relatively higher deviation. PEO produced compacts that were the hardest of all the polymers tested at 297 N. It is important to note that this value represents the upper limit of the hardness tester. It is likely that the excessive hardness was a result of the plastic nature of the polymer, this is supported by the deformation that occurred to the edges of the compacts at this force (Figure 4-7).

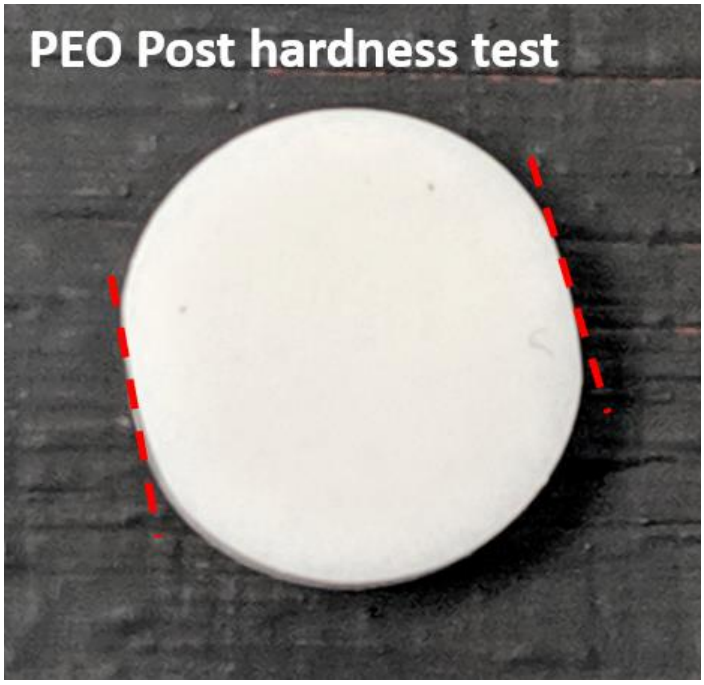

Figure 4-7 - A photograph highlighting the deformation that occurred to the PEO compacts during the hardness test. Note: The red dashed lines indicate the sides of the tablet deformed during testing.

This increased hardness for the PEO compacts was also supported by the lowest compact porosity for all the polymers tested at approximately 5 %. This observation leads to the hypothesis that the PEO compacts will hydrate at a slower rate than the other polymers due to the difficulty for the dissolution media to ingress through the compact, resulting in a lower rate of growth of the gel layer.

The DC grade produced a relatively higher compact porosity to the CR grade (~13 vs. ~10 %) but a relatively lower hardness (~245 vs. ~288.12 N) at 10 kN. The DC polymer also produced the softest tablets of all the polymers tested. The lower porosity of the CR grade and increased hardness could be attributed to interlocking of the ribbon like CR particles (Figure 4-5). This potentially reduces core porosity and increases compact strength. Also, the presence of more rounded particles in the bulk DC powder potentially led to larger pores between the particles in the compact.

4.5.3 Focus Variation Analysis

Table 4-2 - Table displaying surface parameter values (mean (n=5) +/- SD) at 5 and 10 x magnification for the four hydrophillic polymers.

Surface Parameters				
5 x Magnification				
Parameter	**Xanthan Gum**	**PEO**	**HPMC CR**	**HPMC DC**
Str	0.98 ± 0.02	0.87 ± 0.06	0.91 ± 0.05	0.94 ± 0.01
Sal (mm)	0.02 ± 0	0.06 ± 0.01	0.05 ± 0.01	0.04 ± 0
Sdr (%)	4.43 ± 0.18	4.09 ± 0.29	5.19 ± 0.52	4.26 ± 0.27
Smr2 (%)	89.52 ± 0.26	90.18 ± 0.56	90.18 ± 0.30	89.48 ± 0.19
10 x Magnification				
Str	0.96 ± 0.26	0.93 ± 0.03	0.90 ± 0.04	0.94 ± 0.02
Sal (mm)	0.03 ± 0.02	0.07 ± 0.01	0.06 ± 0.00	0.04 ± 0
Sdr (%)	3.63 ± 0.28	2.38 ± 0.11	4.38 ± 0.33	4.96 ± 0.98
Smr2 (%)	89.82 ± 0.26	90.96 ± 0.48	91.50 ± 0.31	89.06 ± 0.27

Focus variation microscopy provided a unique insight into how the morphology of the bulk powders identified in SEM influenced the surface topography of the polymer only compacts. Images obtained from the surface assessment of the polymer compacts are shown in Figure 4-8. These are also accompanied by areal roughness plots displayed in Figure 4-9.

The areal roughness plots are used to calculate the surface parameters in Table 4-2. S*al* is a measurement of the lateral scale of a surface. However, in this work it was used as a confirmatory tool to ensure that the surface analysis had been conducted correctly and only surface roughness was considered in all surface calculations. All surface profiles displayed a S*al* value of below 0.1 mm. This indicates that only high frequency components (i.e. roughness) were considered and that the analysis had been successful. The presence of the smaller angular particles in the xanthan gum bulk powder can be seen across the surface of the polymer compact in Figure 4-8. This can also be visualised in the 3D roughness plot where a uniform spread of small peaks can be seen across the surface (Figure 4-9). The *Str* parameter which provides a measurement of the uniformity of the texture on the surface of the polymer compacts indicated that the surface texture was uniform in all directions due to a value greater than 0.5. Xanthan gum displayed a low S*dr* value of 4.43 ± 0.18 % at the 5x magnification despite the texture on the surface of the compact. ISO guidelines recommend that S*dr* values are below 5 % for a surface as in theory all manufactured surfaces will display some texture. An interesting observation was that Xanthan Gum displayed the second lowest S*mr2* value of the polymers tested with a value of 89.52 ± 0.26 % at the 5 x magnification. The S*mr2* parameter is influenced by the deeper surface pores present across the surface and suggests that 10.48 % of the surface is suitable for ‘lubricant’ retention. This correlates with the observation from the tablet porosity assessment and could provide a further indicator to a faster hydration and growth rate for the Xanthan Gum compacts.

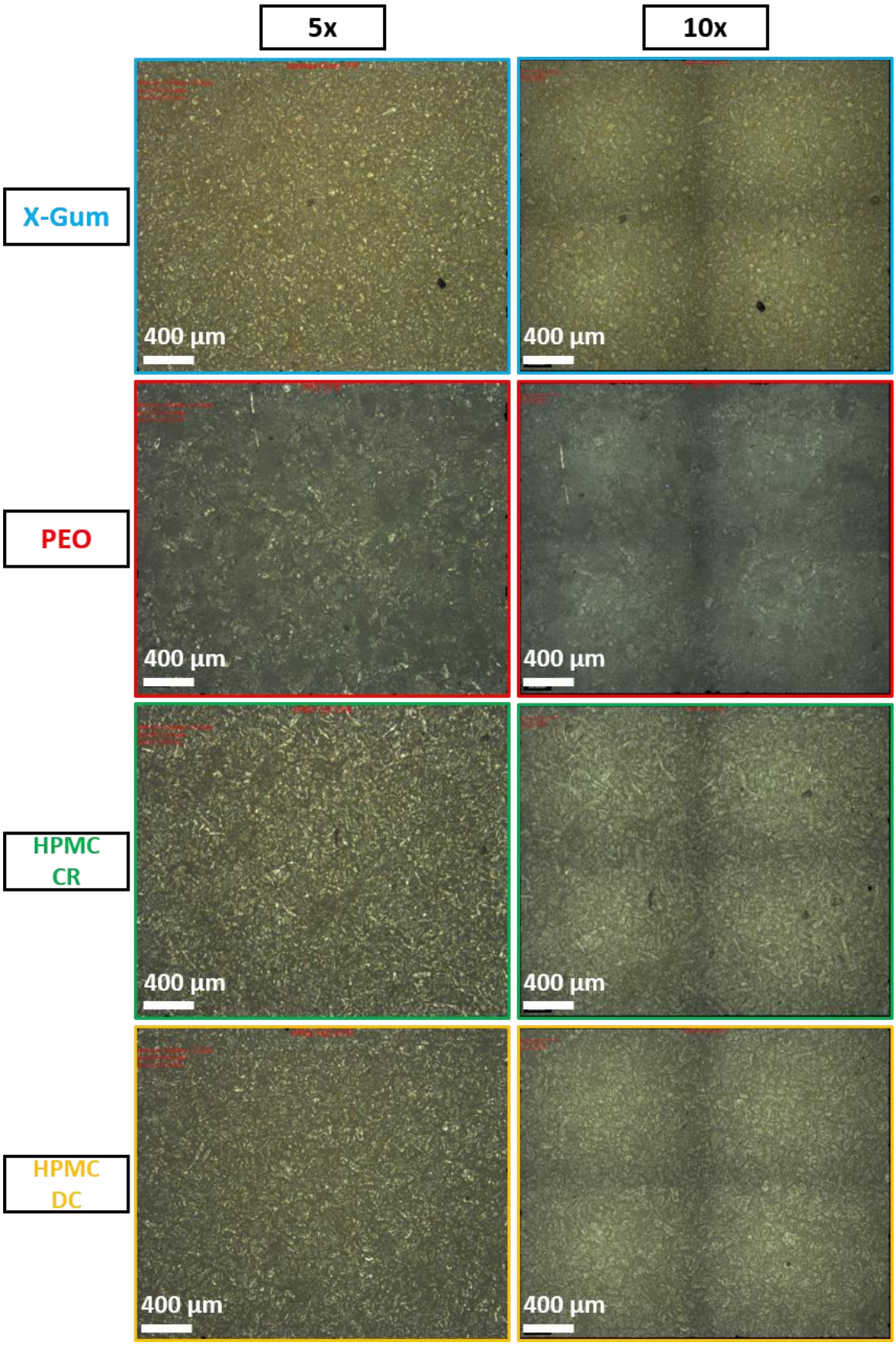

Figure 4-8 - Optical images obtained from focus variation microscopy of the polymer only compact surfaces at magnifications of 5x and 10x.

The PEO polymer surface showed the presence of the larger spherical particulates across the surface of the compact identified via SEM earlier. These particulates can be seen clearly in the areal roughness maps in Figure 4-9. The optical images in Figure 4-8, also highlighted potential points of plastic deformation indicated by the darker grey areas across the surface. Despite the presence of the larger agglomerates, they were still distributed evenly across the compact surface leading to a S*tr* value of 0.87 ± 0.06. However, it is important to identify that this value was the lowest of all four polymers. The PEO compact surface also displayed the lowest S*dr* value of the four polymers tested with values of 4.09 ± 0.29 % and 2.38 ± 0.11 % for 5 x and 10 x magnifications, respectively. This is a good indicator of the plastic behaviour experienced by the polymer during compaction and correlates with the high hardness required to deform the compact. This is further supported by the relatively higher S*mr*2 value of 90.96 ± 0.48 % indicating a lower percentage of the surface suitable for 'lubrication' correlating well with the porosity results discussed in 4.5.2. Focus variation microscopy further reinforces the hypothesis that the PEO compacts will take longer to wet and hydrate than the other three polymers tested in this study.

In the comparison between the two HPMC grades, compacts surfaces displayed the effects of the ribbon like particles of the CR grade and the more spherical engineered particles of the DC grade (Figure 4-8). This was further supported by the areal roughness maps (Figure 4-9), which displayed the more spherical nature of the DC grade polymer across the surface and longer valleys caused by the ribbon like particulates of the CR grade. In a similar trend to the xanthan gum and PEO polymers, both HPMC grades displayed S*dr* values close to 5 %. However, the S*mr*2 parameter correlated well with the porosity and hardness data by indicating that the CR polymer had a lower percentage of the surface suitable for 'lubrication' with a value of 91.50 ±

0.31 % at the 10 x magnification. This helps to reinforce the hypothesis that during hydration the CR polymer should hydrate and swell at a slower rate than the DC grade.

The focus variation microscopy therefore provided a novel assessment of the compact surfaces for the four polymers in this study with the production of both 2D optical and 3D images. The technique also helped to reinforce the conclusions determined from both porosity and hardness measurements with the calculation of surface parameters such as S*dr* and S*mr*2.

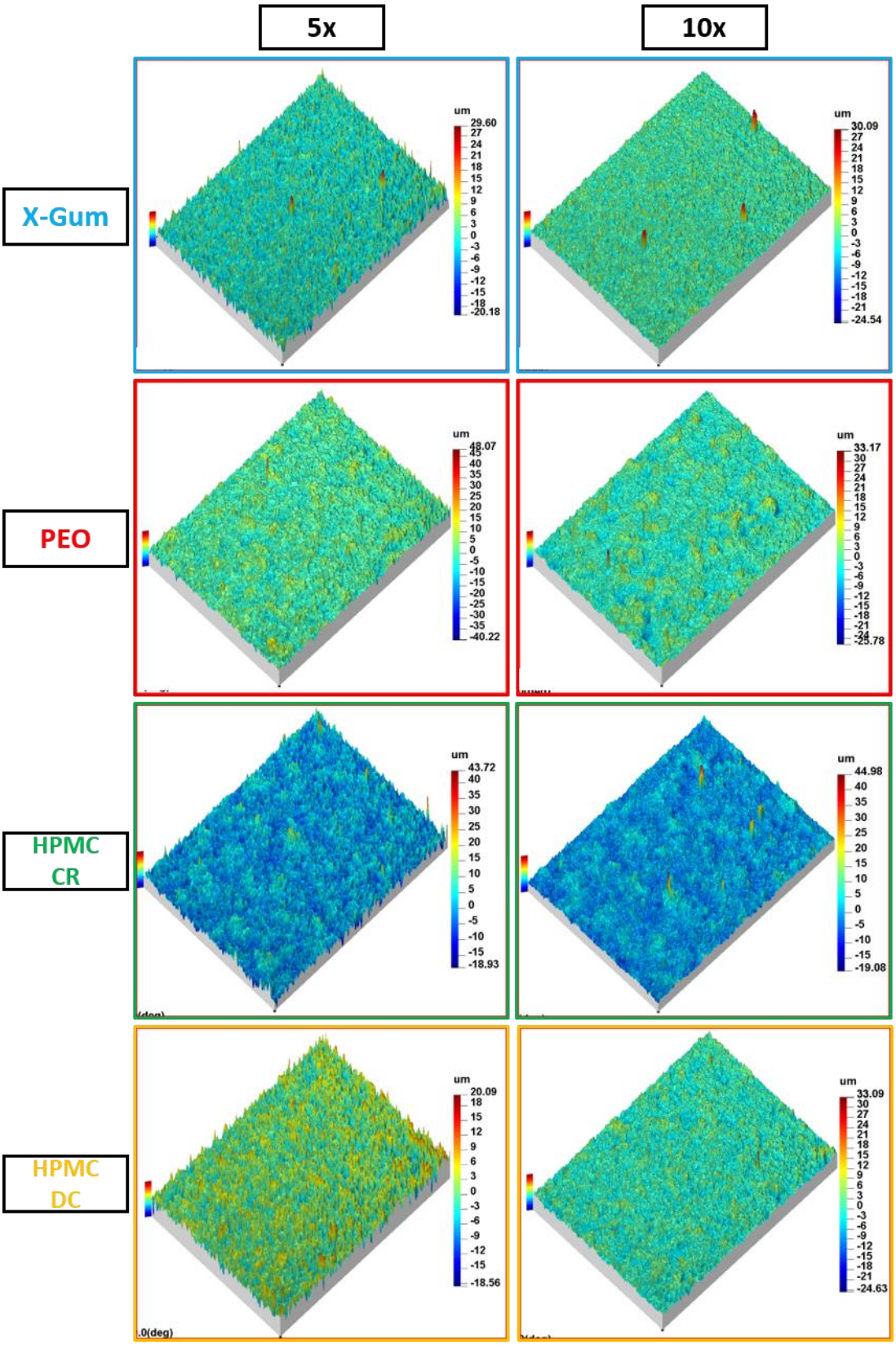

Figure 4-9 - Areal roughness maps obtained from focus variation microscopy of the polymer only compact surfaces at magnifications of 5x and 10x.

4.5.4 Dissolution imaging and swelling assessment

Figure 4-10a displays the dissolution images obtained for the Xanthan Gum polymer compacts. It was clear from visual assessment that Xanthan Gum hydrated rapidly leading to a significantly greater level of gel formation and growth when compared to the other polymers tested in this study. The 20 min image also displays the formation of deep channels in the gel layer, potentially caused by the high porosity of the polymer compact. This observation can be particularly useful as it is likely that channels such as these could be the cause of dose dumping and formulation failure for novel controlled release therapies. As the experiment progressed from the 60 min time point onwards, the gel became increasingly translucent indicative of complete polymer hydration. This was also reflected in the percentage growth profile displayed in Figure 4-12a. The profile displayed a plateau from 80 min onwards suggesting that growth rate had reached an equilibrium with erosion of the gel layer. The growth profile also showed the extent to which Xanthan Gum “out swelled” the other polymers in this study with regards to both the extent and rate of growth. By the end-point of the experiment at 120 min, the Xanthan Gum compacts reached an average growth percentage of 214.18 ± 24.26 % at least 70 % greater than the other polymers. The initial hydration of Xanthan Gum is also shown in Figure 4-12b, this graph displays how the polymer reached an average growth of 49.27 ± 1.81 % in the first 5 min of the dissolution. This supports the predictions from both the focus variation assessment (4.5.3) and the porosity assessment (4.5.2) that the significant porosity of the Xanthan Gum compacts will lead to a faster initial hydration and consequently growth.

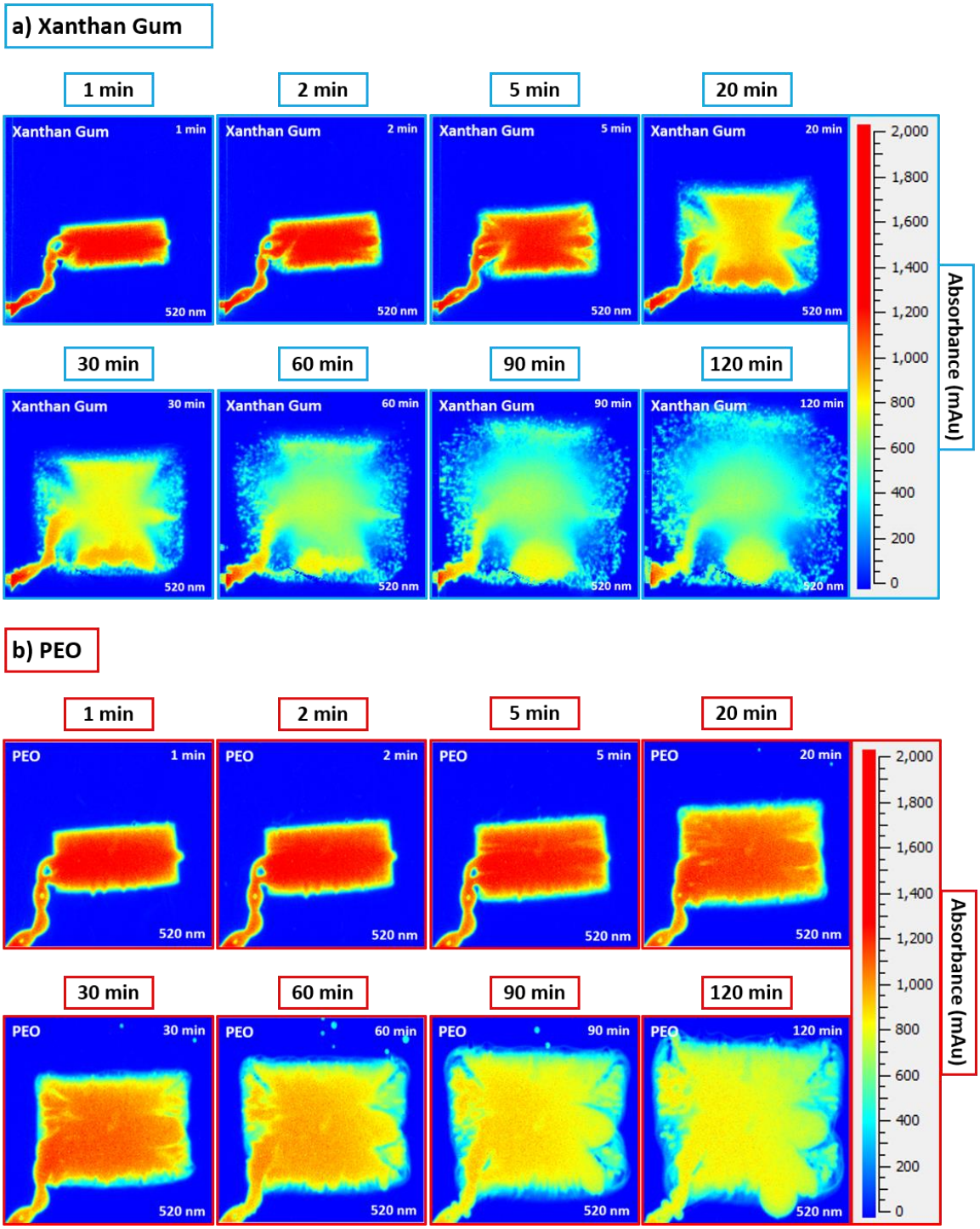

Figure 4-10 - Optical images obtained from the SDi2 system at the 520 nm wavelength. a) Xanthan Gum and b) PEO. Note: Images are taken from the 2 hour experiment at intervals of 1, 2, 5, 20, 30, 60, 90 and 120 minutes.

Figure 4-10b displays the dissolution images for the PEO compacts. The images highlight that PEO still exhibited significant gel formation and growth despite the lowest compact porosity of all four polymers tested. When compared to the xanthan gum compacts, PEO also developed a square shaped gel layer, indicating equal rates of growth in both the axial and radial directions. In contrast to the Xanthan Gum compacts, the PEO gel layer remained particularly dense (as depicted by the

consistent yellow and red colouring in the image), this indicates a slower ingress of water to the tablet core. This observation is also supported by the slower development of the deeper channels in the gel layer, which appeared from the 60 min time point onwards. The dissolution images of the PEO compacts also provided further evidence for the use of colour adjustment which allowed for clear distinction of the various gel densities developing around the compact core. The growth profile for the PEO compacts is shown in Figure 4-12 and unlike the Xanthan Gum profile the PEO compacts showed no signs of plateau by the 2 hour end-point. The PEO compacts showed a similar growth rate to the HPMC CR and DC compacts despite a significantly lower compact porosity (Figure 4-6) and reached an average growth percentage 135.22 ± 8.64 %. Interestingly, the PEO growth profile contradicted the hypothesis that the PEO compacts will take longer to wet and hydrate than the other three polymers tested in this study. This indicates that the chemistry of the polymer had a greater influence on gel growth than surface topography and physical characteristics.

In the comparison of the HPMC polymers, the dissolution images shown in Figure 4-11 showed similar behaviour to the relatively smaller polymer compacts (250 mg) tested in Chapter 3. The HPMC CR compacts developed a gel layer with a circular shape, which was in contrast to the DC compacts which developed a square gel shape. Interestingly, the growth profiles shown in Figure 4-12a showed very similar rates for both CR and DC compacts. However, it is important to note that there was a significant influence of air bubbles on the CR growth profile, indicated by the spike in the pink dashed box of Figure 4-12a. The initial hydration profiles shown in Figure 4-12b highlight an interesting difference in the initial hydration between the two polymers. The DC polymer showed a greater initial hydration than the CR polymer with a total percentage growth of 20.13 ± 0.41 % vs. 17.03 ± 1.35 %.

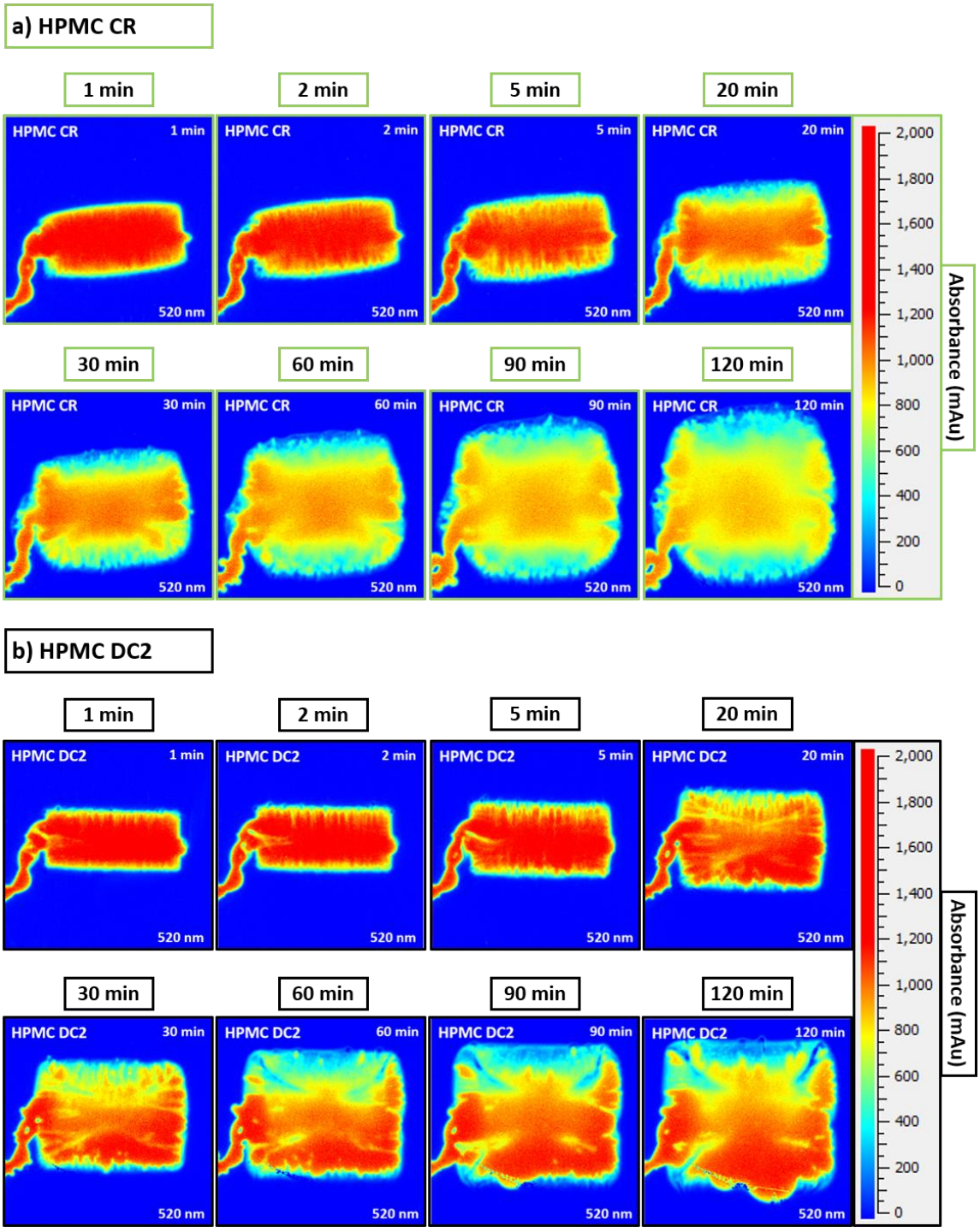

Figure 4-11 - Optical images obtained from the SDi2 system at the 520 nm wavelength. a) HPMC CR and b) HPMC DC. Note: Images are taken from the 2 hour experiment at intervals of 1, 2, 5, 20, 30, 60, 90 and 120 minutes.

This observation was in keeping with the hypothesis from the focus variation microscope that the DC polymer would initially hydrate faster than the CR polymer. This observation was also supported by the greater porosity and lower compact hardness of the DC polymer compacts.

This subtle difference in the hydration behaviour can be attributed to the fibrous morphology of the CR particles resulting in interlocking particulates inhibiting the hydration of the compact and producing a denser gel as indicated by the denser colouration in the UV images.

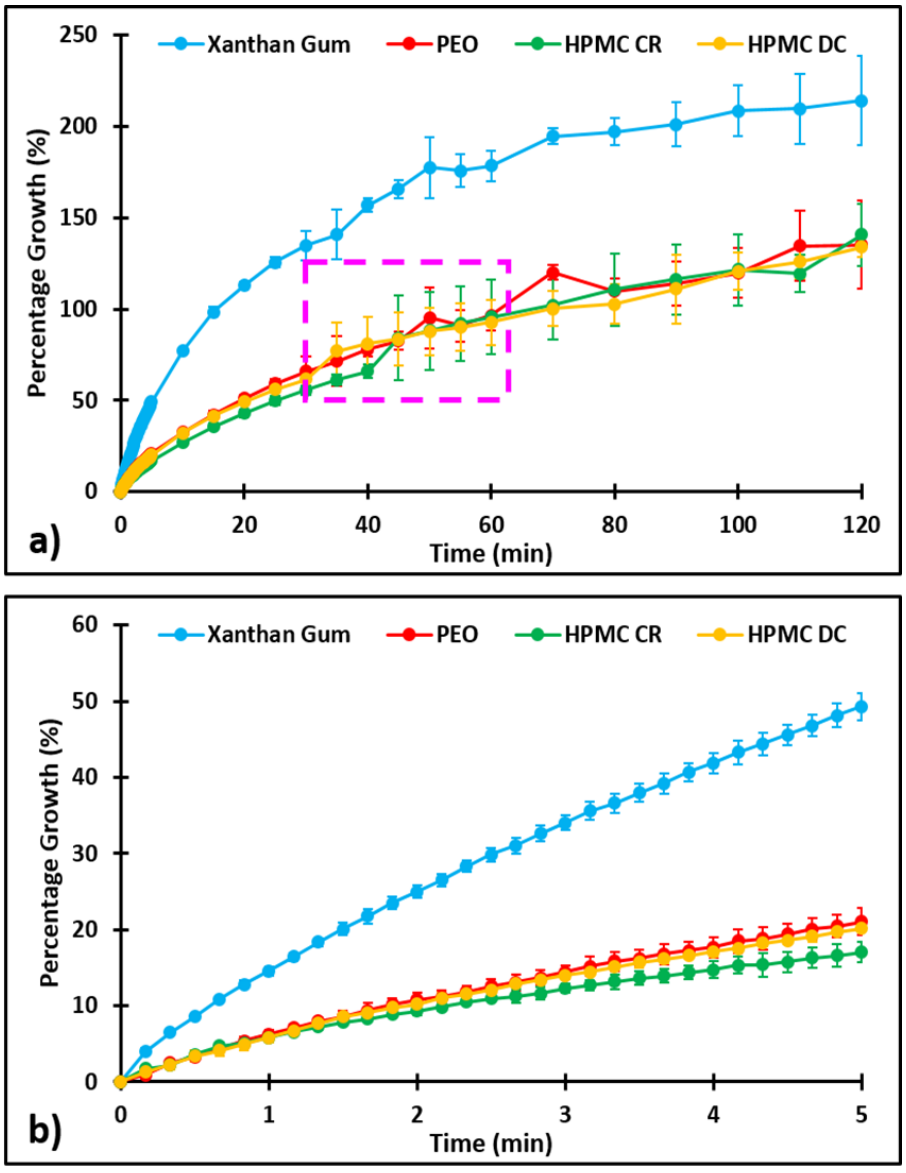

Figure 4-12 - Percentage growth profiles obtained for the polymer only compacts. a) Percentage growth over the full 2 hour experiment and b) Initial percentage growth in the first 5 minutes of dissolution. Note: The percentage growth is relative to the starting height of each compact. The pink dashed box indicates deviation as a result of air bubbles.

4.6 Conclusions

In conclusion, this chapter represents a development and validation of the method developed in chapter 3 by testing the method specifics against four different hydrophilic polymers representing the 3 different classifications of hydrophilic polymers. This chapter also introduces the use of focus variation microscopy to profile the surface topography of the polymers post compaction and attempt to attribute differences in surface topography to dissolution behaviour.

All four polymers tested were successfully profiled and displayed significantly different physical properties when compacted at equivalent force and mass. Xanthan gum produced compacts with the highest compact porosity, whilst the PEO produced compacts with the highest compact hardness. Focus variation microscopy also successfully profiled compacts from all four polymers and provided a deeper insight into the influence of particle morphology on surface roughness. Crucially, the focus variation microscope produced similar conclusions to the porosity and hardness assessment by suggesting the Xanthan Gum would hydrate and swell at the greatest rate with PEO hydrating at a much slower rate.

The dissolution imaging instrument successfully profiled all four polymers using the new methodology described in chapter 3. The dissolution imaging instrument was found to be capable in distinguishing the subtle nuances between the hydration of all four polymers particularly HPMC CR and DC. Dissolution imaging found the Xanthan Gum compacts to swell rapidly and at a greater rate than the other polymers tested. The images produced provided a novel insight into the growth and development of gels by imaging features such as deep channels, density differences and air bubbles. The data from the dissolution instrument correlated well with the hypotheses from both the focus variation microscope and the physical characterisation of the polymer compacts

with the exception of the PEO polymer which contradicted all hypotheses possibly as a result of the chemistry of the polymer.

Overall, this chapter represents a novel investigation into the assessment and analysis of four common hydrophilic polymers using two novel imaging techniques. This chapter also highlights that the combination of focus variation microscopy with UV imaging can provide a rapid assessment of pharmaceutical materials and provide and in-depth insight to a formulator.

Chapter 5 - Use of advanced imaging techniques for the purpose of salt selection.

5.1 Note to Reader

Some aspects of the following chapter are published in the International Journal of Pharmaceutics Volume 551 under the title *'Direct imaging of the dissolution of salt forms of a carboxylic acid drug'. (99)*

5.2 Rationale

The following chapter looks to explore the use of the dissolution imaging system for the purposes of ranking the dissolution performance of a number of cycloamine salts of gemfibrozil as a model drug. This chapter showcases the full range and capability of the dissolution imaging system including; the IDR flow cell, the whole dosage cell and dual wavelength recording. Focus variation microscopy was also used to assess how the topography of IDR compacts was influenced by the compaction methodology employed by the dissolution imaging system.

5.3 Introduction

Within the field of pharmaceutics, poor aqueous solubility is becoming an increasingly common occurrence in the majority of emerging active pharmaceutical ingredients (API) creating a significant challenge during development (100-103). Alongside this, many new API's also have additional undesirable properties as a result of their crystal structures affecting their physicochemical and mechanical properties including; poor compaction, low bioavailability, poor stability, excessive hygroscopicity and poor dissolution (104-106). Also, under the biopharmaceutical classification system (BCS) many new API's are classified as BCS class 2, indicating they are poorly soluble but highly permeable. API's in this classification are thus dependent on solubility and dissolution rate to achieve therapeutic levels of uptake and absorption (107).

A common method used by formulators to overcome the poor solubility issue is salt formation. Salt formation is often the first and preferred choice for a formulator, and remains an effective and widely used technique for improving solubility and improving many of the physiochemical and mechanical properties discussed earlier (108,109). Salt formation is also a preferred option by formulators in improving solubility with regards to other techniques such as co-crystallisation (the process of forming a new crystal lattice between the drug molecule and often another soluble active entity) and development of new polymorphs (110). Salt formation is principally an acid/base reaction that involves neutralisation/proton transfer between the drug molecule and a counter ion that is oppositely charged. This results in the formation of strong ionic interactions between the drug molecule and the counterion (108,111).

UV Imaging, Intrinsic Dissolution Rate (IDR) and Salt selection

An important parameter determined in early stage drug development is intrinsic dissolution rate (IDR) as it can help to predict API behaviour *in vivo*. Intrinsic dissolution is a feasible alternative to equilibrium solubility to determine the BCS class and has several advantages, especially with respect to time, quantity of material, and handling of samples. Drugs with an intrinsic dissolution rate above 0.1 mg $min^{-1}cm^{-2}$ would be considered highly soluble, and rates below this limit would indicate drugs with low solubility (112). IDR measurements can be conducted using a conventional USP 2 rotating apparatus however, this can require a large amount of API >50 mg (often not available during pre-formulation) and large volumes of dissolution media typically 900 mL. The surface dissolution imaging instrument offers a compound sparing approach requiring typically 5–10 mg of API and an experimental run time of 20–30 min in determining the IDR of an API. Several authors have used the SDI in monitoring IDRs of APIs (32,113-115) as well as in a variety of other applications (20,116,117).

As discussed in previous chapters, the new model of the SDI2 is an upgrade on its predecessor introducing a 520 nm optical LED alongside four UV LED's at 255, 280, 300 and 320 nm. Secondly, the system can record two different wavelengths of light simultaneously allowing for example, drug release and tablet disintegration to be monitored at the same time. Finally, the CMOS detector chip in the new model has been upgraded to 13 MP allowing greater resolution and detail to be monitored in real time. The new system has also retained the flow through cell albeit vastly improved to conduct IDR experiments.

gemfibrozil and counter ion selection

Gemfibrozil (GEM) is a fibric acid derivative and is a lipid regulating drug. It is primarily used to reduce total cholesterol and triglycerides in the management of hyperlipidaemias. Gemfibrozil has also been indicated for the prevention of ischaemic heart disease (118).

Gemfibrozil has been utilised as a model drug in the investigation of salt formation by a number of different groups. David et al. compared the physical, mechanical, and crystallographic properties of a series of gemfibrozil salts (105). In this work, the authors found that salt formation increased the aqueous solubility of gemfibrozil. They also discovered that solubility increased with the number of hydroxyl groups on the counterion.

It was also observed that the increased capacity for hydrogen bond formation had an influence on the crystal structure of the salt and that the increasing hydrophilicity of the counterion was beneficial in solubility enhancement.

Ramirez et al. characterised the crystal packing, chain conformation and physiochemical properties of crystalline gemfibrozil amine salts (106). They found that the cyclic amine counterions increased the melting point, which correlated with an

increase in counterion molecular weight whereas the linear amine counterions had a decrease in melting point with an increasing molecular weight and volume. Yang et al. explored the structure-property relationship of three diamine gemfibrozil salts. Thermal analysis showed an increase in melting point with the use of the counterion. The three salts showed an increased dissolution rate compared to that of the free acid (119).

In this chapter, 4 structurally related cyclical molecules were utilised as counter ions in the salt formation with the active ingredient gemfibrozil starting with cyclopropylamine (C_3) increasing in chain length and hydrophobicity to cyclohexylamine (C_6). A fifth counterion, tertiary butylamine (C_4) was also selected to compare to the Cyclobutylamine to investigate what influence a straight chain counter ion has on dissolution in salt formation.

5.4 Objectives

Ward et al. used a range of advanced imaging techniques to assess the surface properties of ibuprofen compacts used in an SDI study to determine IDR (120). The objective of this chapter was to build upon this investigation by utilising both UV imaging and focus variation microscopy to investigate a structurally-related series of counterions with gemfibrozil. The focus variation microscope was used to investigate how the surface topography of the IDR compacts influences IDR measurement. The whole dosage cell for the dissolution imaging system was employed to investigate the effects of counterions on dissolution rate.

5.5 Materials and Methods

5.5.1 Materials

The materials for this experiment were as follows; The active ingredient gemfibrozil was purchased from Sigma Aldrich (UK). The counter ions; Cyclopropyl amine (CPROP), Cyclobutyl amine (CBUT), Tertiary Butylamine (TBUT), Cyclopentyl amine (CPENT) and Cyclohexyl amine (CHEX) were purchased from Sigma Aldrich (UK). The solvents for salt manufacture Acetonitrile and Methanol were purchased from Fisher (UK). Potassium Phosphate Monobasic and Sodium Hydroxide for the preparation of the pH 7.2 dissolution media, were purchased from Fisher (UK) and Arcos Organics (Germany) respectively, De-ionised water at approximately pH 5 was also used.

5.5.2 Methods

5.5.2.1 Salt Preparation

Each salt was prepared following a method devised by Ramirez et al. (101). Firstly, equimolar ratios of the drug (GEM) and counterions (CPROP, CBUT, TBUT, CPENT and CHEX) were dissolved in 50 mL of acetonitrile and the resultant precipitated salt filtered under vacuum. The recovered salts were re-crystallised from methanol after which they were dried at 50 °C for up to 12 h in a vacuum oven. All the salts produced were then sealed in glass vials and stored until required.

5.5.2.2 Solid State Characterization

Differential scanning calorimetry (DSC)

All DSC measurements were conducted on a Mettler-Toledo DSC 1 Differential Scanning Calorimeter. The enthalpy, onset temperatures and melting points of the active drug GEM, and its salts with CPROP, CBUT, TBUT, CPENT or CHEX were obtained using the software provided by Mettler-Toledo, Switzerland. Each

assessment was completed by first placing approximately 3-6 mg of GEM, or its salts with CPROP, CBUT, TBUT, CPENT and CHEX in standard aluminium pans (40 µL) with a vented lid. The crimped aluminium pans were heated from 20 to 250 ˚C at a scanning rate of 10 °C/min with nitrogen gas used as the purge gas.

X-ray powder diffraction (XRPD)

XRPD measurements were performed following a method described by Laity et al. (121) GEM and its salts with CPROP, CBUT, TBUT, CPENT and CHEX were scanned in Bragg–Brentano geometry, over a scattering (Bragg, 2θ) angle range from 5 to 100°, in 0.02° steps at 1.5° min−1 using a D2 Phaser diffractometer (Bruker AXS GmbH, Karlsruhe, Germany). The XRPD patterns were collected and analysed further using Microsoft Excel.

5.5.2.3 Dissolution Imaging

In this study both the flow through cell for determining IDR and the whole dosage cell were used. The method specifics are outlined as follows:

Dissolution Media Preparation

The media used for IDR determination and whole dosage imaging was a 0.2 M phosphate buffer (pH 7.2) prepared according to the USP 2003 using sodium hydroxide and potassium phosphate monobasic. In summary this media was prepared by first making a 0.2 M solution of sodium hydroxide (NaOH) by dissolving 8 g of NaOH pellets in 1 L of deionised water. Next, a 0.2 M solution of potassium phosphate monobasic (KH_2PO_4) was prepared by dissolving 27.22 g of KH_2PO_4 in 1 L of deionised water. Once both solutions were prepared, 347 mL of the NaOH and 500 mL of the $+KH_2PO_4$ were measured into a 2 L volumetric flask and made to volume with deionised water. If required, the buffer was titrated to target pH using either 1 M Hydrochloric Acid or 1 M NaOH.

UV Calibration of gemfibrozil

Prior to analysis, a calibration curve was produced to determine the Molar Extinction Coefficient (MEC) of gemfibrozil. Firstly, two stock solutions were prepared by weighing 10 mg of GEM into a 10 mL volumetric flask and made to volume with pH 7.2 buffer producing a 1 mg/mL solution. Next, two series of standards were produced (1 from each stock) following Table 5-1 below:

Table 5-1 - Standard concentrations used in the calibration of gemfibrozil at 280 nm Note: The standards indicated with a star were produced following a 1 in 10 serial dilution of the 10 and 50 stock, respectively.

Concentration (µg/mL)	Amount of Stock used (µL)
100	1000
75	750
50	500
30	300
20	200
10	100
5*	50
2.5	25
1*	10

Once all the standards were prepared, each series was analysed at an absorbance of 280 nm using a UV Spectrophotometer and a 1 cm quartz cuvette. 280 nm was chosen upon review of the lambda max of gemfibrozil (275 nm) as this was the closest possible wavelength supported by the dissolution imaging system. Each series was then plotted using Microsoft Excel to produce a calibration curve, a line of best fit was added to the graph with the gradient of the line indicating the Molar Extinction Coefficient of each salt.

Flow through Cell and IDR Determination

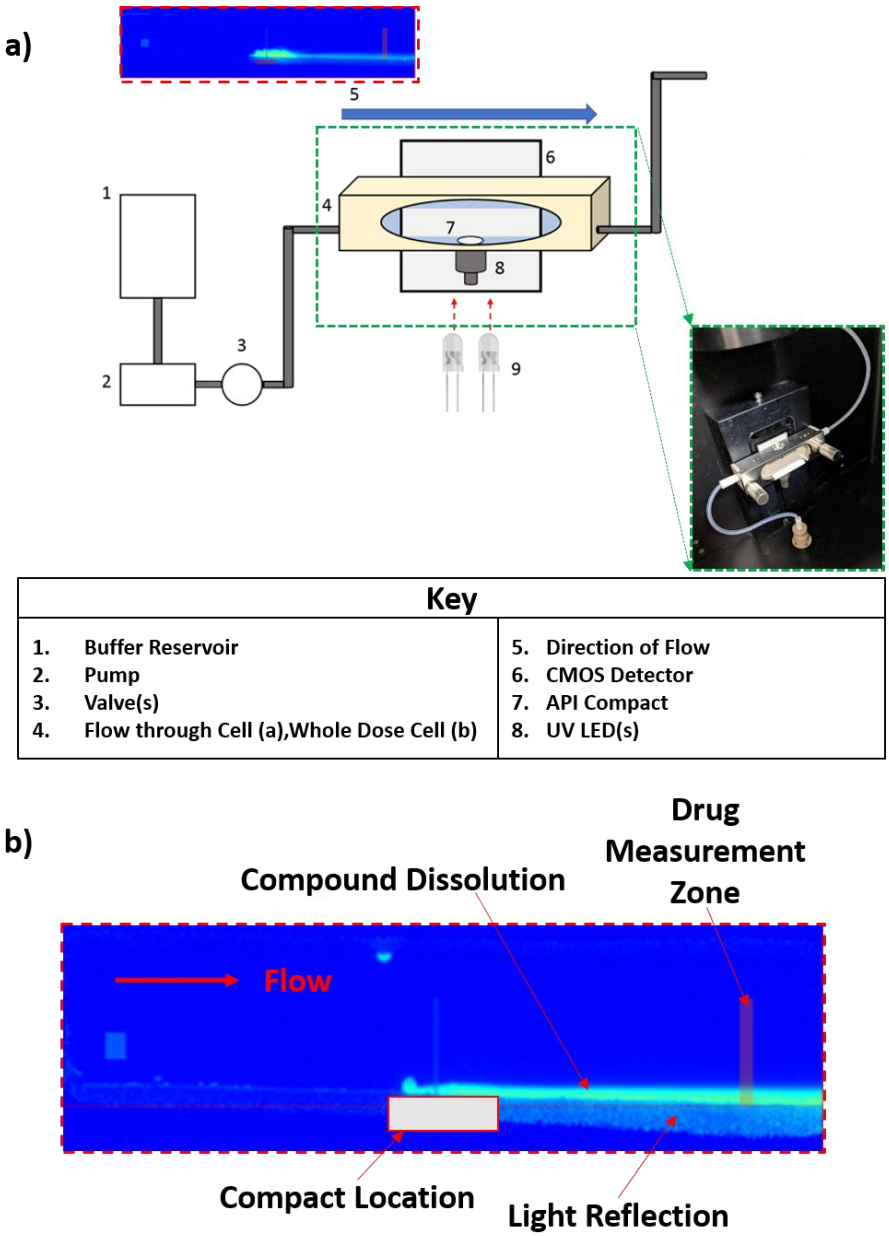

Figure 5-1 - a) A schematic representation of the flow through set-up of the SDI2, the figure includes a key and descriptor numbers associated with each component. b) A schematic displaying a typical dissolution image obtained from the SDI2 system. Highlighting the flow direction and measurement zones.

The flow through cell indicated in Figure 5-1a was what was used to primarily carry out IDR experiments. For this project, the manufacturer guidelines were followed to perform IDR measurements. The first step was to prepare the IDR compacts. This was achieved by weighing approximately 10 mg of the active or its salt into a specially manufactured IDR sample insert of 3 mm diameter (Figure 5-2a). Next, the IDR sample was placed in a steel rig and a compaction pin was inserted into the top of the IDR

sample (Figure 5-2b). Once completed, the entire steel rig was placed in a hand crank press supplied by the manufacturer and a force of 100 kgF (as recommended by the manufacturer) was applied (Figure 5-2c).

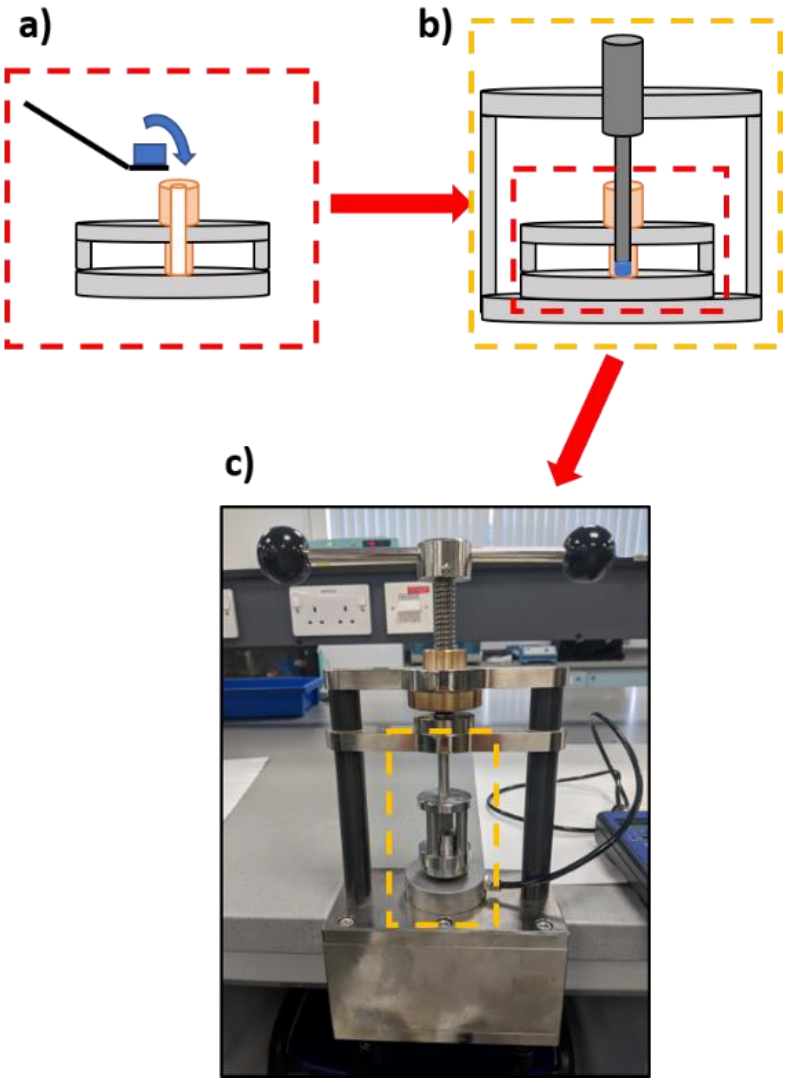

Figure 5-2 - A schematic representation of IDR compact preparation. a) Powder filling of IDR holder. b) Insertion of compact pin prior to compaction. c) Stainless steel rig in compact press.

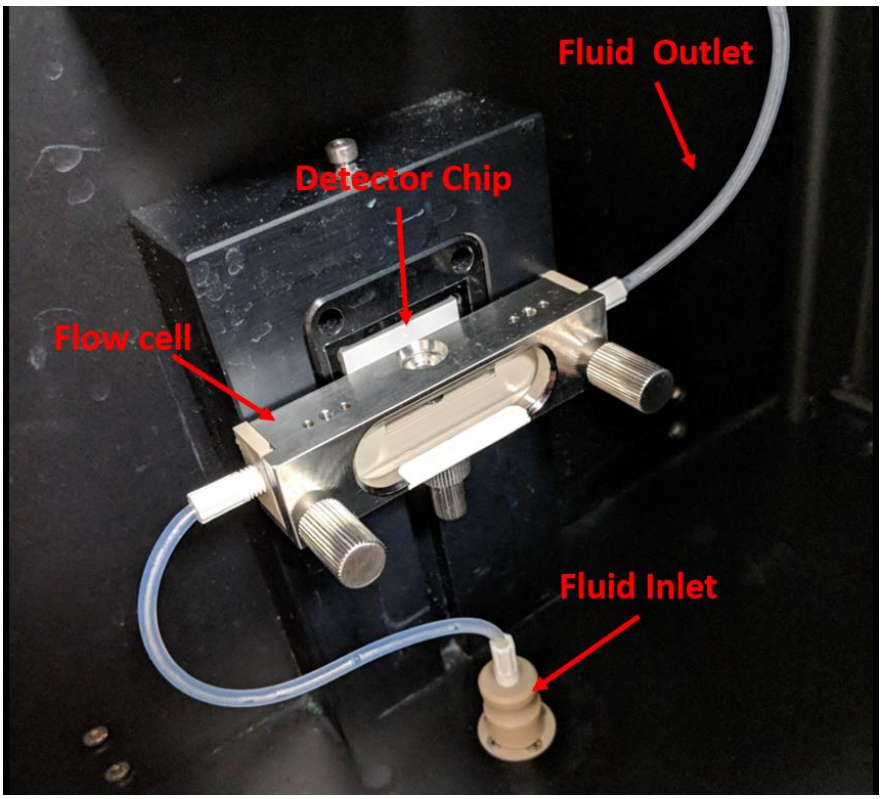

Figure 5-3 - Figure showing the flow through cell in the SDi2 system connected to the fluid lines ready to conduct an IDR experiment.

Once all the IDR compacts were prepared, the flow through cell was placed in the dissolution imaging system and connected to the fluid lines (Figure 5-3). Prior to each dissolution experiment a flush program was run with deionised water with the flow cell at a 45° angle. This removed any contaminants from the flow cell and also encouraged air bubbles out of the system and lines. Once the flush program was complete a dissolution experiment was conducted. pH 7.2 phosphate buffer was used as the dissolution medium at a temperature of 37 °C at a flow rate of 2 mL/min. The duration of each experiment was 30 min with each IDR test conducted in triplicate at a wavelength of 280 nm.

IDR Equation and Origin

Intrinsic Dissolution Rate (IDR) is described in pharmacopoeias across the globe and traditionally utilises the rotating disk system (or Wood's apparatus). A modified USP I/II set up is used whereby a disc of API with a known surface area is rotated in a dissolution vessel and the concentration at set time points measured. The IDR equation is fundamentally derived from the Nernst-Brunner adaptation of the Noyes Whitney equation. (Equation 5-1) (112)

$$\frac{\delta C}{\delta t} = \frac{DA}{Vh}(C_s - C_b)$$

Equation 5-1 – Nernst-Brunner adaptation of the Noyes-Whitney Equation where; C is the concentration, t is time, D is the diffusion coefficient, A is the surface area, V is the volume, h is the boundary layer, C_s is the saturation concentration and C_b is the concentration in the bulk solution.

Thus, IDR is calculated as shown in Equation 5-2 and results in units on mass per minute per area e.g. mg/min/cm^2.

$$IDR = \frac{\delta C}{\delta t} * \frac{V}{A} = \frac{D}{h}(C_s - C_b)$$

Equation 5-2 – Calculation of IDR where; C is the concentration, t is time, D is the diffusion coefficient, A is the surface area, V is the volume, h is the boundary layer, C_s is the saturation concentration and C_b is the concentration in the bulk solution.

Once each experiment was completed the data was analysed using the dissolution imaging analysis software. Images such as those displayed in Figure 5-1b were generated and IDR calculated using the MEC determined from the UV calibration and the equation displayed above.

Whole Dosage Cell measurement

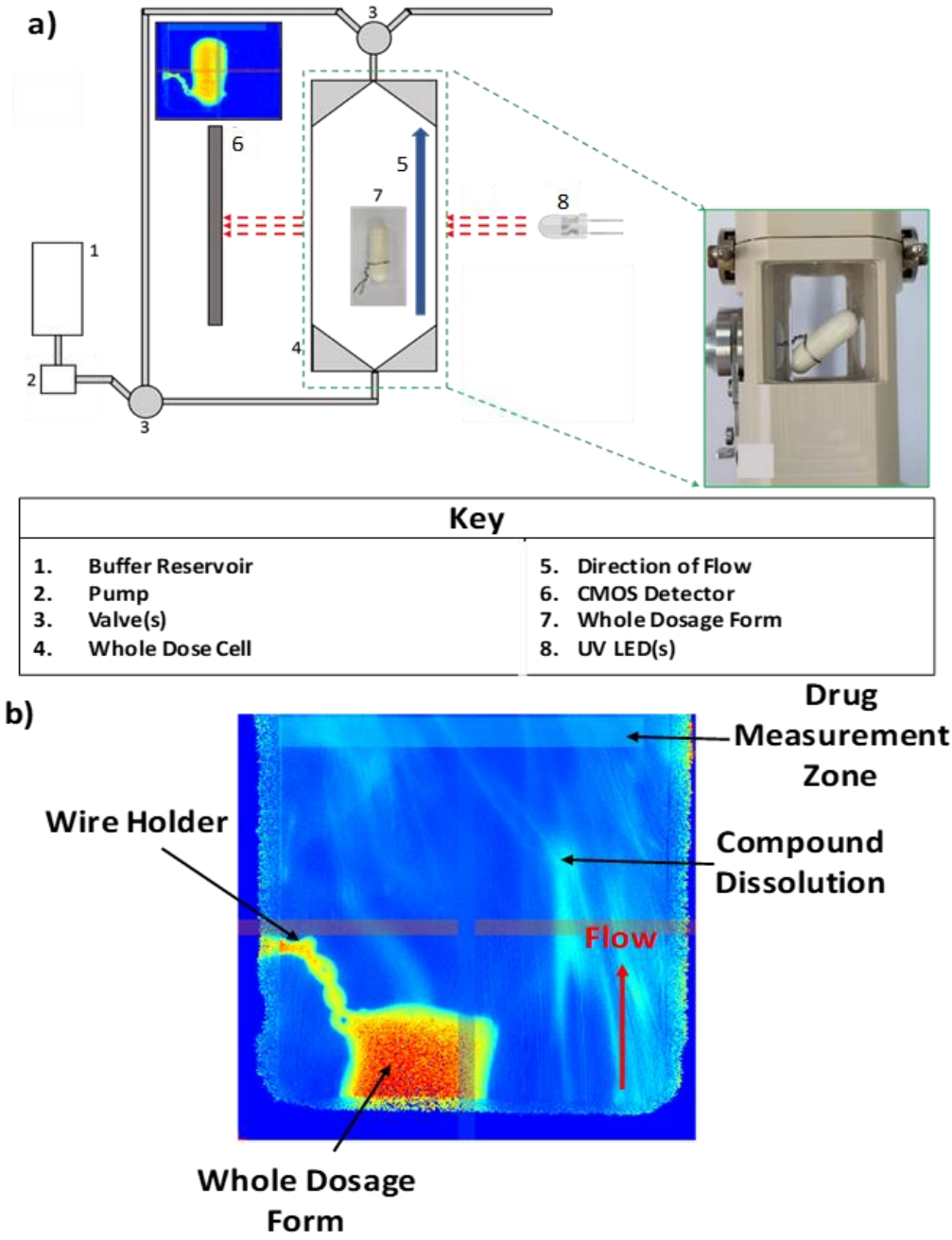

Figure 5-4 - A schematic representation of capsule dissolution using the whole dosage cell. a) Schematic of the dissolution set-up with a key and descriptor numbers. b) A whole dosage experiment image displaying dissolution absorbance zones and media flow direction.

This work also ranked the active and salt form dissolution rates from a whole dosage form (a hard gelatin capsule). This utilised the whole dosage functionality of the dissolution imaging system. Size 0 capsules were prepared containing 150 mgA of GEM, the salt fraction of each salt was determined before capsule filling. Capsules were then mounted into a stainless steel wire holder as shown in Figure 5-5 before being mounted the whole dosage cell for analysis (Figure 5-5).

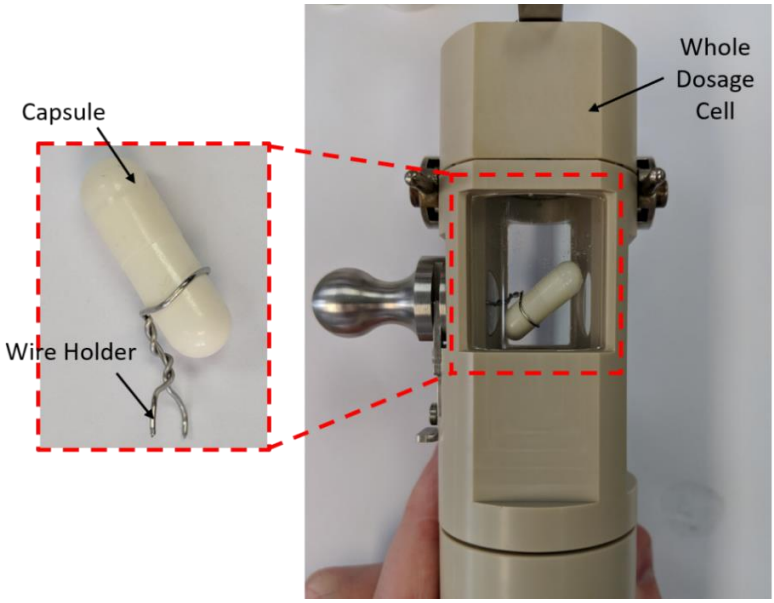

Figure 5-5 - A picture displaying mounting of a capsule in a stainless steel wire holder before insertion into the whole dosage cell unit.

Similarly, to the flow through cell, the whole dosage cell was then mounted in the dissolution imaging system and connected to the fluid lines. Prior to insertion in to the system, the whole dosage cell was filled with 12.3 g of 3 mm borosilicate glass beads. This was to ensure laminar flow in the cell. A flush program was run to clean the bead bed and remove any contaminants from the cell and lines. Once the flush program was completed, the dissolution experiment was conducted. As above, pH 7.2 phosphate buffer was used as the dissolution medium at a temperature of 37 °C and a flow rate of 8.2 mL/min. The release of GEM was imaged at various time points over a period of 60 min at a wavelength of 280 nm. All experiments were conducted in triplicate.

The dissolution imaging analysis software was used to analyse the dissolution footage obtained. Figure 5-4b displays a typical image obtained from each run indicating the location of the measurement zone used to measure the amount of drug in solution. The MEC obtained from the calibration curve was used by the dissolution imaging analysis to determine the concentration of drug in solution at set time points.

5.5.2.4 Focus variation microscopy

This thesis chapter explores the use of focus variation microscopy within the field of pharmaceutics with a primary purpose to characterise and profile the surface roughness of IDR compacts. A more detailed description of focus variation microscopy can be found in Chapter 2.

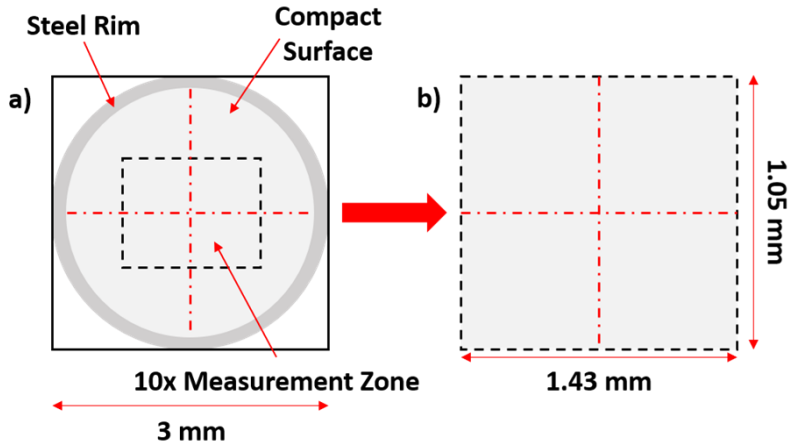

Figure 5-6 - A schematic representation of IDR compact analysis using focus variation microscopy.

Figure 5-6 displays a schematic of how IDR topography measurements were taken. The specific parameters set for each measurement are displayed in Table 5-2.

Table 5-2 - Specific method parameters used for both magnifications in the assessment of surface topography of IDR compacts for the gemfibrozil salts.

Parameter	Value at 5x	Value at 10x
Magnification	5x	10x
Image Area	1x1	1x1
Vertical Resolution (µm)	0.50	0.12
Lateral Resolution (µm)	7.82	3.91
Contrast	2	2

5.6 Results

5.6.1 Solid State Characterisation

5.6.1.1 Differential Scanning Calorimetry (DSC)

The active ingredient, GEM, exhibited an onset melt temperature of 60.3 °C with a peak melt temperature of 62.29 °C. This was supported by published work by Ramirez and Aigner (106,122). DSC also displayed a single endothermic peak for the active ingredient, this confirmed the thermal stability of the drug and also the absence of polymorphs within the bulk API. A characteristic endotherm for GEM was present in all salts along with the endothermic peak for the counterion. Interestingly, the peak for GEM shifted to a lower onset temperature with the formation of a salt. The characteristic endotherm of GEM was present in each of the butyl salts indicating successful formation of each salt. Interestingly, the onset melt point of the GEM was lower at 42 °C for the Cyclobutylamine salt compared to 50.12 °C for the tert-butylamine salt. DSC thermograms are shown in Figure 5-7.

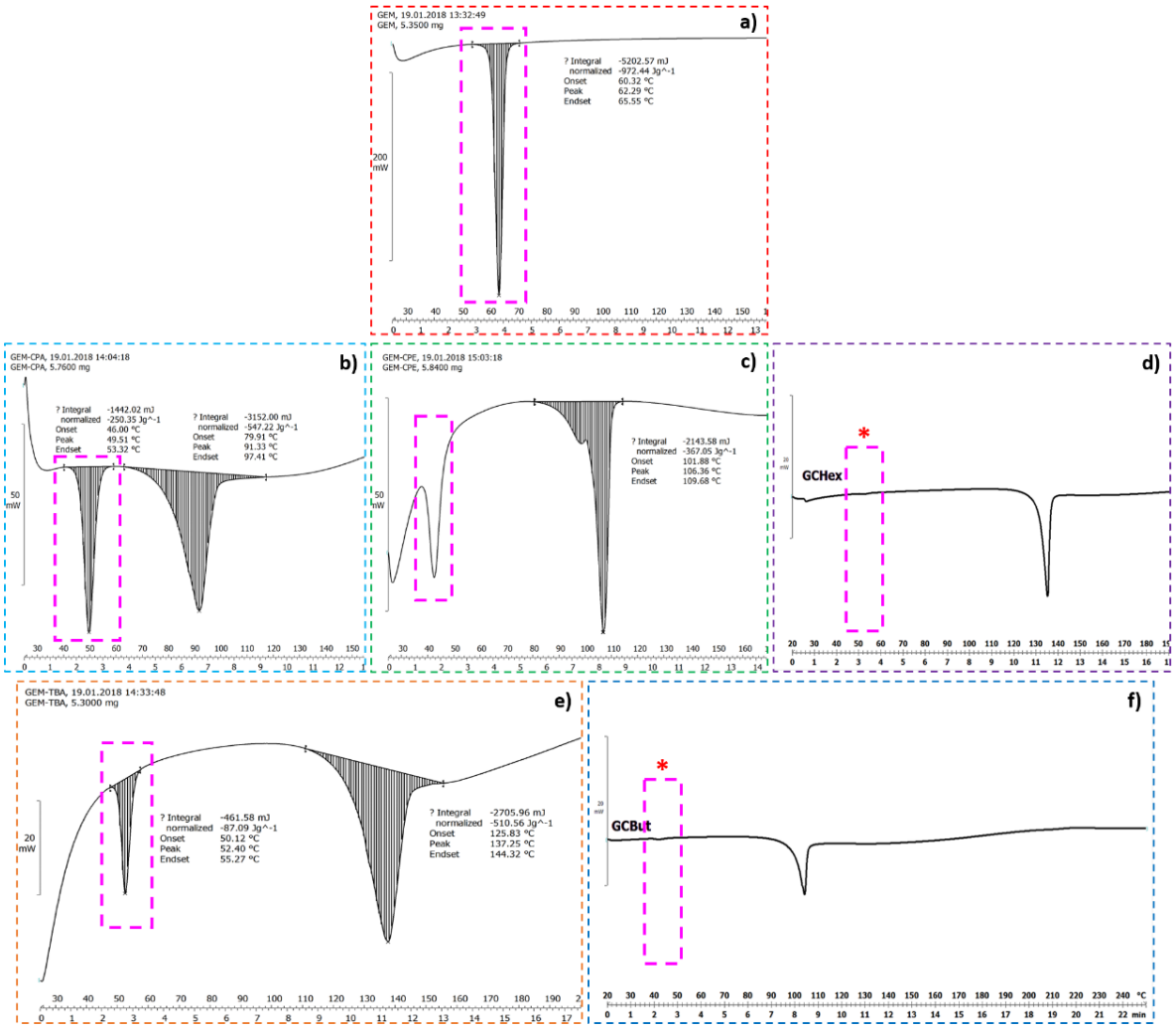

Figure 5-7 - DSC thermograms of a) the active ingredient GEM and the salts; b) CProp, c) CPent, d) CHex, e) TBut and f) CBut.

5.6.1.2 *X-Ray Powder Diffraction (XRPD)*

XRPD was utilised in this study to identify the crystallinity and characteristic peaks of GEM as well as the manufactured salts. Chen et al. report that the characteristic peaks for the active ingredient GEM can be found at 2theta angles of; 11.6, 14, 18 and 24 ° (123). These notable peaks are indicated on Figure 5-8 in the form of black dashed lines with red stars.

XRPD found GEM to be crystalline in nature (Figure 5-8a). Figure 5-8 b-d display XRPD spectra for the salts CProp, CPent and CHex respectively. Figure 5-8 e-f also displays the XRPD spectra for the TBut and CBut salts. All the salts produced were crystalline in nature. Interestingly, the TBut salt produced a more intense XRPD spectra than the CBut salt indicating a greater crystallinity for the TBut salt.

When the XRPD is combined with the DSC, both assessments confirm that the manufacture of the salts was successful. This indicated that the salt screen via dissolution could occur providing a discriminatory analysis of the influence of chain length on dissolution rate.

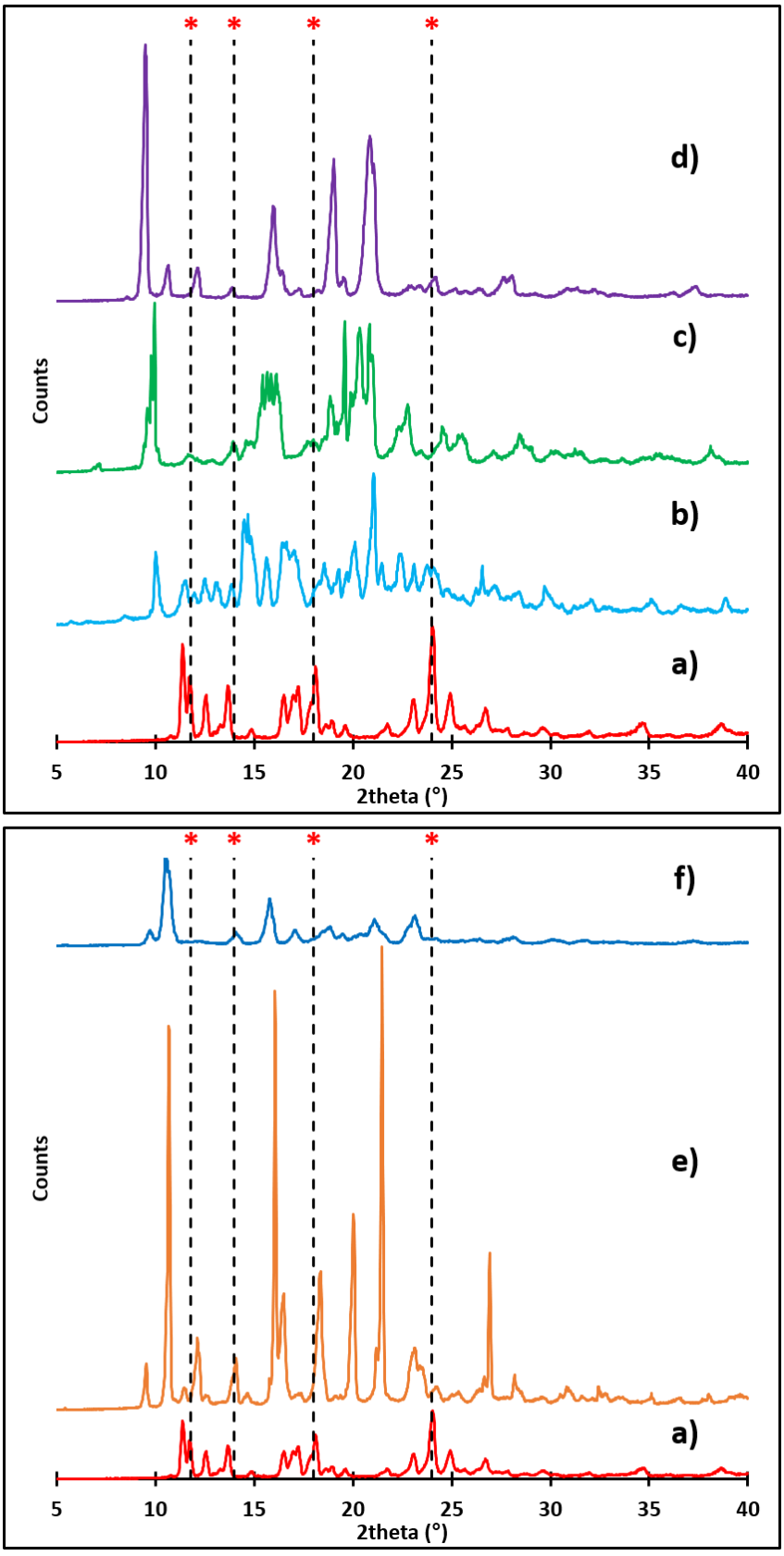

Figure 5-8 - XRPD spectra of a) the active ingredient GEM and the salts; b) CProp, c) CPent, d) CHex, e) TBut and f) CBut. Note: The black dashed lines with red stars indicate the characteristic 2theta angles for gemfibrozil as reported by Chen et al. (116).

5.6.2 Dissolution Assessment

5.6.2.1 IDR compact inspection

Prior to IDR assessment, the IDR compact surfaces were assessed using the focus variation microscope. In this chapter the aim was to use this analysis to build upon work by Niederquell and Ward et al with the dissolution imaging system (113,120). Both groups discovered that often with IDR compacts, uneven surfaces were produced through the compaction process, or API built up on the stainless steel rim of the IDR compact holder. The microscope offered the ability to produce an optical image to assess for surface damage, heterogeinity or homogeinity of surfaces whilst also providing a 3D representation of the surface to monitor surface roughness and and any increases in surface area as a result.

Figure 5-9 displays the optical images of the IDR compact surfaces of the active ingredient GEM and the manufactured salts. With the exception of the CPROP salt, the remaining surfaces all experienced an ebossed ring pattern on the surface. This was found to be as a result of the tooling used to make the compacts for the dissolution imaging system. This was an unexpected discovery, it appeared that the IDR press was machined to a finish (indicated by repeating symmetrical nature of the rings) instead of polished like a conventional tablet compaction tooling. The optical images also showed significant damage to the surfaces of the active ingredient GEM caused by the poor compactability of the GEM powder and larger particulates stuck on the surface of the IDR compacts. These discoveries could lead to significant variability in the IDR values obtained from the dissolution imaging system.

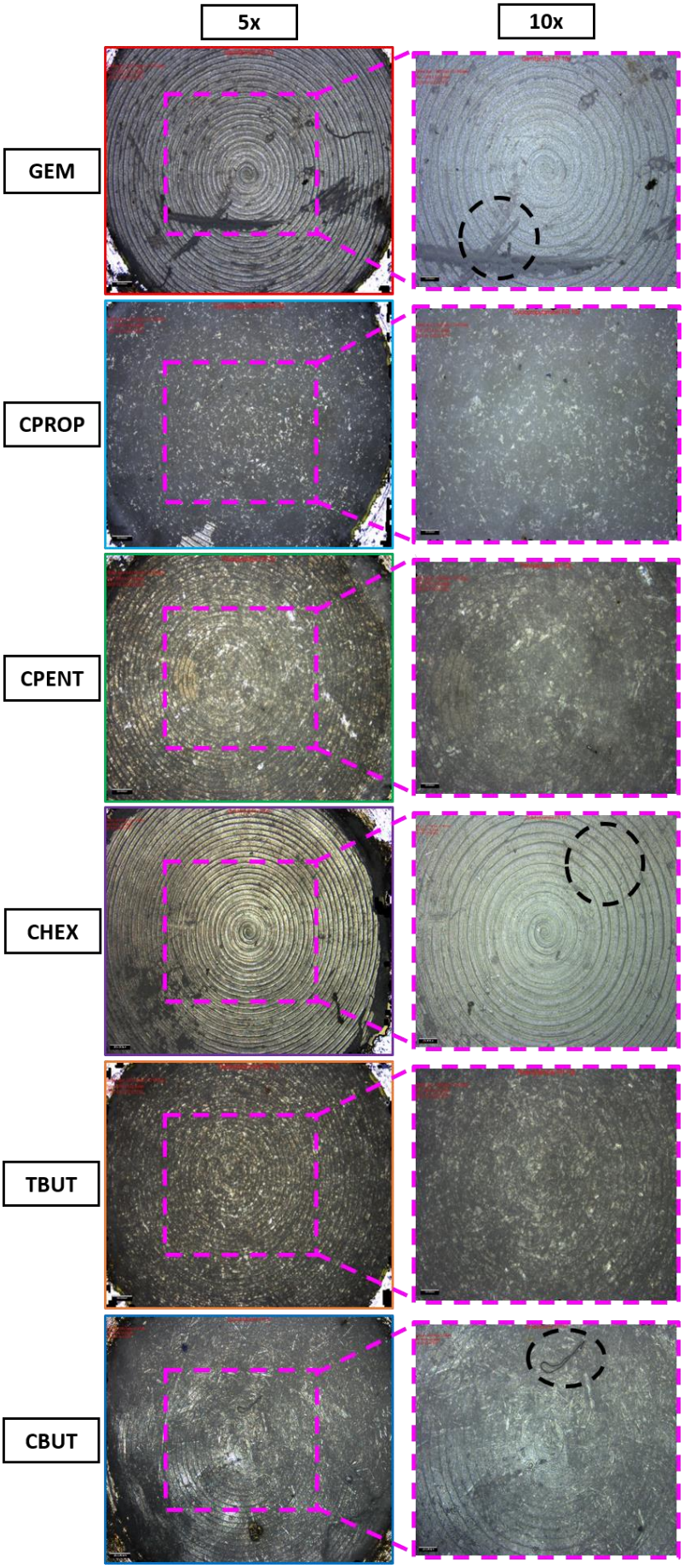

Figure 5-9 - Optical images of the IDR compact surfaces of the active ingredient and the manufactured salts at 5x and 10x magnification. The black dashed circles highlight surface damage, particulates and embossed texture.

Figure 5-10 displays the 3D surface representations of the IDR compacts at the 10x magnification. These surface maps are used to assess the surface roughness of the IDR compacts and the influence of this roughness on the surface area of the compacts.

Table 5-3 - Surface parameters of pharmaceutical interest obtained from the 3D surface maps of the IDR compacts for the active ingredient and its salts (n=1).

Parameter	Active Ingredient					
	GEM	**CPROP**	**CPENT**	**CHEX**	**TBUT**	**CBUT**
Sal	0.003	0.055	0.072	0.02	0.049	0.049
Str	0.536	0.859	0.736	0.497	0.843	0.723
Sdr	2.277	1.776	1.43	2.597	1.616	4.278
Smr2	87.9	89.1	88.6	90.1	88.2	88.5

The calculation of the surface parameters indicated in Table 5-3 provided a few key conclusions regarding both the analysis of the IDR compacts and the influence of the roughness on the surface topography. As described in chapter 2, *Sal* is a measurement of the lateral scale of a surface. However, in this work it was used as a confirmatory tool to ensure that the surface analysis had been conducted correctly and only surface roughness was considered in all surface calculations. All surface profiles displayed a *Sal* value of below 0.1, this indicates that only high frequency components (i.e. roughness) were considered and that the analysis had been successful. *Str* provides a measurement of the uniformity of the texture on the surface of the IDR compacts. A value of greater than 0.5 indicates that the surface texture is uniform in all directions, whereas a value lower than 0.5 indicates that the texture is dominated by a significant direction. Interestingly, only CHEX displayed a Str value of lower than 0.5 (0.497) however upon further review it is likely that this was influenced by the large spike in the surface profile caused by a surface particulate. All the other surfaces displayed values above 0.5.

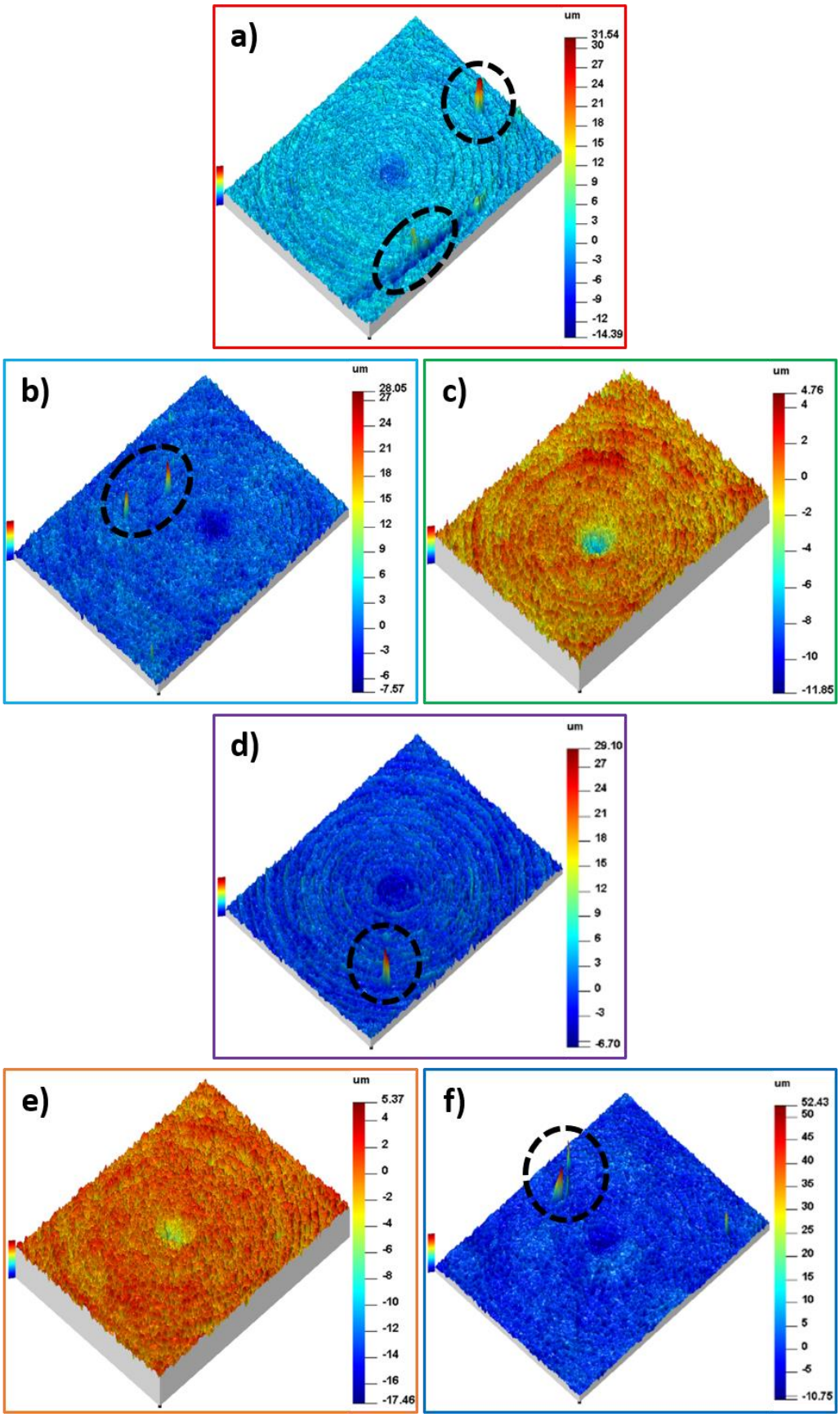

Figure 5-10 - 3D representations of the IDR compacts using Surfstand™. a) the active ingredient GEM and its salts b) CPROP, c) CPENT, d) CHEX, e) TBUT and f) CBUT. Images shown from the 10x magnification. The black dashed circles highlight the roughness caused by particulates and the embossed circular pattern.

Sdr provides an indication as to the additional surface area gained by a surface as a result of its texture when compared to a theoretical plane of the same size. The CBUT surface appeared to have the highest *Sdr* of all the surfaces measured with a surface area gain of 4.28 %. However, this value is likely to have been influenced by the particulate on the surface of the IDR compact. This seems to also be the case for the CHEX surface which also may have been influenced by interference from surface particulates. CPENT and TBUT surfaces provided the cleanest surface profiles and gave similar Sdr values of 1.43 and 1.62 % respectively. It is important to note that all surfaces provide a Sdr value as no manufactured surface will theoretically be 0 %. Following ISO guidelines, the aim is to keep Sdr values below 5 %. All surfaces fell below this value despite the damage seen in the GEM surface.

Smr2 provides an indication of the percentage of the surface comprised of deeper valleys. Interestingly, the GEM surface that suffered from the surface damage had the lowest Smr2 which indicates that this surface has more exposed deeper valleys than any of the other IDR surfaces. This could influence the IDR of GEM as more dissolution media could potentially ingress deeper into the IDR compact and thereby increase wetting and as a result dissolution.

5.6.2.2 IDR Assessment

For the determination of IDR, the first five points of the dissolution profile were excluded (Figure 5-13 – pink dashed box). Due to the flow through nature of the dissolution imaging system, it is important that IDR is measured once the dissolution rate has reached equilibrium with the media flowing over the IDR compact. From the dissolution profiles in Figure 5-13 this was found to be after the 5 min time point. Hulse et al. reported IDR values post the 3 min mark as a result of loose particulates (115). Ward et al. found that in the first few min of an IDR experiment loose particulates can wash off the surface of the IDR compact leading to inflated IDR and high standard deviations (120).

Table 5-4 - Average IDR (mean +/- SD) (n=3) values obtained from the SDi2 system over 10 and 30 minutes of the active ingredient and its salts.

Active Ingredient	**Average IDR (µg/min/cm^2)**	
	10 min	30 min
GEM	46.46±1.02	35.21±8.91
CPROP	93.17±4.02	333.78±189.276
CPENT	127.61±1.87	122.92±3.66
CHEX	52.97±1.10	35.82±13.00
CBUT	91.63±2.12	81.42±13.88
TBUT	99.95±2.88	87.31±9.41

Table 5-4 displays the average IDR values taken from the dissolution imaging system. As expected, the active ingredient GEM provided the lowest IDR of all the compounds tested in the flow cell with an IDR of 46.46 µg/min/cm^2 over the first ten min of the test (excluding the initial 5 time points). This is supported by the UV images in Figure 5-11a showing a small dissolution stream (with a light blue colour) indicating a low absorbance and thus a low amount of drug in solution. This is supported by Ramirez et al as they reported the aqueous solubility of GEM at 37 °C to be 0.002 mg/mL (106).

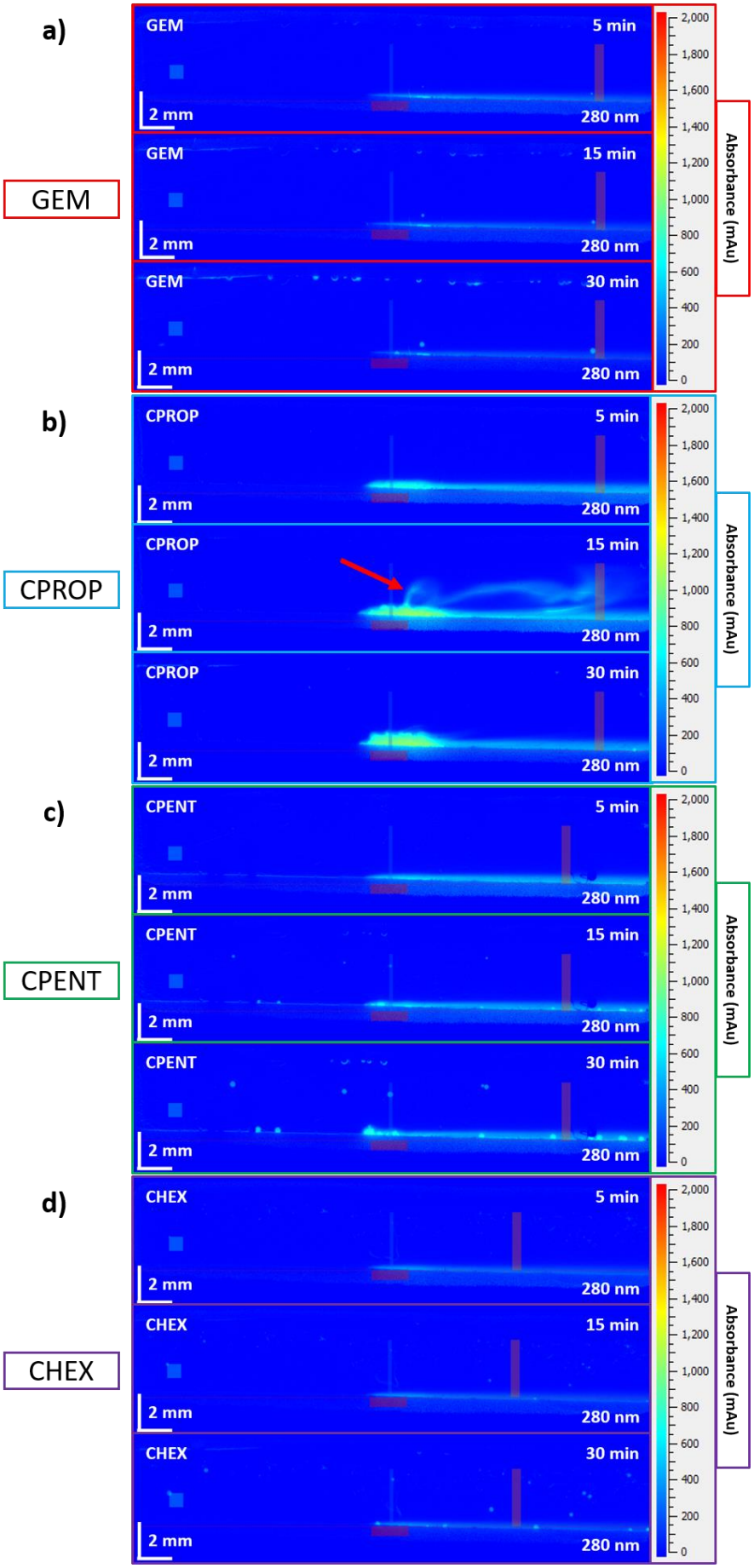

Figure 5-11 - UV images from the IDR assessment in Phosphate media of a) the active ingredient GEM and the salts; b) CPROP, c) CPENT and d) CHEX. The red arrow depicts the dissolution wave that led to inflated IDR values for the CPROP salt.

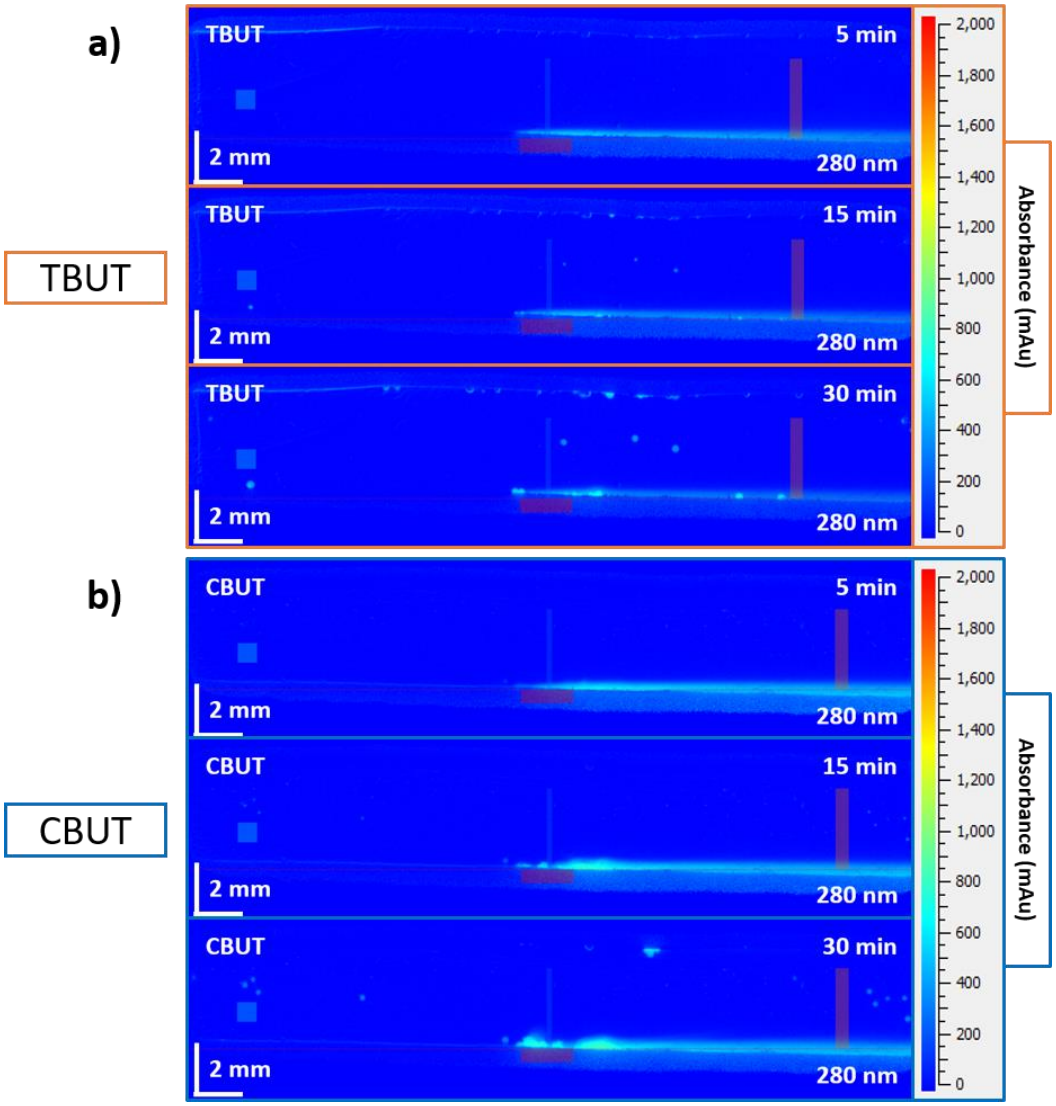

Figure 5-12 - UV images for the IDR assessment in Phosphate media of a) the TBUT salt and b) the CBUT salt.

The images taken from the dissolution imaging system for the CPROP salt also found some interesting dissolution phenomenon. It initially appeared that the salt displayed a high intrinsic dissolution rate as indicated by the dissolution profile in Figure 5-13b. However, the dissolution footage highlighted that there was a potential disintegration of the compact surface similar to those reported by Ward et al. with the first version of the SDI system (120). This is indicated by the red arrows in Figure 5-11b and Figure 5-13b. This is likely the cause of the inflated and erratic behaviour of the dissolution profile for this salt. As a consequence of this, only the averages of the first 10 min of the IDR measurement were used to compare the salts with the base drug.

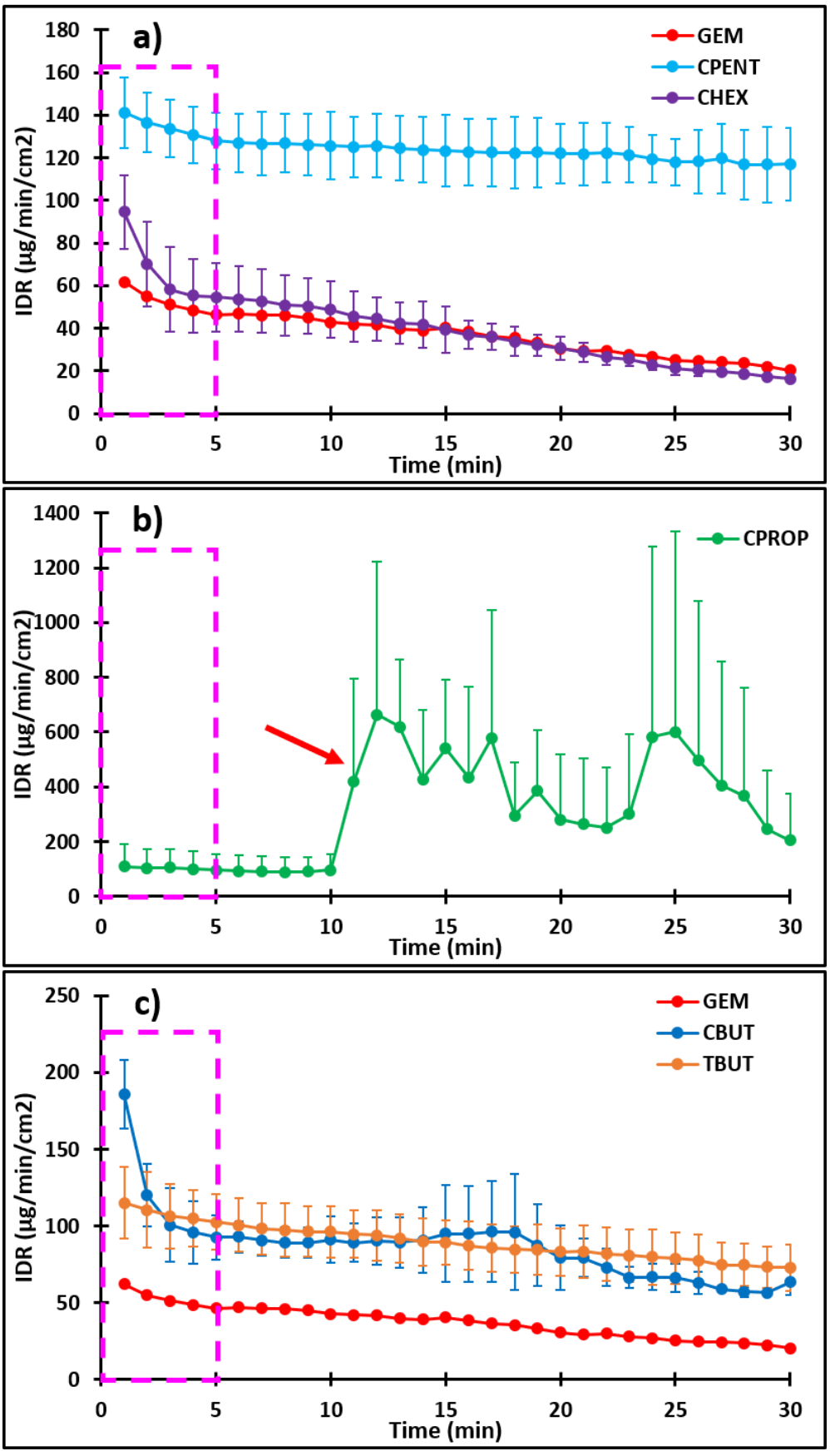

Figure 5-13 - IDR Dissolution profiles from the SDi2 system in Phosphate media(n=3). a) IDR profiles of the active ingredient GEM compared to the salts CPENT and CHEX. b) The salt CPROP. c) The active ingredient GEM compared to the salts TBUT and CBUT. Note: The pink IDR box highlights the first five minutes of data excluded from Average IDR calculation. The red arrow highlights the effects on the dissolution profile of the dissolution waves seen in the UV images.

From the IDR assessment of the salts, it appeared that all the salts displayed a greater IDR than the base drug (Figure 5-13 and in Table 5-4). The CPROP and CBUT salts displayed similar IDR values of 93.17 and 91.63 µg/min/cm^2 respectively. This can be seen visually in Figure 5-11b and Figure 5-12b. This is also supported by relatively similar solubilities of the salts reported by Ramirez et al of 14.24 and 20.39 mg/mL respectively at 37 °C (106). The CPENT salt provided the greatest increase in IDR over the base drug with an IDR of 127.61 µg/min/cm^2. This could be linked back to the lower Smr2 value for the surface of these IDR compacts compared to the other cyclic salts, consequently resulting in a greater area available for lubrication/wetting. The CHEX salt produced the lowest IDR of all the salts tested with an average IDR value of 52.97 µg/min/cm^2. This could be due to the low solubility reported for this salt of 2.36 mg/mL at 37 °C and also the greater molecular weight of the counterion. It is also likely that the increased “chain length” in this salt could lead to increased hydrophobicity of the crystal lattice and thus inhibit dissolution rate.

When the CBUT and TBUT salts were compared in Figure 5-12 and Figure 5-13c, it appeared that the TBUT salt displayed a slightly higher average IDR of 99.95 µg/min/cm^2. This was despite a lower reported aqueous solubility of 7.82 mg/mL at 37 °C, this could indicate that surface porosity differs between the two salts when compacted at the same force leading to an earlier hydration of the TBUT salt. This is supported by the images in Figure 5-12 which showed a greater absorbance at 15 min for the CBUT salt over the TBUT salt.

The dissolution imaging system therefore provided a hypothesis that going into whole dosage formulation and dissolution testing that the CPENT salt should provide the greater dissolution rate.

5.6.2.3 Whole Dosage Dissolution assessment

This section of this chapter demonstrates the capability of the dissolution system to record and measure dissolution phenomena from a whole dosage form. In this instance, a custom wire holder was designed to hold a hard gelatin capsule containing the salt. All capsules were monitored over a 60 min period using the 280 and 520 nm LED's simultaneously.

Table 5-5 - A table displaying the average concentration (mean +/- SD) (n=3) over the 60 minute period for Gem and its salts. The table also displays associated AUC measurements.

Active Ingredient	Average Conc. (µg/mL)	AUC
GEM	16.0±11.1	0.99
CPROP	43.9±1.9	2.55
CPENT	28.1±4.6	1.73
CHEX	26.2±2.9	1.54
CBUT	42.7±4.1	2.46
TBUT	33.3±6.6	2.02

Similarly, to the IDR analysis in 5.6.2.2, all the salts produced greater drug dissolution over the parent drug GEM (Figure 5-16). It was interesting to note that the GEM profile appeared to start approximately 4 times higher than the salts (Figure 5-16a). There are two possible causes for this; the first is that all capsules were filled with an equivalent amount of the active ingredient (150 mgA). As result of this, less bulk API was contained in the GEM capsules and during capsule dissolution the drug may have had a greater opportunity to flow through the measurement zone at the top of the cell. The second cause may be that due to the lighter nature of the GEM capsules, the uneven distribution of the weight occasionally led to the bending of the capsule into the measurement zone leading to interference and an inflated result. An example of this is in Figure 5-14a.

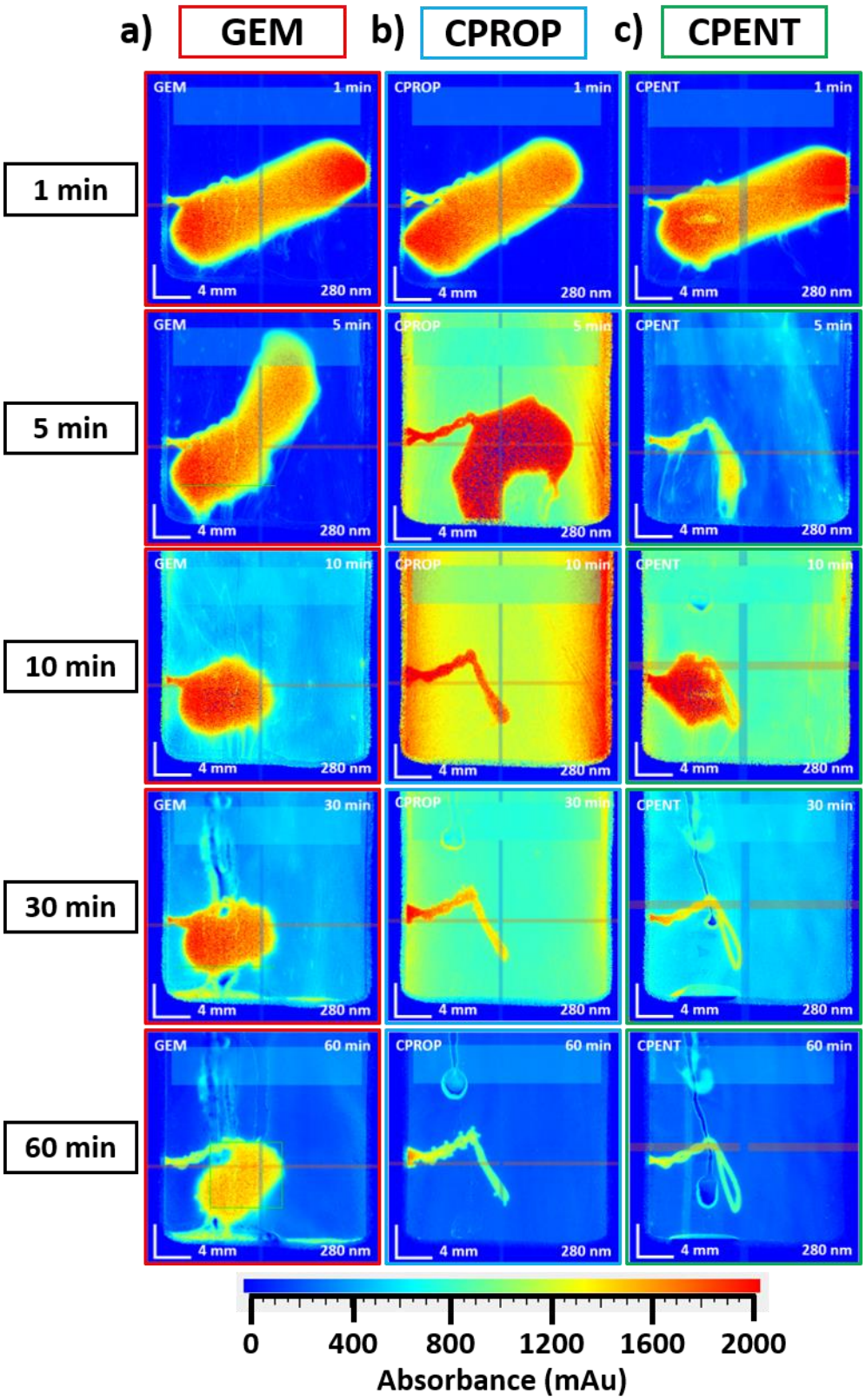

Figure 5-14 - UV images from the whole dosage assessment in phosphate media of a) the active ingredient GEM and the salts b) CPROP and c) CPENT.

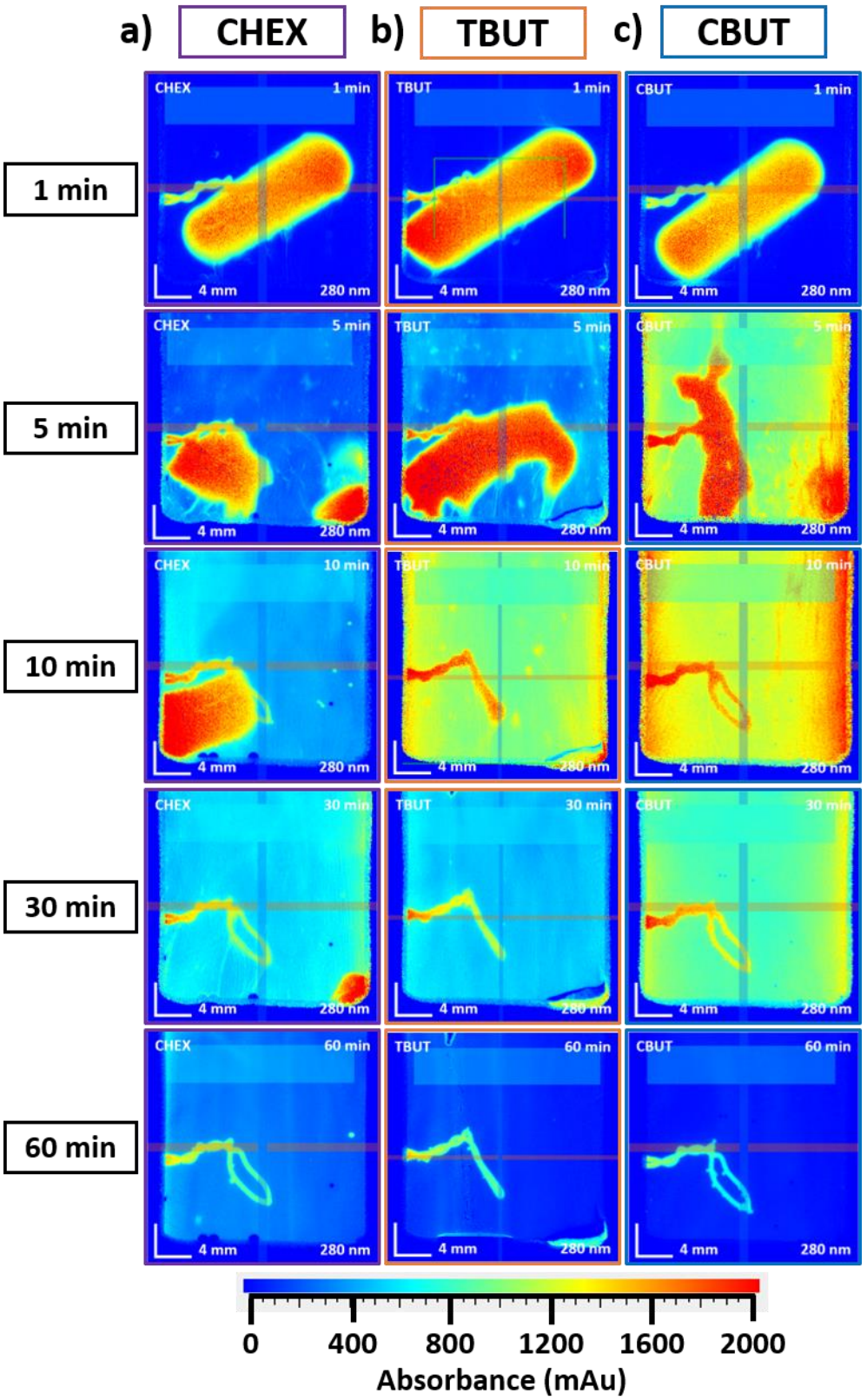

Figure 5-15 - UV images from the whole dosage assessment in phosphate media of the salts a) CHEX, b) TBUT and c) CBUT.

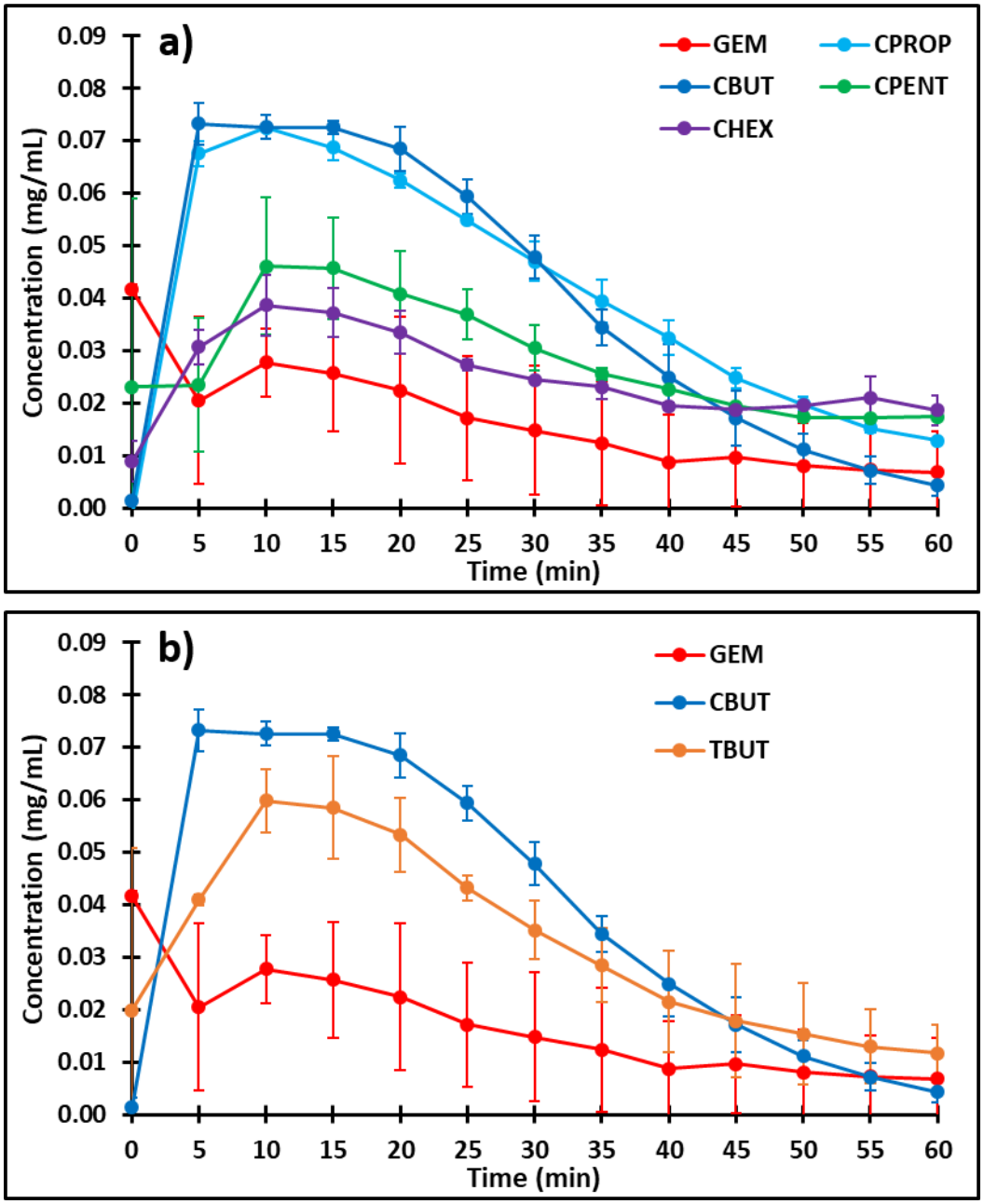

Figure 5-16 - Dissolution profiles obtained from the SDi2 system. a) Comparison of the active ingredient GEM and the cycloamine salts of CPROP, CBUT, CPENT and CHEX. b) Comparison of the active ingredient GEM and the CBUT and TBUT salts.

The whole dosage assessment of the capsules also displayed a significant trend between the cycloamine salts. It appeared that as "chain length" of the counterion increased, dissolution rate decreased. The CPROP salt displayed the highest average concentration of 0.0439 mg/mL (Table 5-5). This was supported by the intense orange-red colouration of the UV images in Figure 5-14b. The CHEX salt displayed the lowest average concentration of all the salts at 0.0262 mg/mL (Table 5-5). This again was supported by the light blue colouration of the UV images in Figure 5-15a. AUC

measurements also confirmed the trend in the salts starting at 2.55 for CPROP before decreasing to 1.54 at CHEX. It is increasingly likely that an increasing hydrophobicity was caused by the increase in “chain length” of the counterion. This may have resulted in a fall in dissolution performance. A secondary comparison was also conducted between the TBUT and CBUT salts of GEM (Figure 5-15 and Figure 5-16). The CBUT salt provided a greater benefit to dissolution over the linear TBUT salt. CBUT displayed an average concentration of 0.0427 mg/mL compared to 0.0333 mg/mL for TBUT. This was supported by AUC values of 2.46 compared to 2.02 and the UV images in Figure 5-15 which displayed a greater intensity of colouration for the CBUT salt.

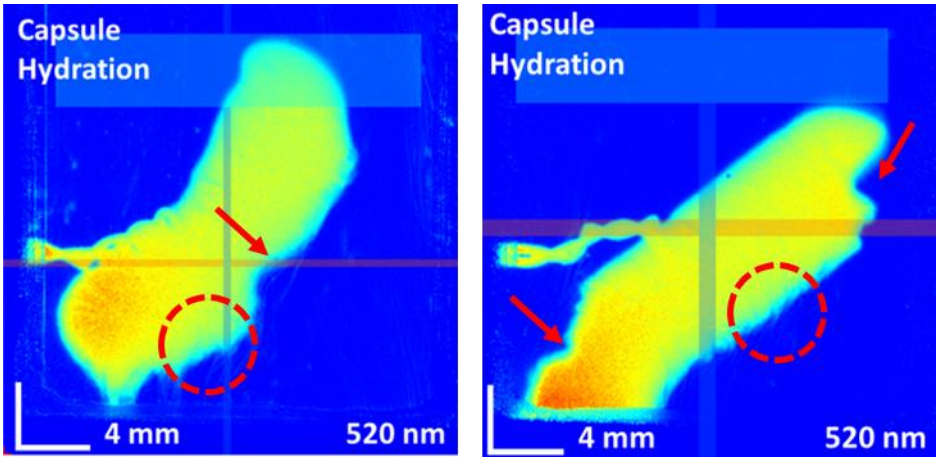

Figure 5-17 - Optical images recorded by the SDi2 system using the 520nm LED. Note: The red dashed circles highlight fluid ingress into the capsule, whilst the red arrows highlight capsule breakdown.

This section also simultaneously recorded the breakdown of the capsules in real time using the 520 nm LED alongside the 280 nm LED used for monitoring drug dissolution. Figure 5-17 displays some example images from the dissolution imaging displaying some key phenomena such as the imbibement of media and capsule dissolution. This feature could be of particular use to formulators in the field of quality control for measuring the integrity and consistency of manufactured dosage forms.

5.7 Conclusion

This chapter represents the successful manufacture, characterisation and ranking of a range of prepared salts using two novel imaging techniques in the form of focus variation microscopy and UV imaging.

Cycloamine salts (CPROP, CBUT, CPENT and CHEX) and a Tertiary amine salt (TBUT) of the carboxylic acid drug GEM were successfully prepared. This was confirmed using both DSC and XRPD. The use of focus variation microscopy detected a number of anomalies/defects on the surface of the IDR compacts not visible by eye, from embedded particulates to rings from the tooling. The use of the microscopy data to determine the parameters *Sdr* and *Smr*2 provided information on the variation in surface gain for all the salts. This could be used to give insights into how the compacts undergo compression during IDR compact preparation. The use of the different counter ions in this study could have contributed to different plasticities of the different salts which could have contributed to the different surface gains measured by the microscope. However, further investigation will be required to fully determine the correlation between the surface parameters measured by Focus Variation and the compaction properties of pharmaceutical materials.

The flow through cell provided a visual assessment of the IDR of the parent drug and its salts. However, the flow through cell also visualised the influence of surface anomalies on the measured IDR values. This chapter also displayed the need for further investigation into the methodology used to conduct IDR measurements as it is likely that this could have also impacted on some of the results observed.

Imaging of the powder dissolution via a capsule was successful and confirmed differences in the dissolution behaviour of the salts. The results suggested that an increase in “chain length” brought about a decrease in the dissolution of the salts over

the parent drug i.e. CPROP > CBUT > CPENT > CHEX > GEM. The powder dissolution assessment also showed an added benefit of a cyclic counterion over a tertiary ion in the form of CBUT and TBUT. With CBUT providing a greater dissolution rate. The dissolution imaging system also provided a visual imagery of the dissolution of a capsule which could be of significant interest to a formulator.

This chapter therefore has highlighted how UV imaging could be utilised by a formulator as it has the capability to provide quick insights into the ranking of salt forms whilst also providing a visual assessment to quickly troubleshoot any anomalies. UV imaging could be a vital tool for salt screening during the preformulation stages.

Chapter 6 – Use of advanced imaging techniques for characterising solid dispersions.

6.1 Note to Reader

Some aspects of the following chapter is published in the European Journal of Pharmaceutics and Biopharmaceutics Volume 137 under the title *'Effect of preparation method on the surface properties and UV imaging of indomethacin solid dispersions'.*(124).

6.2 Rationale

The following chapter looks to explore the use of UV imaging with solid dispersion systems. The purpose of this chapter is to determine if advanced imaging techniques can be used to provide useful insights into the dissolution properties of solid dispersions, manufactured through 3 different processes; Spray Drying (SD), Freeze Drying (FD) and Homogenizing (HG). Both the IDR flow through cell and the whole dosage cell were utilised alongside the focus variation microscopy for the compacts for the IDR determination.

6.3 Introduction

As discussed in chapter 5, poor aqueous solubility is becoming an increasingly common occurrence with an estimated 80 % of new chemical entities suffering from poor aqueous solubility (125). The improvement of aqueous solubility in poorly soluble drugs can be costly, challenging and time consuming. Therefore, the choice of correct technique is vital, currently there are several methods that can be utilised by a formulation scientist including; salt formation (106,108,111), complexation (126,127), co-crystallisation (110,128), particle size reduction (129,130) and additive addition (131,132).

Included amongst these techniques is solid dispersion manufacture. A successful solid dispersion occurs when an API of choice is molecularly dispersed within an appropriate carrier. The API can exist in a solubilised, finely crystalline or often an amorphous state

(133). The selection of the appropriate carrier is often vital (134). Whilst some groups have investigated more novel carriers such as glucosamine (133,135), often the more common approach is the selection of natural or synthetic water-soluble polymers. This includes polymers such as; Polyethylene Glycol (136-138), Hydroxypropyl Methylcellulose (HPMC) (139-141) and Polyvinyl pyrrolidone (PVP).

Included amongst these water soluble polymers is Soluplus™. Soluplus is a grafted co-polymer of polyvinyl caprolactam, polyvinyl acetate and polyethylene glycol, specifically developed to produce solid dispersions (142,143). Soluplus is classed as a fourth generation polymer as it possesses both the ability to form a matrix and solubilise the drug dispersed within (144). Homayouni et al. also found that Soluplus is amorphous in nature and exhibits good physicochemical characteristics such as; low glass transition temperature, excellent thermal stability, superior flowability, low bulk density and a low toxicity (145). Fule and Amin also found Soluplus demonstrated excellent solubilisation properties for BCS class II and IV compounds (146). As a result of these desired characteristics a number of groups have utilised Soluplus as their carrier of choice in formulating solid dispersions. Reginald-Opara et al. formulated and characterised solid dispersions of Glimepiride-soluplus (144). Whilst, Costa et al investigated drug polymer solubility of Efavirenz-Soluplus solid dispersions (147). In this chapter Soluplus was used as the carrier to formulate solid dispersions of indomethacin (INDO) at polymer:excipient ratios of 1:1, 1:3 and 1:5.

To formulate solid dispersions a number of manufacturing techniques are often employed; including freeze drying (148), spray drying (147), homogenization, Hot melt extrusion (149) and Rotary Evaporation (144), with the end result to achieve a molecularly dispersed matrix of drug in carrier. This chapter specifically explores three manufacturing techniques; spray drying, freeze drying and homogenizing.

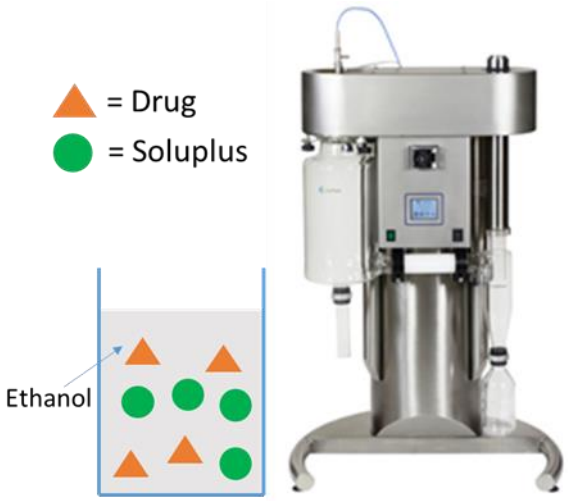

Figure 6-1 - A schematic representation of the spray drying process of producing solid dispersions.

Spray drying (Figure 6-1) has been a fundamental manufacturing technique within pharmaceuticals since the early 1940's (150) and is still in use today for the production of a wide range of formulations including; amorphous solid dispersions (151), inhalation products (152), taste masking (153) and controlled release formulations (154). There are three fundamental steps to spray drying, the first involves the atomisation of a liquid stock (often solvent based) into fine droplets. The second is the mixing of the droplets with a heated inert gas stream. This allows for the liquid to evaporate and produce dried solid particles. The final stage is the collection of the dried particles from the gas stream, often produced by a vacuum. The end result is often low density spherical particles with excellent flowability, compressibility and a reduced moisture content (155).

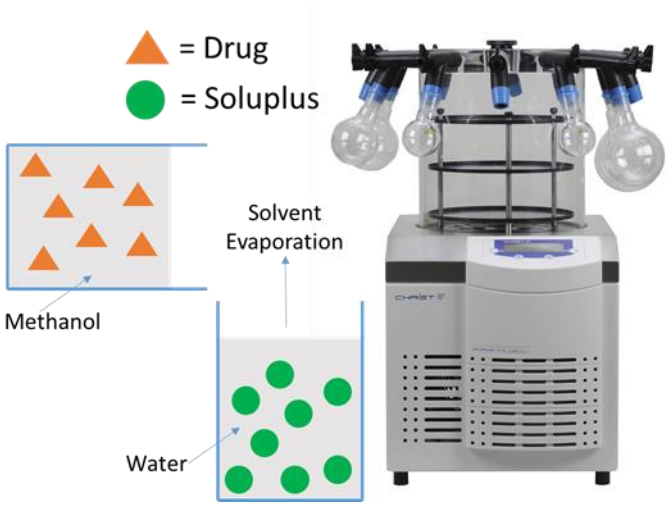

Figure 6-2 - A schematic representation of the freeze drying process to produce solid dispersions.

Freeze Drying (Figure 6-2) also known as lyophilisation is another common manufacturing technique within the pharmaceutical industry. Often freeze drying is used to improve the stability of formulations such as; vaccines (156), viruses (157), proteins (158) and colloidal carriers (159). Similarly, to spray drying, freeze drying consists of three fundamental steps; freezing, primary drying and secondary drying. During the freezing step, the liquid in the sample is cooled and as the liquid freezes this concentrates any solids in the remaining liquid. Freezing is predominantly achieved through the use of liquid nitrogen however, for sensitive samples overnight conventional freezing can also be used. Next, is the primary drying step. During this step, low temperatures and pressures are utilised to induce ice sublimation. The primary drying step is often the longest of all three steps and is affected by the size of the ice crystals. The final step is secondary drying. During this step, any residual water is removed from the solute phase. Once this process is complete the result is often a fibrous porous matrix (160).

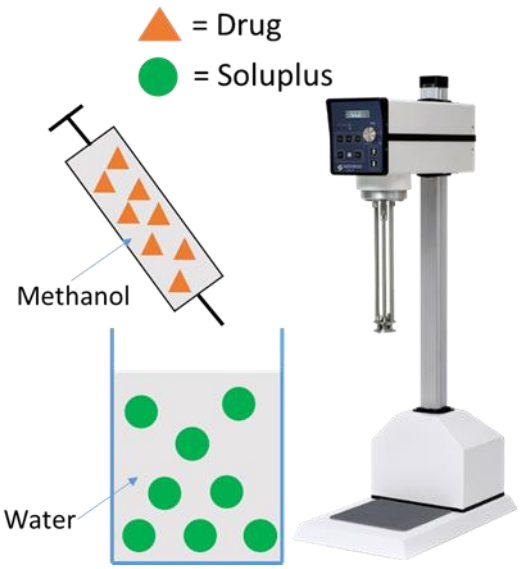

Figure 6-3 - A schematic representation of the homogenization process.

Homogenisation (Figure 6-3) also known within the pharmaceutical industry as micronisation is the process of reducing the particle size of pharmaceutical products using very high pressure, sheer, impact, and turbulence with the aim of making them more stable and effective. A reduction in particle size can increase the effective surface area of a compound, whilst also subsequently improving dissolution rate (161). In this process, drug is dissolved in a solvent and added drop wise into an aqueous solution. Often the aqueous solution can contain a stabiliser such as a hydrophilic polymer. A homogeniser is then used to agitate and shear the solution, this prevents larger crystals of the drug forming in the aqueous solution. The aqueous solution is then freeze dried to produce the solid dispersion matrix (145).

This chapter aims to build upon previous work conducted on the version 1 instrumentation of the SDI by Colombo et al. (162) In this study, the group investigated the matrix effect of a HPMC phthalate polymer on the dissolution kinetics of nilotinib over a range of pH. UV imaging was employed to monitor the effect of drug load on the swelling and dissolution of the polymer matrix as the pH shifted. The group imaged and concluded that a high drug load prevented matrix swelling from acid to neutral pH. In this chapter similar observations of the solid dispersions will be conducted using the flow cell supplied with the SDi2 system. However, to build upon this work, capsules containing the solid dispersions will also be formulated and imaged using the whole dosage cell supplied with the dissolution imaging system. This chapter will also employ focus variation microscopy to monitor the IDR compacts produced from each solid dispersion and provide topographic information. Also, this chapter will explore the use of the 520 nm LED in combination with the 320 nm LED to provide simultaneous measurements of drug release and growth from each IDR compact and dosage form.

Indomethacin (INDO) was selected as the model drug of choice in this chapter. indomethacin is an indole acetic acid derivative and also a non-steroidal anti-inflammatory drug. It is primarily used in the treatment of musculoskeletal and joint disorders such as; osteoarthritis, rheumatoid arthritis, and acute gout. Due to its NSAID nature it is also used to treat inflammation and pain following orthopaedic pain (118). indomethacin is also a BCS Class II drug indicating low solubility and high permeability.

Indomethacin has been used as a model drug in the production of a variety of solid dispersions by a number of different groups. Pezzoli et al. investigated the effect of moisture on the stability and dissolution of indomethacin – PVPVA solid dispersions manufactured by hot melt extrusion. They found that amorphous solid dispersions could be successfully manufactured via twin screw hot melt extrusion and were stable for 12 weeks at 75 % relative humidity (149). Jelić et al. also investigated the thermal

stability of amorphous indomethacin solid dispersions with PVP using thermogravimetric analysis (TGA). They found that the thermal stability of indomethacin increased with an increasing amount of PVP due to an increasing decomposition temperature (163).

Bertoni et al. attempted to address the issue of recrystallisation of amorphous indomethacin by formulating micro particle solid dispersions through spray congealing with Gelucire. They discovered that spray congealing resulted in the successful stabilisation of amorphous indomethacin and also an improved dissolution rate. Also, the formulation was found to be stable for 18 months with no change in the solid state of the indomethacin or its dissolution rate (164).

Xie et al. investigated the impact of Eudragit and HPMC on the dissolution rate of indomethacin amorphous solid dispersions. They discovered that solid dispersions of HPMC dissolved slowly whilst the Eudragit solid dispersions exhibited a rapid initial dissolution phase. They also found that a combination of both Eudragit and HPMC dissolved rapidly leading to a drug concentration higher than the amorphous solubility of indomethacin (165).

6.4 Objectives

The objective of this chapter was to utilise both UV imaging and focus variation microscopy to investigate amorphous solid dispersions (ASD) of indomethacin produced via three manufacturing techniques. The focus variation microscope will be used to investigate how the surface topography of compacts used in flow-through dissolution are influenced by the different manufacturing techniques. The whole dosage cell for the dissolution imaging system will be employed to investigate the dissolution properties of each manufactured solid dispersion. The 520 nm LED will also be employed simultaneously to monitor the *in situ* physical behaviour of the solid dispersions.

6.5 Materials and Methods

6.5.1 Materials

The materials for this experiment were as follows:

- The active ingredient indomethacin (INDO) was purchased from TCI Chemicals, (UK).
- The polymer Soluplus (SOL) from BASF (Germany).
- The solvents methanol and ethanol for the production of the solid dispersions were purchased from Fisher, UK.
- Potassium phosphate monobasic and sodium hydroxide for the preparation of the dissolution media pH 7.2 were purchased from Arcos Organics (Germany) and Fisher (UK) respectively.
- De-ionised water

6.5.2 Methods

6.5.2.1 Solid Dispersion Preparation

Spray Dried Solid Dispersions

8 g of the active ingredient (INDO) was added either to 8, 24 and 40 g of Soluplus. This resulted in drug to polymer ratios of 1:1, 1:3 and 1:5. The dry powder blend was added to approximately 1.6 L of ethanol and stirred at 200 rpm using a Cole-Palmer® Hot plate stirrer until all the blend had completely dissolved. Once complete dissolution had occurred, each resulting solution was spray dried using a Labplant® Spray Drier (UK). The spray dryer was set to pump the solution through the system at a rate of 695 mL/hour. The fan was set at a speed of 3.25 m/s whilst the inlet temperature was set at 90 °C. Spray dried particles were then recovered from the collection bottle. Spray dried particles from all three ratios were stored in a desiccator at room temperature until required.

Freeze Dried Solid Dispersions

1 g of INDO was added to a beaker containing 100 mL of Methanol. The solution was stirred on a Cole-Palmer® Hot plate stirrer at 200 rpm to aid dissolution. In a separate beaker, 1 g of Soluplus was dissolved in 100 mL of deionised water. Next the beaker containing the indomethacin was gradually added to the Soluplus solution. The mixture was stirred at 500 rpm and at a temperature of 70 °C to aid the removal of methanol from the solution prior to the freeze drying process. Once mixing and solvent evaporation was completed the resultant solution was poured into a tray to increase surface area and immersed in liquid nitrogen. The sample was then placed into a Christ Alpha 2-4 LD Plus freeze drier for 24 h. The sample was collected upon freeze drying completion or when the sample had been completely dried. The sample was transferred to a glass vial, labelled, and stored until required. The same process was

repeated for the 1:3 and 1:5 ratios, with the only difference being an increased amount of Soluplus of 3 or 5 g to account for the ratio.

Homogenised Solid Dispersions

To produce these samples the freeze drying method as indicated above was adopted and modified. Three beakers containing 1, 3 or 5 g of Soluplus in 100 mL of deionised were prepared under stirring conditions at room temperature. A separate beaker containing a concentrated amount of (INDO) in methanol equivalent to 1 g in 20 mL was prepared. Next, the beaker containing 1 g of Soluplus was placed under a high shear homogeniser and 20 mL of the concentrated indomethacin was added to a syringe. Under the homogenising speed of 1000 rpm, the INDO was added to the Soluplus solution dropwise. The resulting suspension was then transferred to a tray and immersed in liquid nitrogen. The sample was then placed into a Christ Alpha 2-4 LD Plus freeze drier for 24 h. The same process was then applied to the 1:3 and 1:5 ratios. The collected homogenised and freeze dried particles from the three ratios were then stored in a desiccator until required.

6.5.2.2 Solid State Characterisation

To aid characterisation and analysis all samples were given a shorthand quick reference code. Spray dried samples were given the code ‘SD’ followed by their appropriate ratio i.e. SD1:1. The same format was applied to freeze dried samples ‘FD’ and homogenized samples ‘HG’.

Scanning Electron Microscopy (SEM)

Prior to analysis on the SEM, each sample including the active ingredient (INDO) and Soluplus (SOL) was mounted on a double-sided carbon adhesive tape on a metal stub and sputter-coated with a thin coating of gold/palladium (80:20) for 60 s using a Quorum SC7620 Sputter Coater under vacuum. A Jeol JSM-6060CV SEM operating at 10 kV was used to obtain the electron micrographs. Different magnifications were taken to aid the study of the morphology of the solid dispersions.

Differential scanning calorimetry (DSC)

A Mettler-Toledo DSC 1 Differential Scanning Calorimeter was used to conduct all DSC measurements. Prior to measurement, approximately 5-10 mg of each sample including the active ingredient (INDO) and Soluplus (SOL) was placed into a standard 40 µL aluminium pan. The powder was gently compacted in the pan to ensure even contact and heating. A lid was then crimped in place and pierced to produce a vent. The pan was then heated from 50 to 180 °C at a scanning rate of 10 °C/min with nitrogen gas used as a purge gas. The enthalpy, onset temperatures and melting points of each sample as well as their glass transition temperatures were analysed using the software provided by Mettler-Toledo, Switzerland.

X-ray powder diffraction (XRPD)

XRPD measurements were performed on all samples to determine successful amorphous solid dispersion production and also assess the crystallinity and polymorph of the starting API INDO. All samples were scanned in Bragg–Brentano geometry, over a scattering (Bragg, 2θ) angle range from 5 to 100°, in 0.02° steps at 1.5° min−1 using a D2 Phaser diffractometer (Bruker AXS GmbH, Karlsruhe, Germany). The XRPD patterns were collected and analysed further using Microsoft Excel.

Isothermal Calorimetry (ITC)

Isothermal Calorimetry was employed to determine if there was any interaction between INDO and SOL. Firstly a 0.020 % w/v SOL sample was prepared using 100 mL of pH 7.2 phosphate buffer. The solution was stirred at 400 rpm using a Cole-Palmer® Hot plate stirrer for 24 h to ensure complete polymer hydration. A 0.010% w/v INDO solution was also prepared using 100 mL of pH 7.2 phosphate buffer and stirred at 400 rpm for 24 h to ensure complete dissolution. Calorimetric binding studies were carried out at 25 °C on a Microcal VP ITC micro calorimeter in high-gain equilibration mode. The reference power applied was 10 µcal s-1 and the sample cell contents were stirred at 307 rpm. Titration was carried out with the soluplus dispersion in the sample cell and the indomethacin solution in the syringe. The indomethacin solution was added in 10 injections of 10 µl each into the sample cell every 500 s. The binding isotherm was analysed using Origin 7.0 (Microcal, Inc) software.

6.5.2.3 Dissolution Imaging

In this study both the flow through cell and the whole dosage cell were used. The method specifics are outlined as follows:

Dissolution Media Preparation

The media used for IDR determination and whole dosage imaging was a 0.2M phosphate buffer (pH 7.2) prepared according to the USP 2003 using sodium hydroxide and potassium phosphate monobasic as detailed in chapter 5.

UV Calibration of indomethacin

Prior to analysis, a calibration curve was produced to determine the Molar Extinction Coefficient of INDO. Firstly, two stock solutions were prepared by weighing 10 mg of INDO into a 10 mL volumetric flask and made to volume with pH 7.2 buffer producing a 1 mg/mL solution. Next, two series of standards were produced (1 from each stock) following Table 6-1 below:

Table 6-1 - Standard concentrations used in the calibration of indomethacin at 320 nm Note: The standards indicated with a star were produced following a 1 in 10 serial dilution of the 10 and 50 stock respectively.

Concentration (µg/mL)	Amount of Stock (µL)
100	1000
75	750
50	500
30	300
20	200
10	100
5*	50
2.5	25
1*	10

Once all the standards were prepared, each series was analysed at an absorbance of 320 nm using a Jenway® 72 Series UV/Visible Spectrophotometer and a 1 cm quartz cuvette. 320 nm was chosen upon review of the lambda max of INDO (318 nm) as this was the closest possible wavelength supported by the dissolution imaging system. Each series was then plotted using Microsoft Excel to produce the calibration curve and MEC value.

Flow through Cell and IDR Determination

This methodology has been reported significantly in chapter 5.5.2.3. The same methodology was applied in this work with the only significant change to this methodology being the switch from 280 nm to 320 nm and the inclusion of a second wavelength of 520 nm run simultaneously.

Whole Dosage Cell measurement

This methodology has been reported significantly in chapter 5.5.2.3. The same methodology was applied in this work with two significant changes. The first was a switch in wavelength from 280 nm to 320 nm. Whilst the second was that each capsule was formulated to contain 2.5 mgA of indomethacin.

6.5.2.4 Focus variation microscopy

The methodology for focus variation microscopy is discussed in more detail in Chapter 2 and the methodology for measuring IDR compacts is discussed in section 5.5.2.4. The method specifics for this chapter are shown in Table 6-2.

Table 6-2 - Specific method parameters used for both magnifications in the assessment of surface topography.

Parameter	Value at 5x	Value at 10x
Magnification	5x	10x
Image Area	1x1	1x1
Vertical Resolution (µm)	0.94	0.23
Lateral Resolution (µm)	7.82	3.91
Contrast	2	2

6.6 Results

6.6.1 Solid State Characterisation

6.6.1.1 Scanning Electron Microscopy

SEM images for the active ingredient INDO and the hydrophilic polymer SOL are displayed in Figure 6-4. INDO appeared generally to have a shard like morphology and also a varied blend of larger and smaller particles. SOL however displayed significantly larger particle sizes with a spherical nature. It must also be noted that the SOL bulk powder was very uniform. This observation is typical with synthetic engineered particles manufactured for a specific purpose.

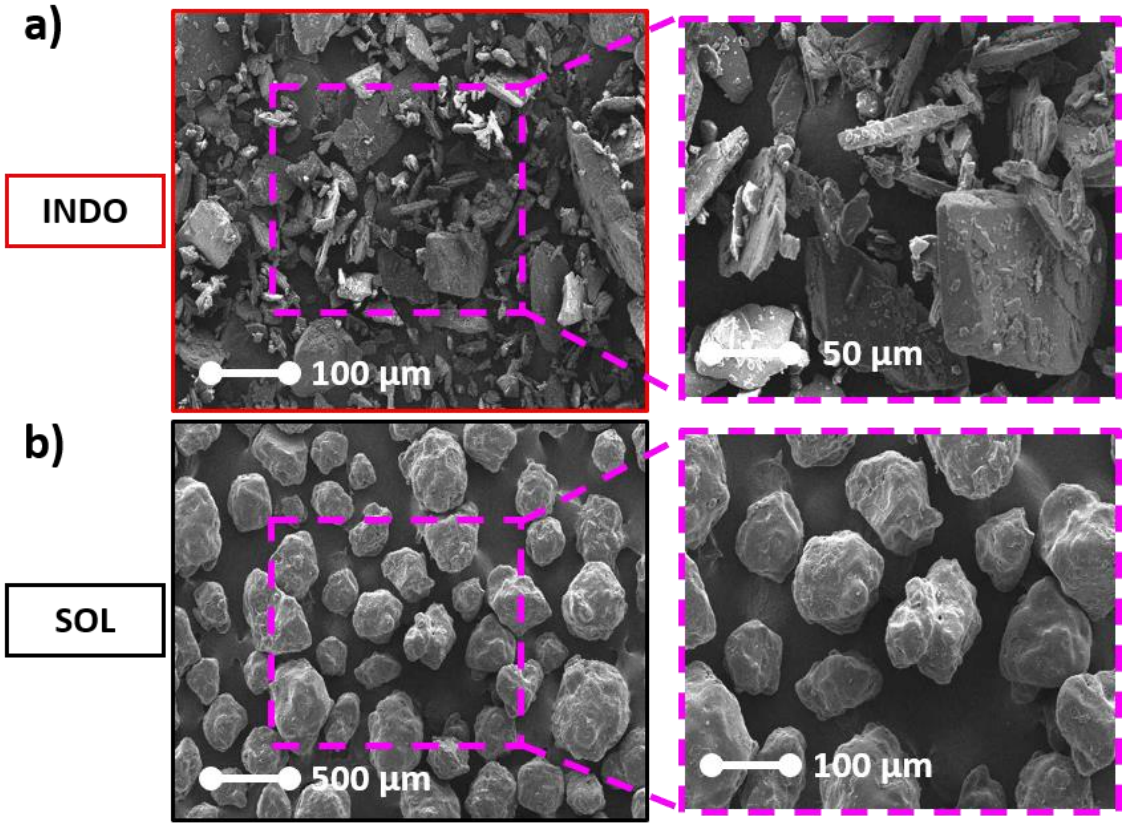

Figure 6-4 - Scanning electron micrographs of a) The active ingredient INDO and b) The hydrophillic polymer SOL.

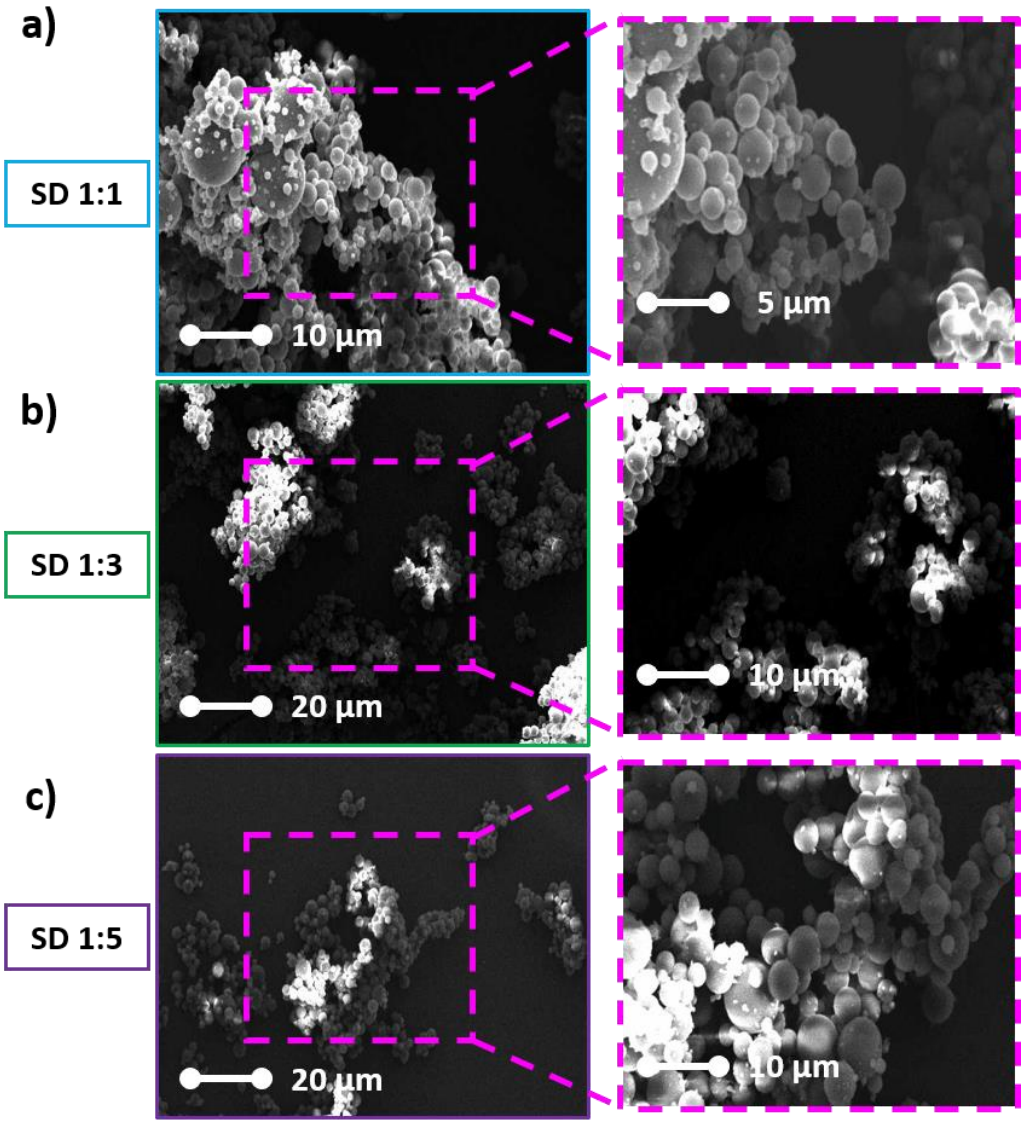

Figure 6-5 - Scanning electron micrographs of the solid dispersions formed via spray drying. a) the 1:1 ratio b) the 1:3 ratio and c) the 1:5 ratio.

The SEM images for the manufactured solid dispersion showed significant differences in morphology and the microstructure between the three techniques. Figure 6-5 displays the images taken from the spray dried solid dispersions at the three ratios tested. As expected from the spray drying technique, small spherical particles were produced. The particles were very consistent across all three ratios and also were very uniform in nature. Interestingly, the spray dried particles clustered together, this is likely to be due to their small particle size and low density. It is expected that the spray dried material will compact very well during IDR compaction and produce a relatively smooth compact.

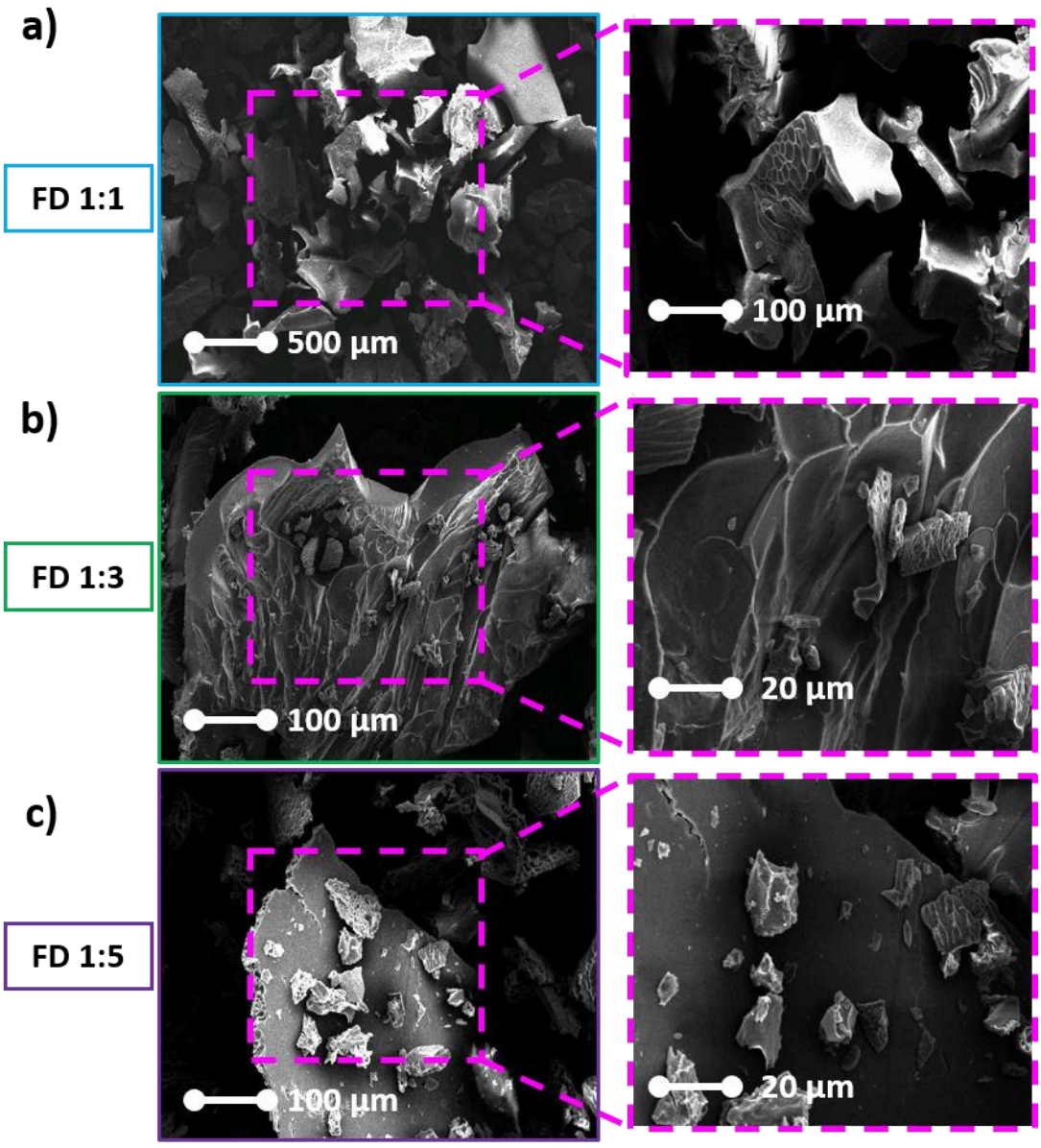

Figure 6-6 - Scanning electron micrographs of the solid dispersions formed via freeze drying. a) the 1:1 ratio b) the 1:3 ratio and c) the 1:5 ratio.

The SEM images for the freeze dried material are shown in Figure 6-6. The freeze drying process appeared to produce highly porous materials with wrinkled surfaces and generally a complex structure. Also, there was no significant morphological difference between the ratios. There was, however, a clear morphological difference between this material and the spray dried material in Figure 6-5.

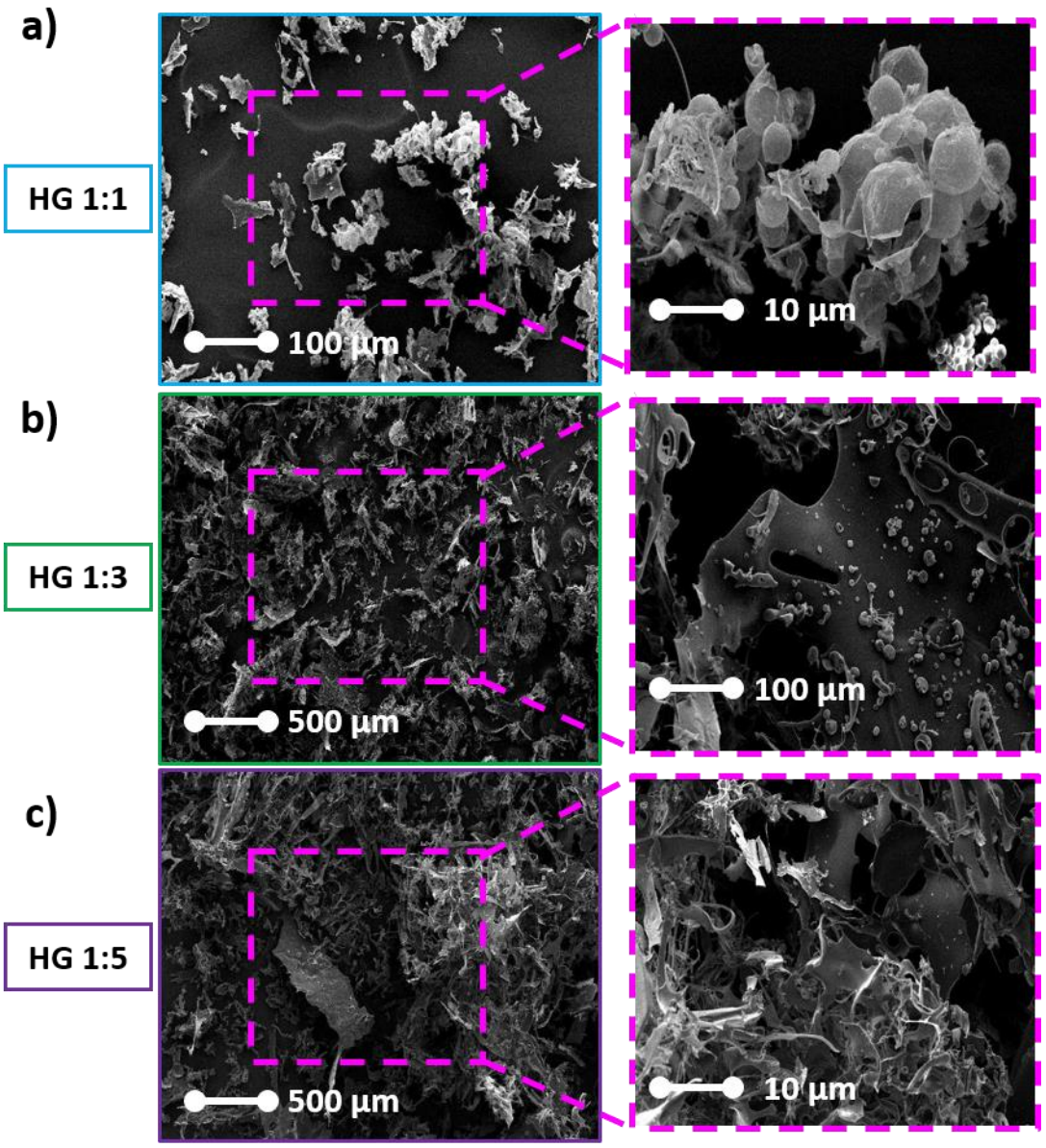

Figure 6-7 - Scanning electron micrographs of the solid dispersions formed via homogenisation. a) the 1:1 ratio b) the 1:3 ratio and c) the 1:5 ratio.

It was interesting to note that despite the freeze dried and homogenised samples being exposed to the same freeze drying process they had different morphologies. The homogenised material shown in Figure 6-7, appeared to have no distinct structure instead producing a varied fibrous network. Interestingly, some particles appeared to show spherical structures which could be attributed to the drop wise nature of the process. Due to these subtle differences in morphology between the homogenised material and the freeze dried material it is likely that the homogenised material may compact differently for IDR assessment despite the similarity in manufacturing methods e.g. use of a freeze-drying step.

6.6.1.2 X-Ray Powder Diffraction (XRPD)

XRPD was utilised in this study to identify the polymorphic form of the bulk INDO and also to confirm the nature of the prepared solid dispersions. It is important to note that XRPD analysis was conducted immediately after sample manufacture and also after 1 year of storage to ensure stability. Pan et al. report the characteristic peaks for the γ-polymorph of INDO to be at 11.6, 16.8, 19.6, and 26.6° 2θ (166). These notable peaks are indicated on each XRPD spectra in the form of black dashed lines with red stars.

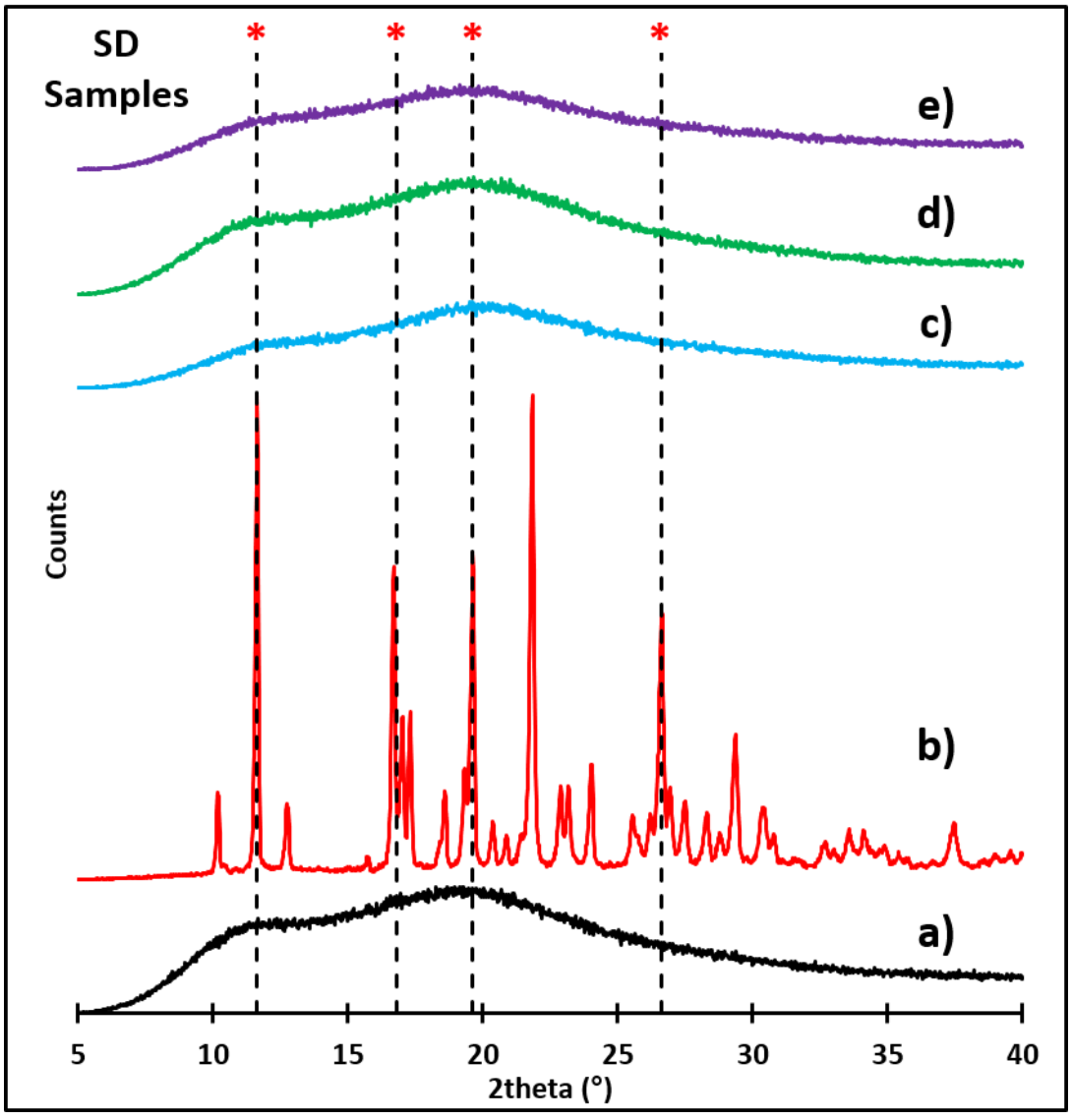

Figure 6-8 - XRPD spectra for the Spray Dried samples. a) Soluplus, b) indomethacin, c) 1:1 ratio, d) 1:3 ratio and e) 1:5 ratio. Note: the black dashed lines with red stars indicate the characteristic peaks for the γ-polymorph of indomethacin.

Figure 6-8 displays the XRPD spectra for the spray dried formulations. The hydrophilic polymer SOL was found to be fully amorphous with no crystalline peaks which was

expected from the polymer material (Figure 6-8a). The bulk INDO was found to crystalline in nature with strong crystalline peaks. The bulk indomethacin also expressed the characteristic peaks for the γ-polymorph (Figure 6-8b). All 3 spray dried ratios showed no crystalline peaks in their XRPD spectra indicating that all products were in the amorphous state and that an amorphous solid dispersion had formed (Figure 6-8c-e).

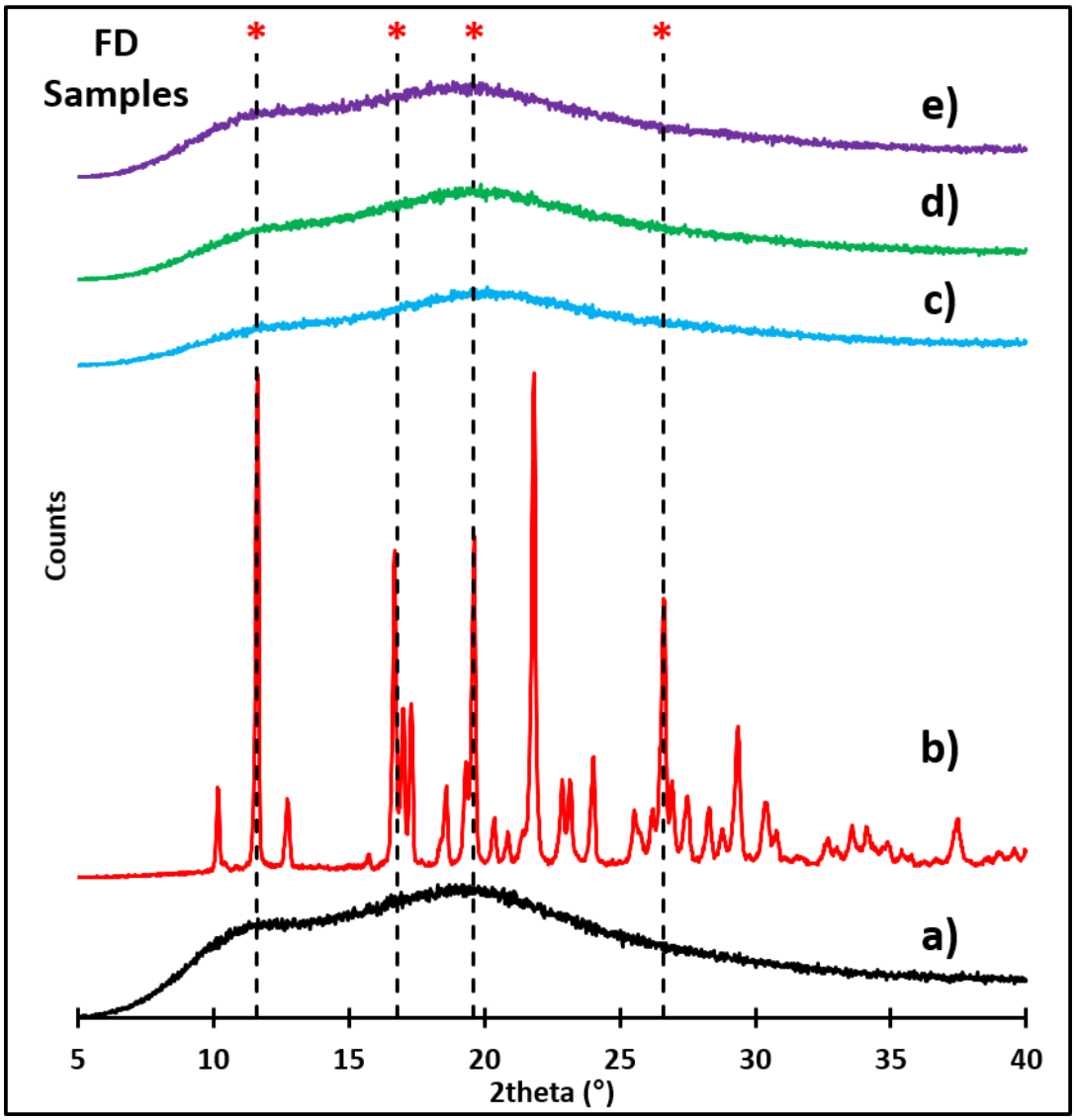

Figure 6-9 - XRPD spectra for the Freeze Dried samples. a) Soluplus, b) indomethacin, c) 1:1 ratio, d) 1:3 ratio and e) 1:5 ratio. Note: the black dashed lines with red stars indicate the characteristic peaks for the γ-polymorph of indomethacin.

Figure 6-9 displays the XRPD spectra for the freeze dried samples. Similarly, to the spray dried samples, all three ratios of solid dispersion showed no crystalline peaks.

This indicated that all the products formed via freeze drying were amorphous in nature and that successful amorphous solid dispersions had been produced (Figure 6-9c-e).

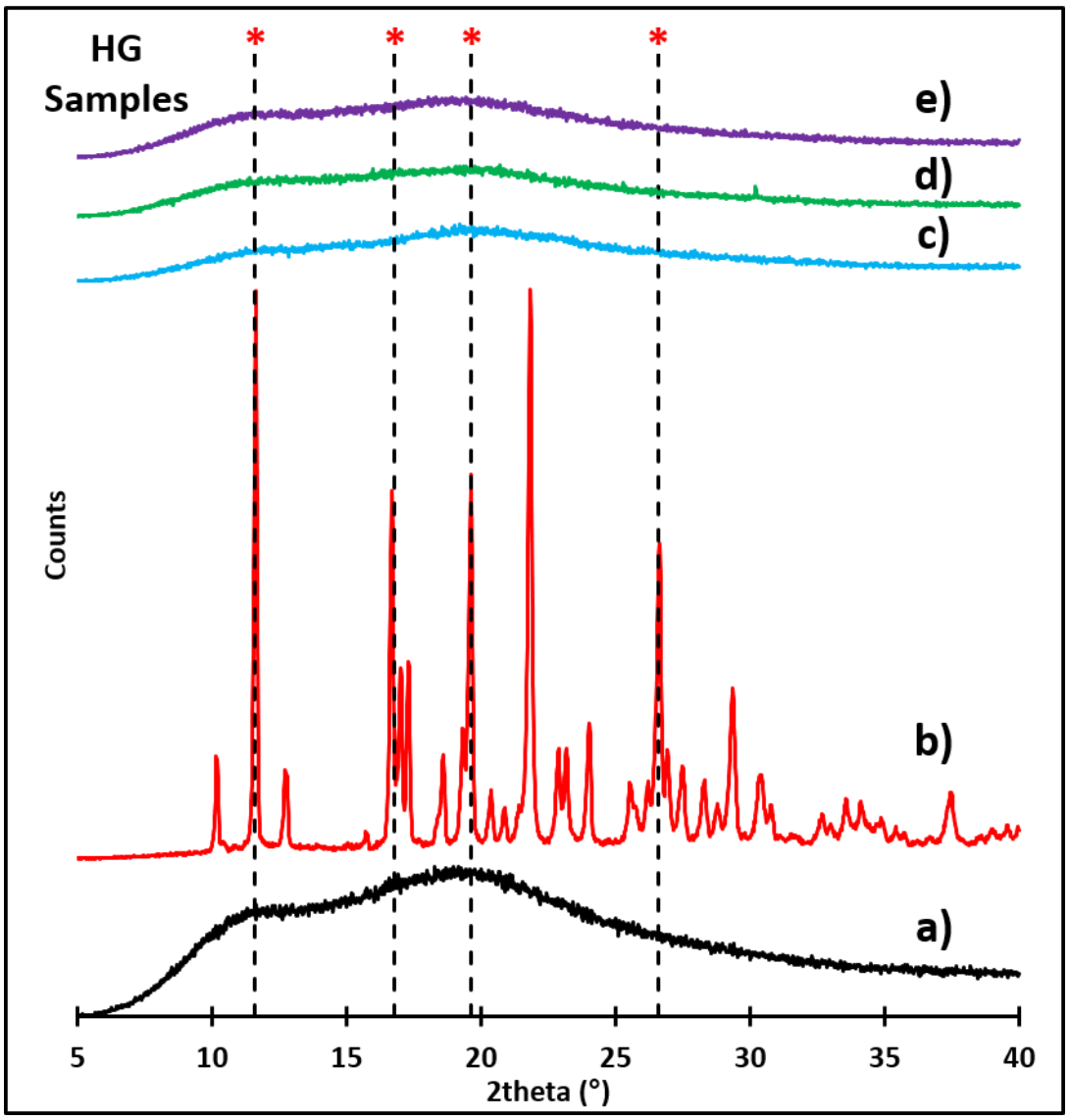

Figure 6-10 - XRPD spectra for the homogenised samples. a) Soluplus, b) indomethacin, c) 1:1 ratio, d) 1:3 ratio and e) 1:5 ratio. Note: the black dashed lines with red stars indicate the characteristic peaks for the γ-polymorph of indomethacin.

Figure 6-10 displays the XRPD spectra for the homogenised samples. The 3 ratios for these samples also displayed no crystalline peaks indicating that amorphous solid dispersions had been successfully formed (Figure 6-10c-e).

XRPD indicated that regardless of manufacturing technique, successful amorphous solid dispersions were produced. The diffused halo diffraction pattern also suggests that INDO was molecularly dispersed within SOL. XRPD was also employed to determine the stability of the solid dispersions after 1 year of storage under ambient

conditions. From Figure 6-11, it can be observed that all 9 solid dispersions remained stable with no crystalline peaks in the spectra.

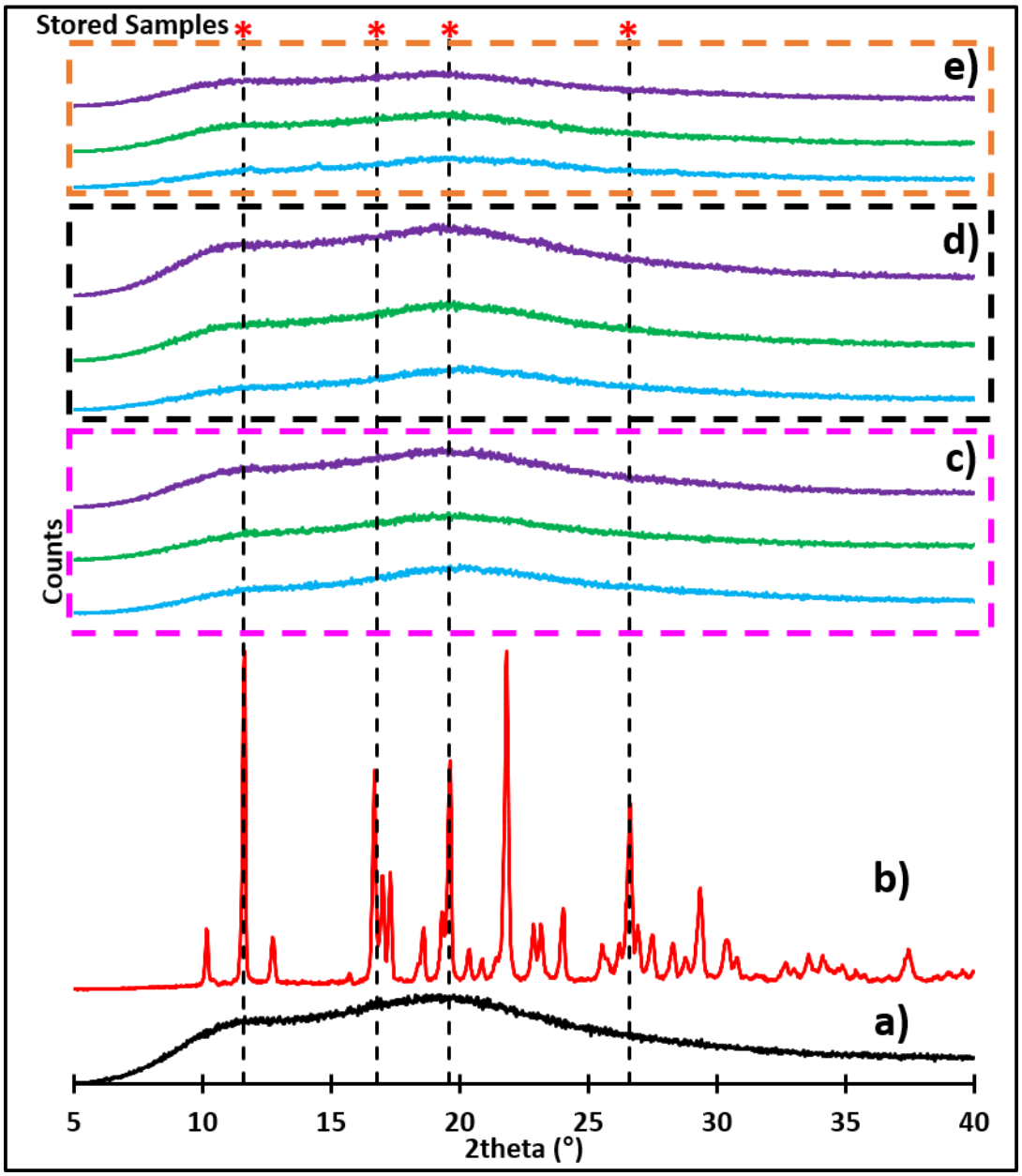

Figure 6-11 - XRPD spectra for all samples after 1 year of storage under ambient conditions. a) Soluplus, b) indomethacin, c) Pink Dashed Box – Spray Dried Samples, d) Black Dashed Box – Freeze Dried Samples and e) Orange Dashed Box – Homogenised Samples. Note: the black dashed lines with red stars indicate the characteristic peaks for the γ-polymorph of indomethacin.

6.6.1.3 Differential Scanning Calorimetry (DSC)

Similarly, to XRPD, DSC was employed to not only characterise the active ingredient INDO and the polymer SOL but also to determine if amorphous solid dispersions had been produced via the three manufacturing techniques.

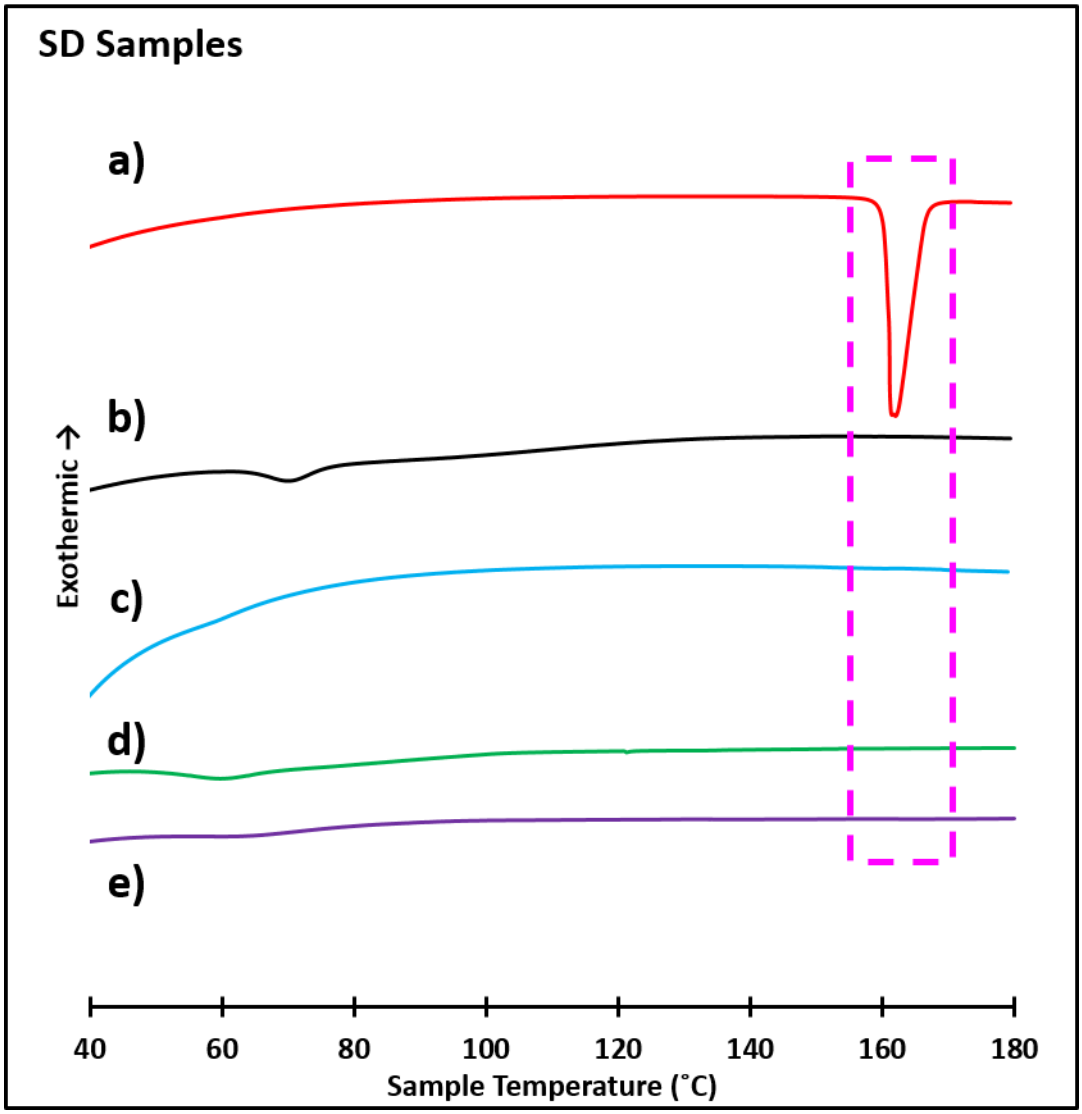

Figure 6-12 - DSC thermograms for the Spray Dried samples. a) indomethacin, b) Soluplus, c) 1:1 ratio, d) 1:3 ratio, e) 1:5 ratio. Note: The pink dashed box indicates the endothermic peak position for indomethacin and highlights the absence of this peak in the solid dispersions.

The active ingredient indomethacin displayed a sharp endothermic peak with a peak temperature of 161.98 °C. This corresponds to the melting point of INDO and also confirms the presence of the γ polymorph (Figure 6-12a). DSC also confirmed the amorphous nature of SOL. This was confirmed by the glass transition at approximately 70 °C (167). Figure 6-12c-e highlights that the indicative endothermic peak for INDO was absent from all the spray dried solid dispersions. This provides further evidence of the successful manufacture of amorphous solid dispersions. Interestingly, the glass transition for the SOL shifted to a lower temperature at the lower ratios of drug:polymer (1:1 - 58.82, 1:3 – 60.26, 1:5 - 63.61 °C).

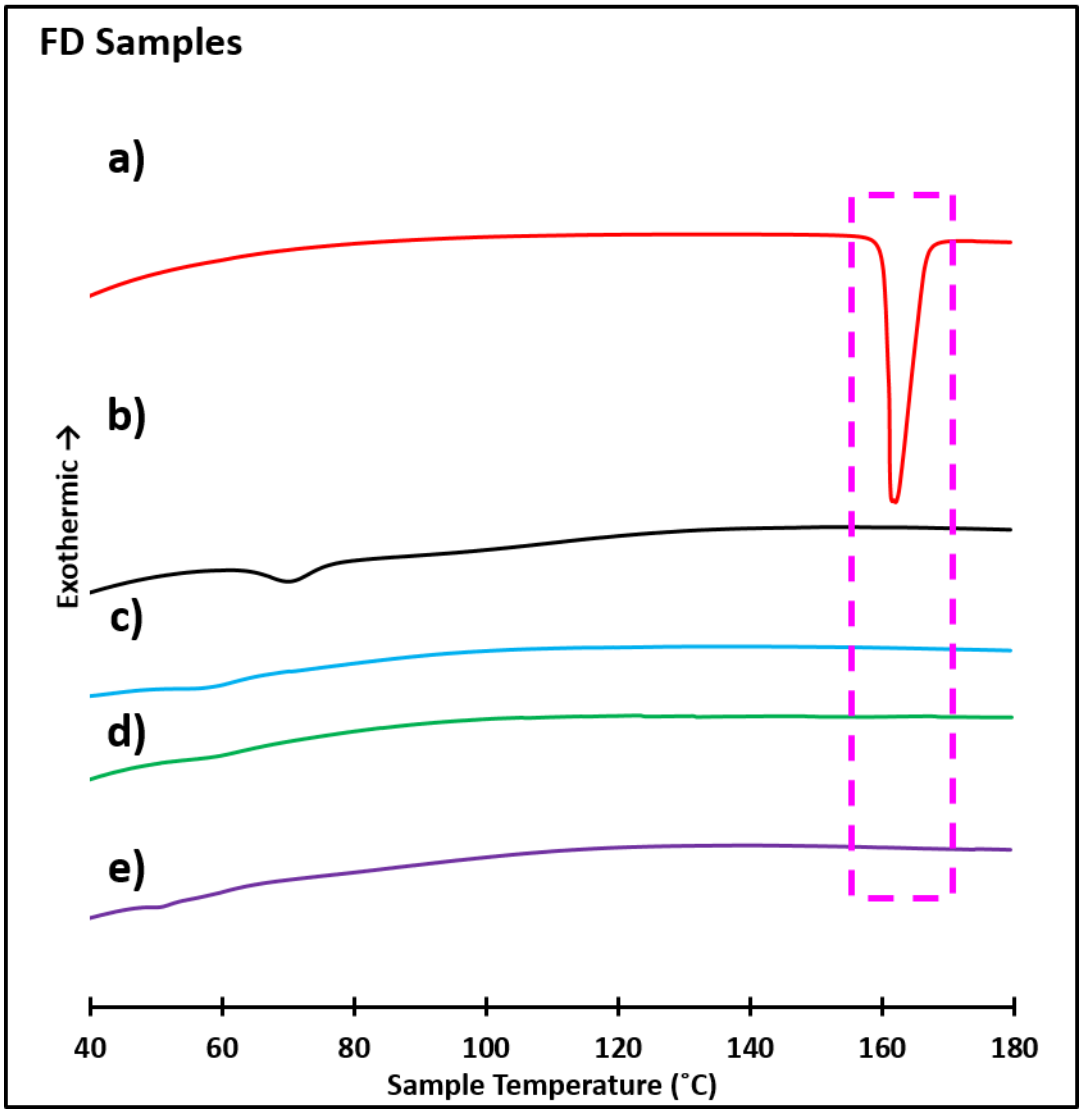

Figure 6-13 - DSC thermograms for the Freeze Dried samples. a) indomethacin, b) Soluplus, c) 1:1 ratio, d) 1:3 ratio, e) 1:5 ratio. Note: The pink dashed box indicates the endothermic peak position for indomethacin and highlights the absence of this peak in the solid dispersions.

Similarly, to the spray dried solid dispersions, the freeze dried solid dispersions also displayed an absence of the endothermic peak for INDO (Figure 6-13). However, with this manufacturing method the glass transition temperature for SOL decreased with an increasing drug:polymer ratio (1:1 – 60.82, 1:3 – 58.98, 1:5 – 50.61 °C). This highlights a potential difference between the two manufacturing techniques.

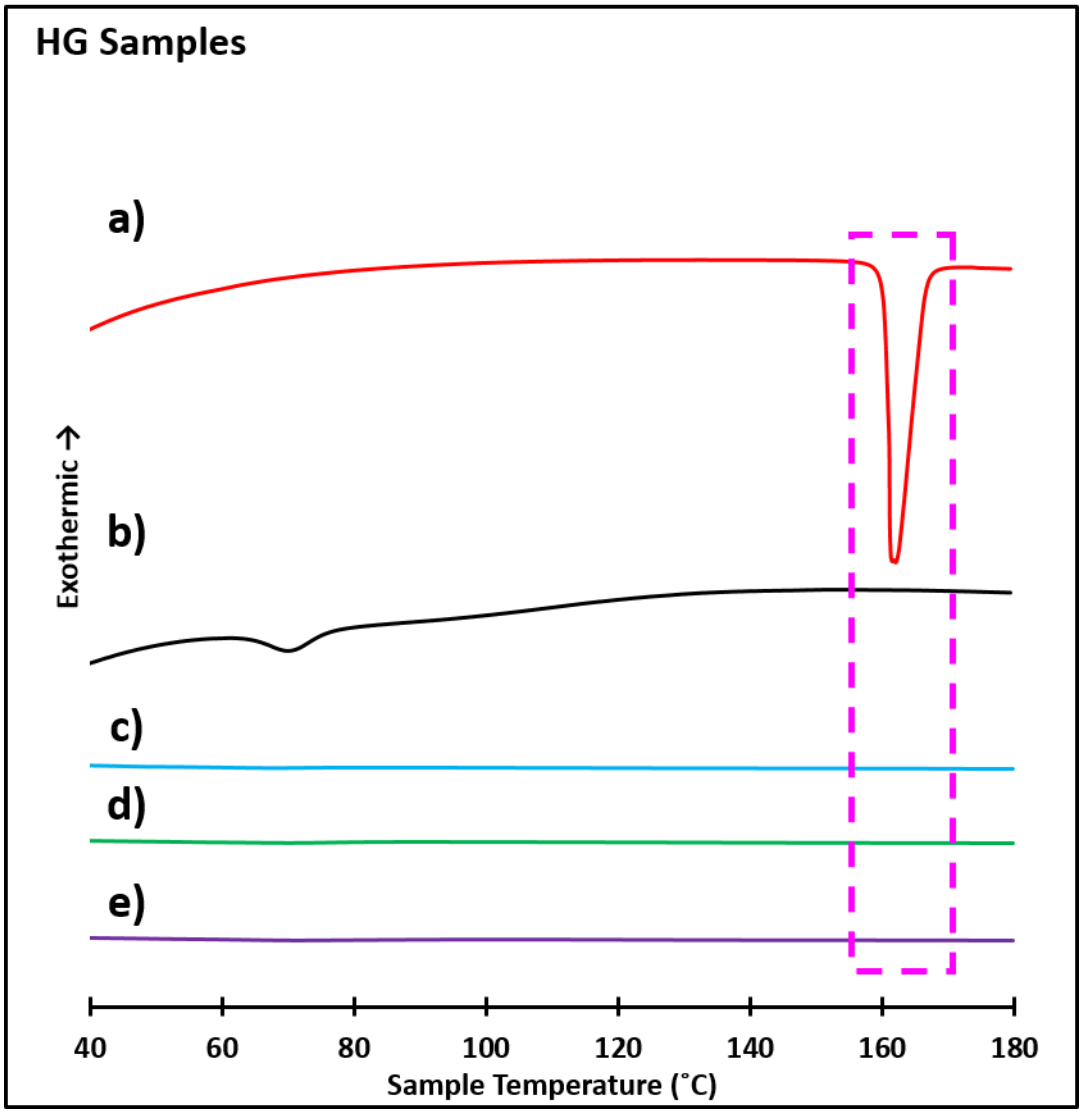

Figure 6-14 - DSC thermograms for the Homogenised samples. a) indomethacin, b) Soluplus, c) 1:1 ratio, d) 1:3 ratio, e) 1:5 ratio. Note: The pink dashed box indicates the endothermic peak position for indomethacin and highlights the absence of this peak in the solid dispersions.

The homogenised solid dispersions also showed an absence of the endothermic peak for INDO at each ratio (Figure 6-14). Despite, being manufactured under similar conditions to the freeze dried samples, the glass transition temperature for SOL showed a similar trend to the spray dried samples. Also, the HG samples displayed temperatures closer to the transition temperature of SOL (1:1 – 66.33, 1:3 – 67.15, 1:5 – 68.60 °C).

6.6.1.4 Isothermal Titration Calorimetry (ITC)

Note: Isothermal calorimetry was conducted by Dr. Ana-Maria Totea for this chapter.

Isothermal titration calorimetry is a highly sensitive analytical technique designed to understand the thermodynamic characteristics of binding reactions (168). In this chapter ITC was employed to determine if there were any significant binding reactions between the active ingredient INDO and the polymer SOL. This was an important determination to ensure that amorphous solid dispersions were manufactured, and that any significant dissolution behaviour was not as a result of a chemical reaction between the two components.

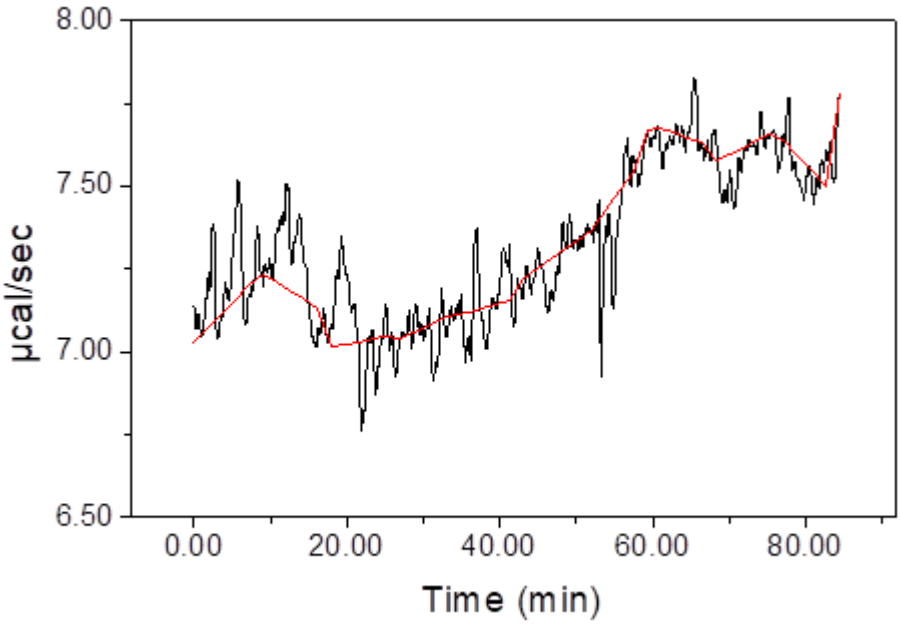

Figure 6-15 - A real time isotherm between indomethacin and Soluplus from ITC. The small spikes indicate no significant interaction between the two components.

The real time isotherm from the ITC is shown in Figure 6-15. Small heats were seen in the isotherm however, these were caused by the dilution of the solution during titration. Therefore, ITC suggested that no interaction occurred between the active ingredient INDO and SOL.

6.6.2 Dissolution Assessment

6.6.2.1 Compact Inspection

Following a similar methodology to that described in Chapter 5, the flow-through compact surfaces were assessed using the focus variation microscope. The microscope offered the ability to produce an optical image to assess for surface damage, whilst also providing a 3D representation of the surface to monitor surface roughness and and any increases in surface area as a result.

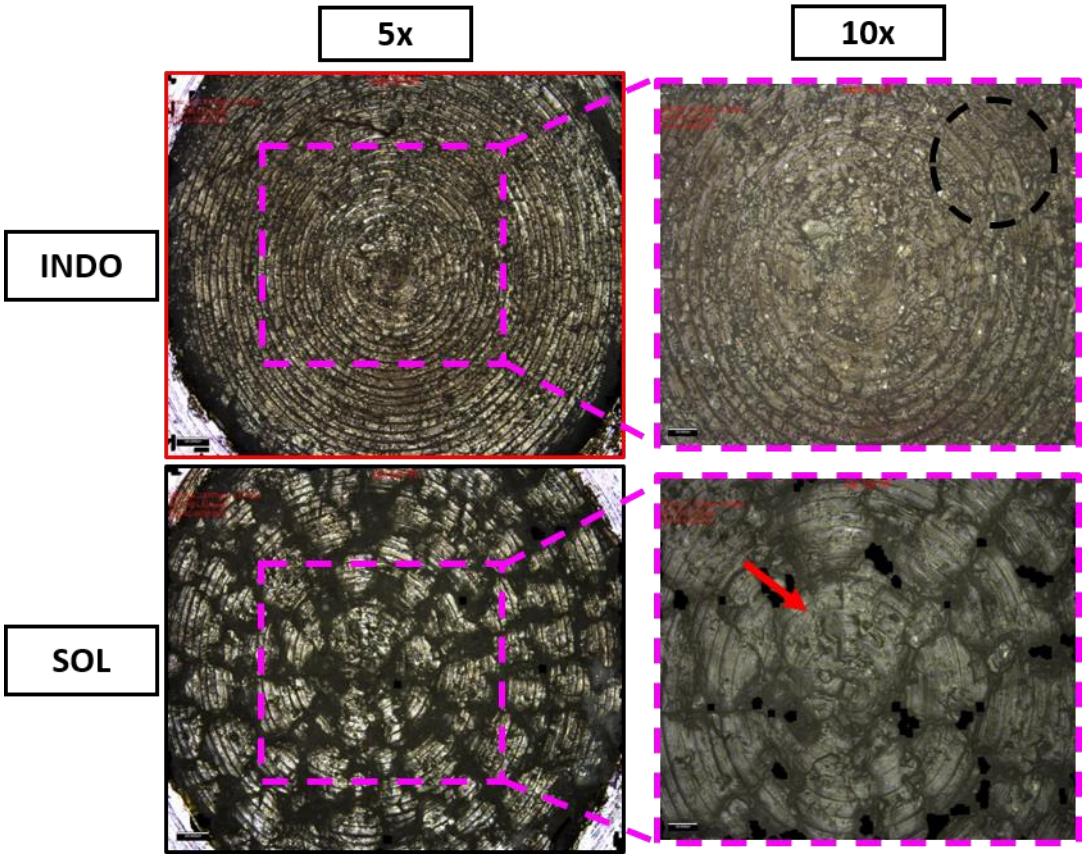

Figure 6-16 - Optical images of the compact surfaces of the active ingredient indomethacin and the polymer soluplus at 5x and 10x magnification. Note: The black dashed circles highlight surface damage, particulates and embossed texture. The red arrow indicates deep porosity on the surface.

Figure 6-16 displays optical microscopy of the compacts for the active ingredient INDO and the polymer SOL. INDO produced a relatively uniform surface however, there was significant evidence that the tooling had embossed a ring pattern on the surface potentially leading to surface area discrepencies. The SOL compact displayed significant porosity post compaction, this is likely to be as a result of the large spherical

particle size displayed in Figure 6-4. It is also possible that the 100 kgF used to produce the compacts was potentially too low to successfully crush or deform and compact the SOL particles.

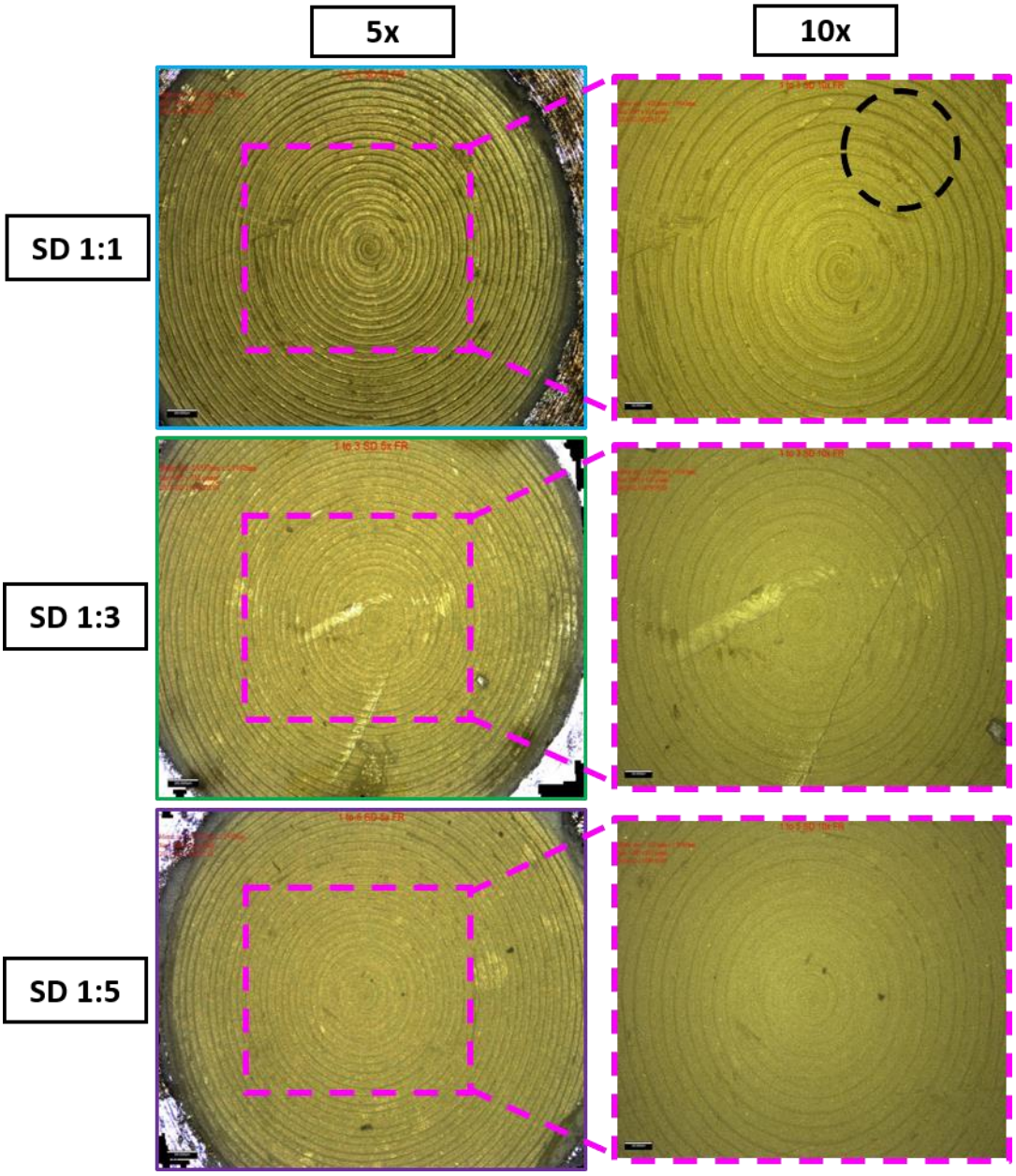

Figure 6-17 - Optical images of the compact surfaces of the Spray Dried Solid Dispersions at 5x and 10x magnification. Note: The black dashed circles highlight surface damage, particulates and embossed texture.

The spray dried solid dispersions are shown in Figure 6-17. It was evident that all 3 ratios of the spray dried solid dispersions produced a significantly more uniform surface than that of the base drug. This is an expected observation as spray dried particles are known to improve compactability of drugs due to their small spherical nature and low density (169). Interestingly, these compacts also picked up the ring pattern from the

tooling. However, the definition of this embossed pattern appeared to reduce with an increase in SOL content within each solid dispersion.

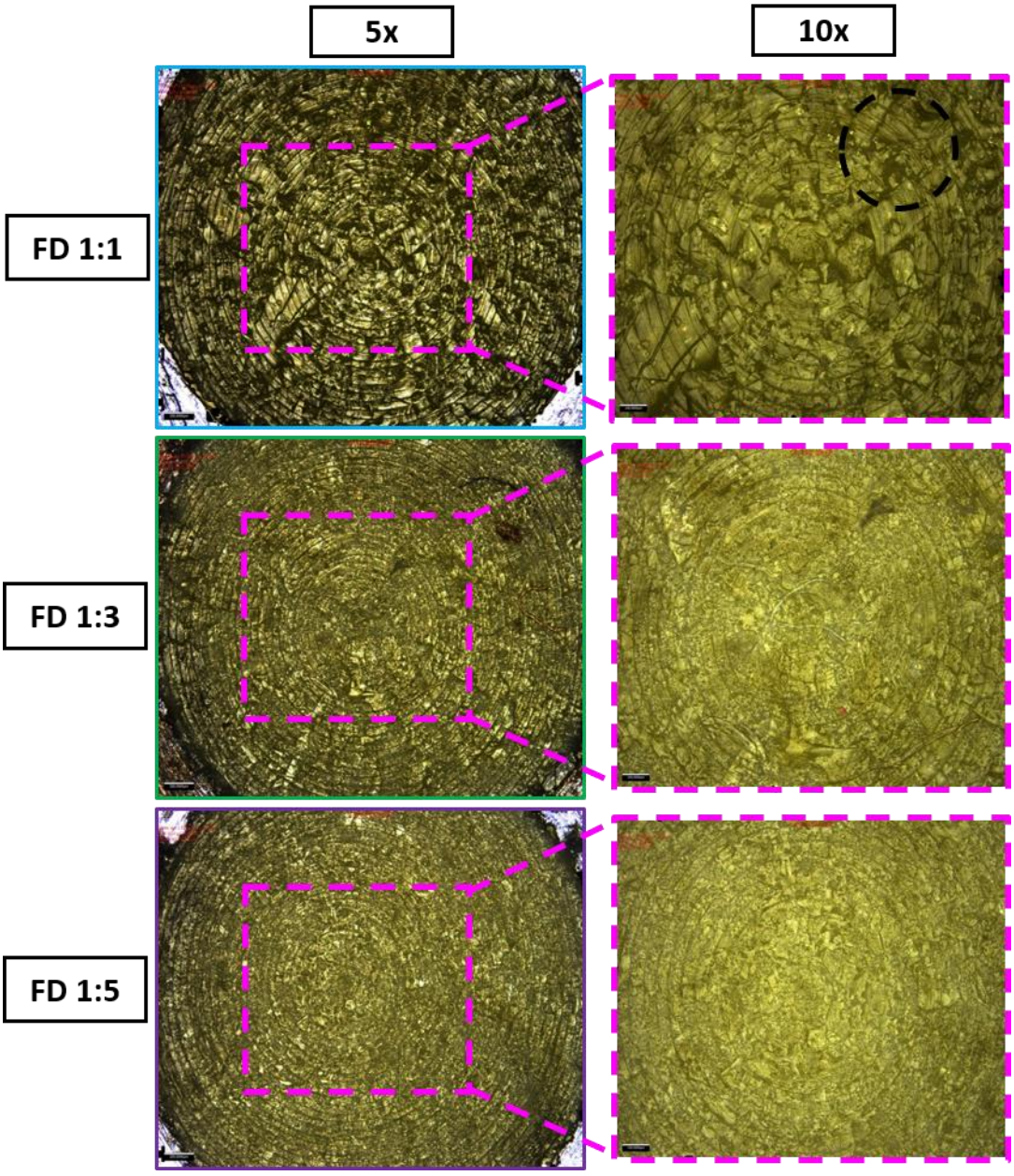

Figure 6-18 - Optical images of the compact surfaces of the Freeze Dried Solid Dispersions at 5x and 10x magnification. Note: The black dashed circles highlight surface damage, particulates, and embossed texture.

In a stark contrast to the spray dried solid dispersions, the freeze dried solid dispersions displayed a different surface texture (Figure 6-18). The variety in particle size and morphology of the freeze dried solid dispersions hilighted in Figure 6-6 led to a more textured compact surface. One similarity between the spray dried and freeze dried samples was the prescence of the ring pattern from the tooling which again also reduced in definition with the increase in soluplus content.

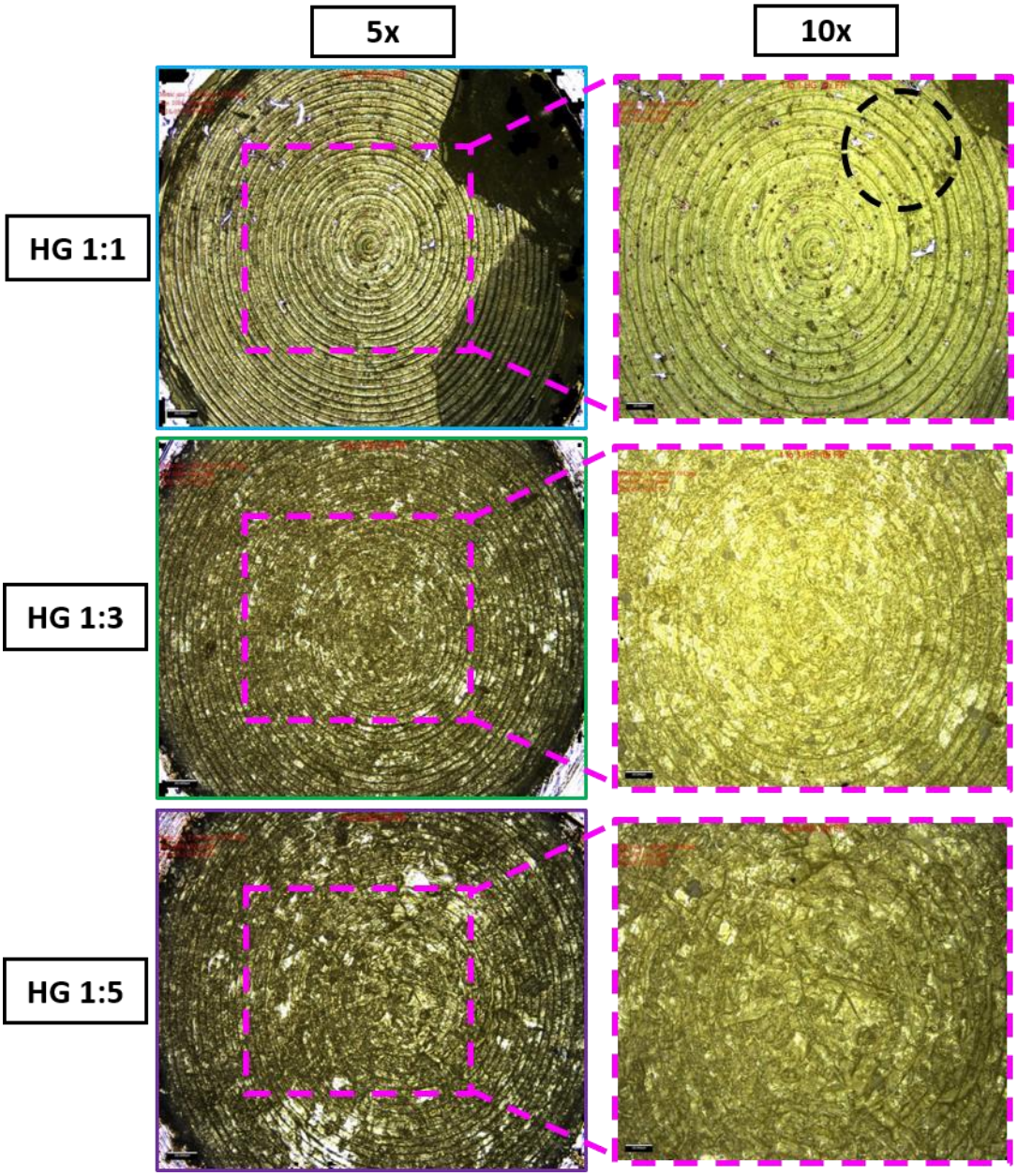

Figure 6-19 - Optical images of the compact surfaces of the Homogenised Solid Dispersions at 5x and 10x magnification. Note: The black dashed circles highlight surface damage, particulates and embossed texture.

Intrestingly, the homogenised samples (Figure 6-19) displayed a uniform compaction surface similar to the spray dried samples whilst also retaining some texture from the freeze drying process. This could be attributed to the complex nature of the material and the particles or particulates formed as indicated in Figure 6-7. In keeping with the other manufacturing processes, the homogenised samples also exhibited the embossed ring pattern from the tooling which again also reduced in definition with an increasing polymer content. The optical images obtained from the FV microscope provided an interesting visual assessment of the compacts formed from each

manufacturing process highlighting the influence of manufacture on compactability. Also, the microscope identified a potential flaw with the dissolution imaging IDR compaction tooling as in chapter 5. Again, the ring pattern was found to be from the base plate of the IDR compaction rig, which appeared to be machined and not polished. For this chapter, as the embossed pattern affected all IDR compacts it was determined to be a controlled variable. Figure 6-20 displays the 3D surface representations of the IDR compacts at the 10x magnification. Whilst the calculated surface parameters are shown in Table 6-3.

The parameters shown in Table 6-3 help to establish a few conclusions regarding the surface roughness of the compacts and the influence this has on the surface topography. As described previously in chapter 2, S*al* is a measure of the lateral scale of a surface. Therefore, it can be used as a confirmatory parameter to ensure that surface roughness has been considered during parameter calculation. All S*al* values reported in Table 6-3 are below 0.1 indicating that only surface roughness has been considered and that the analysis has been successful.

The next parameter *Str,* provides a measurement of the uniformity of the texture on the surface of the compacts. A value of greater than 0.5 indicates that the surface texture is uniform in all directions, whereas a value lower than 0.5 indicates that the texture is dominated by a significant direction. Only the 1:1 HG sample displayed a value lower than 0.5 (0.362) however upon further investigation of the images shown in Figure 6-20 it appeared that the stainless steel rim of the IDR compact may have had an influence of this calculation. All other surface displayed values above 0.5.

Table 6-3 - Surface parameters of pharmaceutical interest obtained from the 3D surface maps of the IDR compacts for the active ingredient, polymer and the solid dispersions (n=1).

Active Ingredient	Parameter			
	Sal (µm)	***Str***	***Sdr (%)***	***Smr2 (%)***
INDO	0.061	0.776	1.717	87.6
SOL	0.072	0.758	**26.699**	85
1:1 SD	0.066	0.846	0.785	89
1:3 SD	0.053	0.797	0.863	89.6
1:5 SD	0.066	0.918	0.715	89.5
1:1 FD	0.038	0.892	**16.23**	87.4
1:3 FD	0.063	0.675	5.749	89.7
1:5 FD	0.055	0.882	3.37	89.9
1:1 HG	0.063	0.362	**44.65**	84.9
1:3 HG	0.021	0.883	5.838	89.7
1:5 HG	0.026	0.804	9.138	87

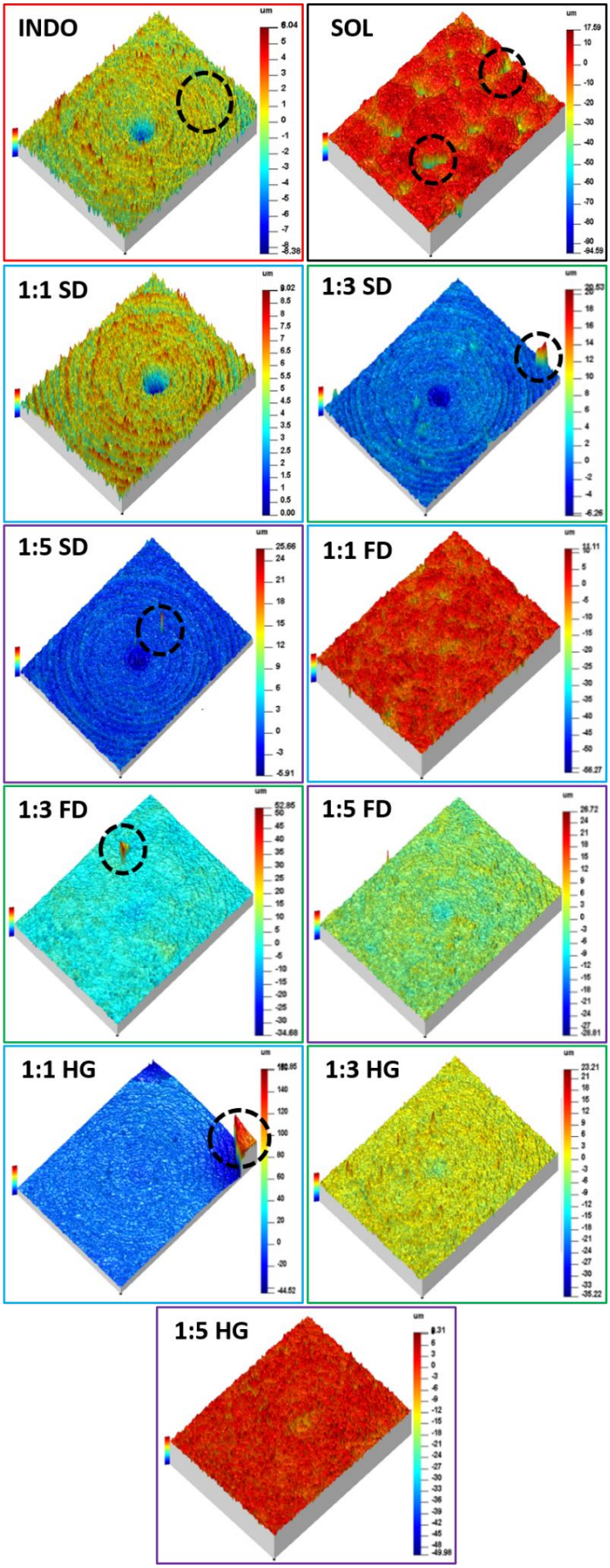

Figure 6-20 - 3D representations of the compacts using Surfstand™ including INDO, SOL and the three manufacturing techniques. Images shown from the 10x magnification. The black dashed circles highlight the roughness caused by particulates and the embossed circular pattern.

Sdr provides an indication as to the additional surface area gained by a surface as a result of its texture when compared to a theoretical plane of the same size. The Spray dried samples displayed the lowest S*dr* values of all surfaces tested even lower than the active ingredient INDO thus supporting the theory of a smoother more uniform surface post compaction of spray dried particles. The homogenised samples displayed the higher S*dr* values of all three manufacturing techniques likely due to the complexity of their morphology. It is important to state that the S*dr* value for the 1:1 ratio (44.65 %) is likely to be due to the presence of the stainless steel rim in the analysis field. A further observation is that the SOL compacts displayed a S*dr* value 26.699%. This is likely to be an accurate result due to the nature of the deep valleys present in the data set indicated in Figure 6-20.

S*mr2* provides an indication of the percentage of the surface comprised of deeper valleys. Interestingly, the SOL surface displayed the lowest S*mr2* value of 85 % indicating a potential surface porosity of 15 % which is likely to be due to the large particle size of the material and the porous surface produced post compaction.

6.6.2.2 Flow-through assessment

The flow through set-up of the SDI2 instrument is used to calculate intrinsic dissolution rate on active pharmaceutical ingredients. However, due to the presence of the polymer in the solid dispersions, any IDR calculation determined by the system does not strictly follow the definition of IDR. For the purpose of this work these are hence referred to as a pseudo-IDR measurement.

For the determination of the average value, the first five points of the dissolution profile were excluded, this is highlighted by the pink dashed box present on the pseudo-IDR profiles in the following figures. Due to the flow through nature of the dissolution imaging system, it is important that IDR is measured once the dissolution rate has reached equilibrium with the media flowing over the compact surface. From visual

assessment of the dissolution profiles this was determined to be from the five min time point just as in chapter 5. IDR was also calculated using the equations described in Chapter 5.

Table 6-4 – Average pseudo- IDR values (mean +/- SD) (n=3) for the active ingredient and the solid dispersions. The average value excludes the first five time points (n=25). The yellow highlighting indicates the formulations with a higher pseudo-IDR than the base drug.

Active Ingredient	Average IDR and pseudo-IDR (µg/min/cm^2)
INDO	58.84±2.63
1:1 SD	24.25±0.94
1:3 SD	31.84±8.77
1:5 SD	18.72±3.62
1:1 FD	73.67±1.64
1:3 FD	36.98±2.84
1:5 FD	16.68±0.37
1:1 HG	68.75±5.73
1:3 HG	31.61±5.86
1:5 HG	32.30±3.26

All IDR values were calculated from the use of the molar extinction coefficient value (9590.5 $M^{-1}cm^{-1}$) obtained from the INDO calibration curve described in section 6.5.2.3. The active ingredient INDO displayed an average IDR of 58.84 µg/min/cm^2 (Table 6-4). This was supported by UV images showing a low absorbance between 500 and 800 mAu (Figure 6-21). INDO also produced a consistent IDR profile with a low standard deviation (Figure 6-22).

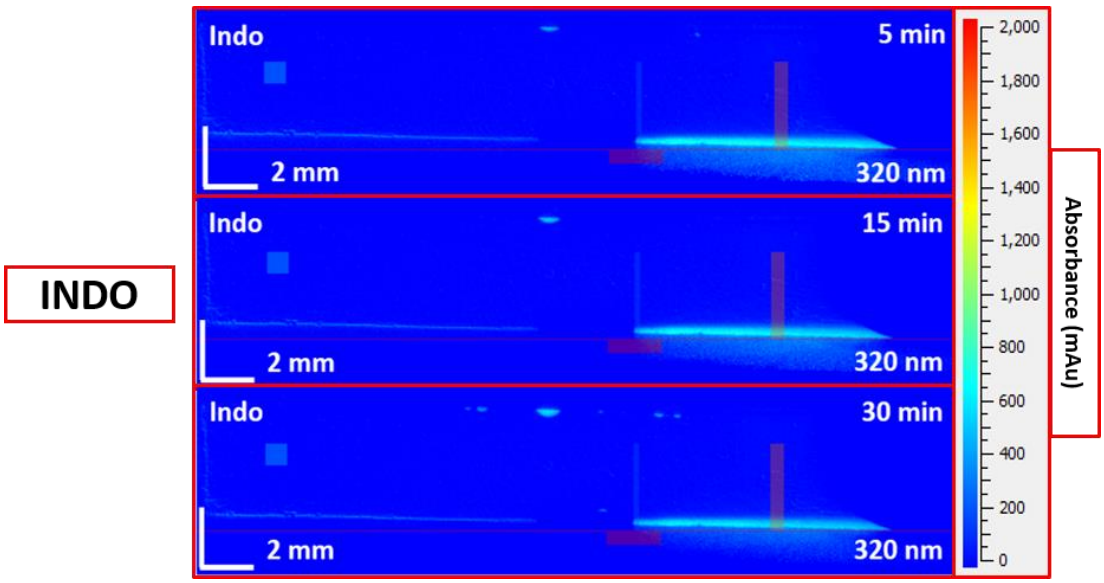

Figure 6-21 - UV images from the IDR assessment of the active ingredient INDO at 320 nm.

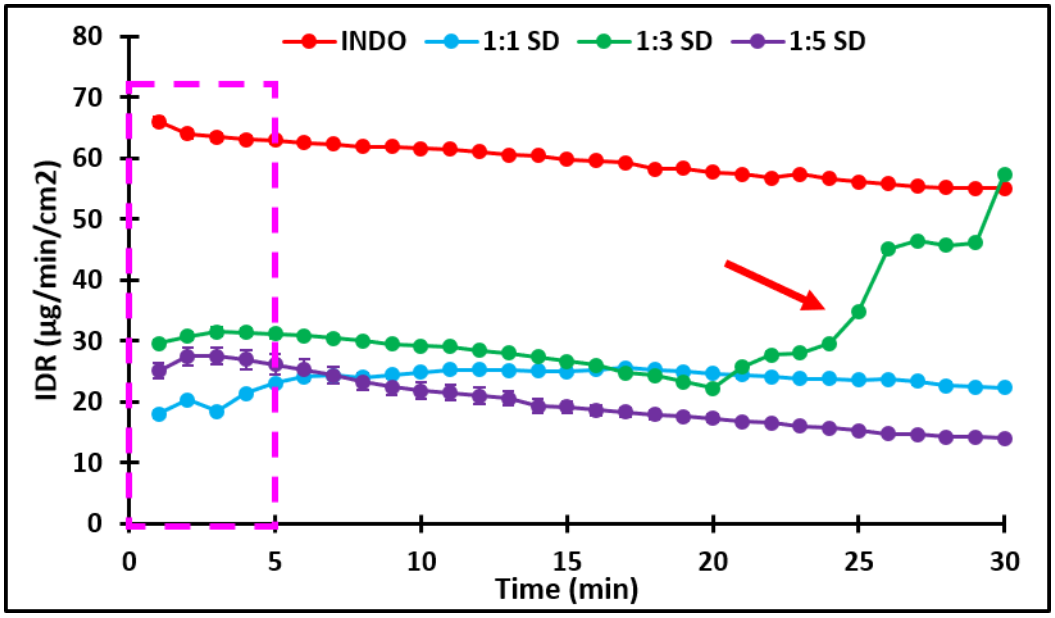

Figure 6-22 – Average Dissolution profiles (mean +/- SD) (n=3) from the SDi2 system of the active ingredient indomethacin and the spray dried solid dispersions. Note: The pink dashed box highlights the first five minutes of data excluded from Average IDR calculation. The red arrow highlights the effects on the dissolution profile of the unexpected dissolution behaviour seen in the UV images.

Table 6-4 highlights that all the spray dried formulations displayed pseudo-IDR values lower than the base drug. This is also further supported by the dissolution profiles in Figure 6-22 which show all three profiles below that of the active ingredient indomethacin. Interestingly, the 1:3 ratio appeared to increase in IDR from the 20 minute time point onwards. Upon review of the UV images in Figure 6-23, it became clear that the 1:3 ratio experienced a web-like phenomenon above the surface of the IDR compact.

It is there for likely that particulates and excess drug may have broken free and passed through the IDR detection zone leading to an inflated IDR reading. Despite this behaviour, the poor performance of the spray dried solid dispersions may be attributed to the increased compactability of the powder. The optical images in Figure 6-17 show very little surface porosity post compaction at 100 kgf and this may have led to reduced wettability and as a consequence poorer dissolution rate.

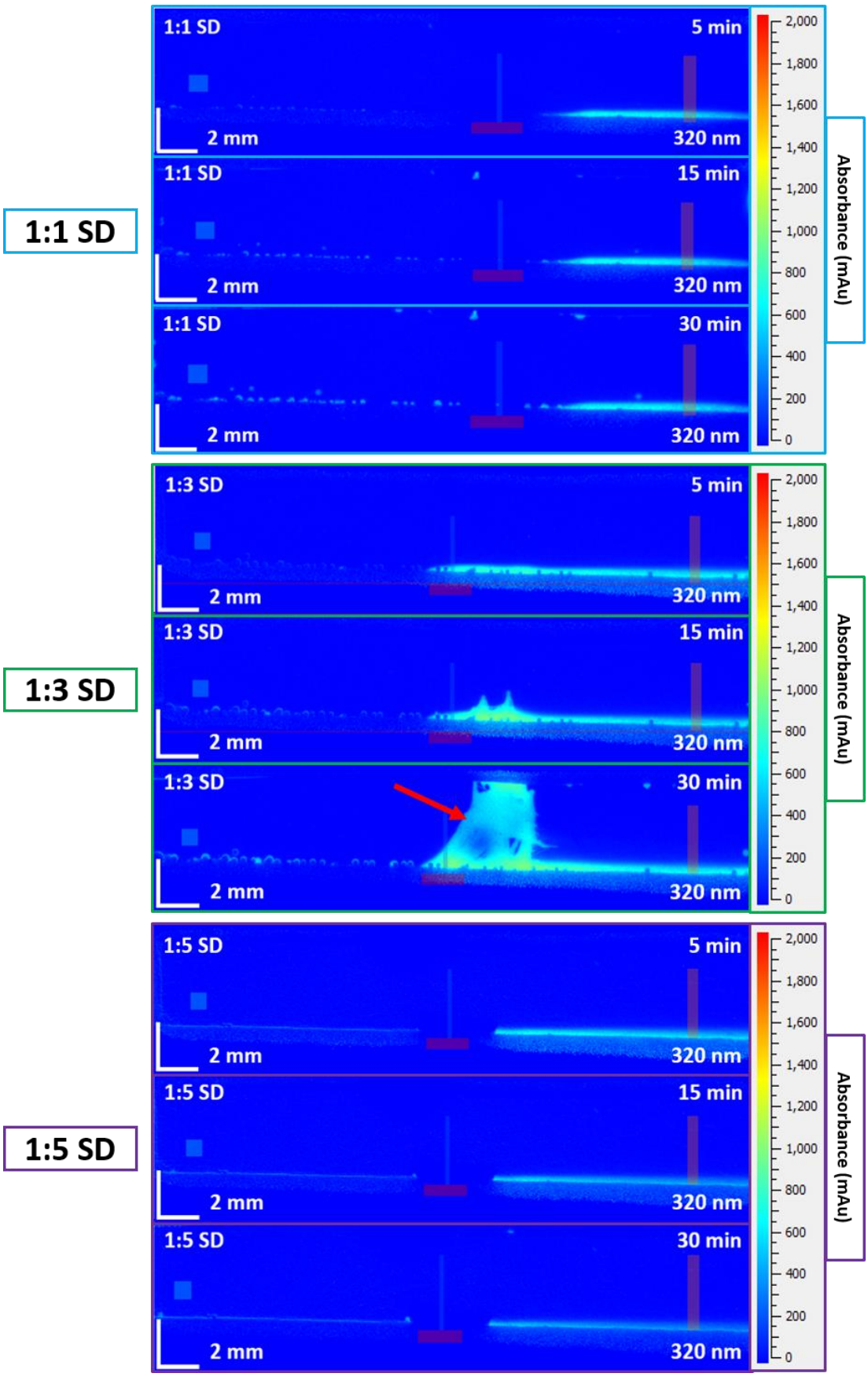

Figure 6-23 - UV images from the pseudo-IDR assessment of the spray dried solid dispersions at the ratios of 1:1, 1:3 and 1:5. Note: the red arrow indicates unexpected dissolution behaviour from the compact.

Table 6-4 also shows that only the 1:1 ratio of the freeze dried solid dispersions exhibited an pseudo-IDR value greater than the base drug at 73.67 µg/min/cm^2 this can be seen in the dissolution profiles in Figure 6-24 and in the UV images which highlight a stronger absorbance reading for the 1:1 ratio at approximately 1000 mAu. The other two ratios also highlighted a decrease in performance with an increase in polymer content. This could indicate that when utilising freeze drying as a manufacturing technique the 1:1 ratio is optimal. Upon review of the dissolution images indicated in Figure 6-26, it appeared that the web-like dissolution behaviour also occurred with the 1:3 and 1:5 ratios and may potentially have inhibited dissolution of INDO from the solid dispersion matrix.

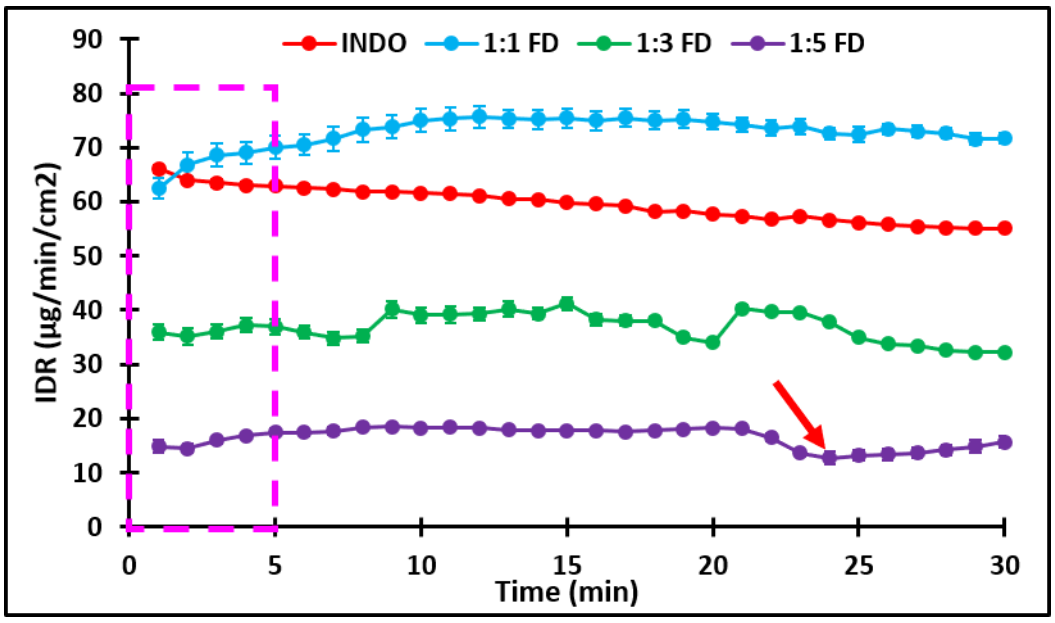

Figure 6-24 - Average Dissolution profiles (mean +/- SD) (n=3) from the SDi2 system of the active ingredient indomethacin and the freeze dried solid dispersions. Note: The pink dashed box highlights the first five minutes of data excluded from Average IDR calculation. The red arrow highlights the effects on the dissolution profile of the unexpected dissolution behaviour seen in the UV images.

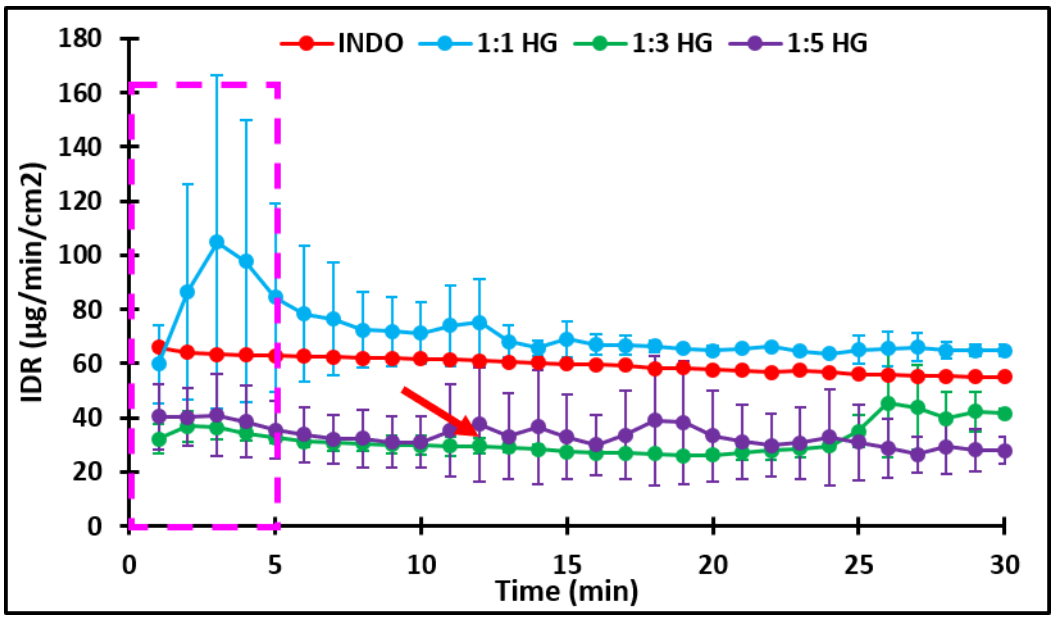

Figure 6-25 - Average Dissolution profiles (mean +/- SD) (n=3) from the SDi2 system of the active ingredient indomethacin and the homogenised solid dispersions. Note: The pink dashed box highlights the first five minutes of data excluded from Average IDR calculation. The red arrow highlights the effects on the dissolution profile of the unexpected dissolution behaviour seen in the UV images.

The homogenised samples showed very similar conclusions to the freeze dried samples which can be expected as both samples are exposed to the same freeze drying conditions. The 1:1 ratio for the homogenised samples, produced an pseudo-IDR value greater than that of the bulk drug indomethacin at 68.75 µg/min/cm^2 (Table 6-4). This was supported by the intense absorbance reading in the UV images in Figure 6-27 and the dissolution profile in Figure 6-25. Again, the 1:3 and 1:5 ratios showed a significantly poorer pseudo-IDR and in a similar fashion to the other manufactured samples these also showed the web-like behaviour within the flow cell. As this trend was witnessed with all manufacturing techniques it was therefore important to conduct further assessments on both the drug and polymer to ensure there was no interaction or contamination within the bulk powders and the resulting solid dispersions.

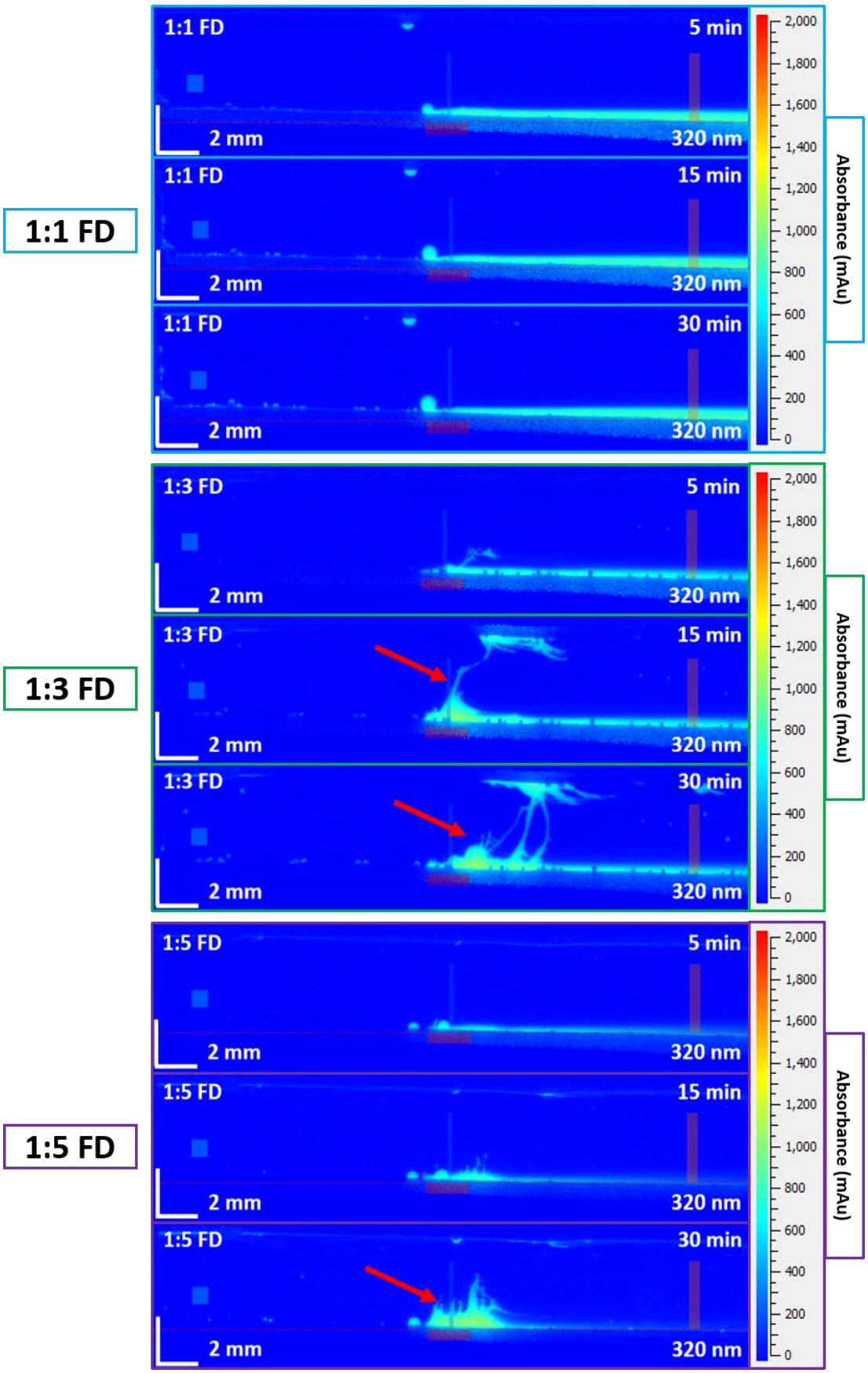

Figure 6-26 - UV images from the pseudo-IDR assessment of the freeze dried solid dispersions at the ratios of 1:1, 1:3 and 1:5. Note: the red arrow indicates unexpected dissolution behaviour from the compact.

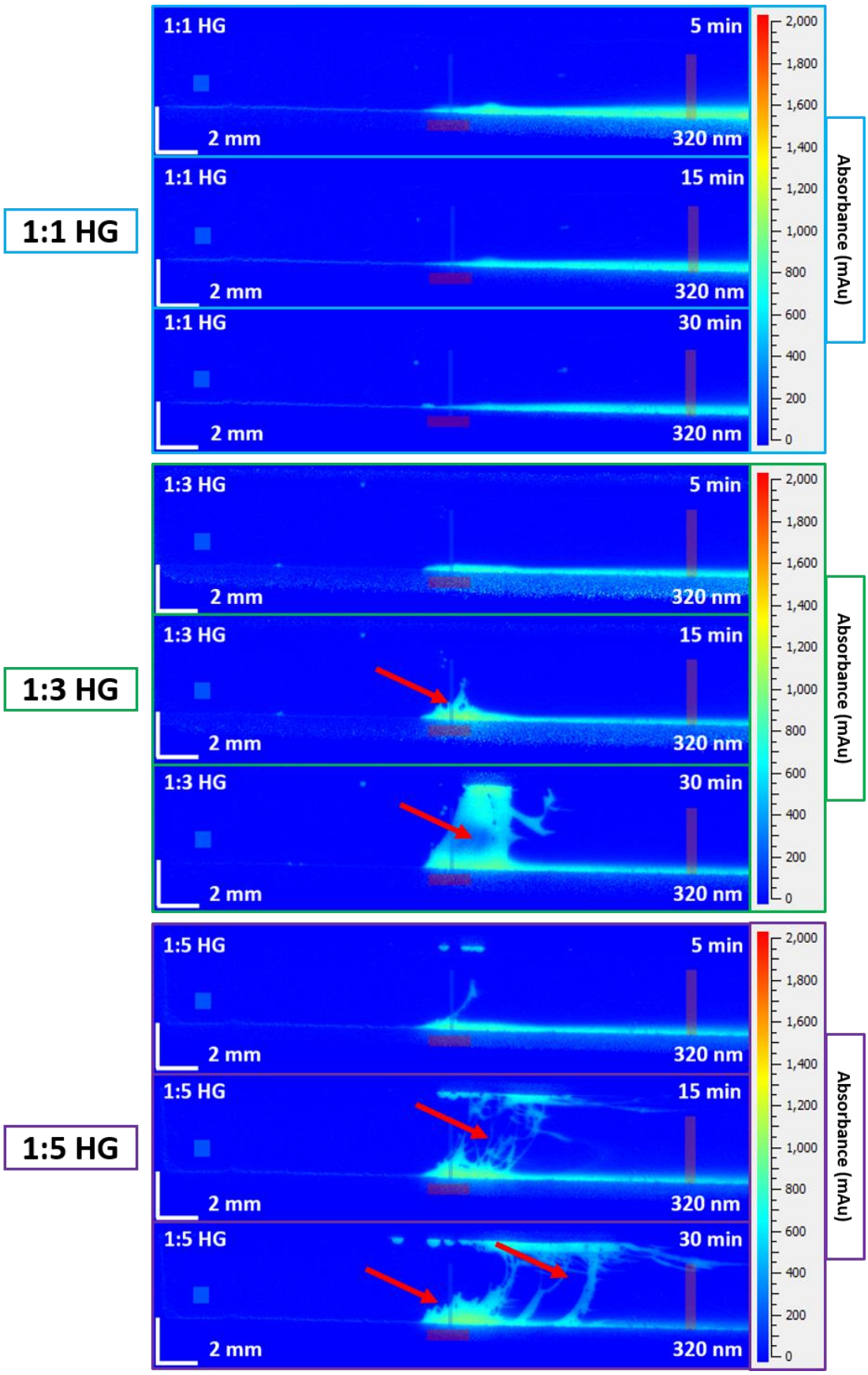

Figure 6-27 - UV images from the pseudo-IDR assessment of the homogenised solid dispersions at the ratios of 1:1, 1:3 and 1:5. Note: the red arrow indicates unexpected dissolution behaviour from the compact.

6.6.2.3 IDR assessment – Web-like behaviour investigation

In this investigation, UV imaging proved vital in detecting the web-like behaviour (Figure 6-28) between different batches of solid dispersion and different manufacturing techniques and also highlighted the use of the system for quality control and batch to batch testing.

To understand what caused this behaviour, a number of questions were posed:

- Interactions – Was there an interaction between INDO and SOL at the higher ratios (not investigated by the ITC technique)?
- Polymorphism – Did INDO undergo a polymorphic change when exposed to the dissolution media?
- Manufacturing – Did remanufacturing the polymer or drug alter their chemistry?

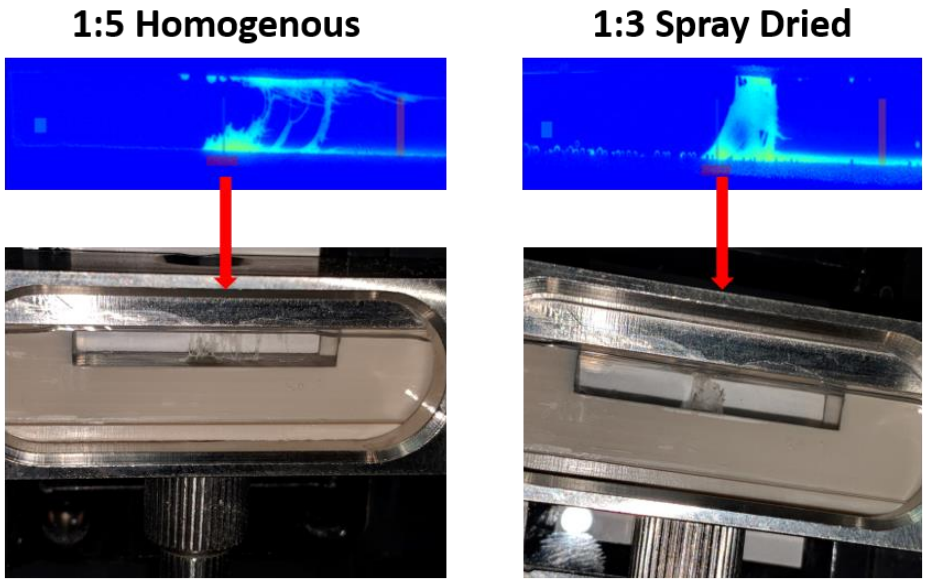

Figure 6-28 - Example Web-like behaviour during IDR testing of the amorphous solid dispersions.

The first step in this study was to take some INDO and SOL and remanufacture them separately via spray drying and freeze drying. The aim of this was to indicate if remanufacturing led to the web-like behaviour during dissolution process. Also, physical mixtures of the bulk INDO and SOL were formulated to indicate drug

interaction during wetting and dissolution. It is important to note ITC had indicated that drug-polymer interaction was unlikely to have occurred (section 6.6.1.4).

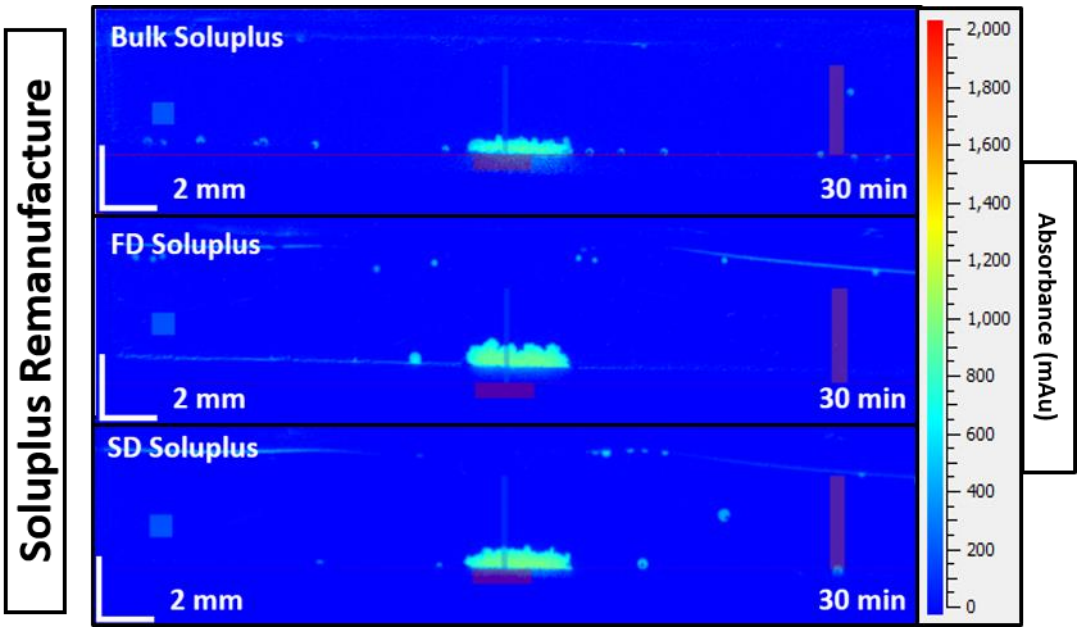

Figure 6-29 - UV images taken from the SDi2 system for the remanufactured Soluplus powders at the 30 minute time point. Note: The soluplus was exposed to same conditions and dissolution media as the solid dispersions.

Figure 6-29 displays the UV images taken from the dissolution imaging system at the 30 min time point. It was clear from this assessment that whilst wetting and hydration did occur at the compact surface there was no clear evidence of the web like behaviour observed in the solid dispersions. This provided an indication that the manufacturing process had no significant impact on the chemistry of SOL and thus its behaviour.

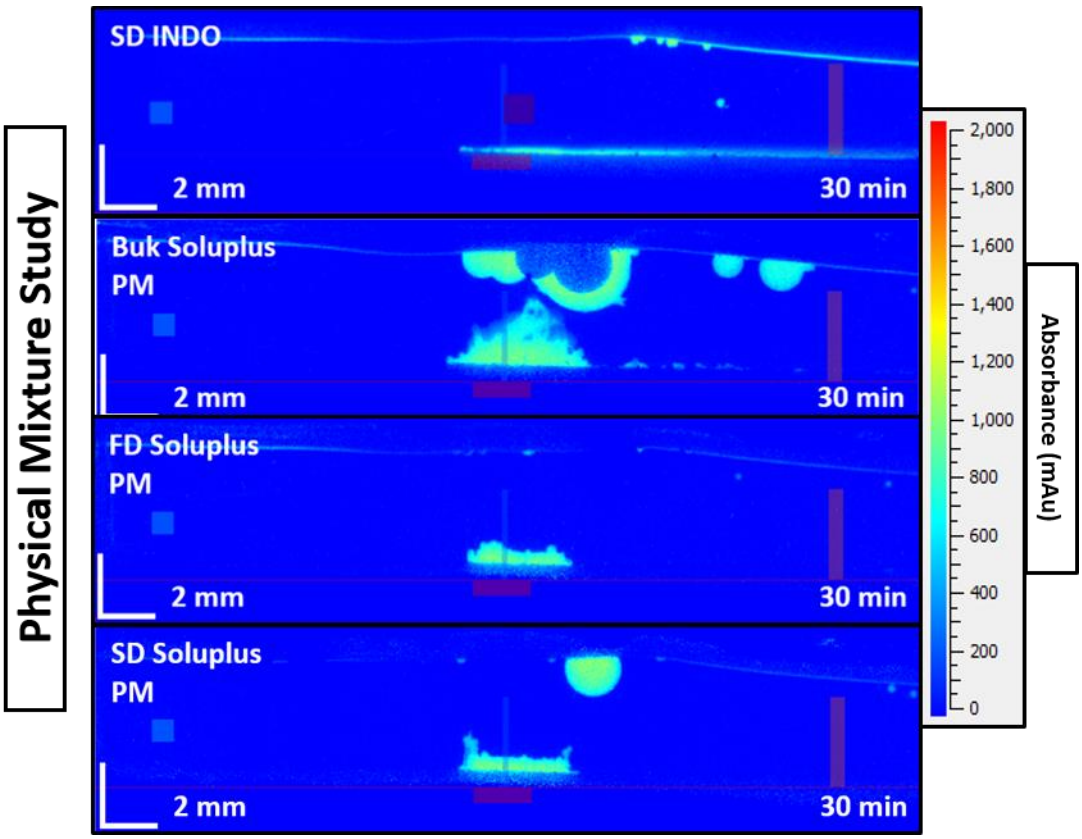

Figure 6-30 - UV images taken from the SDi2 system for the remanufactured Soluplus powders in a physical mixture with the bulk indomethacin. This figure also displays the dissolution images of spray dried indomethacin at the 30 minute time point. Note: all samples were exposed to the same conditions and dissolution media as the solid dispersions.

Figure 6-30 displays some of the UV images taken from the assessment of the physical mixtures alongside the spray dried INDO. The physical mixtures were manufactured to the 1:1 ratio and blended for 10 min using a Turbula™ mixer (Willy. A Bachofen, Switzerland) to ensure blend uniformity. Again, the UV images showed hydration but not the web like behaviour seen with the solid dispersions. This combined with ITC ruled out chemical interactions. Also, the spray dried INDO showed no signs of the web like behaviour either thus effectively ruling out the manufacturing process as a cause for the behaviour. The final step was to perform XRPD on the samples post dissolution to check for polymorphism and/or recrystallization from the polymer matrix.

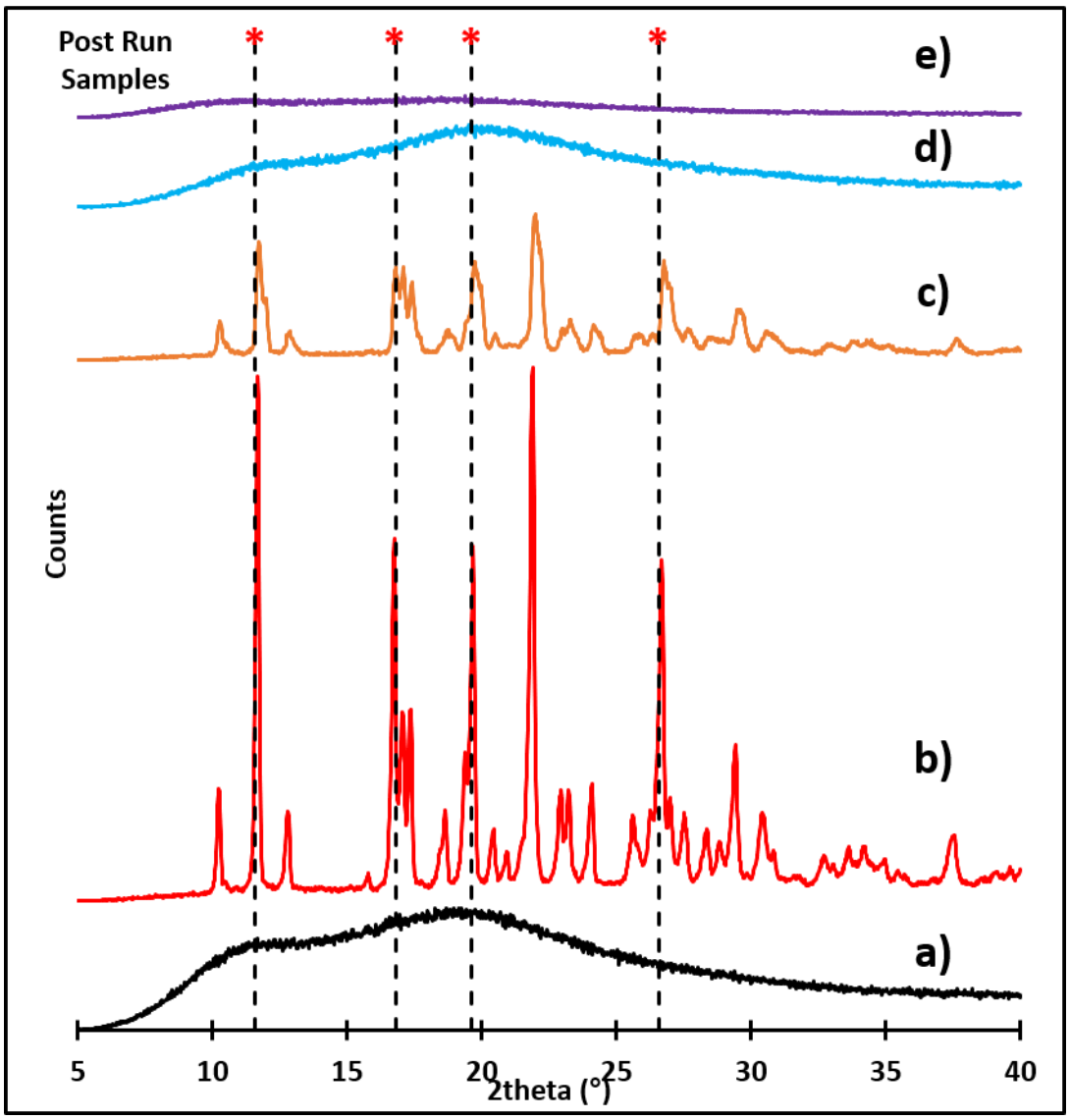

Figure 6-31 - XRPD spectra for the bulk and post run samples. a) Bulk Soluplus, b) Bulk indomethacin, c) Post run Bulk indomethacin, d) 1:1 Spray Dried e) Post run 1:1 Spray Dried. Note: the black dashed lines with red stars indicate the characteristic peaks for the γ-polymorph of indomethacin.

The XRPD assessment of the post run samples was also conclusive (Figure 6-31). Whilst the intensity of the post run INDO sample was less than that of the bulk powder, it still contained the characteristic peaks for the γ-polymorph. This indicated that during dissolution the INDO did not change polymorphic form. XRPD was also employed to ensure that the solid dispersion retained its amorphous nature post dissolution. This was also found to be the case thereby ruling out recrystallisation as a potential cause for the web-like behaviour. With these additional tests it became clear and apparent that the behaviour was inherent to the solid dispersions themselves, however it did not answer why the solid dispersions containing the greater amount of SOL expressed this

behaviour more explicitly. After a further review of literature, an article by Salawi and Nazzal provided a potential answer. In the article the authors investigated the influence of concentration of SOL on the rheological properties of vitamin E composites. The authors discovered that an increase in polymer content led to the formation of a tacky and highly adhesive material with high viscosity (170). It is therefore likely that in the solid dispersions containing a higher concentration of SOL, a similar tacky substance formed and due to the low flow nature of the flow cell, it caused the SOL to form the web-like structures that stuck to the inside of the flow cell. This was an important discovery. Without UV imaging, it is unlikely that this behaviour would have been discovered via the conventional dissolution testing methods.

6.6.2.4 Whole Dosage Dissolution assessment

This section demonstrates the capability of the dissolution imaging system to record and measure dissolution phenomena from a whole dosage form. In this instance a custom wire holder was designed to hold a hard gelatin capsule in vertical orientation containing 2.5 mg of INDO or active equivalent. All capsules were monitored over a 60 min period using the 320 and 520 nm LED's simultaneously.

Figure 6-32 displays UV images taken from the bulk INDO at 320 nm. It is evident from the images that upon capsule dissolution at 5 min, there was very little UV absorbance indicating poor dissolution. This was further supported by a low concentration of 1.62 ± 0.001 µg/mL and an AUC value of 99.12 (Table 6-5).

Unlike in the pseudo-IDR assessment in 6.6.2.2, all three spray dried solid dispersions displayed a greater dissolution performance than the base drug INDO. This provided further evidence that the compaction force used to manufacture the compacts in the flow-through assessment may have resulted in over compaction of the spray-dried bulk powder. This could have led to a reduction in compact porosity and thus inhibited the dissolution performance of the spray dried solid dispersions.

Table 6-5 - A table displaying the average concentration (mean +/- SD) (n=3) over the 60 minute period for INDO and its solid dispersions. The table also displays associated AUC measurements.

Active Ingredient	Average Conc. (µg/mL)	AUC
INDO	1.62 ± 0.001	99.12
1:1SD	5.42 ± 1.12	330.28
1:3 SD	6.62 ± 2.3	403.62
1:5 SD	3.53 ± 1.45	214.10
1:1 FD	4.78 ± 1.82	291.07
1:3 FD	5.04 ± 0.94	307.28
1:5 FD	4.73 ± 2.08	286.55
1:1 HG	6.07 ± 2.45	370.23
1:3 HG	5.00 ± 1.08	305.05
1:5 HG	3.79 ± 1.01	230.60

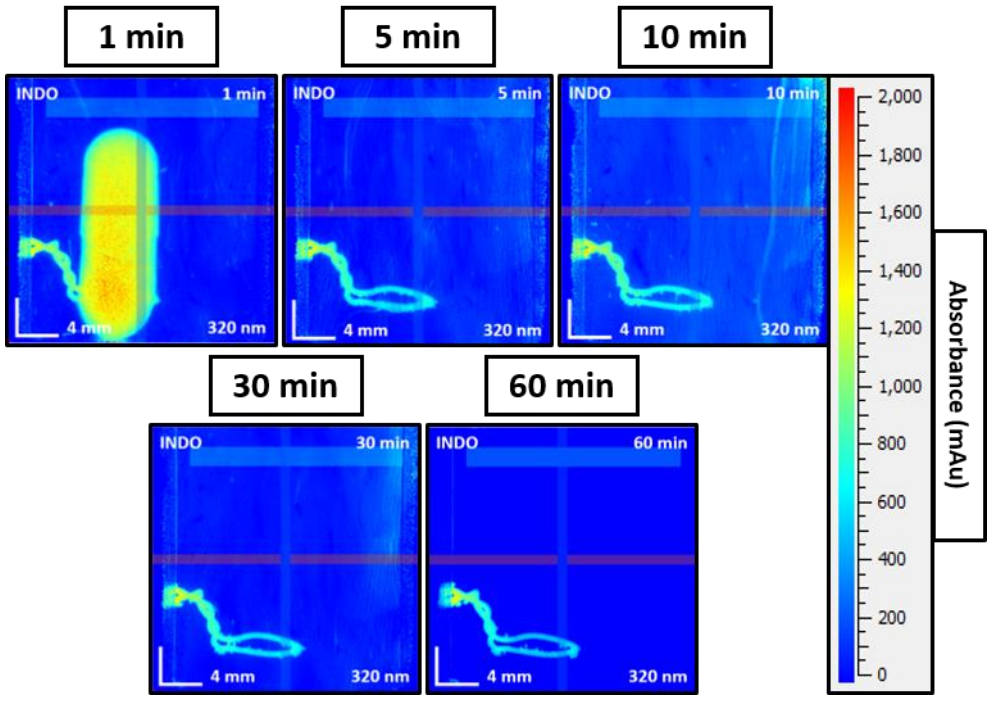

Figure 6-32 - UV images from the whole dosage assessment of indomethacin at 320 nm.

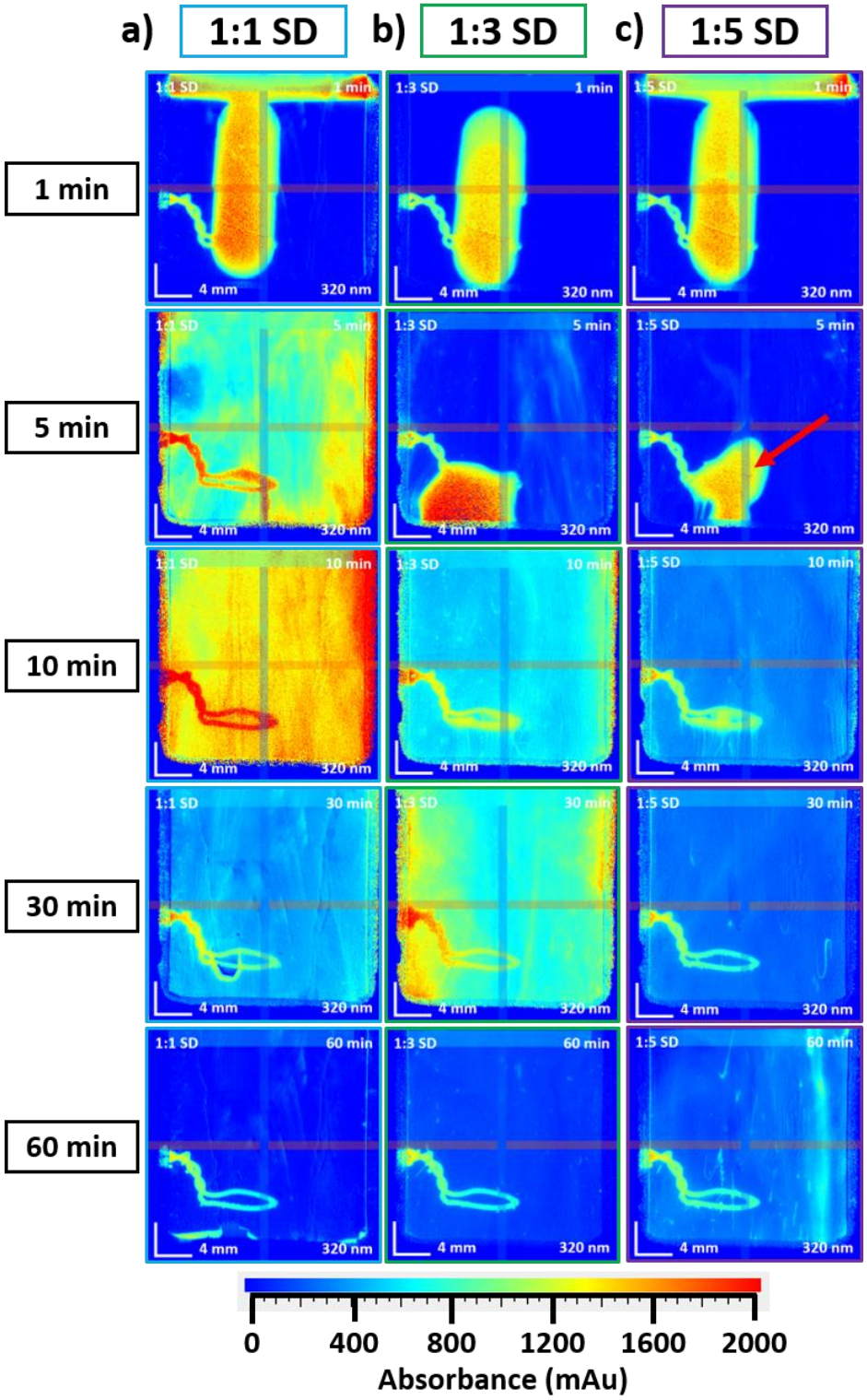

Figure 6-33 - UV images from the whole dosage assessment of the spray dried solid dispersions at all three ratios manufactured. Note: The red arrow indicates gel formation of the solid dispersion.

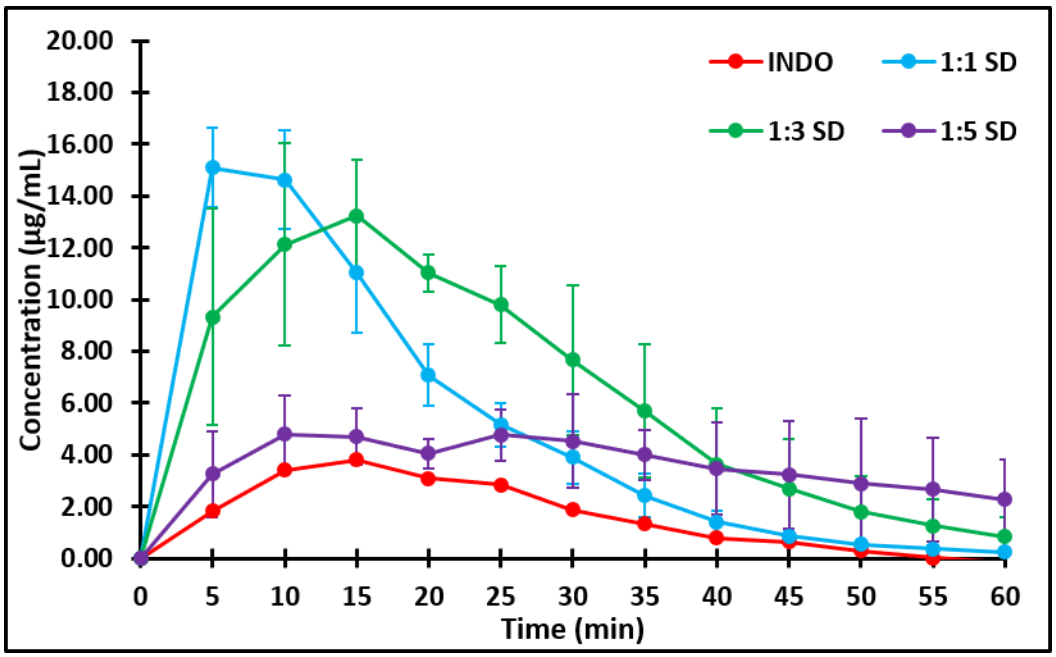

Figure 6-34 – Average Dissolution profiles (mean +/- SD) (n=3) from the whole dosage assessment of the spray dried solid dispersions including the bulk drug indomethacin.

The UV images in Figure 6-33 show three different behaviours for the spray dried solid dispersions. The 1 to 1 ratio appeared to have an initial rapid dissolution upon capsule disintegration at the 5 min time point before rapidly decreasing over the course of the experiment. This gave the 1 to 1 ratio an average concentration of 5.42 ± 1.12 µg/mL. In complete contrast to the 1 to 1 ratio, the 1 to 5 ratio produced a more controlled drug release rate from the capsule. This produced an average concentration of 3.53 ± 1.45 µg/mL. The images in Figure 6-33 suggested that this could have been a result of the higher polymer content producing the same viscous gel as see in the IDR experiment (Indicated by the red arrow). The 1 to 3 ratio appeared to be the optimum ratio for the spray dried solid dispersions as this ratio exhibited an initial burst but also a more controlled dissolution rate. This resulted in the highest average concentration of 6.62 ± 2.3 µg/mL and the highest AUC value of 403.62 (Table 6-5). The dissolution profiles in Figure 6-34 also highlight the difference in behaviours between the three ratios and also how each ratio performed significantly better than the base drug.

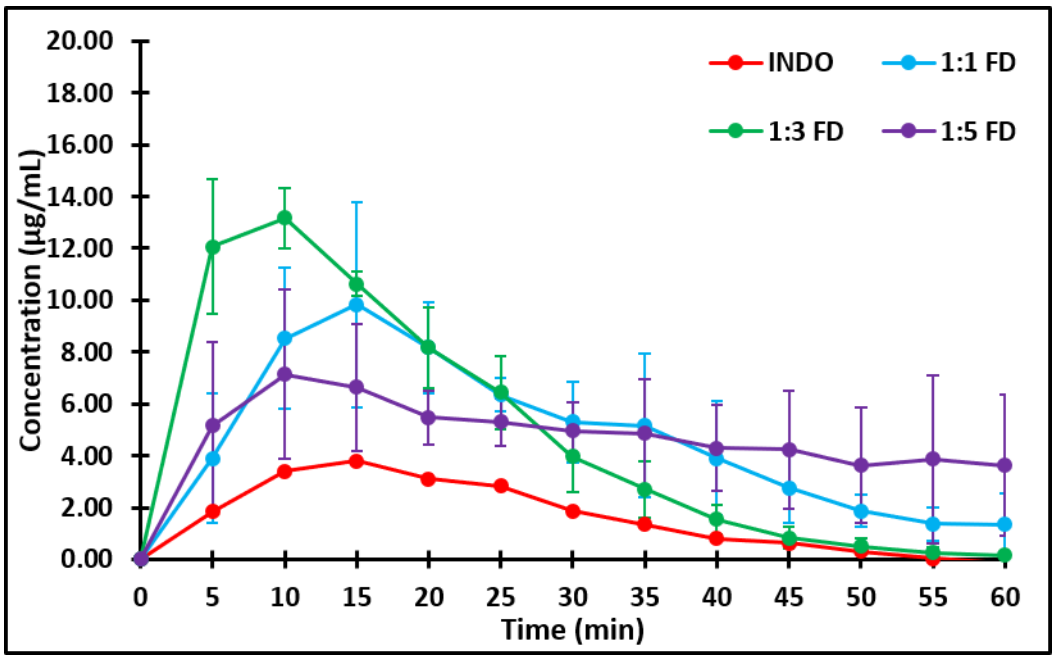

Figure 6-35 - Average Dissolution profiles (mean +/- SD) (n=3) from the whole dosage assessment of the freeze dried solid dispersions including the bulk drug indomethacin.

Also, in contrast to the IDR assessment were the freeze dried samples. All three ratios displayed dissolution rates greater than that of the base drug. Interestingly, similar trends as the spray dried sample were seen in both the images and the dissolution profiles (Figure 6-35 and Figure 6-36). The 1:5 ratio showed a more controlled lower release rate which again seemed to be as a result of gel formation as the solid dispersion hydrated. The 1:3 ratio also produced the greatest performance out of the three ratios tested, with a greater and more prolonged release rate. This led to an average concentration of 5.04 ± 0.94 µg/mL and an AUC value of 307.28. A further observation was that the spray dried samples displayed a greater performance than that of the freeze dried samples. This may be due to the greater surface area and smaller particle size produced from the spray drying process.

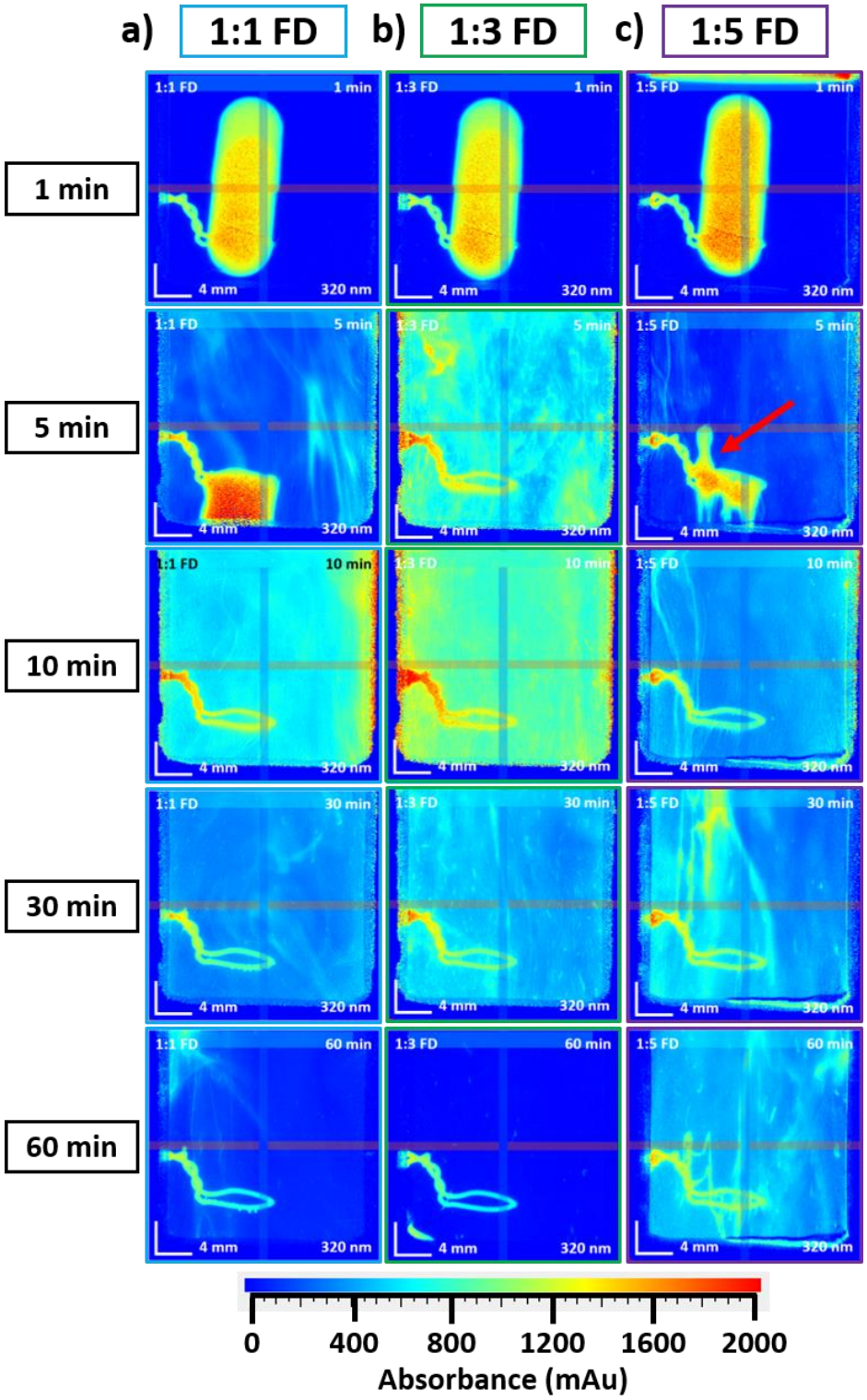

Figure 6-36 - UV images from the whole dosage assessment of the freeze dried solid dispersions at all three ratios manufactured. Note: The red arrow indicates gel formation of the solid dispersion.

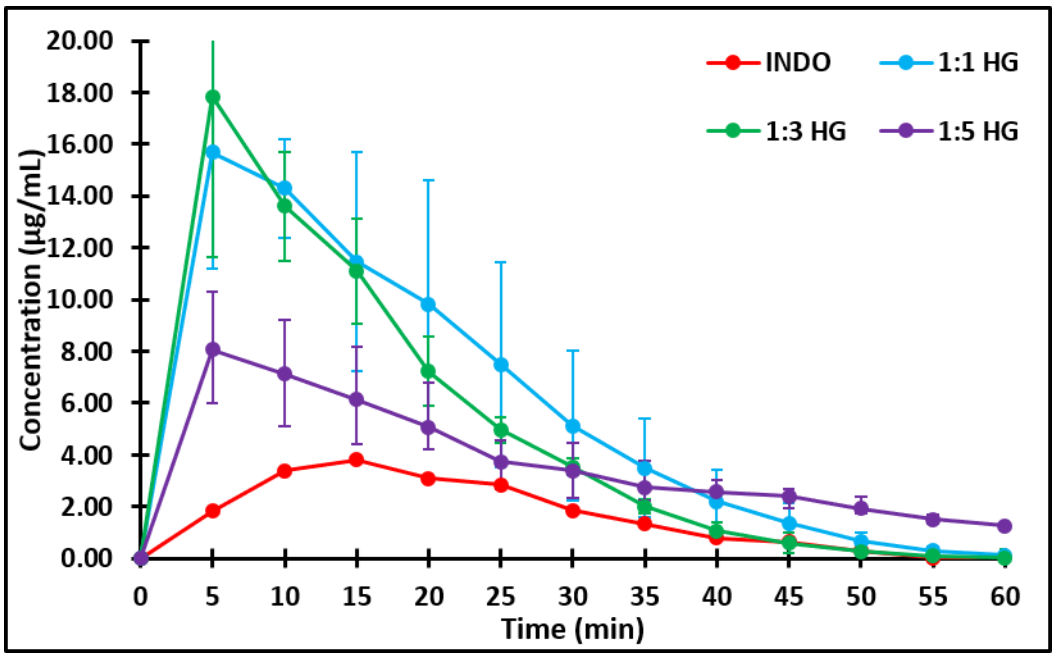

Figure 6-37 - Average Dissolution profiles (mean +/- SD) (n=3) from the whole dosage assessment of the homogenised solid dispersions including the bulk drug indomethacin.

The homogenised samples also displayed a greater dissolution performance than the base drug INDO. The images in Figure 6-38 also displays strong absorbance readings for all three ratios from the 10 min mark onwards indicating a strong dissolution performance. The homogenised samples displayed a reduced dissolution performance with an increase in polymer content (Table 6-5) possibly due to a gelling effect as all 3 samples showed some evidence of the web-like behaviour visualised in the IDR flow cell. A further observation was that the homogenised samples outperformed the freeze dried samples despite being exposed to the same conditions. It is likely that a greater surface area was gained from the complex structure of the homogenised particles. This highlights the influence homogenising can have on amorphous solid dispersion production prior to freeze drying. The 1:1 ratio was also found to be the optimal ratio for thee homogenised samples with a dissolution rate of 6.07 ± 2.45 µg/mL and an AUC value of 370.23 thus potentially saving on the cost of polymer should the technique be the one of choice.

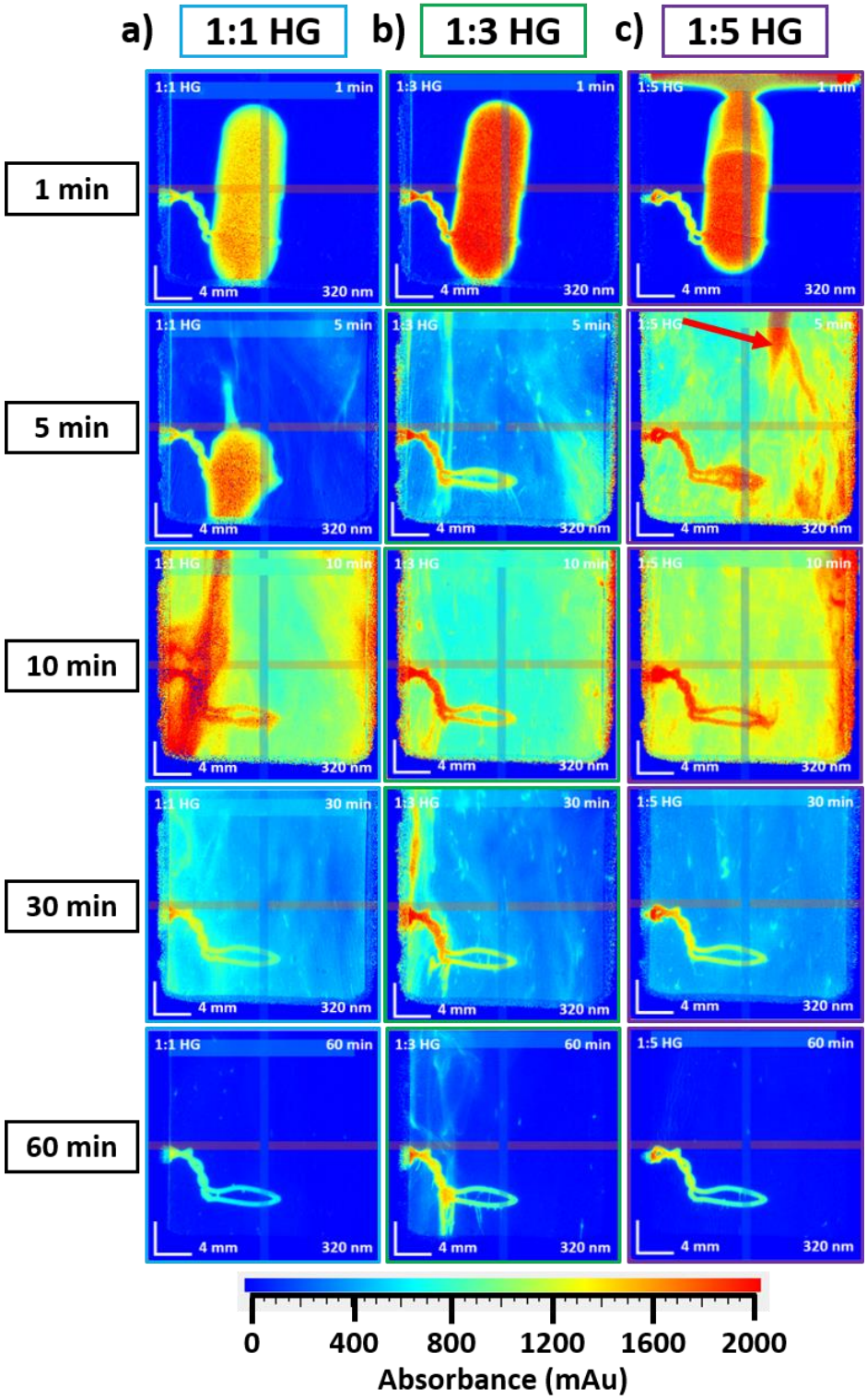

Figure 6-38 - UV images from the whole dosage assessment of the homogenised solid dispersions at all three ratios manufactured. Note: The red arrow indicates gel formation of the solid dispersion.

Overall, the whole dosage assessment of the amorphous solid dispersions found all samples from all three manufacturing techniques to generate a greater dissolution rate of the INDO. The best of which was the 1:3 SD sample.

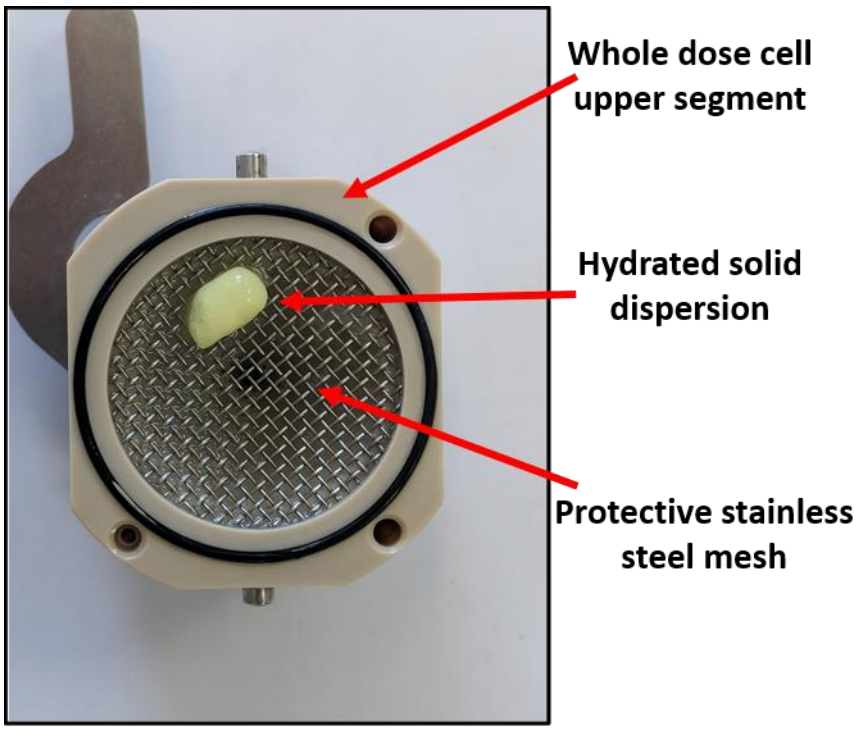

Figure 6-39 - A schematic displaying solid dispersion gel formation at the 1:5 ratio.

To highlight the viscous gel formation within the capsules for the 1:5 ratio samples, each sample left a capsule shaped gel stuck to the top of the whole dosage cell as indicated in Figure 6-39. Whilst this observation was not ideal for an immediate release study, this ratio (high polymer content) could be of interest for a controlled or extended release formation due to the gel formation and the prolonged dissolution profiles.

6.7 Conclusion

This chapter represents an in-depth assessment of the successful manufacture, characterisation and ranking of a number of prepared amorphous solid dispersions using two novel imaging techniques in the form of focus variation microscopy and UV imaging.

This chapter highlights the successful manufacture of amorphous solid dispersions of INDO and Soluplus™ using three manufacturing techniques. The solid dispersions were fully characterised using XRPD and DSC and found to be fully amorphous and crucially stable post 1 year of manufacture. SEM highlighted the influence of each manufacturing technique on the particle morphology of the solid dispersions. The spray dried samples where spherical and small in nature whilst the freeze dried and homogenised samples produced more complex porous particle morphologies. The use of focus variation microscopy in this chapter helped to visualise the influence of particle morphology on the surface of the flow-through compacts prior to IDR determination. Microscopy also detected a number of surface anomalies from surface fractures to embossed ring patterns. Despite the focus variation microscope detecting significant differences in parameters such as S*dr*, further investigation into the correlation between the surface parameters and the compaction properties of the materials needs further investigation.

The flow through cell provided a visual assessment of the IDR of the bulk drug and the pseudo-IDR of its solid dispersions. This proved to be an extremely useful technique as without the imaging capabilities, the web-like behaviour may not have been discovered. This behaviour was then able to be investigated further and found to be the result of an increased viscosity in the hydrated solid dispersions in the higher ratios of polymer content. The pseudo-IDR assessment of the solid dispersions found the majority of the solid dispersions to be poorer in regard to dissolution rate than the base

drug. This may be attributed to the compaction methodology used to produce the compacts and indicates further investigation into the methodology used to conduct IDR measurements.

Imaging of the powder dissolution via a capsule was successful and confirmed differences in dissolution behaviour of the solid dispersions. All manufactured samples displayed superior dissolution to the bulk drug INDO. The results suggested that the best five samples based on dissolution were 1:3 SD > 1:1 HG > 1:1 SD > 1:3 FD > 1:3 HG indicating that a ratio of INDO to SOL in these dispersions of up to 1:3 was sufficient to produce significant dissolution increases. Interestingly, the whole dosage assessment of the 1:5 ratios also displayed the formation of a viscous gel and as a result also detected a controlled drug delivery. Also, post dissolution a significant amount of the hydrated solid dispersion was found stuck to the top of the whole dosage cell.

This chapter has highlighted how UV imaging could be utilised by a formulator as it has the capability to provide quick insights into the behaviour of amorphous solid dispersions and also perform conclusive whole dosage dissolution assessments. This chapter also highlighted the importance of having both complimentary IDR and whole dosage imaging techniques in giving a better understanding of solid dispersion systems.

Chapter 7 – Use of dissolution imaging for the assessment of liquisolid compacts.

7.1 Note to Reader

Some aspects of the following chapter is published in the Journal of drug delivery science and technology under the title *'The use of visible and UV dissolution imaging for the assessment of propranolol hydrochloride in liquisolid compacts of Sesamum radiatum gum'(171)*.

7.2 Rationale

The following chapter demonstrates an explorative study into the use of dissolution imaging with liquisolid systems. The purpose of this chapter is to use dissolution imaging to provide an insight in to the dissolution properties and dynamics of liquisolid compacts prepared using a natural polysaccharide, sesamum, and a smectite clay, veegum. Both the visible and UV capabilities of the dissolution instrument was employed to characterise growth/swelling and drug release.

7.3 Introduction

Liquisolid dosage forms are an innovative way of sustaining the release of water-soluble drugs and increasing the release rate of water-insoluble drugs. The principle of liquisolid formulation is to take liquid formulations such as solutions, suspensions, and emulsions (in the case of water insoluble drugs) and convert them into powders suitable for tabletting and encapsulation (172). Simple blending of a powder mix with a liquid vehicle can result in many pharmaceutical advantages such as good compressibility and a free flowing powder that is often non-adherent.

Fundamentally, a liquisolid formulation consists of two key components; the powder blend and a liquid component. The powder blend often contains a compression enhancing larger particle size carrier such as a cellulose derivative i.e. HPMC, and a flow enhancing, very fine particle size excipient such as silica. Depending on the desired outcome of the liquisolid formulation, the choice of a liquid vehicle is dependent

on the necessity to dissolve or suspend the active ingredient. A number of liquid vehicles have been utilised including polyethylene glycol and polysorbate (173).

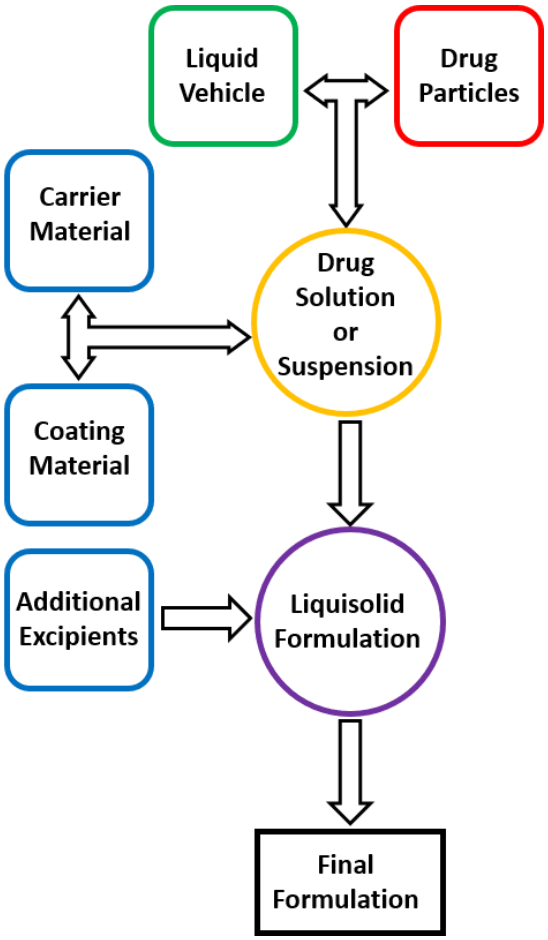

Figure 7-1 - A schematic outlining the manufacture of liquisolid formulations.

Figure 7-1 displays the progression of liquisolid manufacture. Liquisolid formulations can be utilised in two distinctive ways either as a restrictive controlled release formulation or as an enhancer to dissolution for poorly soluble compounds.

Kaialy et al. utilised the liquisolid technique to sustain the release of a highly soluble drug diltiazem HCl. This was achieved by using a number of non-volatile solvents such as polysorbate 80 to produce a suspension before mixing with Polyox as an alternative to HPMC. The authors found that the Polyox liquisolid tablets produced desirable and more sustained release profiles when compared to the equivalent conventional physical mixture tablets (174). Nokhodchi et al. also utilised the liquisolid technique to sustain the release of the soluble drug theophylline. This was achieved by using volatile

solvents such as polysorbate and polyethylene glycol alongside Eudragit and colloidal silica. The authors found that the liquisolid preparation produced zero order release kinetics and sustained release behaviour (175).

With regards to utilising the liquisolid technique with poorly soluble drugs, Chella et al used it for the improvement of the dissolution rate of the model drug valsartan. In their work they used propylene glycol as a solvent to solubilise valsartan before formulating the liquisolid matrix using Avicel PH102 and Aerosil 200. The authors found that the liquisolid formulation was a promising approach for the improvement of the dissolution rate as there was approximately a six-fold increase in the dissolution efficiency and no interaction between the drug and the solvent (176). Javadzadeh et al. also investigated the improvement of the dissolution rate of the poorly soluble model drug carbamazepine using the liquisolid technique. In their study, the authors dispersed carbamazepine in PEG 200 before the addition to a variety of polymers including PVP and HPMC. The authors concluded that significant increases in the dissolution rate were observed from the liquisolid compacts over the conventional tablets and that no changes in crystallinity of the drug over the course of manufacture was observed (177).

For liquisolid manufacture, it is often recommended that a larger particle size carrier be added to the powder blend. Often this is a hydrophilic polymer such as HPMC or PEO. In this chapter a natural polysaccharide, Sesamum gum, is utilised as an alternative to HPMC. Also, it is recommended that a very fine particle size excipient such as silica is used in the dry powder blend. In this chapter Veegum (also known as magnesium aluminium silicate (MAS)) is utilised as an alternative to the commonly used Aerosil.

In developing nations, modern medicines are often beyond the reach and affordability of the majority of the population. This is often as a result of a strong dependence on the petrochemical industry for the importation of a variety of synthetic and semi-

synthetic pharmaceutical materials used in the production of a wide range of pharmaceutical products. This importation therefore drives up the cost of medications in developing nations. In recent years, there has been a strong shift to the investigation of natural alternatives that may be in abundance in the nation of interest and provide an equivalent or superior function to the imported materials. This chapter investigates the use of Sesamum gum as a natural alternative to HPMC. Sesamum gum is a polysaccharide extracted from the leaves of the *Sesamum radiatum* plant which is readily cultivated in Sub-Saharan regions of Africa. Nep et al. found the gum to be a high molecular weight polysaccharide of mannose, galactose, xylose and glucuronic acid. The authors also found that once hydrated the polymer exhibited viscoelastic behaviour consistent with intermolecular entanglement and shear-thinning behaviour (178). Sesamum gum has also been shown to be highly compressible and compactable with superior compaction properties similar to HPMC K4M and had the ability to form a gel layer capable controlling drug release from matrix tablets (179). This chapter also investigates the use of Veegum as an alternative to the colloidal silica conventionally used in liquisolid formulations.

Veegum also known as magnesium aluminium silicate (MAS) is a mixture of naturally occurring smectite clays. Veegum has been used as a carrier in for active pharmaceutical ingredients (API) in modulating their drug release (180-182) due to its inherent ability to form complexes with cationic drugs (183).

propranolol hydrochloride (PPN) was selected as the model drug of choice in this chapter. propranolol is a non-cardio selective beta blocker and is widely used in therapeutics for the treatment of hypertension and anxiety disorders (118). PPN also exhibits good aqueous solubility and has a short elimination half-life of three hours making it a suitable candidate for controlled drug delivery (184). Javadzadeh et al. utilised the liquisolid technique to sustain the release of PPN. In this instance

polysorbate 80 was used as the liquid vehicle and Eudragit was the carrier material along with colloidal silica. They also observed that the liquisolid preparation produced a greater retardation on the PPN release rate when compared to equivalent physical mixture tablets (185).

7.4 Objectives

As shown in previous chapters, the dissolution imaging system has been utilised for both whole dosage assessments of hydrophilic matrix systems, salts and solid dispersions and the use of both the UV and the optical LED's have monitored drug release and capsule dissolution. This chapter explores the first use of UV imaging in liquisolid systems with the primary aim of simultaneously measuring the release of the model drug propranolol hydrochloride (PPN) and the compact swelling behaviour from liquisolid systems using the polysaccharide, sesamum radiatum gum, by exploiting the visible and UV imaging capabilities of the novel surface dissolution instrument. This chapter will also aim to use the UV imaging to compare and contrast directly compressed and liquisolid formulations.

7.5 Materials and Methods

7.5.1 Materials

The materials for this experiment were as follows:

- The active ingredient propranolol hydrochloride (PPN) was purchased from TCI Chemicals (UK).
- The natural polysaccharide, Sesamum gum, was extracted from the *Sesamum radiatum* leaves in our lab.
- The clay-mineral Veegum F was a kind gift from Lake Chemicals and Minerals (UK).
- Colloidal Silica was purchased Sigma-Aldrich (UK).
- The liquid carrier Polysorbate 80 was purchased from Fluka (UK).
- The solvent ethanol for gum extraction was purchased from Fisher (UK).
- Potassium phosphate monobasic and sodium hydroxide for the preparation of the dissolution media was purchased from Arcos Organics (Germany) and Fisher (UK) respectively.
- De-ionised water

7.5.2 Methods

7.5.2.1 Extraction of Sesamum Gum

The extraction of sesamum gum was conducted as reported in Nep et al. (179) In brief, 1 kg of leaves from the sesamum radiatum plant were macerated for 30 min at ~22 °C in 7.5 L of distilled water containing 0.1 %w/v sodium metabisulphite. The resulting mucilage was filtered using a muslin cloth then precipitated with 96 % ethanol. The precipitate was filtered again using a 200 µm sieve and oven dried at 50 °C for 24 h.

7.5.2.2 Liquisolid Formulation and Tablet Manufacture

For the liquisolid formulation, it is necessary to select an appropriate solvent to disperse the PPN in. 4 solvents were tested; propylene glycol, PEG 400, Glycerin and polysorbate 80. In summary, saturated solutions were prepared by adding PPN in excess to 10 mL of each solvent. The saturated solutions were then shaken using a water bath shaker for 48 h set at 25°C. Once this period had elapsed the solutions were diluted 1000 times with deionised water and measured using a Jenway® 72 Series UV/Visible Spectrophotometer set at 288.5 nm to calculate the solubility of propranolol. Polysorbate 80 was chosen due to PPN's low solubility within it (Table 7-1).

Table 7-1 - Measured solubility values of propranolol Hydrochloride in the four non-volatile solvents selected for liquisolid manufacture. Note: Due to low solubility of propranolol Polysorbate 80 was selected for liquisolid formulation.

Solvent	Solubility of propranolol (g/100 mL)
Propylene Glycol	10.3
PEG 400	8.0
Glycerin	4.0
Polysorbate 80	1.3

To explore the use of imaging in liquisolid systems in comparison to their directly compressed (DC) counterparts, four formulations as in Table 7-2 were prepared. For the DC tablets F2 and F3, all the required excipients and API were mixed and blended using a Turbula™ mixer (Willy. A Bachofen, Switzerland) for 10 min before tabletting.

Table 7-2 - Formulation table displaying formulation composition and associated formulation codes. Note: The blue colour indicates liquisolid formulation whilst the orange colour indicates the DC formulation.

Formulation Code	propranolol HCl (g)	Sesamum Gum (g)	Polysorbate 80 (g)	Colloidal Silica (g)	Veegum (g)
F1	2	2.727	2	0.273	X
F2	2	2.727	X	0.273	X
F3	2	2.727	X	X	0.273
F4	2	2.727	2	X	0.273

For the liquisolid formulations, F1 and F4, 2 g of the PPN was dispersed in 2 g polysorbate 80 using a pestle and mortar for 2 min. Depending on the formulation, a dry powder blend of the sesamum gum, colloidal silica or veegum (prepared using a Turbula™ mixer (Willy. A Bachofen, Switzerland) for 10 min) was then added to the PPN in small amounts (~500 mg) under continuous stirring until a homogenous blend was achieved. For the tablet manufacture, round cylindrical tablets with a diameter of 10 mm and target weights of 285 mg (DC) or 400 mg (liquisolid compacts) were compacted using a manual single punch hydraulic press (Globalpharma) at 2500 psi.

7.5.2.3 Powder flow, tablet friability and tablet hardness

The flow properties of all the formulations were determined using a 10 mL glass cylinder with 10 mL of powder from each of the formulations. The weight of the powder formulation was noted each time and then the glass cylinder tapped to allow the particles of powder to consolidate. After 50 taps, the final volume was recorded. Carr's consolidation index was determined using Equation 7-1 (186).

$$Carr's\ Index = 100\ x\ (\frac{1 - Bulk\ Density}{Tapped\ Density})$$

Equation 7-1 – Equation for the determination of Carr's consolidation index.

Friability testing was carried out on 10 tablets for each formulation using a Pharmatest Friability tester. The tablets were dusted gently using a brush in order to remove any powder debris and then weighed. The tablets were then dusted again after being subjected to 25 rpm for 4 min and re-weighed to measure any loss in weight. Friability (%) was determined using Equation 7-2.

$$\left(\frac{Initial\ weight - post\ weight}{Initial\ weight}\right)\ X\ 100 = Friability\ (\%)$$

Equation 7-2 – Equation for the determination of percentage friability.

For tablet hardness assessment, tablets from each formulation were allowed at least 24 h recovery time before being subjected to the Pharmatest hardness tester to determine breaking force. The point at which the tablet fractured was recorded in Newton (N).

7.5.2.4 Solid state characterisation

Differential scanning calorimetry (DSC)

A Mettler-Toledo DSC 1 Differential Scanning Calorimeter was used to conduct all DSC measurements. Prior to measurement, approximately 3.5 mg of powder was placed into a standard 40 µL aluminium pan. The powder was gently compacted in the pan to ensure even contact on heating. A lid was then crimped in place and pierced to produce a vent. The pan was then heated from 30 to 300 °C at a scanning rate of 10 °C/min with nitrogen gas used as a purge gas. The enthalpy, onset temperatures and melting points of each sample as well as potential glass transition temperatures were analysed using the software provided by Mettler-Toledo, Switzerland.

X-ray powder diffraction (XRPD)

XRPD measurements were performed on all samples as well as the starting materials. All samples were scanned in Bragg–Brentano geometry, over a scattering (Bragg, 2θ) angle range from 5 to 45°, in 0.02° steps at 1.5° min^{-1} using a D2 Phaser diffractometer (Bruker AXS GmbH, Karlsruhe, Germany). The XRPD patterns were collected and analysed further using Microsoft Excel.

7.5.2.5 Dissolution Imaging

In this study the whole dosage cell was exclusively used. The method specifics are outlined as follows:

Dissolution Media Preparation

The media used was a 0.2M phosphate buffer (pH 6.8) prepared according to the USP 2003 using sodium hydroxide and potassium phosphate monobasic. The pH was selected to mimic intestinal conditions and deliver a bio-relevant assessment of the tablets. In summary this media was prepared by first making a 0.2 M solution of sodium hydroxide (NaOH) by dissolving 8 g of NaOH pellets in 1 L of deionised water. Next, a 0.2 M solution of potassium phosphate monobasic (KH_2PO_4) was prepared by dissolving 27.22 g of KH_2PO_4 in 1 L of deionised water. Once both solutions were prepared, 224 mL of the NaOH solution and 500 mL of the KH_2PO_4 solution were measured into a 2 L volumetric flask and made to volume with deionised water. If required, the buffer was titrated to target pH using either 1 M HCL or 1 M NaOH.

UV Calibration of propranolol

In a different approach to the calibration methodologies outlined in chapters 5 and 6, a new calibration methodology was devised for this work. This new methodology trialled a calibration conducted using the dissolution imaging system and the whole dosage cell as opposed to the traditional quartz cell and UV spectrophotometer. There are many advantages to conducting a calibration on the testing system including; exposure to the same light intensity, experimental conditions, and path length. Also, reference images of the standards could also be obtained which could be used retrospectively to confirm dissolution behaviour observed during dissolution experiments.

To conduct the calibration, two stock solutions were prepared by weighing 100 mg of PPN into a 100 mL volumetric flask and made to volume with pH 6.8 buffer producing

a 1 mg/mL solution. Next, two series of standards were produced (1 from each stock) following Table 7-3 below:

Table 7-3 - Standard concentrations used in the calibration of propranolol at 280 nm Note: The standards indicated with a star were produced following a 1 in 10 serial dilution of the 10 and 50 stock respectively.

Concentration (µg/mL)	Amount of Stock (mL)
50	5
40	4
30	3
20	2
10	1
5*	10 from 50 standard
1*	10 from 10 standard

Once all the standards were prepared, they were placed in a water bath set at 37 °C. This was to allow the standards to reach experimental temperature before analysis as due to the nature of the analysis the standards would not be passing through the heating element in the dissolution imaging system. Whilst the standards reached temperature, the system was prepared as follows.

Firstly, the whole dosage cell absent of the glass beads was placed in the dissolution imaging system and filled with pH 6.8 buffer (blank). Care was taken to ensure the buffer covered the windows but did not overflow from the cell. Next, using the data collection software supplied, a method was devised to record each standard for 5 min (10 readings) with a 5 min gap to allow for the changeover of the standard using the 280 nm LED. This included a 5 min reading of the pH 6.8 (blank media) at the start to ensure a successful blanking of the system had occurred. When the experiment was started, blank readings were automatically taken by the system at the start of the experiment. During the changeover, the whole dosage cell was emptied, rinsed, dried and filled with the next standard starting with 1 µg/mL (Table 7-3). The calibration continued until all standards had been measured. The calibration was then repeated for the second series of standards.

The recorded calibration data was then analysed using the supplied analysis software to extract the images and absorbance readings for the standards. To achieve this, an absorbance window as shown in Figure 7-2 was used to read each standard.

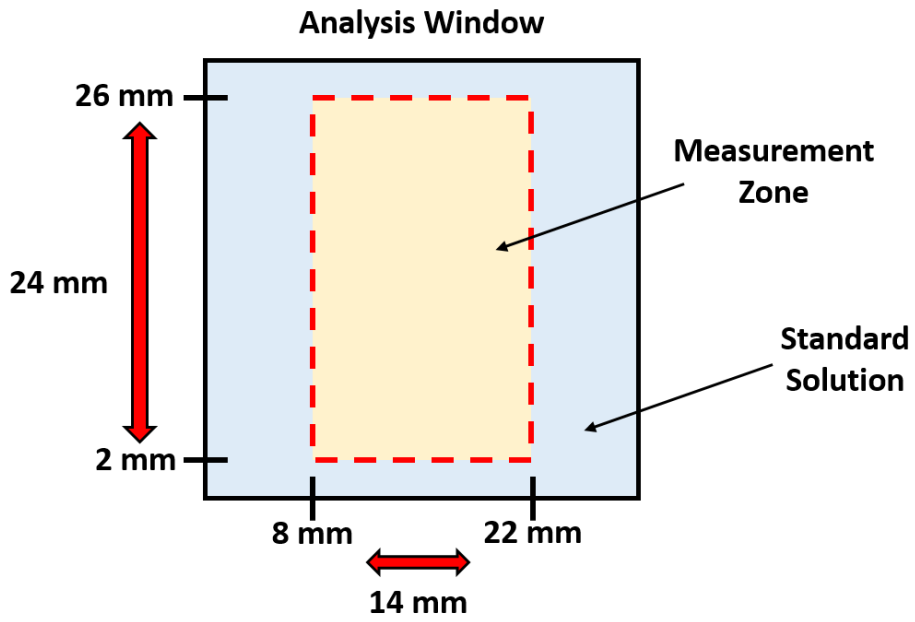

Figure 7-2 - A schematic representation of the measurement zone and analysis window used to obtain readings of the propranolol standards.

Each series was then plotted using Microsoft Excel™ to produce a calibration curve specific to the dissolution imaging system. The calibration curve obtained and associated UV images are displayed in Figure 7-3. The 40 and 50 µg/mL standards saturated the detector and as a result were outside of linearity and excluded.

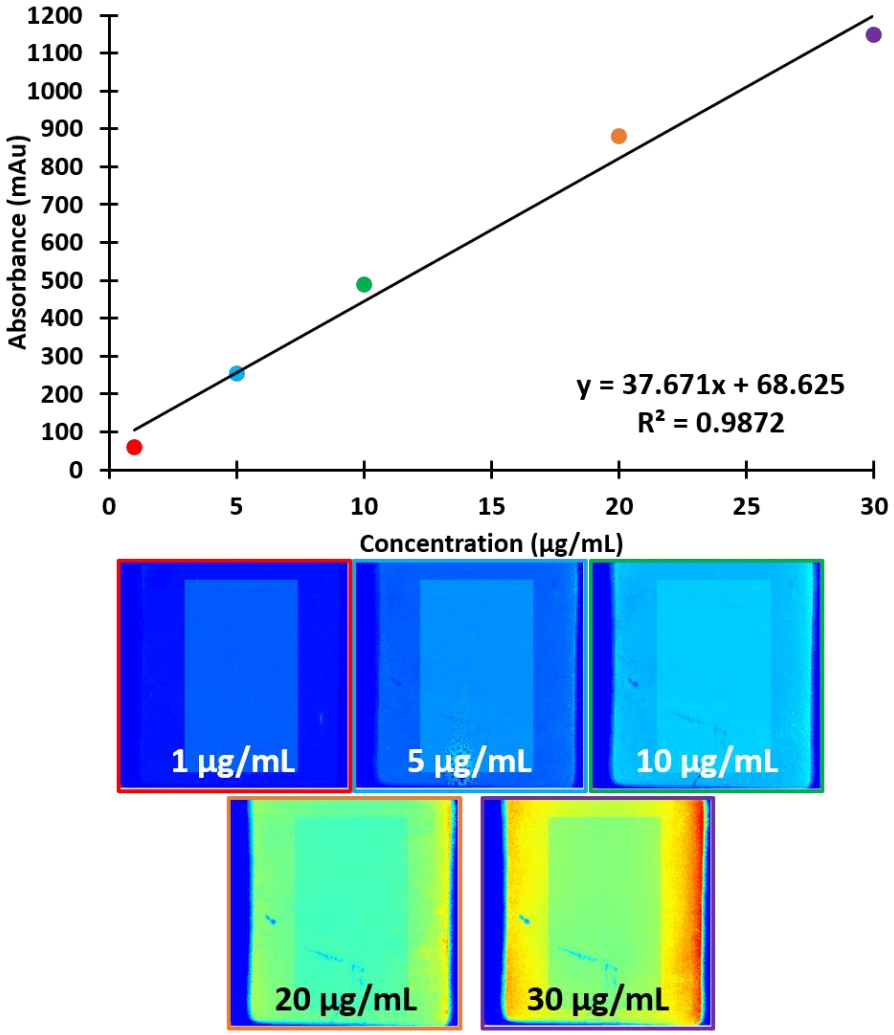

Figure 7-3 - The obtained schematic for propranolol at 280 nm with the SDi2 system with associated images. Note: the 40 and 50 µg/mL standards were excluded due to readings outside of the linear range.

Whole Dosage Cell measurement

Figure 7-4 outlines how the whole dosage experiments were analysed for the liquisolid compacts at 280 and 520 nm for the purpose of recording drug release and tablet growth. The conventional or liquisolid tablets were mounted using a custom designed stainless steel wire holder. Prior to insertion into the whole dosage cell, the whole dosage cell containing 12.3 g of 3 mm borosilicate glass beads was inserted into the dissolution imaging system and connected to the fluid lines. The conventional or liquisolid tablets were inserted into the whole dosage cell when instructed by the data collection software.

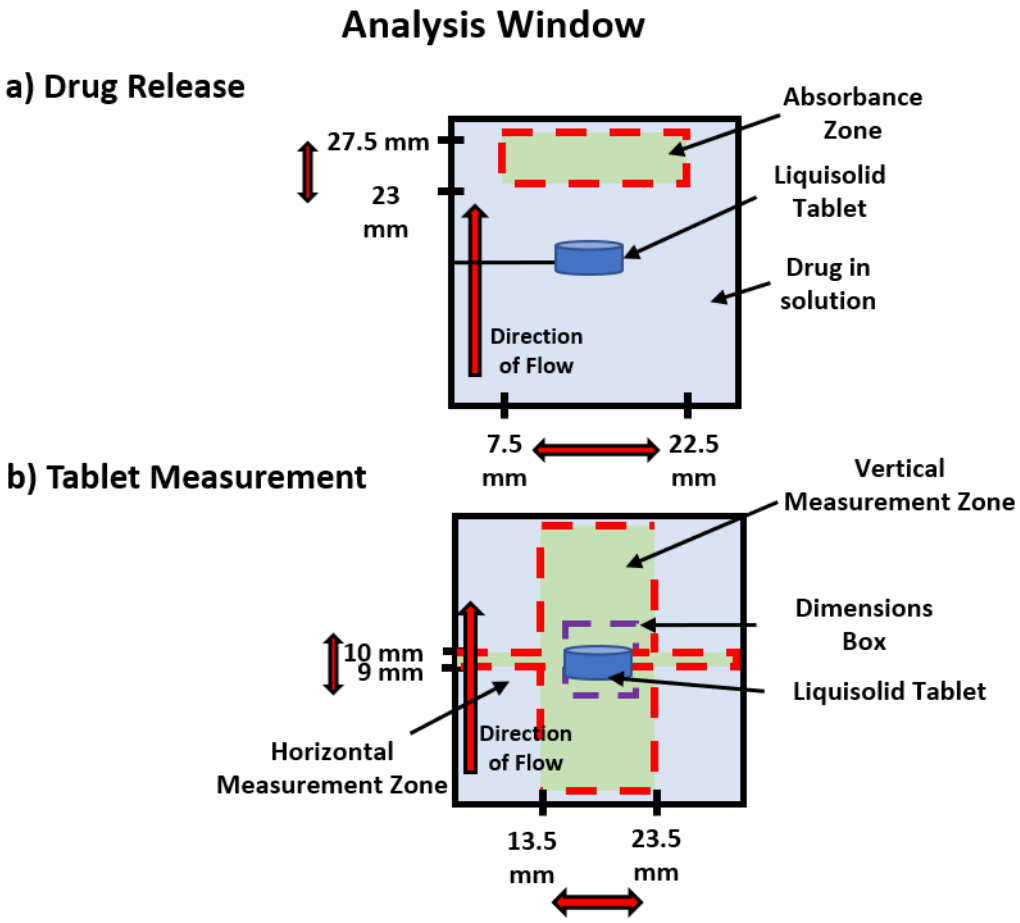

Figure 7-4 - A schematic representation of the analysis windows for the liquisolid tablets. a) The analysis window for drug release measurement at 280 nm. b) The analysis window for the tablet growth measurement at 520 nm.

Each experiment was conducted using pH 6.8 phosphate buffer at a flow rate of 8.2 mL/min at 37 °C. The release of PPN was imaged over 120 min at various time points at a wavelength of 280 nm. Tablet growth measurements were also taken using the 520 nm LED run simultaneously during the experiment. Tablet growth measurements are displayed as a percentage gain based on the initial reading of tablet size. Equation 7-3 describes how this was calculated.

$$\frac{(h_{t=x} - h_{t=0})}{h_{t=0}} \times 100$$

Equation 7-3 – Equation for the calculation of percentage gain where; h = tablet height, t = time and x = a given time point.

7.6 Results

7.6.1 Solid State Characterisation

7.6.1.1 X-Ray Powder Diffraction (XRPD)

XRPD was utilised in this study to characterise the starting ingredients including the sesamum gum and the active ingredient PPN. XRPD was also used to determine the presence of the characteristic peaks of PPN in the conventional and liquisolid formulations. Bartolomei et al. report the characteristic peaks for PPN to be at 2 theta angles of 12.51, 16.73, 17.19, 19.76, 23.22, 25.08 and 27.47° (187). These notable peaks are indicated on each XRPD spectra in the form of black dashed lines with red stars.

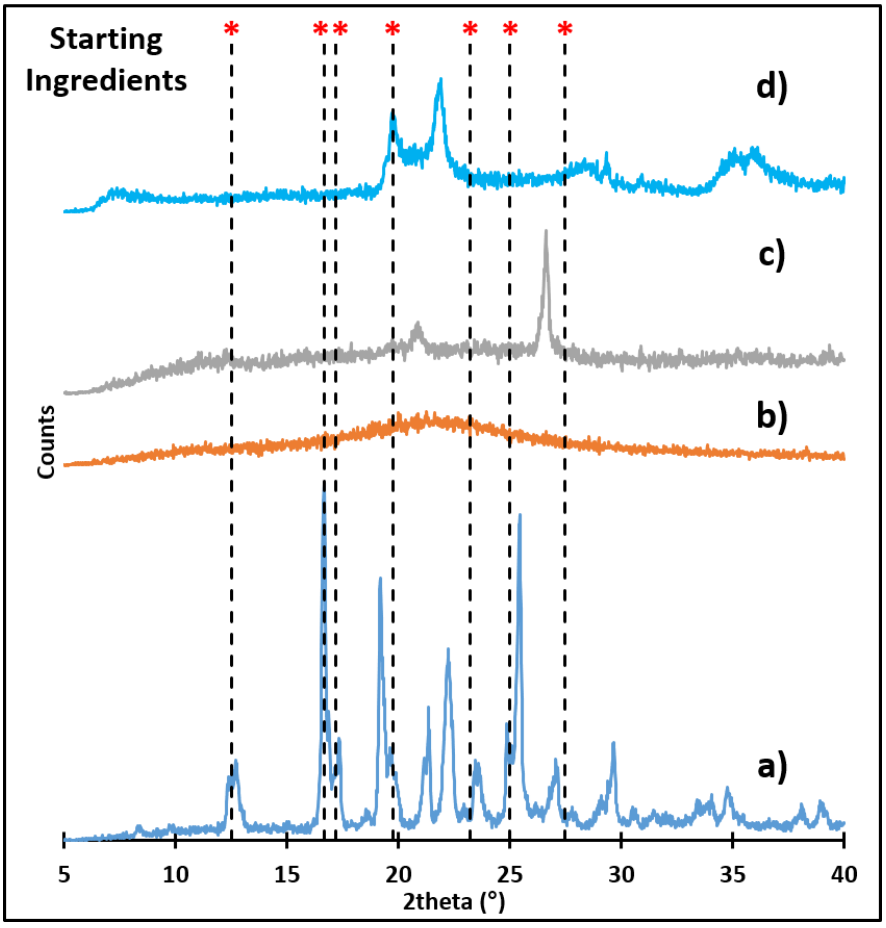

Figure 7-5 - XRPD spectra for the starting materials. a) propranolol, b) Colloidal Silica, c) Sesamum Gum and d) Veegum. Note: the black dashed lines with red stars indicate the characteristic peaks for propranolol.

Figure 7-5 displays the XRPD spectra for the starting materials. As expected, the active ingredient PPN was found to be crystalline in nature and demonstrated sharp intensity

at the characteristic 2 theta angles (Figure 7-5a). XRPD also displayed that colloidal silica used in the formulation of the F1 and F2 blends was amorphous in nature (Figure 7-5b). Sesamum gum has been characterised extensively by other groups and is expected to display an amorphous pattern similar to other polymeric systems (178,179). This was found to be the case following the XRPD characterisation of the extracted sesamum gum (Figure 7-5c). Veegum displayed an XRPD pattern with a number of broad reflections in the XRPD spectra. This had been reported by Laity et al. and is found to be as a result of small distorted crystallites present in the clay matrix (121) (Figure 7-5d).

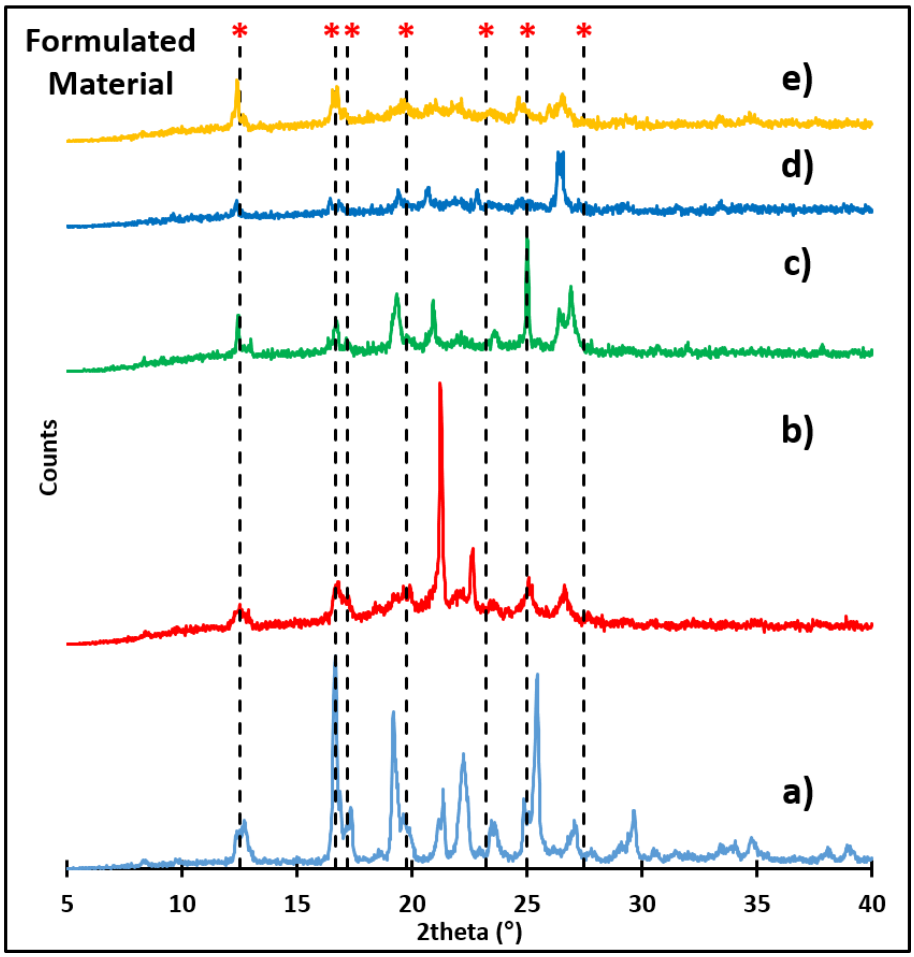

Figure 7-6 - XRPD spectra for the formulated materials. a) propranolol, b) F1, c) F2, d) F3 and e) F4. Note: the black dashed lines with red stars indicate the characteristic peaks for propranolol.

Figure 7-6 displays the XRPD spectra for the formulated materials. In keeping with literature observations, the characteristic peaks for propranolol were present in all the formulated material. There also seemed to be no significant differences in the

diffraction pattern between the conventional or liquisolid formulations and between the formulations containing colloidal silica or veegum.

7.6.1.2 Differential Scanning Calorimetry (DSC)

DSC was employed to characterise the active ingredient and the starting materials and also to determine the presence of the active ingredient within the formulated blends.

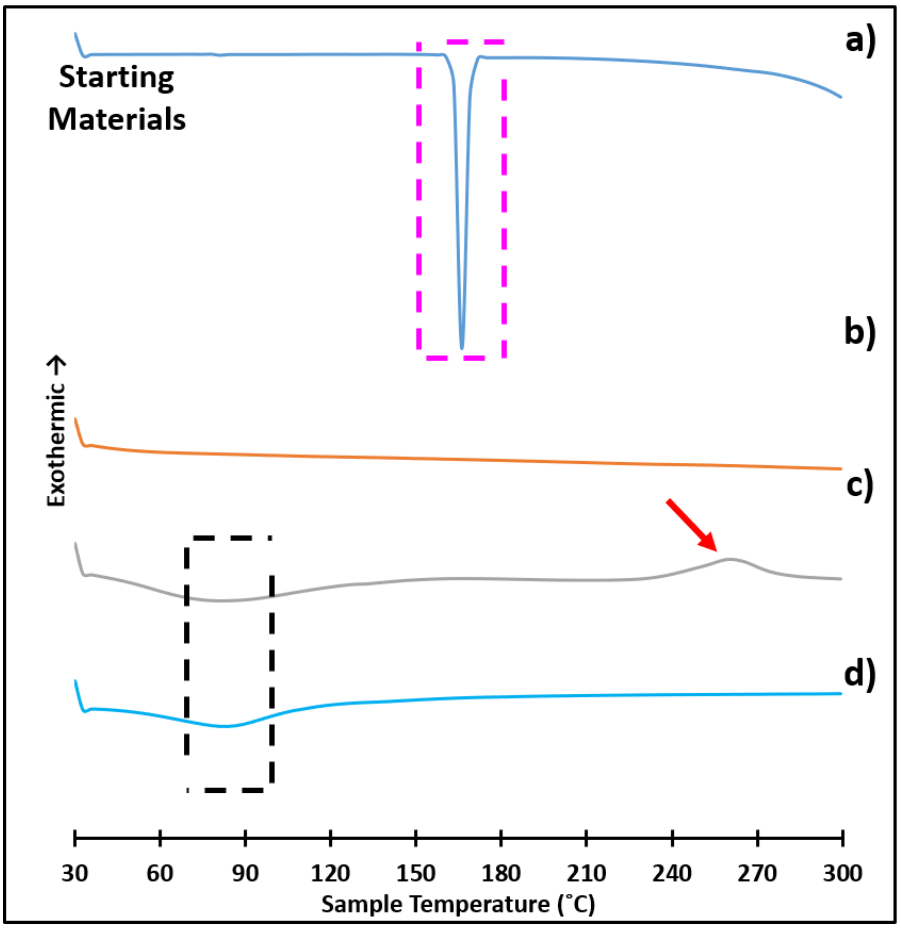

Figure 7-7 - DSC thermograms for the starting materials. a) propranolol, b) colloidal silica, c) sesamum gum and d) veegum. Note: The pink dashed box indicates the endothermic peak position for propranolol. The black dashed box water loss and the red arrow indicates polysaccharide decomposition.

Figure 7-7 displays the DSC thermograms for the starting ingredients. PPN displayed a sharp endothermic peak with a melt of 165.8 °C and an enthalpy of 271.8 mJ. This melt was consistent with DSC data reported by Javadzadeh et al (188). This peak is indicated by a pink dashed box (Figure 7-7a). DSC also confirmed the amorphous nature of the colloidal silica used in the F1 and F2 blends (Figure 7-7b). The extracted sesamum gum displayed two thermal events. The first event between 50 and 140 °C,

indicated by the black dashed box is likely to be the result of desorption of moisture from the polysaccharide structure. This observation is supported by thermogravimetric (TGA) analysis conducted by Nep et al. where they observed a minor weight loss of approximately 11.5% over the same temperature range (189). The second thermal event between 250 and 270 °C indicated by the red arrow can be attributed to polysaccharide decomposition. Again, TGA conducted by Nep et al. observed a similar event and a weight loss of approximately 54.6 %. They attributed the weight loss to the thermal scission of carboxylate or carboxylic acid groups resulting in the evolution of CO_2 from the corresponding carbohydrate backbone (Figure 7-7c) (189). The veegum sample also displayed a similar thermal event to that of the sesamum gum between 50 and 140 °C. This again can be attributed to water loss from the clay composite structure (Figure 7-7d).

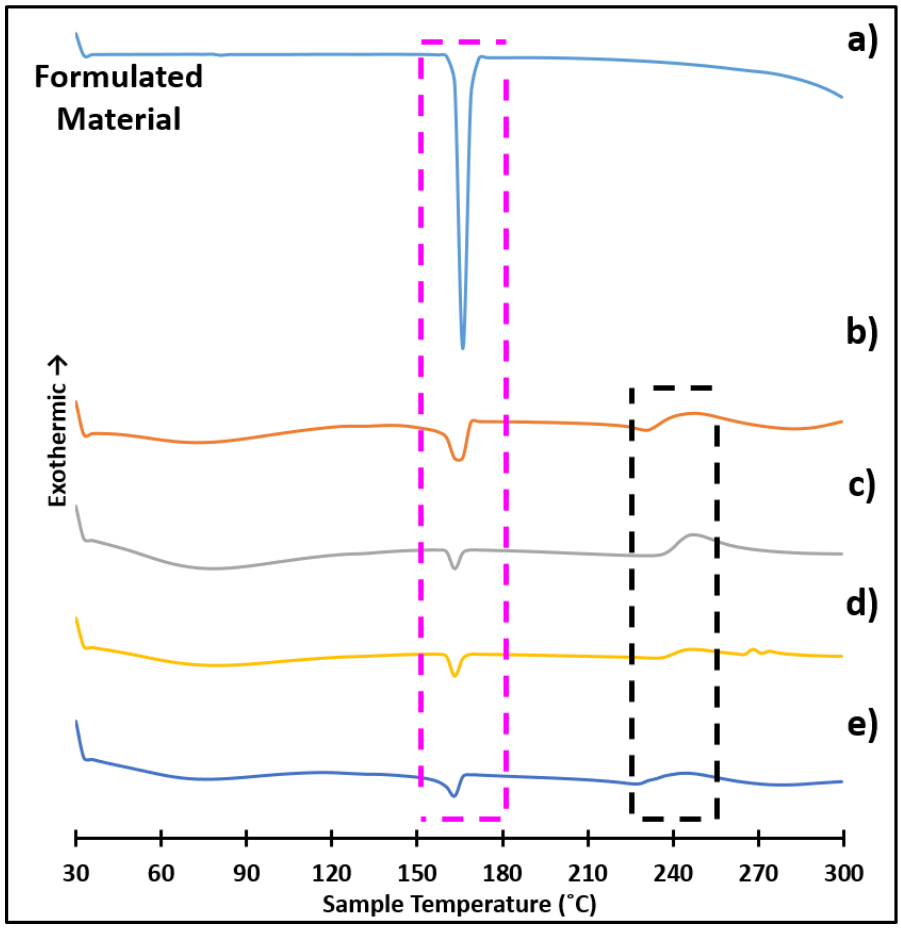

Figure 7-8 - DSC thermograms for the formulated materials. a) propranolol, b) F1, c) F2, d) F3 and e) F4 Note: The pink dashed box indicates the endothermic peak position for propranolol. The black dashed indicates polysaccharide decomposition.

Figure 7-8 displays the DSC thermograms for the formulated blends. In a similar trend to the XRPD all the formulated materials displayed the endothermic peak for PPN. F1 displayed an onset temperature of 160 °C, melt peak of 164.7 °C and enthalpy of 72.9 mJ. F2 displayed an onset temperature of 160.7 °C, melt peak of 163.5 °C and enthalpy of 16.93 mJ. F3 displayed an onset temperature of 160.6 °C, melt peak of 163.9 °C and enthalpy of 22.46 mJ. F4 displayed an onset temperature of 157.3 °C, melt peak of 163.2 °C and enthalpy of 37.3 mJ. The reduction in enthalpy in the formulations can be attributed to a reduced quantity of crystalline PPN present in the DSC sample compared to the bulk DSC sample.

7.6.2 Tablet Characterisation

Table 7-4 displays the results from the physical characterisation of the powder blend and tablets used in this study. The conventional and liquisolid formulations displayed a Carr's consolidation index of 27 to 32 indicating poor flowability. It was interesting to observe the formulations containing the colloidal silica (F1 and F2) displayed slightly better flow properties particularly in the DC formulations. With regards to tablet hardness, both the DC formulations (F2 and F3) displayed higher tablet hardness (207.90 ± 5.88 and 248.10 ± 20.59 N respectively) than the liquisolid formulations F1 and F4 (15.98 ± 1.96 and 8.14 ± 1.96 N respectively). The relatively lower mechanical hardness of the liquisolid compacts can be attributed to the introduction of the liquid vehicle polysorbate 80 into the liquisolid compacts. It was also noted that the presence of veegum in place of the colloidal silica inferred further hardness to the DC formulations. This observation is supported by work conducted by Laity et al. who reported veegum to make hard compacts (121). A further observation was that the formulations containing colloidal silica F1 and F2 did experience a small amount of friability at 0.5 %. This was in contrast to the samples containing veegum which did not appear to display any friability issues. Visual inspection was also conducted on the formulated tablets, this is shown in Figure 7-9.

Table 7-4 - Table displaying formulation composition and associated tablet characterization including Carr's Index, Hardness and Friability. Note: The blue colour indicates liquisolid formulation whilst the orange colour indicates conventional formulation.

Formulation Code	Carr's Index		Hardness (N)	Friability (%)
F1	32	Poor	15.98 ± 1.96	0.5
F2	32	Poor	207.90 ± 5.88	0.5
F3	27	Poor	248.10 ± 20.59	0
F4	31	Poor	8.14 ± 1.96	0

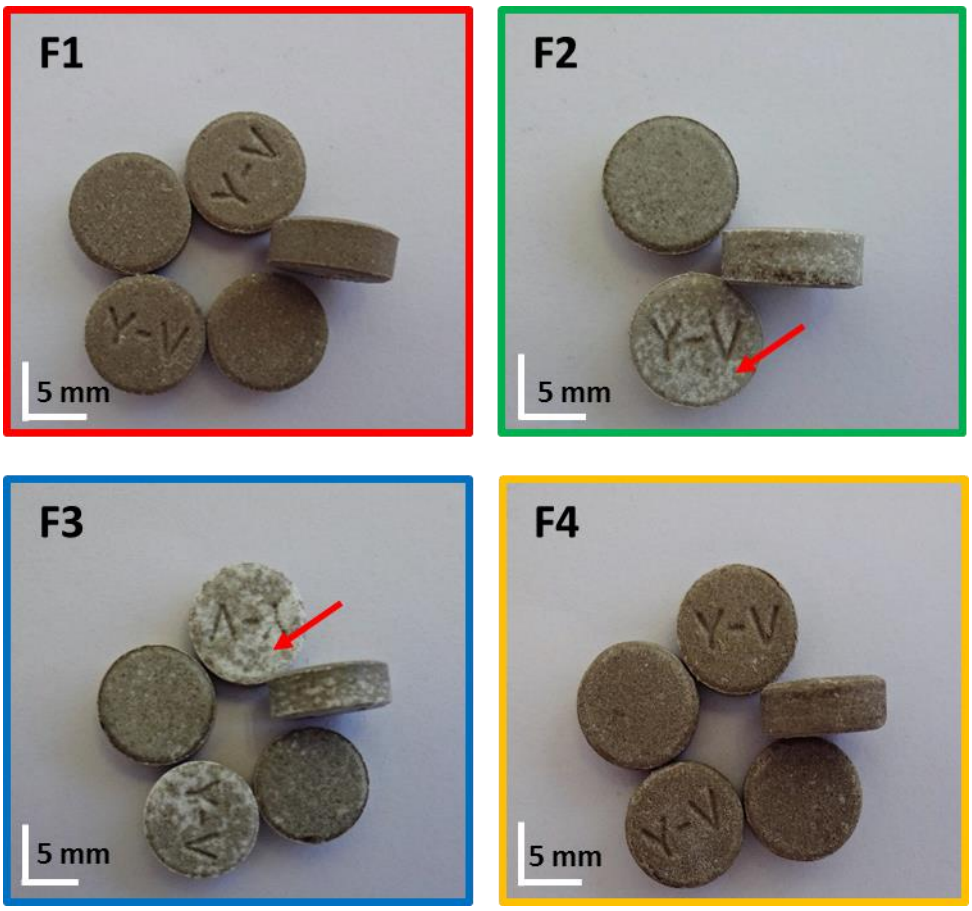

Figure 7-9 - Optical images of the formulated tablets F1 to F4. Note: The red arrow highlights mottling and uneven distribution of excipients.

From the visual assessment of the tablets post compaction, it appeared that the DC compacts (F2 and F3) experienced a large amount of mottling, indicated by the red arrows (Figure 7-9). This could be due in part to the differing particle sizes of the colloidal silica, PPN, sesamum gum and veegum present in the tablet blends. It is likely that this could have also contributed to segregation issues in the DC tablet blends. It was interesting to observe that this was not the case with the liquisolid compacts. The liquisolid compacts were uniform in appearance and this is likely to be as a result of their preparation method.

7.6.3 Dissolution Assessment

This section demonstrates the capability of the dissolution imaging system to record and measure dissolution phenomena from the whole dosage form. In this instance, a custom wire holder was designed to hold a 10 mm liquisolid compact formulation in axial orientation. All compacts were monitored over a 120 min period using the 280 and 520 nm LED's simultaneously.

Table 7-5 - A table displaying the average concentration (mean ± SD n=3) over the 120 minute period the liquisolid formulations.

Formulation Code	Average Concentration (µg/mL)
F1	41.61 ± 8.80
F2	49.40 ± 9.52
F3	45.15 ± 8.53
F4	44.91 ± 8.97

Figure 7-10 displays the UV images obtained from the formulations containing colloidal silica (F1 and F2). Visual assessment of the UV images highlight that the DC formulation F2 appeared to release a greater amount of the active ingredient particularly during the first 30 min of the dissolution experiment. This observation is supported by the drug release and cumulative release profiles in Figure 7-12. F2 was found to have a greater drug release profile than F1 and a higher cumulative release of 50.93 % vs 42.23 % for F1. Also Table 7-5 highlights the difference between the formulations with the DC formulation displaying an average concentration of 49.40 ± 9.52 vs. 41.61 ± 8.80 for the liquisolid formulation. These observations support the conclusion that liquisolid formulation can retard drug release of highly soluble compounds, particularly with the inclusion of polysorbate 80 in the formulation recipe as described by Javadzadeh et al (177). Interestingly, the images obtained from the dissolution imaging system also showed a greater level of hydration and swelling for the liquisolid compacts. This was also visible in the percentage growth profiles in Figure

7-12. F1 appeared to swell to a slightly greater percentage (65.68 % vs. 62.86 %) for F2. This increase could be attributed to the partially hydrated liquisolid formulation and also provide a further explanation for the lower drug release.

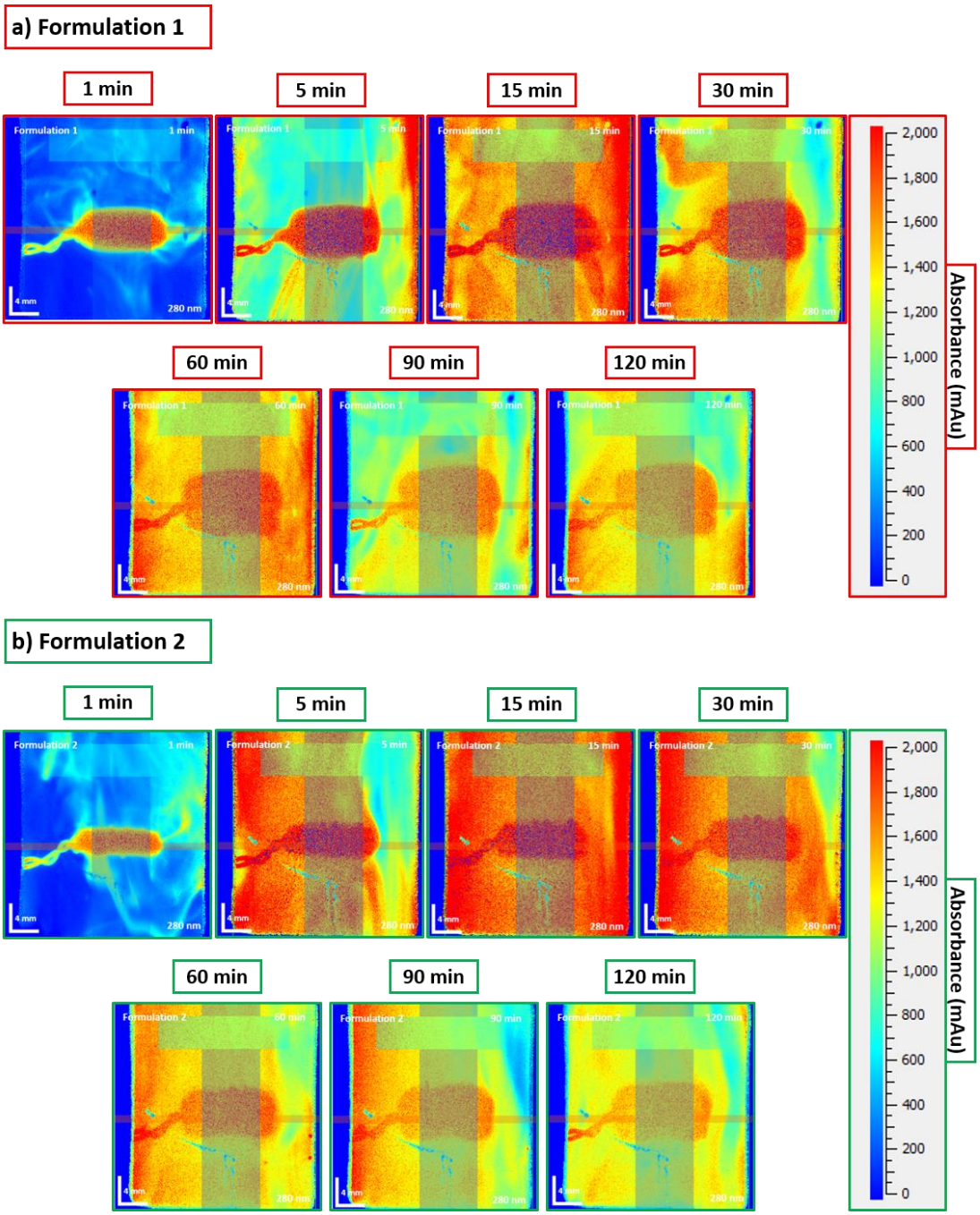

Figure 7-10 - UV images from the whole dosage assessment of the formulations F1 and F2 at the 280 nm wavelength.

The increase in compact size will have led to an increase in diffusion path length and a reduction in drug mobility through the matrix contributing to a further reduction in drug release.

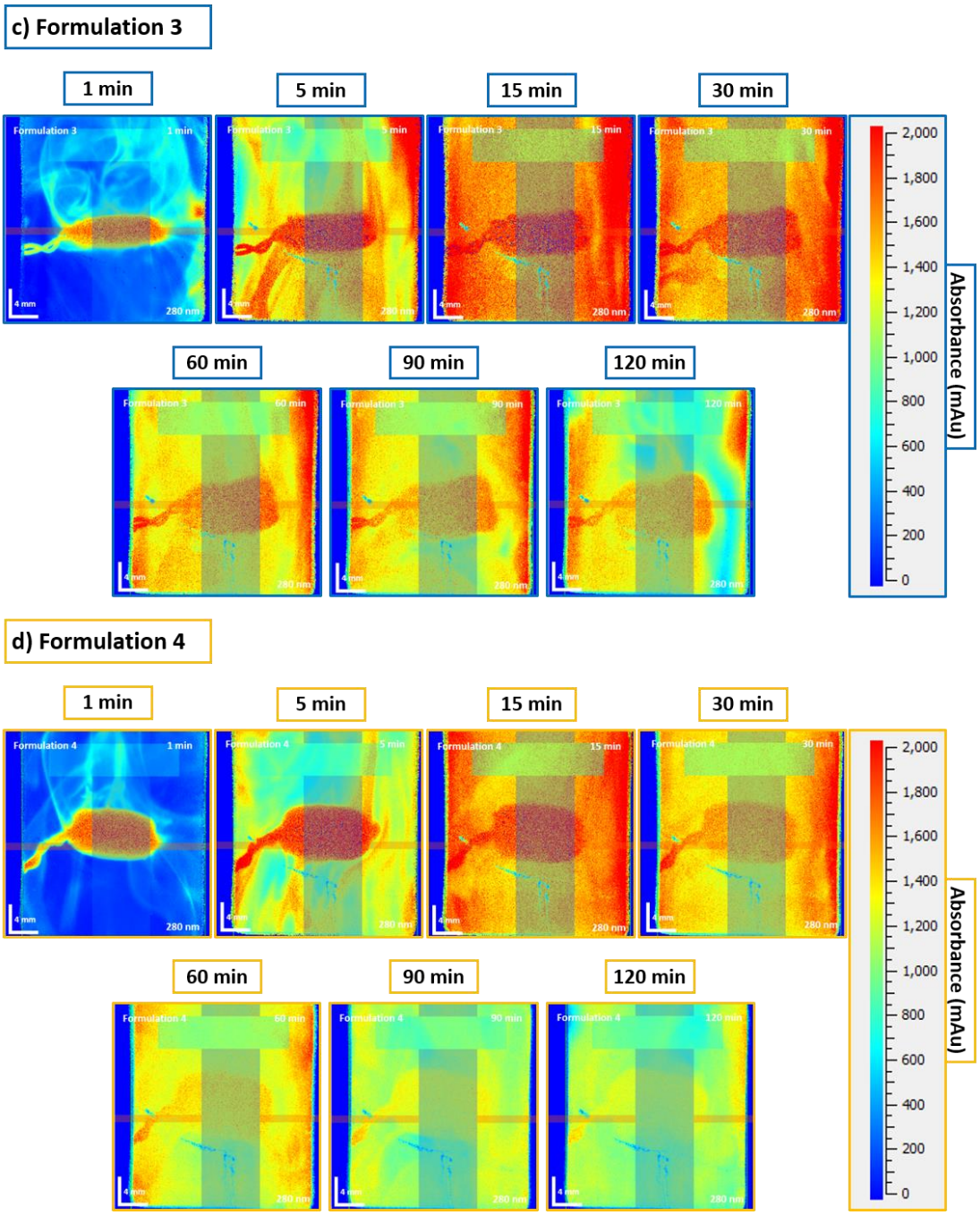

Figure 7-11 - UV images from the whole dosage assessment of the liquisolid formulations F3 and F4 at the 280 nm wavelength.

Figure 7-11 displays the UV images obtained from the formulations containing veegum as a replacement for the colloidal silica (F3 and F4). Visual assessment of the UV images appears to show similar drug release rates between F3 and F4 particularly in the first 15 minutes. This observation is supported by the average concentrations in Table 7-5 and the dissolution profiles in Figure 7-12. F3 and F4 were found to have similar drug release profiles and similar cumulative release values of 46.18 % and 45.91 % respectively. This similarity was also further complemented by the average

concentrations of 45.15 ± 8.53 for F3 and 44.91 ± 8.97 for F4. An interesting observation came from the review of the percentage growth profiles in Figure 7-12. It appeared that the DC formulation, F3, hydrated to a greater level than the liquisolid formulation which appeared to reach a plateau. This was in complete contrast to the formulations containing colloidal silica and may explain the similarity in drug release between the formulations.

When the formulations containing veegum and colloidal silica were compared, it appeared that in the liquisolid formulation, the veegum did not control drug release as effectively as colloidal silica at the ratio tested. However, as a physical mixture, veegum did exert a greater control of drug release which can be attributed to the swelling properties of the veegum. It also appeared from this work that the use of veegum in a liquisolid formulation appeared to have an influence on tablet hydration as the growth profile reached plateau earlier in the dissolution study than that of the liquisolid formulations containing colloidal silica. It is likely that the tablet may potentially have begun to erode and disintegrate had the dissolution experiment been continued further.

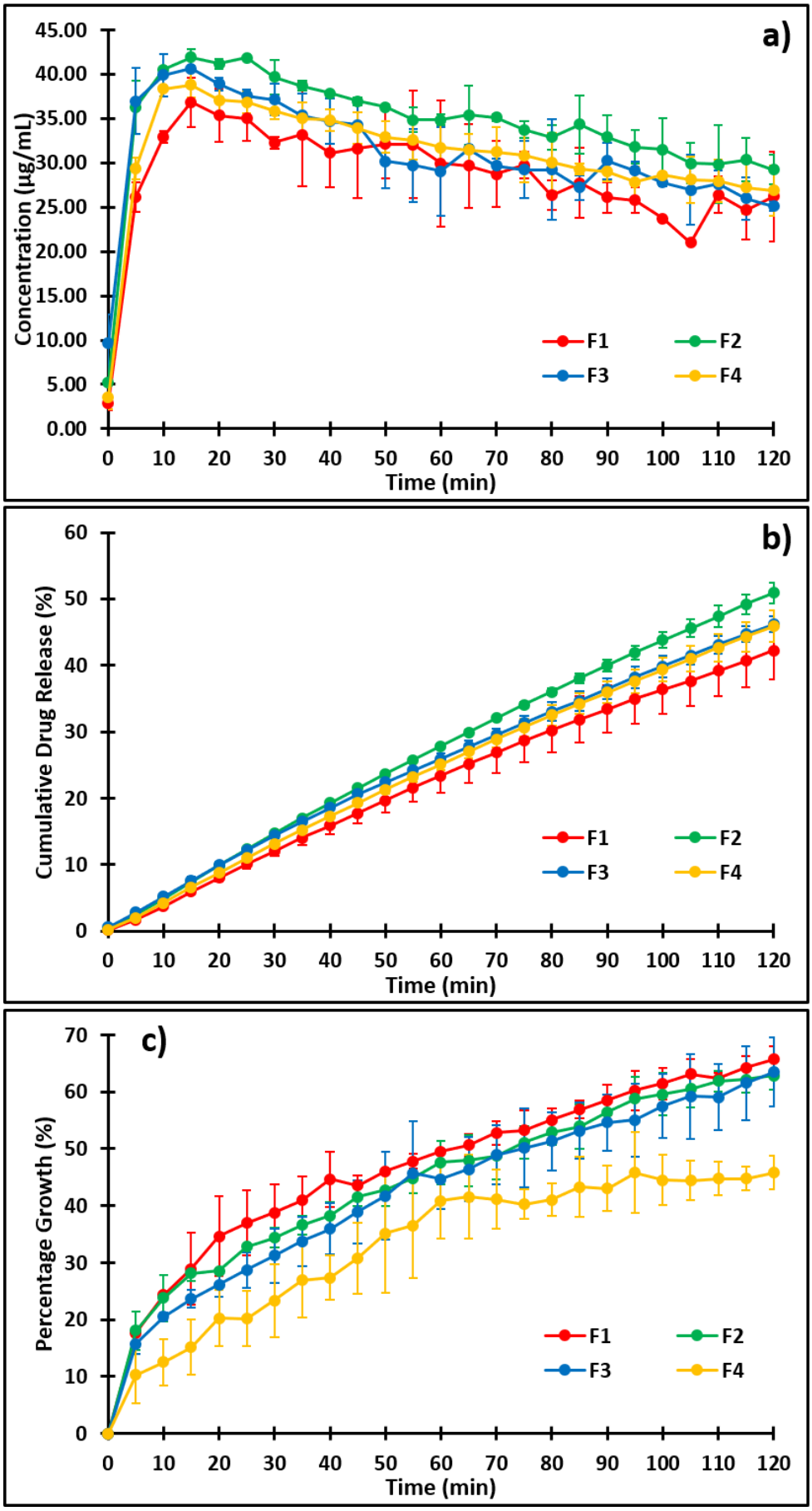

Figure 7-12 - Profiles obtained from the dissolution assessment of the formulations F1 to F4. a) Concentration profiles, b) Cumulative drug release profiles and c) Percentage growth profiles.

7.7 Conclusion

This chapter represents a novel assessment of the successful manufacture, characterisation and dissolution analysis of liquisolid formulations using the natural polysaccharide, sesamum gum and a smectite clay, veegum.

All formulations were characterised using XRPD and DSC and found to contain the characteristic peaks and endothermic melt for the crystalline PPN. Characterisation of the powder blends found all four formulations to have a poor flow however the liquisolid formulations showed an equal if not greater flow than the physical mixtures. Compacts produced from each of the four formulations showed the liquisolid formulations to produce much softer mechanical compacts compared to the physical mixture compacts. The liquisolid compacts were also uniform in distribution unlike the physical mixtures which showed a significant amount of mottling.

UV imaging was successfully employed to determine drug release and growth of the four formulations and crucially provided a visual assessment of the dissolution phenomena experienced by each formulation. The design of a methodology to calibrate the dissolution imaging system using the whole dosage cell was successful and good linearity was achieved. This opens the door to further improvements to this methodology (determination of limit of detection (LOD) of the system and an additional wavelength to allow for higher doses to be tested). The whole dosage cell was successfully employed to test the drug release and the growth of the liquisolid formulations and represents a complete assessment based on learnings from previous chapters in this thesis.

Veegum was successfully incorporated into a liquisolid formulation as a substitute for colloidal silica, however at the ratio tested, it was unable to control drug release as effectively. UV imaging detected and discovered that the liquisolid formulation

containing colloidal silica was able to restrict drug release to a greater extent than the physical mixture. This highlights that the replacement of conventional carriers such as HPMC with sesamum gum can be achieved with a similar desirable outcome. UV imaging also accurately tracked the growth of all the dosage forms tested with the 520 nm LED. This shows that the methodology designed and developed for hydrophilic matrices shown in earlier chapters can be applied to other controlled release delivery systems including active ingredients.

This chapter has highlighted how UV imaging could be utilised by a formulator to provide detailed insights into the dissolution behaviour of liquisolid formulations and has highlighted the potential of the systems calibration and the compatibility of the hydrophilic growth methodology designed in previous chapters.

Chapter 8 – Conclusion

This thesis constitutes an in-depth review into the use of two novel advanced imaging techniques in the field of pharmaceutics in the form of dissolution imaging and focus variation microscopy.

8.1 – Dissolution Imaging

This thesis set out to demonstrate the use of the SDI2 system as a routine dissolution instrument capable of providing robust and accurate data in the measurement of pharmaceutical actives, excipients, and formulations. To achieve this a number of milestones were established:

1. Develop an operational methodology for the SDI2 system exploring all of the systems features and capabilities.
2. Test any developed methodologies with different classifications of pharmaceutical materials to build up a knowledge base and aid method development.
3. Improve system versatility and reliability by identifying areas of improvement in the system and its operation.
4. Conduct comparative testing between already established techniques and the SDI2.
5. Highlight and showcase how the novel features of the SDI2 system can be a benefit to a formulator.

Chapters 3 and 4 successfully demonstrated design and use of a methodology for the whole dosage cell and showcased all the features of the SDI2 system from wavelength selection to the tailoring of the software to produce reliable and reproducible data. Chapters 6, 7 and 8 added to the method development by taking these learnings and applying that knowledge to different actives, excipients and dosage forms and successfully producing a data set that provided a wealth of insights to a formulator e.g.

webbing of solid dispersions, capsule dissolution and drug release from compacts. Crucially though, chapters 6, 7 and 8 also uncovered further areas of improvement in the system including compaction of the IDR compacts and calibration of the system.

Whilst this thesis demonstrated vast advances in the capabilities of UV imaging and the versatility of the instrument to provide reliable data it must be acknowledged that there remains two significant areas of investigation still remain before the technique can become a routine instrument of choice. The first is that this thesis focused predominantly on the development of the whole dosage cell, designing methods for its use, and also defining the limits of what the cell could be used for. This same level of investigation and method development also needs to be applied to the flow through cell, to establish a robust and comprehensive method of operation in the new system. The second area of investigation lies around milestone 4, despite this thesis testing the designed methodologies on a variety of pharmaceutical formulations and comparing the results with published work on conventional instrumentation a direct in-house assessment was not conducted. It is important that this milestone is explored before conclusions can be on the use of UV imaging as a routine assessment tool.

However, despite the remaining milestones yet to be completed, what this thesis has shown is that UV imaging and the SDI2 system have significant potential to be go-to instrumentation for the assessment of novel formulations. The insights that the system can provide are invaluable and with further investigation into this technique with those already established, there is potential for this technique to become a modern alternative to traditional instrumentation.

8.2 – Focus Variation Microscopy

This thesis set out to introduce Focus Variation Microscopy as a novel tool for the for the assessment of pharmaceutical surfaces and correlate the data gathered with their dissolution behaviour. To help achieve this, four milestone objectives were explored:

1. Build upon preliminary published data to establish a robust methodology for assessing pharmaceutical surfaces.
2. Identify useful meteorological parameters that can help predict pharmaceutical behaviour.
3. Assess the versatility of the system by using different materials and different forms of surface i.e., conventional tablets, IDR compacts.
4. Combine Focus Variation Microscopy with UV imaging to correlate observed behaviour with surface properties.

Chapters 5 and 6 successfully built upon previously published data by Ward et al. (58) and further tested the use of the microscope and the developed test methodology to successfully analyse IDR compacts of both the solid dispersions and the salts. This additional data also helped to build up a database of information on four useful ISO parameters that could be of interest to a formulator in ; *Sal, Str, Sdr* and *Smr2*. The microscope also proved its value by identifying key surface texture issues in the IDR compacts that could impact dissolution by providing both a high resolution 2D image and a detailed 3D surface profile.

Chapters 4 also tested the capabilities of the technique to measure tablet surfaces by developing a methodology to inspect the surfaces of polymer compacts. Focus variation microscopy also provided a deeper insight into the influence of polymer particle morphology on surface roughness. But perhaps most importantly, the focus variation microscope produced similar conclusions to physical assessment of the

compacts by suggesting that the Xanthan Gum compacts would hydrate and swell at the greatest rate with PEO hydrating at a much slower rate.

This thesis has successfully introduced focus variation microscopy to the field of pharmaceutics, however despite this success a number of further details will require examination before this technique can become the standard technique for surface measurement. The first is that only four surface parameters have been identified in this thesis and many more are defined in the ISO guidelines that could have potential use in the field of pharmaceutics and these will require exploring. In addition to this, a larger more robust study is required to provide more information on the correlation between the conclusions produced from the surface parameters currently explored and dissolution behaviour. The second detail that needs to be explored is that this thesis only exposed the technique to a small selection of formulations in salts, solid dispersions, and polymers. Further work will need to test the microscope against other formulations to fully understand the versatility of the instrument and improve the methods designed so far.

8.3 – Concluding Remarks

In conclusion, this thesis opens the door to two novel instruments and techniques that cannot only benefit the research and development of new novel therapeutics but also have the potential to be used in scale-up, manufacture and quality control within industry.

Chapter 9 – Future Work

There are a number of directions this project could continue to go. The first and foremost would be an in-depth and focused method development on the flow through cell and IDR analysis. This should include an investigation into the tooling marks left on the surface of the compact post compaction and how they influence IDR measurement. Also, this investigation could look at the method specifics for conducting IDR measurement as this thesis only experimented and used the manufacturer's recommended methodology specifics such as flow rate and compaction force. A final part of this development could be to design a calibration methodology for the IDR cell as the benefits identified with the whole dose cell could be useful in the determination of IDR i.e. same light source, path length and same equipment.

A number of innovative projects were also designed during this project. The first is an extension to chapter 4 of this thesis whereby three excipients in the form of lactose, DCP and MCC were added to the four polymers with the aim of cataloguing and imaging the influence of these on gel formation and dissolution. Also, blends containing excipients and active such as PPN were manufactured to investigate and image drug release from hydrophilic polymers. The second was an investigation into the drug release from 3D printed tablets. With this area of pharmaceutics gaining popularity, it would be interesting to see how both advanced imaging techniques perform in this field. The last but perhaps the most significant was the development of a novel whole dosage cell capable of imaging transdermal drug delivery systems. The design, material and method of manufacture had been selected and prototype testing completed. The next steps are to manufacture a second prototype and conduct a robust series of experiments to demonstrate versatility and reliability. Further development of this project may provide the dissolution imaging system to a variety of transdermal delivery systems including; creams, gels and patches.

Chapter 10 – References

(1) Kaufman K. CMOS Technology for Scientific Imaging. 2010; Available at: http://www.spectroscopyonline.com/cmos-technology-scientific-imaging-0. Accessed Aug 7, 2019.

(2) M. Hillebrand, N. Stevanovic, B. J. Hosticka, J. E. Santos Conde, A. Teuner, M. Schwarz. High speed camera system using a CMOS image sensor. Proceedings of the IEEE Intelligent Vehicles Symposium 2000 (Cat. No.00TH8511) 2000:656-661.

(3) Hoffman A, Loose M, Suntharalingam V. CMOS detector technology. Experimental Astronomy 2005;19(1-3):111-134.

(4) Paraytec Ltd. Actipix Software Manual Version 1.2. 2009 06 Jun.

(5) Bigas M, Cabruja E, Forest J, Salvi J. Review of CMOS image sensors. Microelectronics Journal 2006;37(5):433-451.

(6) Lulé T, Benthien S, Keller H, Mutze F, Rieve P, Seibel K, et al. Sensitivity of CMOS based imagers and scaling perspectives. IEEE Trans Electron Devices 2000;47(11):2110-2122.

(7) Low-FPN high-gain capacitive transimpedance amplifier for low-noise CMOS image sensors. Sensors and Camera Systems for Scientific, Industrial, and Digital Photography Applications II: International Society for Optics and Photonics; 2001.

(8) Xu C, Ki W, Chan M. A low-voltage CMOS Complementary Active Pixel Sensor (CAPS) fabricated using a 0.25 μm CMOS technology. IEEE Electron Device Lett 2002;23(7):398-400.

(9) Kulp M, Urban PL, Kaljurand M, Bergström ET, Goodall DM. Visualization of electrophoretically mediated in-capillary reactions using a complementary metal oxide semiconductor-based absorbance detector. Analytica Chimica Acta 2006;570(1):1-7.

(10) Bergström ET, Goodall DM, Pokrić B, Allinson NM. A Charge Coupled Device Array Detector for Single-Wavelength and Multiwavelength Ultraviolet Absorbance in Capillary Electrophoresis. Anal Chem 1999;71(19):4376-4384.

(11) Goodall DM, Bergstrom ET, Allinson NM, Moon KJ. Optical assembly and method for detection of light transmission. Optical assembly and method for detection of light transmission 2007.

(12) Urban PL, Goodall DM, Bergström ET, Bruce NC. Electrophoretic assay for penicillinase: Substrate specificity screening by parallel CE with an active pixel sensor. ELECTROPHORESIS 2007 Jun 12,;28(12):1926-1936.

(13) Urban PL, Bergström ET, Goodall DM, Narayanaswamy S, Bruce NC. Electrophoretic method for assessment of substrate promiscuity of a heterogeneous

biocatalyst using an area imaging ultraviolet detector. The Analyst 2007 Oct;132(10):979.

(14) Urban PL, Goodall DM, Bergström ET, Bruce NC. Electrophoretically mediated microanalysis of a nicotinamide adenine dinucleotide-dependent enzyme and its facile multiplexing using an active pixel sensor UV detector. Journal of Chromatography A 2007;1162(2):132-140.

(15) Alexander J S Chapman, David M Goodall - Paraytec Ltd, 1a St Georges Place, Tadcaster Road, York, YO24 1GN, et al. A novel approach to measurement of hydrodynamic radius for a standard protein using UV area imaging detection.

(16) Urban PL, Goodall DM, Carvalho AZ, Bergström ET, Van Schepdael A, Bruce NC. Multi-compound electrophoretic assays for tyramine oxidase with a UV area detector imaging multiple windows on a looped capillary. Journal of Chromatography A 2008;1206(1):52-63.

(17) Amantonico A, Urban PL, Zenobi R. Facile analysis of metabolites by capillary electrophoresis coupled to matrix-assisted laser desorption/ionization mass spectrometry using target plates with polysilazane nanocoating and grooves. The Analyst 2009 Aug;134(8):1536-1540.

(18) Østergaard J, Jensen H. Simultaneous Evaluation of Ligand Binding Properties and Protein Size by Electrophoresis and Taylor Dispersion in Capillaries. Analytical Chemistry 2009 Oct 15,;81(20):8644-8648.

(19) Goodall David M, Bergstrom Ed, Surve Mebs. Separation, size and charge determination of small molecules using CE in combination with UV area imaging.

(20) Østergaard J, Meng-Lund E, Larsen SW, Larsen C, Petersson K, Lenke J, et al. Real-Time UV Imaging of Nicotine Release from Transdermal Patch. Pharm Res 2010;27(12):2614-2623.

(21) Østergaard J, Ye F, Rantanen J, Yaghmur A, Larsen SW, Larsen C, et al. Monitoring lidocaine single-crystal dissolution by ultraviolet imaging. J Pharm Sci 2011;100(8):3405-3410.

(22) Pajander J, Baldursdottir S, Rantanen J, Østergaard J. Behaviour of HPMC compacts investigated using UV-imaging. International Journal of Pharmaceutics 2012;427(2):345-353.

(23) Ye F, Yaghmur A, Jensen H, Larsen SW, Larsen C, Østergaard J. Real-time UV imaging of drug diffusion and release from Pluronic F127 hydrogels. European Journal of Pharmaceutical Sciences 2011;43(4):236-243.

(24) Ye F, Larsen SW, Yaghmur A, Jensen H, Larsen C, Østergaard J. Drug release into hydrogel-based subcutaneous surrogates studied by UV imaging. J Pharm Biomed Anal 2012;71:27-34.

(25) Ye F, Larsen SW, Yaghmur A, Jensen H, Larsen C, Østergaard J. Real-time UV imaging of piroxicam diffusion and distribution from oil solutions into gels mimicking

the subcutaneous matrix. European Journal of Pharmaceutical Sciences 2012;46(1–2):72-78.

(26) Boetker JP, Savolainen M, Koradia V, Tian F, Rades T, Müllertz A, et al. Insights into the Early Dissolution Events of Amlodipine Using UV Imaging and Raman Spectroscopy. Molecular Pharmaceutics 2011 Aug 1,;8(4):1372-1380.

(27) Gordon S, Naelap K, Rantanen J, Selen A, Mllertz A, stergaard J. Real-time dissolution behavior of furosemide in biorelevant media as determined by UV imaging. Pharmaceutical Development & Technology 2013 Nov;18(6):1407-1416.

(28) Nielsen LH, Gordon S, Pajander JP, Østergaard J, Rades T, Müllertz A. Biorelevant characterisation of amorphous furosemide salt exhibits conversion to a furosemide hydrate during dissolution. International Journal of Pharmaceutics 2013 Nov 30,;457(1):14-24.

(29) Larsen SW, Østergaard J, Yaghmur A, Jensen H, Larsen C. Use of in vitro release models in the design of sustained and localized drug delivery systems for subcutaneous and intra-articular administration. Journal of Drug Delivery Science and Technology 2013;23(4):315-324.

(30) Sarnes A, Østergaard J, Jensen SS, Aaltonen J, Rantanen J, Hirvonen J, et al. Dissolution study of nanocrystal powders of a poorly soluble drug by UV imaging and channel flow methods. European Journal of Pharmaceutical Sciences 2013;50(3–4):511-519.

(31) Gaunø MH, Vilhelmsen T, Larsen CC, Boetker JP, Wittendorff J, Rantanen J, et al. Real-time in vitro dissolution of 5-aminosalicylic acid from single ethyl cellulose coated extrudates studied by UV imaging. Journal of Pharmaceutical and Biomedical Analysis 2013 Sep;83:49-56.

(32) Boetker JP, Rantanen J, Rades T, Müllertz A, Østergaard J, Jensen H. A new approach to dissolution testing by UV imaging and finite element simulations. Pharm Res 2013;30(5):1328-1337.

(33) Qiao N, Wang K, Schlindwein W, Davies A, Li M. In situ monitoring of carbamazepine–nicotinamide cocrystal intrinsic dissolution behaviour. European Journal of Pharmaceutics and Biopharmaceutics 2013;83(3):415-426.

(34) Li M, Qiao N, Wang K. Influence of sodium lauryl sulfate and Tween 80 on carbamazepine–nicotinamide cocrystal solubility and dissolution behaviour. Pharmaceutics 2013;5(4):508-524.

(35) Jensen SS, Jensen H, Cornett C, Møller EH, Østergaard J. Insulin diffusion and self-association characterized by real-time UV imaging and Taylor dispersion analysis. Journal of Pharmaceutical and Biomedical Analysis 2014 Apr 15,;92:203-210.

(36) Østergaard J, Jensen H, Larsen SW, Larsen C, Lenke J. Microenvironmental pH measurement during sodium naproxenate dissolution in acidic medium by UV/vis imaging. Journal of Pharmaceutical and Biomedical Analysis 2014 Nov;100:290-293.

(37) Østergaard J, Wu JX, Naelap K, Boetker JP, Jensen H, Rantanen J. Simultaneous UV imaging and Raman spectroscopy for the measurement of solvent-mediated phase transformations during dissolution testing. J Pharm Sci 2014;103(4):1149-1156.

(38) Østergaard J, Lenke J, Sun Y, Ye F. UV Imaging for In Vitro Dissolution and Release Studies: Intial Experiences. Dissolution Technologies 2014;21(4).

(39) Niederquell A, Kuentz M. Biorelevant dissolution of poorly soluble weak acids studied by UV imaging reveals ranges of fractal-like kinetics. International Journal of Pharmaceutics 2014 Mar 10,;463(1):38-49.

(40) Jensen SS, Jensen H, Cornett C, Møller EH, Østergaard J. Real-time UV imaging identifies the role of pH in insulin dissolution behavior in hydrogel-based subcutaneous tissue surrogate. European Journal of Pharmaceutical Sciences 2015;69:26-36.

(41) Kuentz M. Analytical technologies for real-time drug dissolution and precipitation testing on a small scale. J Pharm Pharmacol 2015;67(2):143-159.

(42) Gautschi N, Van Hoogevest P, Kuentz M. Amorphous drug dispersions with mono-and diacyl lecithin: on molecular categorization of their feasibility and UV dissolution imaging. Int J Pharm 2015;491(1-2):218-230.

(43) Early developability screen of therapeutic antibody candidates using Taylor dispersion analysis and UV area imaging detection. MAbs: Taylor & Francis; 2015.

(44) Jensen SS, Jensen H, Goodall DM, Østergaard J. Performance characteristics of UV imaging instrumentation for diffusion, dissolution and release testing studies. J Pharm Biomed Anal 2016;131:113-123.

(45) Jensen SS, Jensen H, Møller EH, Cornett C, Siepmann F, Siepmann J, et al. In vitro release studies of insulin from lipid implants in solution and in a hydrogel matrix mimicking the subcutis. European journal of pharmaceutical sciences 2016;81:103-112.

(46) Madelung P, Bertelsen P, Jacobsen J, Müllertz A, Østergaard J. Dissolution enhancement of griseofulvin from griseofulvin-sodium dodecyl sulfate discs investigated by UV imaging. Journal of Drug Delivery Science and Technology 2017;39:516-522.

(47) Sun Y, Jensen H, Petersen NJ, Larsen SW, Østergaard J. Phase separation of in situ forming poly (lactide-co-glycolide acid) implants investigated using a hydrogel-based subcutaneous tissue surrogate and UV–vis imaging. J Pharm Biomed Anal 2017;145:682-691.

(48) Sun Y, Østergaard J. Application of UV imaging in formulation development. Pharm Res 2017;34(5):929-940.

(49) Lu Y, Li M. Simultaneous rapid determination of the solubility and diffusion coefficients of a poorly water-soluble drug based on a novel UV imaging system. J Pharm Sci 2016;105(1):131-138.

(50) Sun Y, Jensen H, Petersen NJ, Larsen SW, Østergaard J. Concomitant monitoring of implant formation and drug release of in situ forming poly (lactide-co-glycolide acid) implants in a hydrogel matrix mimicking the subcutis using UV–vis imaging. J Pharm Biomed Anal 2018;150:95-106.

(51) Østergaard J. UV imaging in pharmaceutical analysis. J Pharm Biomed Anal 2018;147:140-148.

(52) Hiew TN, Alaudin MIB, Chua SM, Heng PWS. A study of the impact of excipient shielding on initial drug release using UV imaging. Int J Pharm 2018;553(1-2):229-237.

(53) Ross SA, Ward A, Basford P, McAllister M, Douroumis D. Coprocessing of Pharmaceutical Cocrystals for High Quality and Enhanced Physicochemical Stability. Crystal Growth & Design 2018;19(2):876-888.

(54) International Standards Organisation. BS EN ISO 25178-2:2012: Geometrical product specifications (GPS). Surface texture. Areal. Terms, definitions and surface texture parameters. 2012 Apr 30,.

(55) Leach R. Optical Measurement of Surface Topography: : Springer Verlag; 2011.

(56) Meyer G, Amer NM. Novel optical approach to atomic force microscopy. Appl Phys Lett 1988;53(12):1045-1047.

(57) Danzl R, Helmli F, Scherer S. Focus Variation – a Robust Technology for High Resolution Optical 3D Surface Metrology. Strojniški vestnik – Journal of Mechanical Engineering 2011 Mar 15,;2011(3):245-256.

(58) Ward A, Walton K, Box K, Østergaard J, Gillie LJ, Conway BR, et al. Variable-focus microscopy and UV surface dissolution imaging as complementary techniques in intrinsic dissolution rate determination. International Journal of Pharmaceutics 2017;530(1):139-144.

(59) Ward A, Walton K, Mawla N, Kaialy W, Liu L, Timmins P, et al. Development of a novel method utilising dissolution imaging for the measurement of swelling behaviour in hydrophilic matrices. International journal of pharmaceutics: X 2019;1:100013.

(60) Tahara K, Yamamoto K, Nishihata T. Overall mechanism behind matrix sustained release (SR) tablets prepared with hydroxypropyl methylcellulose 2910. J Controlled Release 1995;35(1):59-66.

(61) Kavanagh N, Corrigan OI. Swelling and erosion properties of hydroxypropylmethylcellulose (Hypromellose) matrices—influence of agitation rate and dissolution medium composition. International Journal of Pharmaceutics 2004;279(1):141-152.

(62) Kaunisto E, Abrahmsen-Alami S, Borgquist P, Larsson A, Nilsson B, Axelsson A. A mechanistic modelling approach to polymer dissolution using magnetic resonance microimaging. J Controlled Release 2010;147(2):232-241.

(63) Kulinowski P, Dorożyński P, Młynarczyk A, Węglarz WP. Magnetic Resonance Imaging and Image Analysis for Assessment of HPMC Matrix Tablets Structural Evolution in USP Apparatus 4. Pharm Res 2011;28(5):1065-1073.

(64) Pygall SR, Whetstone J, Timmins P, Melia CD. Pharmaceutical applications of confocal laser scanning microscopy: The physical characterisation of pharmaceutical systems. Advanced Drug Delivery Reviews 2007;59(14):1434-1452.

(65) Melia CD, Marshall P, Stark P, Cunningham S, Kinahan A, Devane J. Investigating in vitro drug release mechanisms inside dosage forms. Adv Exp Med Biol 1997;423:129-135.

(66) Avalle P, Pygall SR, Gower N, Midwinter A. The use of in situ near infrared spectroscopy to provide mechanistic insights into gel layer development in HPMC hydrophilic matrices. European Journal of Pharmaceutical Sciences 2011;43(5):400-408.

(67) Avalle P, Pygall SR, Pritchard J, Jastrzemska A. Interrogating erosion-based drug liberation phenomena from hydrophilic matrices using near infrared (NIR) spectroscopy. European Journal of Pharmaceutical Sciences 2013;48(1):72-79.

(68) Ashraf M, luorno VL, Coffin-Beach D, Evans CA, Augsburger LL. A Novel Nuclear Magnetic Resonance (NMR) Imaging Method for Measuring the Water Front Penetration Rate in Hydrophilic Polymer Matrix Capsule Plugs and Its Role in Drug Release. Pharm Res 1994;11(5):733-737.

(69) Rajabi-Siahboomi A, Bowtell RW, Mansfield P, Davies MC, Melia CD. Structure and Behavior in Hydrophilic Matrix Sustained Release Dosage Forms: 4. Studies of Water Mobility and Diffusion Coefficients in the Gel Layer of HPMC Tablets Using NMR Imaging. Pharm Res 1996;13(3):376-380.

(70) Yassin S, Su K, Lin H, Gladden LF, Axel Zeitler J. Diffusion and Swelling Measurements in Pharmaceutical Powder Compacts Using Terahertz Pulsed Imaging. Journal of Pharmaceutical Sciences 2015;104(5):1658-1667.

(71) Boetker JP, Rantanen J, Rades T, Müllertz A, Østergaard J, Jensen H. A New Approach to Dissolution Testing by UV Imaging and Finite Element Simulations. Pharm Res 2013;30(5):1328-1337.

(72) Hulse WL, Gray J, Forbes RT. A discriminatory intrinsic dissolution study using UV area imaging analysis to gain additional insights into the dissolution behaviour of active pharmaceutical ingredients. International Journal of Pharmaceutics 2012;434(1):133-139.

(73) Pajander J, Baldursdottir S, Rantanen J, Østergaard J. Behaviour of HPMC compacts investigated using UV-imaging. International Journal of Pharmaceutics 2012;427(2):345-353.

(74) Ervasti T, Simonaho S, Ketolainen J, Forsberg P, Fransson M, Wikström H, et al. Continuous manufacturing of extended release tablets via powder mixing and direct compression. International Journal of Pharmaceutics 2015;495(1):290-301.

(75) Bonferoni MC, Rossi S, Ferrari F, Bertoni M, Caramella C. A study of three hydroxypropylmethyl cellulose substitution types: effect of particle size and shape on hydrophilic matrix performances. STP Pharma Sciences 1996;6(4):277-284.

(76) Ward A, Brown B, Walton K, Timmins P, Conway BR, Asare-Addo K. Application of Focus Variation Microscopy and Dissolution Imaging in Understanding the Behaviour of Hydrophilic Matrices. Pharmaceutics 2020;12(12).

(77) Timmins P, Pygall SR, Melia CD. Hydrophilic matrix tablets for oral controlled release. : Springer; 2014.

(78) Lazzari A, Kleinebudde P, Knop K. Xanthan gum as a rate-controlling polymer for the development of alcohol resistant matrix tablets and mini-tablets. International Journal of Pharmaceutics 2018;536(1):440-449.

(79) Kadajji VG, Betageri GV. Water soluble polymers for pharmaceutical applications. Polymers 2011;3(4):1972-2009.

(80) Sharma BR, Naresh L, Dhuldhoya NC, Merchant SU, Merchant UC. Xanthan gum-A boon to food industry. Food promotion chronicle 2006;1(5):27-30.

(81) Talukdar MM, Michoel A, Rombaut P, Kinget R. Comparative study on xanthan gum and hydroxypropylmethyl cellulose as matrices for controlled-release drug delivery I. Compaction and in vitro drug release behaviour. International Journal of Pharmaceutics 1996;129(1):233-241.

(82) Talukdar MM, Vinckier I, Moldenaers P, Kinget R. Rheological Characterization of Xanthan Gum and Hydroxypropylmethyl Cellulose with Respect to Controlled-Release Drug Delivery. Journal of Pharmaceutical Sciences 1996;85(5):537-540.

(83) Lazzari A, Kleinebudde P, Knop K. Xanthan gum as a rate-controlling polymer for the development of alcohol resistant matrix tablets and mini-tablets. International Journal of Pharmaceutics 2018;536(1):440-449.

(84) Cai XJ, Mesquida P, Jones SA. Investigating the ability of nanoparticle-loaded hydroxypropyl methylcellulose and xanthan gum gels to enhance drug penetration into the skin. International Journal of Pharmaceutics 2016;513(1):302-308.

(85) Santos H, Veiga F, Pina ME, Sousa JJ. Compaction, compression and drug release properties of diclofenac sodium and ibuprofen pellets comprising xanthan gum as a sustained release agent. International Journal of Pharmaceutics 2005;295(1):15-27.

(86) Crowley MM, Zhang F, Koleng JJ, McGinity JW. Stability of polyethylene oxide in matrix tablets prepared by hot-melt extrusion. Biomaterials 2002;23(21):4241-4248.

(87) Moroni A, Ghebre-Sellassie I. Application of poly (oxyethylene) homopolymers in sustained release solid formulations. Drug Dev Ind Pharm 1995;21(12):1411-1428.

(88) Kim C. Drug Release from Compressed Hydrophilic POLYOX-WSR Tablets. Journal of Pharmaceutical Sciences 1995;84(3):303-306.

(89) Shojaee S, Cumming I, Kaialy W, Nokhodchi A. The influence of vitamin E succinate on the stability of polyethylene oxide PEO controlled release matrix tablets. Colloids and Surfaces B: Biointerfaces 2013;111:486-492.

(90) Apicella A, Cappello B, Del Nobile MA, La Rotonda MI, Mensitieri G, Nicolais L. Poly (ethylene oxide)(PEO) and different molecular weight PEO blends monolithic devices for drug release. Biomaterials 1993;14(2):83-90.

(91) Stringer JL, Peppas NA. Diffusion of small molecular weight drugs in radiation-crosslinked poly (ethylene oxide) hydrogels. J Controlled Release 1996;42(2):195-202.

(92) Efentakis M, Vlachou M. Evaluation of high molecular weight poly (oxyethylene)(Polyox) polymer: studies of flow properties and release rates of furosemide and captopril from controlled-release hard gelatin capsules. Pharm Dev Technol 2000;5(3):339-346.

(93) Zhang F, McGinity JW. Properties of sustained-release tablets prepared by hot-melt extrusion. Pharm Dev Technol 1999;4(2):241-250.

(94) Asare-Addo K, Kaialy W, Levina M, Rajabi-Siahboomi A, Ghori MU, Supuk E, et al. The influence of agitation sequence and ionic strength on in vitro drug release from hypromellose (E4M and K4M) ER matrices—The use of the USP III apparatus. Colloids and Surfaces B: Biointerfaces 2013;104:54-60.

(95) Levina M, Rajabi-Siahboomi A. An Industrial Perspective on Hydrophilic Matrix Tablets Based on Hyproxypropyl Methylcellulose (Hypromellose). In: Timmins P, Pygall SR, Melia CD, editors. Hydrophilic Matrix Tablets for Oral Controlled Release New York, NY: Springer New York; 2014. p. 53-85.

(96) Hu A, Chen C, Mantle MD, Wolf B, Gladden LF, Rajabi-Siahboomi A, et al. The Properties of HPMC:PEO Extended Release Hydrophilic Matrices and their Response to Ionic Environments. Pharm Res 2017;34(5):941-956.

(97) Khaled SA, Burley JC, Alexander MR, Yang J, Roberts CJ. 3D printing of five-in-one dose combination polypill with defined immediate and sustained release profiles. J Controlled Release 2015;217:308-314.

(98) Van Snick B, Holman J, Cunningham C, Kumar A, Vercruysse J, De Beer T, et al. Continuous direct compression as manufacturing platform for sustained release tablets. Int J Pharm 2017;519(1–2):390-407.

(99) Asare-Addo K, Walton K, Ward A, Totea A, Taheri S, Alshafiee M, et al. Direct imaging of the dissolution of salt forms of a carboxylic acid drug. Int J Pharm 2018;551(1-2):290-299.

(100) Korn C, Balbach S. Compound selection for development – Is salt formation the ultimate answer? Experiences with an extended concept of the “100mg approach”. European Journal of Pharmaceutical Sciences 2014;57:257-263.

(101) Al-Hamidi H, Edwards AA, Mohammad MA, Nokhodchi A. Glucosamine HCl as a new carrier for improved dissolution behaviour: Effect of grinding. Colloids and Surfaces B: Biointerfaces 2010;81(1):96-109.

(102) Ku MS, Dulin W. A biopharmaceutical classification-based Right-First-Time formulation approach to reduce human pharmacokinetic variability and project cycle time from First-In-Human to clinical Proof-Of-Concept. Pharm Dev Technol 2012;17(3):285-302.

(103) Williams HD, Trevaskis NL, Charman SA, Shanker RM, Charman WN, Pouton CW, et al. Strategies to address low drug solubility in discovery and development. Pharmacol Rev 2013;65(1):315-499.

(104) Asare-Addo K, Conway BR. Solubility Determinations for Pharmaceutical API. Poorly Soluble Drugs: Pan Stanford; 2017. p. 43-108.

(105) David SE, Ramirez M, Timmins P, Conway BR. Comparative physical, mechanical and crystallographic properties of a series of gemfibrozil salts. J Pharm Pharmacol 2010;62(11):1519-1525.

(106) Ramirez M, David SE, Schwalbe CH, Asare-Addo K, Conway BR, Timmins P. Crystal packing arrangement, chain conformation, and physicochemical properties of gemfibrozil amine salts. Crystal Growth & Design 2017;17(7):3743-3750.

(107) Amidon GL, Lennernäs H, Shah VP, Crison JR. A theoretical basis for a biopharmaceutic drug classification: the correlation of in vitro drug product dissolution and in vivo bioavailability. Pharm Res 1995;12(3):413-420.

(108) Stahl PH, Wermuth CG. Handbook of pharmaceutical salts: properties, selection and use. Chem.Int 2002;24:21.

(109) He Y, Ho C, Yang D, Chen J, Orton E. Measurement and accurate interpretation of the solubility of pharmaceutical salts. J Pharm Sci 2017;106(5):1190-1196.

(110) Pindelska E, Sokal A, Kolodziejski W. Pharmaceutical cocrystals, salts and polymorphs: Advanced characterization techniques. Adv Drug Deliv Rev 2017;117:111-146.

(111) Berge SM, Bighley LD, Monkhouse DC. Pharmaceutical salts. J Pharm Sci 1977;66(1):1-19.

(112) Etherson K, Dunn C, Matthews W, Pamelund H, Barragat C, Sanderson N, et al. An interlaboratory investigation of intrinsic dissolution rate determination using surface dissolution. European Journal of Pharmaceutics and Biopharmaceutics 2020;150:24-32.

(113) Niederquell A, Kuentz M. Biorelevant dissolution of poorly soluble weak acids studied by UV imaging reveals ranges of fractal-like kinetics. International Journal of Pharmaceutics 2014;463(1):38-49.

(114) Gordon S, Naelap K, Rantanen J, Selen A, Müllertz A, Østergaard J. Real-time dissolution behavior of furosemide in biorelevant media as determined by UV imaging. Pharm Dev Technol 2013;18(6):1407-1416.

(115) Hulse WL, Gray J, Forbes RT. A discriminatory intrinsic dissolution study using UV area imaging analysis to gain additional insights into the dissolution behaviour of active pharmaceutical ingredients. Int J Pharm 2012;434(1-2):133-139.

(116) Østergaard J, Wu JX, Naelapää K, Boetker JP, Jensen H, Rantanen J. Simultaneous UV Imaging and Raman Spectroscopy for the Measurement of Solvent-Mediated Phase Transformations During Dissolution Testing. J Pharm Sci 2014;103(4):1149-1156.

(117) Ye F, Yaghmur A, Jensen H, Larsen SW, Larsen C, Østergaard J. Real-time UV imaging of drug diffusion and release from Pluronic F127 hydrogels. European Journal of Pharmaceutical Sciences 2011;43(4):236-243.

(118) Wisher D. Martindale: The complete drug reference. Journal of the Medical Library Association 2012;100(1):75-77.

(119) Yang Q, Ren T, Yang S, Li X, Chi Y, Yang Y, et al. Synthesis and Pharmacokinetic Study of Three Gemfibrozil Salts: An Exploration of the Structure–Property Relationship. Crystal Growth & Design 2016;16(10):6060-6068.

(120) Ward A, Walton K, Box K, Østergaard J, Gillie LJ, Conway BR, et al. Variable-focus microscopy and UV surface dissolution imaging as complementary techniques in intrinsic dissolution rate determination. International Journal of Pharmaceutics 2017;530(1):139-144.

(121) Laity PR, Asare-Addo K, Sweeney F, Šupuk E, Conway BR. Using small-angle X-ray scattering to investigate the compaction behaviour of a granulated clay. Appl Clay Sci 2015;108:149-164.

(122) Aigner Z, Hassan HB, Berkesi O, Kata M, Erős I. Thermoanalytical, FTIR and X-ray studies of gemfibrozil-cyclodextrin complexes. Journal of thermal analysis and calorimetry 2005;81(2):267-272.

(123) Chen Y, Lin P, Tang M, Chen Y. Solid solubility of antilipemic agents and micronization of gemfibrozil in supercritical carbon dioxide. The Journal of Supercritical Fluids 2010;52(2):175-182.

(124) Asare-Addo K, Alshafiee M, Walton K, Ward A, Totea A, Taheri S, et al. Effect of preparation method on the surface properties and UV imaging of indomethacin solid dispersions. European Journal of Pharmaceutics and Biopharmaceutics 2019;137:148-163.

(125) Kanikkannan N. Technologies to improve the solubility, dissolution and bioavailability of poorly soluble drugs. J.Anal.Pharm.Res. 2018;7:00198.

(126) Totea AM, Dorin I, Gavrilov G, Laity PR, Conway BR, Waters L, et al. Real time calorimetric characterisation of clay – drug complex dispersions and particles. International Journal of Pharmaceutics: X 2019;1:100003.

(127) Pongjanyakul T, Khunawattanakul W, Puttipipatkhachorn S. Physicochemical characterizations and release studies of nicotine–magnesium aluminum silicate complexes. Appl Clay Sci 2009;44(3-4):242-250.

(128) Évora AOL, Castro RAE, Maria TMR, Silva MR, ter Horst JH, Canotilho J, et al. A thermodynamic based approach on the investigation of a diflunisal pharmaceutical co-crystal with improved intrinsic dissolution rate. International Journal of Pharmaceutics 2014;466(1):68-75.

(129) Al-Hamidi H, Asare-Addo K, Desai S, Kitson M, Nokhodchi A. The dissolution and solid-state behaviours of coground ibuprofen–glucosamine HCl. Drug Dev Ind Pharm 2015;41(10):1682-1692.

(130) Al-Hamidi H, Edwards AA, Douroumis D, Asare-Addo K, Nayebi AM, Reyhani-Rad S, et al. Effect of glucosamine HCl on dissolution and solid state behaviours of piroxicam upon milling. Colloids and Surfaces B: Biointerfaces 2013;103:189-199.

(131) Srinarong P, Faber JH, Visser MR, Hinrichs WLJ, Frijlink HW. Strongly enhanced dissolution rate of fenofibrate solid dispersion tablets by incorporation of superdisintegrants. European Journal of Pharmaceutics and Biopharmaceutics 2009;73(1):154-161.

(132) Gonnissen Y, Remon JP, Vervaet C. Effect of maltodextrin and superdisintegrant in directly compressible powder mixtures prepared via co-spray drying. European Journal of Pharmaceutics and Biopharmaceutics 2008;68(2):277-282.

(133) Adebisi AO, Kaialy W, Hussain T, Al-Hamidi H, Nokhodchi A, Conway BR, et al. Solid-state, triboelectrostatic and dissolution characteristics of spray-dried piroxicam-glucosamine solid dispersions. Colloids and Surfaces B: Biointerfaces 2016;146:841-851.

(134) Mogal SA, Gurjar PN, Yamgar DS, Kamod AC. Solid dispersion technique for improving solubility of some poorly soluble drugs. Der Pharmacia Lettre 2012;4(5):1574-1586.

(135) Asare-Addo K, Šupuk E, Al-Hamidi H, Owusu-Ware S, Nokhodchi A, Conway BR. Triboelectrification and dissolution property enhancements of solid dispersions. International Journal of Pharmaceutics 2015;485(1):306-316.

(136) Jiménez de los Santos, Cesáreo J., Pérez-Martínez JI, Gómez-Pantoja ME, Moyano JR. Enhancement of albendazole dissolution properties using solid dispersions with Gelucire 50/13 and PEG 15000. Journal of Drug Delivery Science and Technology 2017;42:261-272.

(137) Otto DP, Otto A, de Villiers MM. Experimental and mesoscale computational dynamics studies of the relationship between solubility and release of quercetin from PEG solid dispersions. International Journal of Pharmaceutics 2013;456(2):282-292.

(138) Eloy JO, Marchetti JM. Solid dispersions containing ursolic acid in Poloxamer 407 and PEG 6000: A comparative study of fusion and solvent methods. Powder Technology 2014;253:98-106.

(139) Ghosh I, Snyder J, Vippagunta R, Alvine M, Vakil R, Tong W(, et al. Comparison of HPMC based polymers performance as carriers for manufacture of solid dispersions using the melt extruder. International Journal of Pharmaceutics 2011;419(1):12-19.

(140) Milovanovic S, Djuris J, Dapčević A, Medarevic D, Ibric S, Zizovic I. Soluplus®, Eudragit®, HPMC-AS foams and solid dispersions for enhancement of Carvedilol dissolution rate prepared by a supercritical CO2 process. Polymer Testing 2019;76:54-64.

(141) Alonzo DE, Gao Y, Zhou D, Mo H, Zhang GGZ, Taylor LS. Dissolution and Precipitation Behavior of Amorphous Solid Dispersions. Journal of Pharmaceutical Sciences 2011;100(8):3316-3331.

(142) BASF SE. Technical Information Soluplus. 2010.

(143) Shamma RN, Basha M. Soluplus®: A novel polymeric solubilizer for optimization of Carvedilol solid dispersions: Formulation design and effect of method of preparation. Powder Technology 2013;237:406-414.

(144) Reginald-Opara JN, Attama A, Ofokansi K, Umeyor C, Kenechukwu F. Molecular interaction between glimepiride and Soluplus®-PEG 4000 hybrid based solid dispersions: Characterisation and anti-diabetic studies. International Journal of Pharmaceutics 2015;496(2):741-750.

(145) Homayouni A, Sadeghi F, Varshosaz J, Afrasiabi Garekani H, Nokhodchi A. Promising dissolution enhancement effect of soluplus on crystallized celecoxib obtained through antisolvent precipitation and high pressure homogenization techniques. Colloids and Surfaces B: Biointerfaces 2014;122:591-600.

(146) Fule R, Amin P. Development and evaluation of lafutidine solid dispersion via hot melt extrusion: Investigating drug-polymer miscibility with advanced characterisation. Asian Journal of Pharmaceutical Sciences 2014;9(2):92-106.

(147) Costa BLA, Sauceau M, Del Confetto S, Sescousse R, Ré MI. Determination of drug-polymer solubility from supersaturated spray-dried amorphous solid dispersions: A case study with Efavirenz and Soluplus®. European Journal of Pharmaceutics and Biopharmaceutics 2019;142:300-306.

(148) Fong SYK, Ibisogly A, Bauer-Brandl A. Solubility enhancement of BCS Class II drug by solid phospholipid dispersions: Spray drying versus freeze-drying. International Journal of Pharmaceutics 2015;496(2):382-391.

(149) Pezzoli R, Lyons JG, Gately N, Higginbotham CL. Stability studies of hot-melt extruded ternary solid dispersions of poorly-water soluble indomethacin with poly(vinyl pyrrolidone-co-vinyl acetate) and polyethylene oxide. Journal of Drug Delivery Science and Technology 2019;52:248-254.

(150) Wang B. No title. Development of spray drying technology for microencapsulation of bioactive materials 2015.

(151) Sawicki E, Beijnen JH, Schellens JHM, Nuijen B. Pharmaceutical development of an oral tablet formulation containing a spray dried amorphous solid dispersion of docetaxel or paclitaxel. International Journal of Pharmaceutics 2016;511(2):765-773.

(152) Chen L, Okuda T, Lu X, Chan H. Amorphous powders for inhalation drug delivery. Advanced Drug Delivery Reviews 2016;100:102-115.

(153) Taki M, Tagami T, Ozeki T. Preparation of polymer-blended quinine nanocomposite particles by spray drying and assessment of their instrumental bitterness-masking effect using a taste sensor. Drug Dev Ind Pharm 2017;43(5):715-722.

(154) Lu Z, Yang Y, Covington R, Bi Y(, Dürig T, Ilies MA, et al. Supersaturated controlled release matrix using amorphous dispersions of glipizide. International Journal of Pharmaceutics 2016;511(2):957-968.

(155) Gohel M, Parikh RK, Nagori SA, Gandhi AV, Shroff MS, Patel PK, et al. Spray drying: A review. Pharmaceutical Reviews 2009;7.

(156) Anamur C, Winter G, Engert J. Stability of collapse lyophilized influenza vaccine formulations. International Journal of Pharmaceutics 2015;483(1):131-141.

(157) Chen S, Guo D, Guo B, Liu J, Shen Y, Xu X, et al. Investigation on formulation and preparation of adenovirus encoding human endostatin lyophilized powders. International Journal of Pharmaceutics 2012;427(2):145-152.

(158) Freeze-Drying of Proteins, Formulation and Delivery of Proteins and Peptides. ACS Symp. Ser.; 1994.

(159) Abdelwahed W, Degobert G, Stainmesse S, Fessi H. Freeze-drying of nanoparticles: Formulation, process and storage considerations. Advanced Drug Delivery Reviews 2006;58(15):1688-1713.

(160) Morais, Andreza Rochelle do Vale, Alencar ÉdN, Xavier Júnior FH, Oliveira CMd, Marcelino HR, Barratt G, et al. Freeze-drying of emulsified systems: A review. International Journal of Pharmaceutics 2016;503(1):102-114.

(161) Singh A, Worku ZA, Van dM. Oral formulation strategies to improve solubility of poorly water-soluble drugs. Expert Opinion on Drug Delivery 2011;8(10):1361-1378.

(162) Colombo S, Brisander M, Haglöf J, Sjövall P, Andersson P, Østergaard J, et al. Matrix effects in nilotinib formulations with pH-responsive polymer produced by carbon dioxide-mediated precipitation. International Journal of Pharmaceutics 2015;494(1):205-217.

(163) Jelić D, Liavitskaya T, Vyazovkin S. Thermal stability of indomethacin increases with the amount of polyvinylpyrrolidone in solid dispersion. Thermochimica Acta 2019;676:172-176.

(164) Bertoni S, Albertini B, Ferraro L, Beggiato S, Dalpiaz A, Passerini N. Exploring the use of spray congealing to produce solid dispersions with enhanced

indomethacin bioavailability: In vitro characterization and in vivo study. European Journal of Pharmaceutics and Biopharmaceutics 2019;139:132-141.

(165) Xie T, Gao W, Taylor LS. Impact of Eudragit EPO and hydroxypropyl methylcellulose on drug release rate, supersaturation, precipitation outcome and redissolution rate of indomethacin amorphous solid dispersions. International Journal of Pharmaceutics 2017;531(1):313-323.

(166) Pan X, Julian T, Augsburger L. Quantitative measurement of indomethacin crystallinity in indomethacin-silica gel binary system using differential scanning calorimetry and X-ray powder diffractometry. Aaps Pharmscitech 2006;7(1):E72-E78.

(167) Khanfar M, Al-Taani B, Alsmadi M, Zayed A. Enhancement of the dissolution and bioavailability from freeze-dried powder of a hypocholesterolemic drug in the presence of Soluplus. Powder Technol 2018;329:25-32.

(168) Duff Jr MR, Grubbs J, Howell EE. Isothermal titration calorimetry for measuring macromolecule-ligand affinity. JoVE (Journal of Visualized Experiments) 2011(55):e2796.

(169) Wang B, Liu F, Xiang J, He Y, Zhang Z, Cheng Z, et al. A critical review of spray-dried amorphous pharmaceuticals: Synthesis, analysis and application. Int J Pharm 2021;594:120165.

(170) Salawi A, Nazzal S. The rheological and textural characterization of Soluplus®/Vitamin E composites. International Journal of Pharmaceutics 2018;546(1):255-262.

(171) Ward A, Walton K, Stoycheva S, Wallis M, Adebisi A, Nep E, et al. The use of visible and UV dissolution imaging for the assessment of propranolol hydrochloride in liquisolid compacts of Sesamum radiatum gum. Journal of Drug Delivery Science and Technology 2020:101511.

(172) Spireas S, Wang T, Grover R. Effect of powder substrate on the dissolution properties of methyclothiazide liquisolid compacts. Drug Dev Ind Pharm 1999;25(2):163-168.

(173) Nokhodchi A, Hentzschel CM, Leopold CS. Drug release from liquisolid systems: speed it up, slow it down. Expert opinion on drug delivery 2011;8(2):191-205.

(174) Kaialy W, Bello H, Asare-Addo K, Nokhodchi A. Effect of solvent on retarding the release of diltiazem HC l from Polyox-based liquisolid tablets. J Pharm Pharmacol 2016;68(11):1396-1402.

(175) Nokhodchi A, Aliakbar R, Desai S, Javadzadeh Y. Liquisolid compacts: The effect of cosolvent and HPMC on theophylline release. Colloids and Surfaces B: Biointerfaces 2010;79(1):262-269.

(176) Chella N, Shastri N, Tadikonda RR. Use of the liquisolid compact technique for improvement of the dissolution rate of valsartan. Acta Pharmaceutica Sinica B 2012;2(5):502-508.

(177) Javadzadeh Y, Jafari-Navimipour B, Nokhodchi A. Liquisolid technique for dissolution rate enhancement of a high dose water-insoluble drug (carbamazepine). Int J Pharm 2007;341(1-2):26-34.

(178) Nep EI, Carnachan SM, Ngwuluka NC, Kontogiorgos V, Morris GA, Sims IM, et al. Structural characterisation and rheological properties of a polysaccharide from sesame leaves (Sesamum radiatum Schumach. & Thonn.). Carbohydrate Polymers 2016;152:541-547.

(179) Nep E, Asare-Addo K, Ngwuluka N, Conway BR, Smith AM. Evaluation of sesamum gum as an excipient in matrix tablets. British Journal of Pharmacy 2016;1(1).

(180) Trivedi V, Nandi U, Maniruzzaman M, Coleman NJ. Intercalated theophylline-smectite hybrid for pH-mediated delivery. Drug delivery and translational research 2018;8(6):1781-1789.

(181) Adebisi AO, Conway BR, Asare-Addo K. The influence of fillers on theophylline release from clay matrices. American Journal of Pharmacological Sciences 2015;3(5):120-125.

(182) Aguzzi C, Cerezo P, Viseras C, Caramella C. Use of clays as drug delivery systems: possibilities and limitations. Appl Clay Sci 2007;36(1-3):22-36.

(183) Totea A, Dorin I, Gavrilov G, Laity PR, Conway BR, Waters L, et al. Real time calorimetric characterisation of clay–drug complex dispersions and particles. International journal of pharmaceutics: X 2019;1:100003.

(184) Gil EC, Colarte AI, Bataille B, Pedraz JL, Rodríguez F, Heinämäki J. Development and optimization of a novel sustained-release dextran tablet formulation for propranolol hydrochloride. International Journal of Pharmaceutics 2006;317(1):32-39.

(185) Javadzadeh Y, Musaalrezaei L, Nokhodchi A. Liquisolid technique as a new approach to sustain propranolol hydrochloride release from tablet matrices. Int J Pharm 2008;362(1-2):102-108.

(186) Takeuchi Y, Tomita T, Kuroda J, Kageyu A, Yonekura C, Hiramura Y, et al. Characterization of mannitol granules and powder: A comparative study using two flowability testers. Int J Pharm 2018;547(1):106-113.

(187) Bartolomei M, Bertocchi P, Ramusino MC, Santucci N, Valvo L. Physico-chemical characterisation of the modifications I and II of (R, S) propranolol hydrochloride: solubility and dissolution studies. J Pharm Biomed Anal 1999;21(2):299-309.

(188) Javadzadeh Y, Musaalrezaei L, Nokhodchi A. Liquisolid technique as a new approach to sustain propranolol hydrochloride release from tablet matrices. International Journal of Pharmaceutics 2008;362(1):102-108.

(189) Nep EI, Mahdi MH, Adebisi AO, Ngwuluka NC, Conway BR, Smith AM, et al. Hydro-alcoholic media effects on theophylline release from sesamum polysaccharide gum matrices. Drug Dev Ind Pharm 2018;44(2):251-260.